

Final Report
for the
**FAA UAS Center of Excellence Task A4: UAS
Ground Collision Severity Evaluation**
Revision 2

**Mr. David Arterburn, Principal Investigator – arterbd@uah.edu
Director, Rotorcraft Systems Engineering and Simulation Center
The University of Alabama in Huntsville**

**Dr. Mark Ewing – mewing@ku.edu
Associate Professor and Director of the Flight Research Laboratory
The University of Kansas**

**Dr. Raj Prabhu – praj@cavs.msstate.edu
Professor, Department of Agricultural and Biological Engineering
Mississippi State University**

**Dr. Feng Zhu – Feng.Zhu@erau.edu
Assistant Professor, Mechanical Engineering Department
Embry-Riddle Aeronautical University**

**Dr. David Francis – dfrancis@cavs.msstate.edu
Post-Doctoral Researcher, Center for Advanced Vehicular Systems
Mississippi State University**

SECURITY STATEMENT: There is no classified or proprietary information in this report.

DISTRIBUTION A: Distribution is unlimited

Legal Disclaimer

The information provided herein may include content supplied by third parties. Although the data and information contained herein has been produced or processed from sources believed to be reliable, the Federal Aviation Administration makes no warranty, expressed or implied, regarding the accuracy, adequacy, completeness, legality, reliability or usefulness of any information, conclusions or recommendations provided herein. Distribution of the information contained herein does not constitute an endorsement or warranty of the data or information provided herein by the Federal Aviation Administration or the U.S. Department of Transportation. Neither the Federal Aviation Administration or the U.S. Department of Transportation shall be held liable for any improper or incorrect use of the information contained herein and assumes no responsibility for anyone's use of the information. The Federal Aviation Administration and U.S. Department of Transportation shall not be liable for any claim for any loss, harm, or other damages arising from access to or use of data or information, including without limitation any direct, indirect, incidental, exemplary, special or consequential damages, even if advised of the possibility of such damages. The Federal Aviation Administration shall not be liable to anyone for any decision made or action taken, or not taken, in reliance on the information contained herein.

Revision History

Revision	Description of Change	Release Date
-	Initial Release as required by Contract	27 Oct 2016
1	<ul style="list-style-type: none"> - Changed footnotes to first citing only unless second reference is included in Figures or Tables throughout document - page 12 – changed eighteen knowledge gaps to twenty three knowledge gaps in the overview. - page 15 changed "but where pre-approved." to "but were pre-approved." In the first paragraph of section 1.2.2 - page 20 changed “to combined” to “to be combined” at the end of the second paragraph of 2.4.6 - page 22 changed “it important” to “It is important” on the second paragraph of section 2.5.1 - page 23 Table 5 change “should” to “Shoulder” in the first row of the Upper Limbs section - page 27 reference 41 was changed from http://www.faa.gov/uas/publications/media/Micro-UAS-ARC-FINAL-Report.pdf to https://www.faa.gov/uas/resources/uas_regulations_policy/media/Micro-UAS-ARC-FINAL-Report.pdf due to the FAA changing the location of the document. - page 28, section 2.7 changed rate of "3.57x10⁻³ fatalities per flight hour" to rate of "3.57x10⁻⁸ fatalities per flight hour" - page 46,47 Figure 6,7 and 8 updated with complete legends - page 84, section 4.9 changed "most baseball fatalities (25 (58 percent) were" to <i>“He was able to confirm 104 deaths with baseball accounting for 43 (41 percent) of them. Of the 43 total baseball fatalities, 25 (58 percent) were due to blows to the head.”</i> - page 85, Section 4.9.1 changed “where” to “were” in the paragraph below Table 32 - page 86, section 4.10.1 deleted rotational energy equation and moment of inertia equation since these equation were already introduced in Equation 5 and 6. Updated all follow-on numbering for equations including those in the text. - page 87, paragraph below Figure 24 “k3” was changed to k₃ 	8 Mar 2017
2	Added a new Figure and Table based upon comments from the FAA following Peer Review and Public Release preparation. Figures 23 and Table 29 were added to show the results of steel and wood impact studies that were conducted after completion of the A4 Task. Edits to the paragraphs were made to discuss the results shown in Figure 23 and Table 29. Added legal disclaimer per FAA request.	28 Apr 2017

Acknowledgements:

The following researchers in addition to the respective university Principal Investigators shown on the title page made fundamental contributions to the content of this UAS Characteristics White Paper, the Ground Collision Final Report and the dialogue with the FAA A4 Project Management Office, Micro-Air Advisory Rulemaking Committee, and UAS Science and Research Panel during the first half of this project – Dr. Brian Landrum (UAH), Mr. Christopher Duling (UAH), Mr. Nishanth Goli (UAH), Mr. Drew Darrah (KU), and Mr. Eric Bodlak (KU).

The A4 team would like thank the following Program Managers and subject matter experts from the FAA – Mr. William Oehlschlager, Mr. Wes Ryan, Mr. Christopher Swider, Mr. Paul Campbell, Mr. Ben Walsh, Mr. Paul Albuquerque and Mr. Paul Rumberger.

The A4 team also recognizes the vital importance of the exchange of ideas with the A3 Air Collision Severity Evaluation team members including Mr. Tom Aldag, Task A3 Principal Investigator, and Dr. Robert Huculak, Wichita State University, and Dr. Doug Cairns, Montana State University, as well as the continued dialogue with the ASSURE Leadership throughout this project.

Executive Summary

The UAS Ground Collision Severity Evaluation Final Report documents the UAS platform characteristics related to the severity of UAS ground collision based upon the literature search of over 300 publications from the automotive industry, consumer battery market, toy standards, and other fields. The literature search included existing standards from a variety of industries and applications as well as methods of analysis and criteria currently in use by other civil and federal agencies. Space debris casualty models were evaluated and extended for proposed use with UAS to determine their viability for ground collision severity assessments and metrics. Parametric analysis, summary data and modified methods are presented to provide insight on the most significant UAS characteristics and how such characteristics are related to the ground collision severity problem. Qualitative characteristics as well as quantitative metrics are presented. Data and Analysis developed during the Task A11 research is also included to update data collected in the early phases of Task A4. Where needed, knowledge gaps are identified for topics outside the scope of the current research.

The literature search included the evaluation of various criteria developed for human blunt force trauma injuries, penetration injuries and laceration injuries. These injury types represent the most significant threats to the non-participating public and crews operating mUAS and sUAS platforms. The kinetic energy for the worst case terminal velocity or maximum cruise airspeed, energy density, and rotor diameter are the most significant UAS characteristics contributing to blunt force trauma penetration and laceration injuries, respectively.

Two impact kinetic energy methodologies are presented to provide a risk and scenario based approach to determining kinetic energy thresholds for safe UAS operations. Parachute mitigations and the application of area weighted kinetic energy methodology for two scenarios are presented to outline thresholds for a broader range of vehicle weights to conduct flight over people than is currently possible with the unmitigated vehicle designs currently available. An initial investigation of energy transfer based on crash testing and dynamic modeling was conducted along with finite element analysis for human head and torso impacts. The crash test results and subsequent analysis strongly suggest that RCC-based thresholds are overly conservative because they do not accurately represent the collision dynamics of elastically-deformable sUAS with larger contact areas in comparison to the metallic debris analysis methods for high speed missiles on the national test ranges. Dynamic modeling is necessary to improve the assessment of UAS failure modes and associated impact energy, to establish appropriate standoff distances, to model impact footprints for severity analysis and to conduct probability assessments as part of an applicant's submission for waiver or certification.

Lithium Polymer batteries dominate the mUAS and sUAS market as the principle energy source for these platforms. While many of the manufacturers state they test their batteries in accordance with Lithium Ion battery testing methods for consumer electronics, the batteries are rarely marked to show compliance with these standards and many of the test methods are not consistent with the forces and energy levels associated with ground collision impact energy. More research is required to address the fire hazard and impact hazard presented by the broad spectrum of batteries and battery chemistries used in mUAS and sUAS platforms.

Twenty-three knowledge gaps were identified during the execution of the literature search and are recommended for future research efforts.

Table of Contents

Executive Summary	5
Table of Contents	6
List of Figures	8
List of Tables	11
1. Overview (UAH).....	13
1.1. Objectives and Research Tasks Based on FAA Research Questions	13
1.2. UAS Characteristics Research Tasks.....	14
2. Severity Definition Review and Discussion (UAH).....	17
2.1. Review of FAA Severity Definition	17
2.2. Standard Man Definitions	18
2.3. Collision Scenarios (KU).....	18
2.4. Discussion of Injury Categories (KU).....	20
2.5. Survey of Injury Criteria	23
2.6. Analysis of Existing Standards and Recommendations for sUAS-related Severity Definitions	27
2.7. Academy of Model Aeronautics (AMA) Operational and Injury Data (UAH).....	29
2.8. Property Standards (KU)	29
2.9. Recommendations for sUAS-Related Severity Definitions (UAH/KU).....	30
3. Discussion of UAS Design Attributes	30
3.1. Vehicle Characteristics Contributing to Ground Collision Severity (UAH)	30
4. Collision Severity Metric Study (UAH)	50
4.1. Potential Injuries Associated with UAS Ground Collision	50
4.2. Impact KE Without Injury Correlation (UAH)	51
4.3. Evaluation of the Modified Area-Weighted KE Threshold Method (UAH).....	63
4.4. KE Sports Ball Analogy (UAH)	65
4.5. Evolution of RCC Standards and Their Applicability to UAS Ground Collisions. (UAH).....	65
4.6. Differences Between UAS Collisions and Low Mass, High Volume Debris Following In-flight Breakup (UAH).....	66
4.7. Larger Contact Area of UAS vs. Fragments. (UAH)	67
4.8. Impact Energy Correlated to Potential Injury Severity (UAH).....	68
4.9. Energy Density and Penetration Injuries (UAH)	85
4.10. Rotating Components and Laceration Injuries (KU)	89

4.11. Standoff Distances and Relationship to Severity (UAH).....	101
4.12. Structural Standards for Sheltering (KU).....	103
4.13. Vehicle Standards (UAH)	110
4.14. Modeling, Analysis, and Recommended Severity Criteria	111
4.15. Head Impact Modeling (MSU)	117
4.16. Study of Primary Impact Criteria (ERAU).....	126
4.17. Frangibility Analysis (KU).....	138
4.18. Knowledge Gaps Associated with Finite Element Analysis Modeling.....	142
4.19. Additional Research Proposed to Address Research Gaps	144
5. Conclusions and Recommendations.....	145
5.1. Key mUAS and sUAS Characteristics.....	145
5.2. Discussion of AIS, HIC and VC, and Respective Applicability to Ground Collision Severity Evaluation	146
5.3. Establishment of mUAS and sUAS Thresholds Other Than RCC.....	146
5.4. Parachute Standards for Category 3 and 4 Operations	147
5.5. Standoff Metrics and UAS Ground Collision Modeling.....	147
5.6. Ground Collision Severity of LiPo Batteries.....	148
5.7. Knowledge Gaps	148
Appendix A: Nomenclature.....	A-1
Appendix B: Aircraft Characterization Tables	B-1
Appendix C: Aircraft Characteristics and Energy Data	C-1
Appendix D: Major Categories of sUAS and Defining Design Attributes	D-1
Appendix E: Knowledge Gap Roundup	E-1
Appendix F: Laceration Testing Materials	F-1
Appendix G. Results of UAS/ATD impact simulations	G-1
Appendix H. Parametric Values of the Meta Model to Describe the VC Response of ATD Chest Due to UAS Impact.....	H-1
Appendix I. Results of UAS/Ground Impact Simulations	I-1
Appendix J. Parametric Values of the Meta Model to Describe the Rebound Distance of UAS After Collision on the Ground.....	J-1

List of Figures

Figure 1 Gadd Severity Index	25
Figure 2 - Ground Collision Severity Taxonomy Defined for the A4 Task.....	31
Figure 3 - Model Outputs Detailing the Collision of a 3 lbs Object with a 6 lbs Object.....	36
Figure 4 -Model Outputs Detailing a Collision Between a 3 lbs Object and a 200 lbs Object	37
Figure 5 - Low Order Modeling of Impact KE Transfer Based on Vehicle and Body CG Offset.....	38
Figure 6 - Comparison of Estimated Terminal Velocity for Several Manned Aircraft and UAS Departing Controlled Flight from 400 ft AGL '.....	47
Figure 7 - Comparison of Estimated Kinetic Energy for Several Manned Aircraft, UAS and UAS Payloads Departing Controlled Flight from 400 ft AGL'	48
Figure 8 - Estimated Terminal KE for UAS and Manned Aircraft'	49
Figure 9 - Comparison Between Rotor Rotational KE for UAS and Manned Aircraft Classes.'	50
Figure 10 - Injury/Fatality Thresholds from Various Studies	52
Figure 11 - Janser KE Thresholds.....	53
Figure 12 - Example Kill Probability Chart and Feinstein Single-Point KE Values ⁴⁶	54
Figure 13 - Probability of Fatality from Debris Impacts for Various Body Parts	55
Figure 14 - Probability of Fatality from Debris Impacts for Various Body Positions	56
Figure 15 - Average Probability of Fatality from Debris Impacts	57
Figure 16 - Janser Standard Man Dimensions and Calculated Projected Areas	58
Figure 17 - Top View of Sled Setup for UAS Drop	70
Figure 18 - Front Left View of Sled Setup (upper left), Vertical Drop Position of Dummy and UAS (upper right), Pendulum Setup for Horizontal Impact Test (lower left), and Dummy and UAS Setup for Angle Impact Test (lower right)	70
Figure 19 - Example NIAR Test Summary for an Individual Test.....	72
Figure 20 - Example NIAR Time History for an Individual Test	72
Figure 21 - Analysis of Phantom 3 Resultant Force for Skull Fractures versus Impact KE.....	80
Figure 22 - Probability of Neck Injury Trends from NIAR Test Data	81
Figure 23 - Resultant Force versus Impact KE for Steel, Wood and Phantom 3	83
Figure 24 - Potential Collisions between UAVs and a Human Head.....	85
Figure 25 - Rotor Speed vs. Rotor Diameter for Multi-Rotor UAS, Compared with APC RPM Curve.....	90
Figure 26 - Rotor Speed vs. Rotor Diameter for Multi-Rotor UAS, Compared with APC RPM Curve.....	91
Figure 27 - Notional injury severity index vs. rotor diameter for reported incidents''	93
Figure 28 – Laceration Testing Setup	94
Figure 29 – Example of Deep Laceration from Propeller Strike.....	94
Figure 30 – Injury Severity vs. Tip Velocity	95
Figure 31 - Lacerations on Syndaver Artificial Skin from Multiple Blade Impacts, Both with and without Blade Guards.....	96
Figure 32 - Laceration length vs impact velocity with and without blade guards	97
Figure 33 - Rotor Enclosures in Existing Micro UAS'.....	98
Figure 34 - Suggested Safety Feature for Toy Rotors.....	99
Figure 35 - Probes for determination of IP Code ratings.....	100
Figure 36 - Example Ballistic Modeling of a Falling Multi-Rotor Aircraft.....	101
Figure 37 - Diagram of sUAS Operating in Vicinity of People (Baseball Stadium Example).....	102
Figure 38 - Penetration Effects on Type A Roof Structure (per Table 40 definition of roofing types)	109

Figure 39 - Images from the Phantom 2 CFD Analysis.....	113
Figure 40 - Plot of Drag Coefficient Versus Airspeed for Phantom 2 CFD Simulations	114
Figure 41 - Phantom 2 Limited Flight Test Telemetry Data; Rate of Descent vs. Time (upper left), Altitude vs. Time (upper right), and Attitude vs. Time (lower)	115
Figure 42 - Relation of MGTOW to KE at Terminal Velocity for Multi-Rotor UAS <4.4 lbs.....	116
Figure 43 - Relation of MGTOW to KE at Terminal Velocity for Fixed Wing UAS < 10 lbs.....	117
Figure 44 - Deflection of the Drone during Simulation #4. The colors represent the following time steps: Green 0 ms, Orange 0.5 ms, Red 1 ms, Blue 1.5 ms.....	120
Figure 45 - Phantom 3 Standard Fuselage Deformation During NIAR 50-foot Drop Test Impacts (Test UA17A-13).....	120
Figure 46 - Mesh of the Human Head and Phantom 3.....	121
Figure 47 - Spherical Coordinate System for Head Impact Simulations.....	122
Figure 48 - Acceleration vs Time History for DOE Simulations	123
Figure 49 - RBFN Result Using a Multiquaric Minimization Approach	125
Figure 50 - Stress Wave (von Mises) Propagation through the Skull at Times (a) 0, (b) 0.375, (c) 1, and (d) 1.275 ms	126
Figure 51 - Stress Wave (von Mises) Propagation through the Brain at Times (a) 0, (b) 0.19, (c) 0.5, and (d) 0.813 ms	126
Figure 52 - Coordinate System Definition in the Ground Collision Analysis.....	126
Figure 53 - (Left) CAD model and (Right) FE Model for a Fixed Wing UAS GZ500	127
Figure 54 - (Left) CAD model and (Right) FE model with details for a rotary wing UAS Phantom 3	127
Figure 55 - Typical ATD/UAS Interaction Simulated with the FE Model.....	128
Figure 56. Contour Diagrams Showing the Relationship between Energy Absorption by Torso and VC Values and Impact Parameters (UAS type; material; θ and V)	129
Figure 57 - Comparison of the VC results predicted by the meta model and numerical simulations.	130
Figure 58 - UAS Collision on the Ground and Rebound	131
Figure 59 - Model Predicted Rebound Behavior of a Rotary Wing UAS (Phantom 3) Collision on the Ground ($V=32.8$ ft/s; $\theta=60^\circ$)	132
Figure 60 - Comparison of the Rebound Distance of UAS Predicted by Meta Model and Numerical Simulations	133
Figure 61 - ATD Torso Model (left) and Human Torso Model (right)	134
Figure 62. Human Torso Modeling Procedure.....	135
Figure 63 - Model Simulated Typical Deformation Response of Human Torso under the Impact of UAS ($\theta=90^\circ$; $V=30$ m/s (98.4 ft/s)): (a) Aluminum Fixed Wing; (b) Aluminum Rotary Wing.....	137
Figure 64 - Comparison of Model-Predicted Displacement-Time History of ATD and Human Torso under the Impact of UAS ($\theta=90^\circ$; $V=30$ m/s (98.4 ft/s)).....	138
Figure 65 - Comparison of Model predicted Compression Velocity-Time History of ATD and Human Torso under the Impact of UAS ($\theta=90^\circ$; $V=30$ m/s (98.4 ft/s)).....	138
Figure 66 – Model for Analysis of Frangibility Effect on Impact	139
Figure 67 - Kinetic Energy Needed for Failure of Quadcopter Boom Compared with Kinetic Energy Transferred Based on Theoretical Flight Condition $u_1 = 50$ ft/s	141
Figure 68 - Kinetic Energy Needed for Failure of Quadcopter Boom Compared with Kinetic Energy Transferred Based on Theoretical Flight Condition $u_1 = 20$ ft/s	141
Figure 69 - Frangibility Zones for Impact at Different Attitudes.....	142

Figure 70 - Impact Modeling with Guarding and Bracing Postures.....	143
Figure 71 - Head and Neck Impact Modeling.....	144
Figure 72 - Posterior UAS Impact Modeling.....	144
Figure D - 1 - Multi-Rotor UAS with Monocoque Body Construction.....	D-2
Figure D - 2 - Multi-Rotor UAS with Modular Construction.....	D-2
Figure D - 3 - Fixed Wing UAS with Flying Wing Configuration.....	D-3
Figure D - 4 - Fixed Wing UAS with Standard Configuration.....	D-4
Figure D - 5 - Helicopter-Style RW UAS	D-5
Figure D - 6 - Smooth Contours on Fuselage (DJI Phantom on left); Sharp Edges on Fuselage (3DR Solo on right)	D-5
Figure D - 7 - Sharp edges on Fuselage main body (left); Plastic casing on the main body (right)	D-6
Figure D - 8 - Low Order Offset Collision Modeling of Multi-Rotor UAS Offset Impact	D-6
Figure D - 9 - Fixed wing UAS with conical-shaped fuselage and fore-mounted engine/propellers (Upper Red/White aircraft); Rounded Leading Edge and Nose Cone (Lower Black and Yellow aircraft). D-7	D-7
Figure D - 10 - Propeller with Sharp LE (left); Propeller with Sharp LE and Rounded Corners (right)	D-9
Figure D - 11 - Propeller Guards (left); Shrouded Propellers (right).....	D-9
Figure D - 12 - Folding Propellers	D-10
Figure D - 13 - Smart Battery and Internal Compartment (left) Battery Held Firmly inside Fuselage (right).....	D-11
Figure D - 14 - Battery Mounted above Main Body with Velcro (left); Battery Mounted Below Main Body (right).....	D-11
Figure D - 15 - LiPo battery Held Firmly inside FW UAS (left), LiPo Battery Mounted Loosely inside FW UAS (right).....	D-12
Figure D - 16 - Rear-Mounted Engine on a 50 lbs UAS (left); LiPo Batteries inside the Fuselage of a 33 lbs UAS (right).....	D-13
Figure D - 17 - Batteries on Side of Fuselage (left); Batteries inside the Fuselage Belly (right).....	D-14
Figure D - 18 - Skid Landing Gear (left); Pointed Cantilever Landing Gear (center); Continuous Landing Gear (right).....	D-14
Figure D - 19 - Retracted Landing Gear	D-15
Figure D - 20 - Fixed Wing UAS with Skid Landing Gear (left); Standard Landing Gear (right)	D-15
Figure D - 21 - Camcopter S-100 Landing Gear	D-16
Figure D - 22 - Small Gimbals and Camera (left); Large Gimbals and Cameras (right)	D-16
Figure D - 23 - UAS with Internal Payloads or Landing Gear.....	D-17
Figure D - 24 - Payload inside the Fuselage (left); Payload Protruding Outside the Fuselage (right)	D-18
Figure D - 25 - Visual Warning Systems on Multirotor UAS (left); Parachutes on Multirotor UAS (right).....	D-19
Figure D - 26 - Fixed Wing UAS with Landing and Position Lights (left) and Parachutes (right)	D-21

List of Tables

Table 1 - Severity Definitions for the FAA AMS Process ¹⁷	17
Table 2 - SMS Manual Version 4.0 Hazard Severity Definitions.....	18
Table 3 – UAS-Related Injury Concerns and Their Respective Applications	19
Table 4 - Correlation of UAS Airframes with Mission Types and Flight Profiles	19
Table 5 - Examples of Injuries and Respective AIS Ratings.....	24
Table 6 - Head Injury Criterion Thresholds for Various Dummy Sizes.....	26
Table 7 – Micro-UAS ARC Recommended FAA Allowable Rates of Serious (or worse) Injury Due to an Impact with a Person on the Ground ⁴¹	28
Table 8. Results of Modelling Collision of a 3 lbs with 6 lbs and 200 lbs Objects.....	35
Table 9 - Battery Types and Models from Proposed Battery Failure Research	39
Table 10 - Testing Content of Lithium Ion Battery Standards ^{58,59,60}	41
Table 11 - Battery Standards Adopted by UAS/LiPo Companies	41
Table 12 - Comparison of NASA 50 th Percentile Male and Janser Standard Man Anthropometric Model Dimensions	58
Table 13 – Area Weighted KE Thresholds by Body Position and POF from the RCC (Derived from Figure 13).....	60
Table 14 - Area Projections for UAS Analysis of Weighted KE for an Open Area.....	60
Table 15 - Area Weighted KE Values for UAS in an Open Area.....	61
Table 16 - Weight of Vehicle Derived from Parachute Descent Rates and Area Weighted KE Thresholds for Flight Over People in an Open Air Scenario such as a City Park.....	62
Table 17 - Projected Area for UAS Analysis of a Rock Concert with Standing Room Only	63
Table 18 - Area Weighted KE Thresholds for UAS Rock Concert Example.....	63
Table 19 - Weight of Vehicle Derived from Parachute Descent Rates and Area Weighted KE Thresholds for Flight Over People in a Rock Concert.....	63
Table 20 - RCC KE Thresholds and Comparisons with Sports Balls.....	65
Table 21 - Injury Characteristics for Some Common Objects	68
Table 22 - UAS Drop Testing Summary.....	69
Table 23 - NIAR Instrumentation for UAS Drop Tests	71
Table 24 - NIAR Summary Test Results and Injury Metrics.....	74
Table 25 - Difference in Injury Metrics Between FMVSS 208 and RCC Standards.....	75
Table 26 - Resultant Head Forces from NIAR Tests.....	77
Table 27 –Biomechanical Data for All Skull Fractures from Gurdjian	78
Table 28 –Biomechanical Data of Skull Fracture Tests Using a 48mm Radius Hydraulic Anvil.....	79
Table 29 – Vertical Drop Test Comparison of Steel and Wood with Phantom 3	83
Table 30 - Comparison of RCC Standards vs. Modified Impact Energy Thresholds for Various Aircraft Weights when Descending under Parachute.....	85
Table 31 - Skin Penetration Threshold Energy Density Values from Literature”	86
Table 32 - Excerpt from Transport Canada's Low Energy RPA Standard.....	87
Table 33 - Impact Energy Density for Various Vehicles and Impact Contact Areas	88
Table 34 - Rooftop KE Absorption Values.....	104
Table 35 - Side Wall KE Absorption Values	104
Table 36 - Type and Size of Materials Used for Impact Testing ¹¹³	105
Table 37 - Case Study of 3 Historical Impacts	106

Table 38 - Mass Burning Rate, Heat of Combustion, and Thermal Flux for Select Fuels ⁴³	107
Table 39 - Ballistic Coefficient Classes for Debris Roof Penetration Analysis	108
Table 40 - Representative Roof Classes for Debris Penetration Analysis	109
Table 41 - STARCCM+ Coefficient of Drag Estimates for the Phantom 2 UAS.....	112
Table 42 - L16 Orthogonal Array for DJI Phantom 3.....	118
Table 43 - Elastic Material Properties for UAS Impact Simulation.....	119
Table 44 - Conversion from Named Locations to Spherical Coordinates.....	121
Table 45 - Configurations of the Four FE UAS Models	128
Table 46. Material Properties of Bones and Soft Tissues in the Human Torso Model.....	136
Table B - 1 - Multi-Rotor mUAS Parameters	B-2
Table B - 2 - FW mUAS/sUAS Parameters.....	B-3
Table C - 1 - Aircraft Characteristics and Energy Data.....	C-1
Table C - 2 Aircraft Characteristics and Energy Data Continued.....	C-2
Table F - 1 - Blades and Motors Used In Testing.....	F-1
Table G - 1 - Aluminum Fixed Wing UAS.....	G-1
Table G - 2 - Engineering Plastic Fixed Wing UAS.....	G-3
Table G - 3 - Aluminum Rotary Wing UAS.....	G-5
Table G - 4 - Engineering Plastic Rotary UAS.....	G-7
Table H - 1 - Parametric Values in Equation 19.....	H-1
Table I - 1 - Aluminum Fixed Wing UAS	I-1
Table I - 2 - Engineering Plastic Fixed Wing UAS.....	I-2
Table I - 3 - Aluminum Rotary Wing UAS.....	I-3
Table I - 4 - Engineering Plastic Rotary Wing UAS.....	I-4
Table J - 1 - Parametric Values in Equation 21.....	J-1

1. Overview (UAH)

The Task A4 Ground Collision Severity Evaluation is being executed by the University of Alabama in Huntsville (UAH), the University of Kansas (KU), Mississippi State University (MSU) and Embry-Riddle Aeronautical University (ERAU). UAH serves as the Principle Investigator for this task and collected inputs for this Final Report from each of the universities in their respective areas as assigned by the research plan¹ submitted to the Federal Aviation Administration (FAA). This report includes the results of the literature search and subsequent analysis conducted by the team to address the research questions shown in Paragraph 1.1. The team has used emerging data from this report to brief the Micro-Air Advisory Rule Making Committee (ARC), to advise members of the UAS Science and Research Panel (SARP) working ground collision and advise members of the Federal Aviation Administration (FAA) working on Rule 107 since the inception of the contracts in September 2015. This document serves as the final deliverable under the Task A4 contract. The results and data in this report have been updated since the June 2016 White Paper on UAS Characteristics based on research progress made through September 2016. Results of modeling efforts being conducted by MSU and ERAU are included in this report. Additionally, UAH has updated this report to reflect the results and some of the data from Task A11 – Part 107 Waiver Request Case Study where the data compliments or informs data collected as part of Task A4.

Probability of collision was not addressed in this report as directed by the FAA. While probability of fatality (POF) is a metric incident to collision severity, these probabilities are used as a source of defining collision severity and not risk calculations.

The team has identified twenty-three knowledge gaps in this report that are outside the scope of the current work and proposes topics that are candidates for or have been submitted as white papers for future work.

1.1. Objectives and Research Tasks Based on FAA Research Questions

The FAA requested that the team address the following research questions during the course of the Ground Collision Severity Evaluation Project.

- 1) What are the hazard severity criteria for a UAS collision (weight, kinetic energy (KE), etc.)?
- 2) What is the severity of a UAS collision with aircraft on the ground?
- 3) What is the severity of a UAS collision with property on the ground?
- 4) What is the severity of a UAS collision with a person on the ground?
- 5) What are the characteristics of a UAS where it will not be a risk to an aircraft or person/property on the ground?
- 6) Can the severity of a UAS collision with an aircraft or person/property on the ground be characterized into UAS categories and what would those categories look like?
- 7) How can UAS be designed as to minimize the potential damage done during a collision?

¹ A4 Ground Collision Severity Research Plan, 15 December 2015

1.2. UAS Characteristics Research Tasks

1.2.1. Overview of the UAS Impact to Public Safety

Technological advancements in the area of unmanned aircraft systems have significantly increased the capability of these aircraft and the desire to use these platforms for a wide variety of missions; however, the associated safety standards for these platforms operating in the National Airspace System (NAS) in terms of certification of vehicles and pilots have not kept pace. Consumer interest has increased greatly because of the demonstrated versatility of these aircraft in both commercial and hobbyist uses. This increase in use has been marked by a commensurate increase in accidents resulting in blunt impact or laceration injuries to bystanders. News media have reported multiple cases where drones flown for recreational or approved filming reasons have caused injuries to people.²³⁴ Newly founded groups, such as Know Before You Fly⁵, have helped to encourage safety by establishing community-based standards. Know Before You Fly is an educational campaign led by the Academy of Model Aeronautics (AMA), Association of Unmanned Vehicle Systems International (AUVSI), and the FAA that is working to educate prospective hobbyist and commercial UAS users about the basic regulatory and safety requirements for operating these platforms. The majority of available research related to bystander safety only contains statistics-based location and population density models that assess risk and safety.⁶⁷⁸⁹¹⁰ These models have largely been developed or have their genesis in the development of casualty models developed to assess safety of space vehicles traversing population centers during launch and reentry. Furthermore, researchers and journalists have focused on the hazards associated with a drone flying in close proximity of an airplane while drawing parallels to bird strikes with aircraft.¹¹¹²¹³ Ground collision impact hazards and their influence on public opinion and rulemaking has not been as noticeable to journalists, but the FAA and the other users of the National Airspace System

² Russon, Mary-Ann, "Drone pilot accidentally knocks himself out with his own quadcopter [Video]," <<http://www.ibtimes.co.uk/drone-pilot-accidentally-knocks-himself-out-his-own-quadcopter-video-1509171>>, Accessed 18 May 2015.

³ Shepard, Dwight B. "Drone hits man in head during Marblehead Memorial Day parade," <http://www.masslive.com/news/index.ssf/2015/05/drone_hits_man_in_head_during.html>. Accessed 18 May 2015.

⁴ Taillier, Sarah. "Triathlete injured as drone filming race falls to ground," <<http://www.abc.net.au/news/2014-04-07/triathlete-injured-as-drone-filming-race-drops-to-ground/5371658>>. Accessed 18 May 2015.

⁵ Know Before You Fly, <www.knowbeforeyoufly.com>, Accessed May 19, 2016.

⁶ Clothier, Reece A., Walker, Rodney A., Fulton, Neale, & Campbell, Duncan A., "A Casualty Risk Analysis for Unmanned Aerial System (UAS) Operations Over Inhabited Areas," AIAC12 – Twelfth Australian International Aerospace Congress, 2nd Australasian Unmanned Air Vehicles Conference, Melbourne, March 2006.

⁷ Dalamagkidis, Konstantinos, Valavanis, Kimon P., Piegel, Les, A., "Evaluating the Risk of Unmanned Aircraft Ground Impacts," 16th Mediterranean Conference on Control and Automation, , June 2008, pp. 709–716.

⁸ Magister, Tone, "The small unmanned aircraft blunt criterion based injury potential estimation," *Safety Science*, Vol. 48, 2010, pp. 1313-1320.

⁹ Weibel, Roland E., Hansman, Jr., R. John. "Safety Considerations for Operation of Different Classes of UAVs in the NAS," , 2004, pp. 1-11.

¹⁰ Wu, Paul, Clothier, Reece A. "The Development of Ground Impact Models for the Analysis of the Risks Associated with Unmanned Aircraft Operations Over Inhabited Areas," , 2012.

¹¹ Peck, Michael, "Close Encounters of the Drone Kind," *Aerospace America*, American Institute of Aeronautics and Astronautics, November 2015, pp. 18–23

¹² "UAS Safety Analysis," *Exponent*, Project No. 1408989.EX0, December 2016, pp. 1-12,

¹³ Smith, W. Hulsey, Main III, Freddie L. "The Real Consequences of Flying Toy Drones in the National Airspace System," *Aero Kinetics Aviation*, 2015, pp. 2-26.

(NAS) have taken notice. Minimal and consistent certification requirements and safety standards of drones based upon their specific operations are needed to increase public acceptance and safety of the general public as well as to maintain the level of safety in the NAS when operating in and among manned aircraft. Failure to develop this regulatory framework for drones is clearly a threat to public safety, and the lack of standards for drones could be due to the lack of experimental data available and irregular comparison of statistical models.¹⁴

1.2.2. UAS Characterization to Support FAA Regulation

The team conducted an extensive review of UAS characteristics that is largely focused on small and micro UAS platforms. These results are qualitatively summarized in Appendix D. These smaller aircraft, as opposed to UAS platforms that are closer to manned aircraft vehicles in terms of weight and speed (such as Shadow, Scan Eagle, Predator, and Global Hawk), are made of different materials than the larger platforms, utilize different construction techniques than manned aircraft and fall into ballistic and aerodynamic regions that are not well documented in terms of their collision severity potential and operational performance. This paper focuses on sUAS based on their configuration (monocoque multi-rotor, modular/collapsible multi-rotor, flying wing fixed wing, standard configuration fixed wing, and helicopter style UAS) and how their fundamental characteristics affect crash lethality to the non-participating public and/or resultant damage to objects and structures. The paper addresses larger vehicles to provide insight as to where sUAS platforms and larger UAS platforms begin to take on characteristics similar to manned aircraft and should be regulated in similar methods to manned aircraft. The analysis of literature search data in conjunction with the credible encounter scenarios has been used to create a taxonomy or classification of vehicle characteristics and encounter characteristics that the FAA and industry can use as a basis for determining standards for certification among the UAS classes and potentially derive new classes of UAS platforms in terms of certification requirements and safety standards.

The focus of the literature research is to define the UAS platform's ability to transfer energy to a person, property or aircraft on the ground during a collision or following blade contact and to define the UAS design characteristics that determine the severity of the collision such as mass, speed, altitude and materials/construction, etc. AUVSI provided the ASSURE Team with access to their database of UAS platforms to support this research effort.¹⁵ The database includes countries from all over the world and provides data necessary to characterize classes of vehicles in terms of their mass, speed, size, etc. The database provided a starting point from which to assess particular characteristics of these vehicles. The data was used to begin developing potential metrics that can be defined by vehicle weight, speed and altitude of operation. The A4 Team coordinated with other members of the ASSURE Team with diverse UAS platform experience and sUAS manufacturers to gain a deeper understanding of the data that was derived from the AUVSI database. The A4 Team also used vehicles and components from various universities and those donated from 3DR and DJI to obtain additional data on platforms to validate the information within the database. The team also received crash damaged and new aircraft and components from DJI and 3DR for analysis. Industry and ASSURE partner school vehicles have been used to assess information, such as mass distribution of various vehicles, to develop parametric data

¹⁴ Elands, P.J.M., de Kraker, J.K., Laarakkers, J., Olk, J.G.E., Schonagen, J.J., "Technical Aspects Concerning the Safe and Secure Use of Drones," TNO Report, March 2016, pp. 1-77,.

¹⁵ <http://roboticsdatabase.auvsi.org/home>, Accessed 05/25/16

that can be used in the modeling and parametric analysis. The team evaluated the FAA Section 333 exemption database¹⁶ to determine the sUAS that are most commonly being used for various types of commercial work. This data was valid up until March 2016 when the FAA began providing exemptions that included a large blanket list of vehicles, which were not necessarily owned by a commercial entity, but were pre-approved. This exemption data helps refine credible use cases and encounter scenarios because it provides a snapshot of what sUAS operators are requesting for use within the national airspace. Furthermore, the exemptions are dominated by sUAS and not larger UAS platforms giving credence to broader coverage of sUAS platforms in the early stages of this research.

Knowledge Gap: FAA Registry data includes vehicle types for commercial operators. Both the aircraft registry and the UAS on-line registry need to be continuously harvested to maintain a clear understanding of actual vehicles that are being used across the National Airspace System (NAS) to refine the research focus of the A4 and other tasks.

The literature survey has identified a significant amount of data and analytical methods from the medical, ballistic, non-lethal munitions, regulatory documents, design standards, and fundamental scientific fields of research to determine appropriate injury severity standards and identify engineering metrics that correlate to levels of injury. Aerodynamic and collision modeling of various UAS has been completed in order to assess sUAS injury and damage potential based on thresholds identified in the literature survey. Analysis has been performed in a variety of areas to address knowledge gaps within the literature in order to better define vehicle characteristics for impact energy and laceration potential from blades for inclusion in this report. Further knowledge gaps that have yet to be addressed by this report or are beyond the scope of this effort are also defined in this report based on the literature search.

To provide a common framework, UAS in this paper are categorized based on their physical design and construction characteristics which affect how they transfer and retain energy during a collision. This framework divides UAS into five major categories. Multi-rotor UAS can be classified into configuration categories with monocoque construction and modular/collapsible construction. Similarly, fixed-wing UAS can be classified into flying wing and standard configurations, respectively. Helicopter-style rotary wing UAS, with either a single main rotor and tail rotor configuration or a tandem rotor configuration, compose the final category. The ground collision severity evaluation of these vehicles remains rooted in quantifying risks associated with laceration, blunt impacts, and ignition sources. However, it is also useful to have a more descriptive overview of the various designs and their related attributes across the five major categories of UAS. The qualitative discussion of current aircraft designs, provided in Appendix D, provides an overview of various sUAS design features with a discussion on the effect of each feature on collision and injury severity. This material is placed in Appendix D because it is more descriptive and qualitative in nature versus being rooted in engineering metrics. The main body of this report focuses on the vehicle parametric analysis and recommended characterization metrics. The qualitative analysis of aircraft also provides an overview of current hazard mitigating design concepts and attributes. This mitigation discussion is based on survey of the AUVSI database, research on manufacturer websites, and discussions with the manufacturers and owners of various aircraft models. All sections of this report

¹⁶ https://www.faa.gov/uas/legislative_programs/section_333/333_authorizations/, Accessed 05/25/16

identify knowledge gaps in literature and modeling inputs and these gaps are summarized in Appendix E: Knowledge Gap Roundup.

2. Severity Definition Review and Discussion (UAH)

2.1. Review of FAA Severity Definition

For the purposes of this analysis, the FAA directed the team to look at the most credible severity conditions for fatal injuries. The team originally used the definitions of the FAA System Safety Handbook¹⁷ (listed in Table 1) to define injuries due to ground collision. Any injury to the general public or personnel on the ground is defined as hazardous.

Table 1 - Severity Definitions for the FAA AMS Process¹⁷

Catastrophic	Results in multiple fatalities and/or loss of the system
Hazardous	Reduces the capability of the system or the operator ability to cope with adverse conditions to the extent that there would be: Large reduction in safety margin or functional capability Crew physical distress/excessive workload such that operators cannot be relied upon to perform required tasks accurately or completely (1) Serious or fatal injury to small number of occupants of aircraft (except operators) Fatal injury to ground personnel and/or general public
Major	Reduces the capability of the system or the operators to cope with adverse operating condition to the extent that there would be – Significant reduction in safety margin or functional capability Significant increase in operator workload Conditions impairing operator efficiency or creating significant discomfort Physical distress to occupants of aircraft (except operator) including injuries Major occupational illness and/or major environmental damage, and/or major property damage
Minor	Does not significantly reduce system safety. Actions required by operators are well within their capabilities. Include Slight reduction in safety margin or functional capabilities Slight increase in workload such as routine flight plan changes Some physical discomfort to occupants or aircraft (except operators) Minor occupational illness and/or minor environmental damage, and/or minor property damage
No Safety Effect	Has no effect on safety

The FAA provided the Safety Management System (SMS) Manual Version 4.0¹⁸ that included different definitions of injury severity, including fatalities, for personnel other than the UAS crew. Table 2 from the SMS Manual shows the severity definitions that raise the fatality definition for persons other than the UAS crew from hazardous to catastrophic. The research presented in this report defines fatalities based on the Table 2 definitions. Since probability was not considered as part of this research, the definitions are sufficiently consistent to understand the most credible scenarios under these definitions without need for labeling the severity as hazardous or catastrophic.

¹⁷ https://www.faa.gov/regulations_policies/handbooks_manuals/aviation/risk_management/ss_handbook/, Accessed 05/25/16

¹⁸ https://www.faa.gov/air_traffic/publications/media/faa_ato_sms_manual_v4_20140901.pdf, Accessed 05/25/16

Table 2 - SMS Manual Version 4.0 Hazard Severity Definitions¹⁸

Hazard Severity Classification					
<i>Note: Severities related to ground-based effects apply to movement areas only.</i>					
	Minimal 5	Minor 4	Major 3	Hazardous 2	Catastrophic 1
CONDITIONS RESULTING IN ANY ONE OF THE FOLLOWING:					
ATC Services	A minimal reduction in ATC services CAT D Runway Incursion ¹ Proximity Event, Operational Deviation, or measure of compliance greater than or equal to 66 percent ²	Low Risk Analysis Event severity, ³ two or fewer indicators fail CAT C Runway Incursion	Medium Risk Analysis Event severity, three indicators fail CAT B Runway Incursion	High Risk Analysis Event severity, four indicators fail CAT A Runway Incursion	Ground collision ⁴ Mid-air collision Controlled flight into terrain or obstacles
Unmanned Aircraft Systems	Discomfort to those on the ground Loss of separation leading to a Measure of Compliance greater than or equal to 66 percent	Low Risk Analysis Event severity, two or fewer indicators fail Non-serious injury to three or fewer people on the ground	Medium Risk Analysis Event severity, three indicators fail Non-serious injury to more than three people on the ground A reduced ability of the crew to cope with adverse operating conditions to the extent that there would be a significant reduction in safety margins Manned aircraft making an evasive maneuver, but proximity from Unmanned Aircraft remains greater than 500 feet	High Risk Analysis Event severity, four indicators fail Incapacitation to Unmanned Aircraft System crew Proximity of less than 500 feet to a manned aircraft Serious injury to persons other than the Unmanned Aircraft System crew	A collision with a manned aircraft Fatality or fatal injury to persons other than the Unmanned Aircraft System crew

Standard Man Definitions

The team conducted the collision severity analysis using the definition of the Janser Standard Man,¹⁹ which closely correlates to the NASA 50th Percentile male. This definition was considered to be relevant to other safety analyses conducted by the FAA and to remain consistent with other safety analyses conducted by the Range Commander’s Council (RCC).²⁰

2.3. Collision Scenarios (KU)

The team also focused on collision scenarios that lead to fatalities and those that could lead to permanent disability. The specific scenarios are discussed in various sections of this document to define impact metrics and to relate how altitude under various scenarios relates to collision severity. While permanent disability is not considered a metric in FAA safety definitions, permanent disability is used in Department of Defense (DoD) and other injury metrics. Permanent disability will likely dominate injury severity and define public acceptance of sUAS when operating near or over people in the near term due

¹⁹ Janser, P.W. “Lethality of Unprotected Persons Due to Debris and Fragments,” Twentieth Explosives Safety Seminar, August 1982

²⁰ Range Commander’s Council, “Common Risk Criteria for National Test Ranges; Inert Debris”, April 2000

to the likelihood of laceration injuries that have limited potential for fatality but have already caused publicly documented permanent disability injuries.

To determine a suite of ground collision scenarios representative of small UAS, one approach is to base the set of scenarios on the types of injuries to be considered. Table 3 lists five such scenarios.

Table 3 – UAS-Related Injury Concerns and Their Respective Applications

Largest Injury Concern	Applications
Head and Shoulders	Real Estate, Surveying, Construction Photography, Wildlife Observation, Flood Planning, Crop Inspection, Emergency Response, Recreational Use
Face and Torso	Drone Racing, FW aircraft takeoff and landing, Remote Sensing, Search and Rescue
Lacerations	Television Filming, News Filming, Weddings, Flight Training
Payload to Head and Shoulders	Crop Management, UAS Delivery
Chemical / Fire	Wildfire Fighting, Chemical Transport

Table 4 lists flight scenarios representing the 5 categories along with the UAS type, speed and altitude.

Table 4 - Correlation of UAS Airframes with Mission Types and Flight Profiles

Largest Injury Concern	Example Flight Scenario	Type of UAS Used	Typical Altitude and Forward Speed
Head and Shoulders	Real Estate Photography	Quadcopters	High altitude, Low speed
Face and Torso	Drone Racing	Quadcopters or Fixed Wing	Low altitude, High speed
Lacerations	Wedding Filming	Quadcopters	Low Altitude, Low Speed
Payload to Head and Shoulders	UAS Delivery	Quadcopters	High Altitude, Medium Speed
Fire	Wildfire Fighting	Quadcopters	Medium Altitude, Medium Speed
Chemical	Crop Spraying	Quadcopters / Helicopters	Medium Altitude, Medium Speed

2.4. Discussion of Injury Categories (KU)

2.4.1. Head and Shoulders Injury Applications

Since most of the applications listed in the 333 exemptions include flying a sUAS with a mounted camera to take pictures or video, the head and shoulder injury category is by far the largest. sUAS taking pictures will be hovering in place often and slowly flying from location to location to capture images, so quadcopters are the sUAS of choice for this application.

Jobs like real estate, surveying, and construction site photography could occur in almost any area, and while they may occur over a small closed site, there could still be bystanders nearby depending on the location. UAS may need to fly off-site in certain instances to capture different angles, but will remain mainly in a controllable area and will maintain relatively low airspeeds.

Other uses, like agriculture inspection, wildlife observation, and flood relief/planning would occur in very sparsely populated areas all the time. In jobs like these, a UAS operator would fly over large plots of land with very few bystanders and inspect and report on different factors of the land, wildlife, or crops. It is unlikely that contact with any non-UAS personnel will occur during these jobs, but since head and shoulder injury is the most likely out of the selected categories, these jobs are part of this group. These applications may be performed using beyond visual line of sight technology like first person view goggles, if allowed under the anticipated Part 107 requirements for beyond visual line of sight flight.

Emergency response applications for UAS use the UAS in a support role, where it is used to gain an aerial view of an emergency site and assist with ground responders. The UAS would be equipped with a camera and/or spotlight and launched on site by an operator. This application has a lot of inherent risk, as flying in the airspace of an emergency could be dangerous for other aircraft in the vicinity, and the population on the ground could be dense if the emergency is in a metropolitan area like New York City. Quadcopters are the main choice for these jobs, as they can be easily launched and landed on site and are flexible in that they can either hover over a situation or quickly move from one location to the next depending on the mission.

2.4.2. Face and Torso Injury Applications

For the face and torso to be the most likely injury locations, the sUAS must be flying with a forward velocity such that the kinetic energy damage caused by the sUAS to a person would be greater than laceration damage at that speed. The sUAS must maintain at least part of this forward velocity all the way to the ground for the most likely injuries to be to the face and torso. If it is falling straight down the more likely injury locations are the head and shoulders. This means applications with mission profiles that have high velocities present the most risk for face and torso injury. Currently, these applications are drone racing, remote sensing, and search and rescue.

Drone racing involves flying custom built or augmented commercially produced sUAS head-to-head through a closed course. In order to maneuver these courses quickly and to see where the UAS is going at all times, racers use cameras and special first-person view goggles to pilot the UAS. In order to be allowed to do this by the FAA, very strict rules are in place to enter a competition, including an insurance check to ensure the event will be covered in case of an accident. Rigorous checks are also performed on the UAS brought by competitors to ensure their airworthiness. Quadcopters are the sUAS of choice for drone racing, as they are highly maneuverable and can take tight turns, and can also sprint when needed.

Depending on the venue and course layout for a drone race, bystanders could be very close to the course. This may change in the coming years as the sport becomes more commercialized since bystanders will likely be kept far away from the course to prevent injury. The main dangers for bystanders are the kinetic energy during sprints and lacerations from rotors. Weight is important in these competitions, as are the aerodynamics of the sUAS. With these things in mind, pilots tend to avoid damage through mitigation technology like rotor guards.

Remote sensing involves flying over areas to obtain information about the area using a suite of sensors. The data obtained and sensors used will depend on the mission at hand, but the sUAS will likely need to cover large distances so fixed wing will be the configuration of choice for this job. Remote sensing is another application where bystanders will be rare, but since the sUAS used will have a large forward velocity, face and torso injuries are more likely than head and shoulder injuries.

Search and rescue would use the sUAS in a similar fashion as emergency response. The main reason the search and rescue scenario is included in the face and torso injury category rather than head and shoulder injury category is the fact that search and rescue needs to cover a lot of ground in most cases, whereas emergency response occurs in a specific known area. This ground coverage requirement leads to high velocity sUAS being used for the job, predominately fixed wing sUAS. This requirement also means high forward velocities will be present during the UAS flight, meaning face and torso injuries are the most likely.

2.4.3. Laceration Injury Applications

For jobs like news and wedding filming, UAS will be flown near densely populated areas in order to capture good images and videos. These UAS will fly at low speeds and low altitudes, so laceration injuries are more likely than blunt force trauma or penetration. Again, for these jobs a camera will be mounted to the UAS and used to take images and videos. Due to the close proximity to dense populations that these jobs present and the fact that untrained bystanders will be flown over, a low-cost and effective mitigation measure is needed.

Flight training will almost always occur without any bystanders or flight over people, other than the UAS operator and crew, as it usually takes place at a controlled site with very strict rules on UAS use. These rules help to offset the inexperience of pilots, but accidents can still happen. Laceration injuries will be most likely, as the pilots will be in close proximity with not only their UAS, but other pilots' UAS. The pilots will also be grabbing their UAS often, which could lead to lacerations on the hands or arms if care is not taken. Multiple UAS could be in use, depending on the layout of the training, and a variety of maneuvers could take place.

2.4.4. Payload Loss Injury Applications

For some UAS applications, such as delivery services, there is a risk of losing the payload in flight. Amazon Prime Air began testing their prototype package delivery UAS in 2015 and have stated it will weigh a maximum of 55 lbs, including a 5 lbs payload, and will fly at a max speed of 50 mph at a max height of 300 ft. If one of these 5 lbs payloads were to drop from the UAS, it could cause serious injury.

Another UAS application involving a payload is crop management, where UAS are fitted with a sprayer and tank of herbicides or fertilizer. The UAS then flies a pattern over a field and sprays the crops. The tanks attached to the UAS are very heavy, weighing 12 to 22 lbs depending on the size of the UAS, and

could do a lot of damage if they were to strike a person, most likely the pilot or crew. It is very unlikely that bystanders would be near the field.

2.4.5. Fire Injury Applications

The main fire concern for all sUAS is ignition of a battery upon crash. While battery fires can cause injury, they could occur in any battery powered UAS crash. Battery fire hazards in a ground collision sequence are poorly documented and require further research (some discussed in A4 characteristics paper, see Section 3.1.2.1).

Currently, UAS are mainly used for observation of wildfires with fighting them being a secondary role. There are, however, some technologies that allow UAS to assist in other ways. For example, a University of Nebraska team designed a UAS mountable hopper system that drops balls filled with potassium permanganate powder. As the balls are prepped to be dropped, they are injected with liquid glycol which causes them to catch flame seconds later. This technology can be used to start controlled burns or backfires safely. Transporting these two chemicals together is dangerous, however, as a crash could cause a fire in an unintended location and cause loss of property or life.

2.4.6. Chemical Injury Applications

One of the few occurrences of sUAS carrying chemicals currently is during crop spraying. While blunt injury to the head and shoulders is most likely the event of a payload loss or crash, the chemicals in the tank could be harmful to humans if dropped on them. These chemicals could also damage the environment if dropped in a sensitive location, like a river or lake.

Another occurrence of sUAS carrying chemicals is the fire starting UAS discussed in the previous section. The chemicals contained in the sUAS may burst into flame when combined, but are relatively harmless on their own. This is a case where the chemicals must be combined to do damage, and as such should be contained in a way that makes it difficult for them to be combined unless it is intended.

As UAS technology advances, more and more applications that transport chemicals like the firefighting assisting UAS are being implemented. Special precautions will need to be taken depending on the chemical in the UAS. One good source of direction for these precautions is the FMCSA (Federal Motor Carrier Safety Administration) code on federal hazardous materials regulations. The FMCSA lists hazardous material regulations that could be used to protect bystanders and property during sUAS chemical transport. Another source for design direction is the Department of Defense Design Criteria for shipping containers (MIL-STD-648C). This document lists design criteria and tests, including multiple drop tests, for containers carrying hazardous materials. Such well-developed programs may easily form the basis for establishing mitigation standards, if required by the FAA.

2.5. Survey of Injury Criteria

2.5.1. Abbreviated Injury Standard (UAH/MSU)

The Abbreviated Injury Scale (AIS)²¹ is an internationally accepted metric for ranking injury severity. The AIS began in the early 1970's with the goal of grouping injuries in automobile crashes.^{22,23} The AIS provides a 1-6 score based on the injury using a standardized medical manual and set of definitions. There is a large crossover between the AIS and the Injury Severity Scale (ISS). Since its beginning, the AIS standard has had multiple revisions with the last update in 2008.²⁴ Based on this early work, many more systems to assess injuries have been developed (e.g. NISS, TRISS, ASCOT, ICISS); however, the AIS/ISS are heavily integrated into trauma centers along with much supporting documentation to assist in injury severity assessment by clinicians.²⁵ As such, AIS/ISS is the preferred method for categorization of injury severity.

It is important to state that the AIS Dictionary provides post-injury assessment of wounds incurred during automobile accidents based on treatment standards in emergency medicine. The injury ratings are normalized to the capabilities and medical knowledge of the emergency room physicians. As such, the injury severity ratings may seem lower than a lay person would expect because, regardless of the apparent trauma of an injury, it may be easily treatable with very low potential for lethality. Examples of injuries and their respective AIS ratings are provided in Table 5. Based on Task A11 Part 107 Waiver Request Case Study, vehicle impact energies can be correlated to AIS (Section 4.8) based on impact collision tests with test dummies. The correlation of these results allows AIS to be used as a viable metric for the evaluation of vehicle safety when determined as a function of impact energy.

²¹ Association for the Advancement of Automotive Medicine Website, <http://www.aaam.org/about-ais.html>. Accessed 02/15/2016

²² States, J., Fenner, H., Flamboe, E., Nelson, W. et al., "Field Application and Research Development of the Abbreviated Injury Scale," SAE Technical Paper 710873, 1971.

²³ Baker, Susan P., O'Neill, Brian, Haddon, William, Jr., Long, William B., "The injury severity score: a method for describing patients with multiple injuries and evaluating emergency care," *Journal of Trauma and Acute Care Surgery*, Vol. 14, pp. 187-196, 1974.

²⁴ Association for the Advancement of Automotive Medicine, *Abbreviated Injury Scale © 2005 Update 2008*, Barrington, IL (2008).

²⁵ Senkowski, Christopher K., McKenney, Mark G., "Trauma scoring systems: a review," *Journal of the American College of Surgeons*, Vol. 189, pp. 491-503, 1999.

Table 5 - Examples of Injuries and Respective AIS Ratings

Body Part	Injury	AIS Rating
Head	Penetrating Injury - Superficial; ≤ 2cm beneath the entrance	AIS 2
	Laceration resulting in blood loss of > 20% by volume	AIS 3
	Total scalp loss or blood loss of > 20% by volume	AIS 3
	Severing of the Optic Nerve	AIS 2
	Severing of the Facial Nerve	AIS 3
Brain	Superficial cerebellum contusions ≤ 15cc; 1-3 cm	< AIS 3
	Concussive Injury Loss of Consciousness 1-6 hours	AIS 3
	All other concussions	AIS 2
Face	Penetrating Injury; with blood loss > 25 cm ²	AIS 2
	Penetrating Injury with blood loss 20% by volume	AIS 3
	Massive destruction of whole face including both eyes	AIS 4
	Complete separation of the facial bones from their cranial attachments or any injury resulting in blood loss > 20% by volume	AIS 3
Neck	Penetrating Injury with blood loss 20% by volume	AIS 3
	Bilateral laceration of the Carotid Artery	AIS 3
Upper Limbs	Single amputation at the shoulder	AIS 4
	Amputation of a single hand, partial of complete	AIS 2
	Amputation of the thumb	AIS 2
	Amputation of other fingers, single or multiple	AIS 1

2.5.2. Head Impact and Damage Metrics (UAH/MSU)

Methods used to classify traumatic brain injuries (TBI) began in the 1960s. Researchers studying impacts on cadaver heads developed a simple metric to predict the potential hazards of accelerations in the head.^{26, 27} This metric, called the Gadd Severity Index, was the first to correlate head impacts. The equation for the Gadd Severity Index is shown in Equation (1). This index recognizes that the duration (t) of an acceleration (a) of the brain is the contributing factor to TBI. The safe and unsafe regions of the Gadd Severity Index are shown in Figure 1.

$$1000 = t \times a^{2.5} \quad \text{Equation 1}$$

²⁶ Lissner, HR. "Experimental Studies on the Relation between Acceleration and Intracranial Pressure Changes in Man." *Surgery, Gynecology and Obstetrics*, Vol. 111, pp. 329–38, 1960.

²⁷ Gadd, C. "Use of a Weighted-Impulse Criterion for Estimating Injury Hazard." *SAE Technical Paper 660793*, 6, 1966.

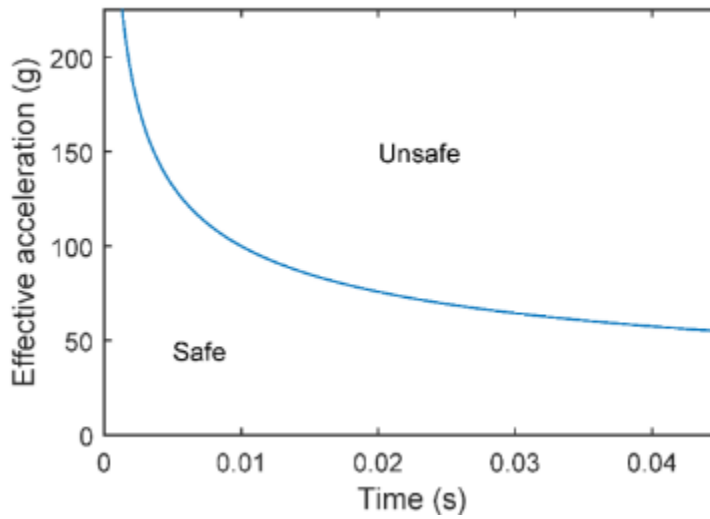


Figure 1 Gadd Severity Index

In the 1970s the Head Injury Criterion (HIC) was developed to assess the likelihood of skull fracture and brain injury based on head acceleration of a test dummy’s head over time. HIC only considers a scalar acceleration’s time history.²⁸ Instead of combining the time and acceleration as a polynomial function, the HIC integrates the acceleration over time to take the form of Equation 2.

$$HIC = \left\{ \left[\frac{1}{t_2 - t_1} \int_{t_1}^{t_2} a(t) dt \right]^{2.5} (t_2 - t_1) \right\}_{\max} \quad \text{Equation 2}$$

The terms t_1 and t_2 in Equation 2 are the beginning and end time for the HIC interval. Generally, the interval is 15 or 36 ms, and therefore the terms HIC15 and HIC36 are used to represent these metrics. For the HIC₁₅ and HIC₃₆ parametric estimation, the value for t_1 is determined by maximizing the HIC value. As of March 2000, HIC₁₅ has been the standard head injury assessment criterion used by the National Highway Transportation Safety Administration (NHTSA).²⁹ However, an increasing amount of academic effort has been expended in the past decade to challenge the notion that only a scalar acceleration vs time profile is needed to adequately predict and diagnose TBIs. Other metrics that are also being considered are angular velocities, angular accelerations, volumetric pressure, shear

²⁸ Versace, John. “A Review of the Severity Index,” SAE Technical Paper 710881, 1971.

²⁹ Eppinger, R., Sun E., Kuppa, Shashi, Supplement Development of Improved Injury Criteria for the Assessment of Advanced Automotive Restraint Systems – II, National Highway Transportation Safety Administration, March 2000

stress/strain, and maximum g-force.^{30'31'32'33'34} However, because the HIC metric has been so heavily used, there is a much larger data set available in the literature to compare current studies against. Table 6 provides the HIC₁₅ thresholds based on various Anthropomorphic Test Dummy (ATD) sizes.

Table 6 - Head Injury Criterion Thresholds for Various Dummy Sizes²⁹

Dummy Type	Large Sized Male*	Mid-Sized Male	Small Sized Female	6-Year-Old Child	3-Year-Old Child	1-Year-Old Infant
HIC ₁₅ Limit	700	700	700	700	570	390

To synergize the A4 team efforts, the HIC15 and g-force data taken from head impact simulations will be correlated to the AIS values based on the available experimental data in the literature regarding traumatic brain injury.^{35'36'37} By correlating the AIS with the HIC15, the A4 team is able to correlate POF with the AIS 1-6 scale, where 1 is a minor injury and 6 is not survivable. Fatality due to an injury does not automatically make the injury rating AIS 6. An injury classified as AIS 2 or greater denotes that the injury may result in a fatality without treatment or if treatment is not received within a timely manner. AIS has also been correlated to POF, which allows some level of cross referencing to other studies that map blunt trauma impact energy levels to POF.³⁸ An AIS rating of 1 equates to a 0% POF, and an AIS 6

³⁰ Takhounts, Erik, Matthew Craig, Kevin Moorhouse, Joe McFadden, and Vikas Hasija. "Development of Brain Injury Criteria (BrIC)." *Stapp Car Crash Journal* 57 (2013): 243–66.

³¹ Olvey, Stephen E, Ted Knox, and Kelly A Cohn. 2004. "The Development of a Method to Measure Head Acceleration and Motion in High-impact Crashes," *Neurosurgery* 54 (3) (March): pp. 672–677

³² Weaver, Christopher S, Brian K Sloan, Edward J Brizendine, and Henry Bock. 2006. "An Analysis of Maximum Vehicle G Forces and Brain Injury in Motorsports Crashes," *Medicine and Science in Sports and Exercise* 38 (2) (February): pp. 246–249.

³³ Prabhu, R., Horstemeyer, M.F., Tucker, M.T., Marin, E.B., Bouvard, J.L., Sherburn, J.A., Liao, Jun, Williams, Lakiesha N., "Coupled experiment/finite element analysis on the mechanical response of porcine brain under high strain rates," *Journal of the Mechanical Behavior of Biomedical Materials*, Vol. 4, pp. 1067–1080, 2011.

³⁴ Sarah Sullivan, Stephanie A. Eucker, David Gabrieli, Connor Bradfield, Brittany Coats, Matthew R. Maltese, Jongho Lee, Colin Smith, Susan S. Margulies, "White matter tract-oriented deformation predicts traumatic axonal brain injury and reveals rotational direction-specific vulnerabilities," *Biomechanics and Modeling in Mechanobiology*, Vol. 14, pp. 877–896, 2015.

³⁵ Rowson, Steven, Duma, Stefan M., "Development of the STAR Evaluation System for Football Helmets: Integrating Player Head Impact Exposure and Risk of Concussion," *Annals of Biomedical Engineering*, Vol. 39, pp. 2130-2140, 2011.

³⁶ Rowson, Steven, Duma, Stefan M., Beckwith, Jonathan G., Chu, Jeffrey J., Greenwald, Richard M., Crisco, Joseph J., Brolinson, P. Gunnar, Duhaime, Ann-Christine, McAllister, Thomas W., Maerlender, Arthur C., "Rotational Head Kinematics in Football Impacts: An Injury Risk Function for Concussion," *Annals of Biomedical Engineering*, Vol. 40, pp. 1-13, 2012.

³⁷ Vos, P. E., Battistin, L., Birbamer, G., Gerstenbrand, F., Potapov, A., Prevec, T., Stepan, Ch. A., Traubner, P., Twijnstra, A., Vecsei, L., Wild, K. von, "EFNS guideline on mild traumatic brain injury: report of an EFNS task force," *European Journal of Neurology*, Vol. 9, pp. 207-219, 2002.

³⁸ http://web.iitd.ac.in/~achawla/public_html/736/6-injury%20severity%20coding-v2.pdf, Accessed 01/15/16

rating is 100% fatal. However, this is a qualitative comparison only. There is no definitive documentation that correlates an estimated 10% POF in one study with a similar estimated 10% POF in another study.

2.5.3. Viscous Criterion (ERAU)

It has been reported in the literature that neither chest compression degree nor velocity alone is sufficient to be applied as the criterion for the thoracic injury under blunt impact. A more sophisticated criterion, known as the Viscous Criterion (VC), is the most promising injury indicator in analyzing chest and thoracic injuries and it is further quantified in the modeling work.

The viscous criterion was first introduced by Lau and Viano^{39,40} to predict the severity of chest injury induced by impact. Human tolerance was defined by the Viscous Criterion response [VC], a time function generated by the instantaneous product of velocity of deformation [V(t)] and amount of compression of the body [C(t)]. This criterion assesses the risk of soft tissue and rib injury by a rate-dependent viscous injury mechanism and has been adopted by a number of vehicle crash safety standards. Considerable studies have been conducted to investigate the effect of body compression [C(t)] on the injury, but there is less research on the influence of [V(t)]. In other words, the sensitivity of thoracic injury to the chest wall deflection velocity is still not very clear. Comprehensive impact simulations with a Hybrid-III ATD chest model, together with a detailed sensitivity analysis on the effect of [V(t)] will help answer this question. In addition, a more precise quantitative relationship between [VC] value and AIS value needs to be established. A non-linear regression analysis on the impact parameters and response will be conducted to achieve this goal.

The focus is placed on the frontal impact in the current project. The existing injury criterion for the vehicle frontal impact safety standards can be used in its existing form, which comes directly from the automotive industry. However, back impacts have not been studied in the automotive industry and require significant work to determine if viscous criterion can be applied to this type of impact. UAV impact to the back is relevant to the operational context of UAS in a ground collision scenario and is particularly dangerous because a person is less able to respond to and protect him or herself from this kind of impact. The injury mechanism of back impact is expected to be different since the injury will likely be dominated by spine damage, while the mechanisms of front impact are mainly rib fracture and internal organ rupture. A new criterion is therefore needed.

2.6. Analysis of Existing Standards and Recommendations for sUAS-related Severity

Definitions

2.6.1. Injury Classifications (KU)

There are no existing, recognized standards for sUAS-related injury severity classifications and or ways to align those injury classifications with the FAA safety definitions. However, severity classifications/definitions for injury to people (in this context, on the ground) have been found in the medical field and have been predominantly applied to automotive injury or to assess crash dynamics in aircraft accidents.^{21,22,39,40} The AIS, which is described in more detail in Section 2.5, rates injuries on a 6-

³⁹ Sturdivan, L., Viano, D. & Champion, R., 2004., "Analysis of injury criteria to assess chest and abdominal injury risks in blunt and ballistic impacts," *The Journal of TRAUMA, Injury, Infection, and Critical Care*, 56(3), pp. 651-663.

⁴⁰ Viano D. & Lau IV, "Thoracic impact: a viscous tolerance criterion," *Proc. 10th Intern. Techn. Conf. on Experimental Safety Vehicles*, 1985; pp. 104-114.

level ascending scale of: (1) minor, (2) moderate, (3) serious, (4) severe, (5) critical, and (6) unsurvivable. The FAA System Safety Handbook scale is a 5-level scale of: (1) no safety effect, (2) minor, (3) major, (4) hazardous and (5) catastrophic. In Section 4.2, a plausible correlation of these two rating systems is proposed in the context of laceration injury.

The major distinction between unmanned aerial vehicle (UAV) safety and the safety of manned aircraft is that the failure of a UAV does not *inherently* put people at risk since no pilot or passengers are onboard. Instead, the greatest risk is experienced by those impacted by a UAV on the ground or possibly in another aircraft. As such, using the definition for “catastrophic” given in the FAA System Safety Handbook as a basis for severity definitions should not include “loss of the system” as a catastrophic event. Using the Safety Management Handbook definition of catastrophic— which includes collision with a manned aircraft—does not appear to be appropriate. However, this issue is within the purview of another research team.

The Micro-UAS ARC, in their 1 April 2016⁴¹ report to the FAA, recommended limits in terms of allowable impact energy density (KE per unit of contact area) on 4 categories of UAS flying in specified flight scenarios to avoid serious injury to persons on the ground due to blunt trauma. In particular, they suggested that allowable energy densities be determined by “industry consensus” standards to avoid an injury rating of AIS 3 or higher due to an impact with a person on the ground at a rate determined by the category. The allowable rate of serious or worse injury (AIS 3 or greater) due to an impact was calculated at the levels shown in Table 7.

Table 7 – Micro-UAS ARC Recommended FAA Allowable Rates of Serious (or worse) Injury Due to an Impact with a Person on the Ground ⁴¹

Category	Flight scenario in which an impact with a person the ground occurs	Acceptable rate of AIS 3 or greater injury
2	No less than 20' above, 10' laterally from people	1%
3	In a specified region not over people except ground crew	30%
4	Over crowds, but with operational/other mitigation	30%

Incidentally, the Micro-UAS ARC also recognized the importance of considering laceration injuries and indicated that more needs to be known about injuries due to rotating blades.

While permanent disability is not considered a metric in FAA safety definitions, permanent disability is used in DoD and other injury metrics.⁴² Laceration injuries with limited potential for fatality have already caused publicly documented permanent disability injuries. Therefore, permanent disability will likely dominate injury severity and define public acceptance of sUAS when operating near or over people.

Regarding severity definitions for property on the ground, the likelihood of penetration of a structure (building) or vehicle (automobile, aircraft, etc.) appears to be the key focus of damage

⁴¹ https://www.faa.gov/uas/resources/uas_regulations_policy/media/Micro-UAS-ARC-FINAL-Report.pdf.

⁴² Military Standard, MIL-STD-882E, “Systems Safety”, 11 May 2012.

assessment/severity definition in the literature. For example, a NAVAIR⁴³ document records the mechanical effect of impact of inert debris. The only metric presented involves roof, wall or window penetration, but there is no assessment of the relationship with regard to FAA severity definitions. The FAA severity definitions provided in Table 1 and Table 2 do not make reference to UAS or manned aircraft damage to structures. The new Part 107 rules do mandate that any incident resulting in at least five hundred dollars or more in damage to property are reportable incidents/accidents.⁴⁴

There is also a concern with regard to fire hazards involving structures. In particular, fires may be set during an impact due to onboard fuels and batteries. Methods for assessing damage due to fuel fires have been developed and are discussed in Section 4.12.

2.7. Academy of Model Aeronautics (AMA) Operational and Injury Data (UAH)

Radio controlled or remotely piloted aircraft are comparable technologies to sUAS and, from an operational standpoint, closely mirror Visual Line of Sight (VLOS) operations for sUAS. RC aircraft operators accumulate approximately 6-8 million flight hours per year with an estimated accrual of 84,000,000 flight hours in the previous 14 years. Therefore, researchers also reviewed injury and accident data from the AMA. Based on self-reported remote control (RC) aircraft pilot data collected by the AMA, the following are high-level statements concerning model aircraft use and accidents.⁴⁵

- 1) There were thirty-nine documented claims of property damage due to model aircraft over the eight years prior to the survey. Most of these claims were due to model aircraft that departed the designated flying area at AMA fields and hit vehicles parked near the flying site.
- 2) The AMA is tracking six model aircraft related fatalities in the U.S. between 1979 and 2013. Only one incident involved a fatal injury to someone not engaged in the operation of the model aircraft, and that incident occurred in 1979. This aircraft, a flying lawn mower, was not flown by an AMA member and was flying in Shea Stadium during a model aircraft exhibition. All other fatalities involved participants in the hobby.
- 3) The AMA estimates a rate of 3.57×10^{-8} fatalities per flight hour.

2.8. Property Standards (KU)

Regarding severity definitions for property on the ground, the likelihood of penetration of a structure (building) or vehicle (automobile, aircraft, etc.) appears to be the key focus of damage assessment/severity definition in the literature. For example, NAVAIR's Crash Lethality Model report documents the mechanical effect of impact of inert debris. The only metric involved is roof, wall or window penetration, but there is no assessment of the relationship with regard to FAA severity definitions.

There is also a concern with regard to fire hazards involving structures. In particular, fires may be set during an impact due to fuels and batteries onboard. Methods for assessing fire damage due to fuel fires have been developed and are discussed in Section 4.12.4.

⁴³ Ball, J. A., Knott, M. and Burke, D, Crash Lethality Model, AAWCADPAX/TR-2012/196, 6 June 2012.

⁴⁴ Advisory Circular on Small Unmanned Aircraft Systems, AC 107-2 (2016)

⁴⁵ E-mail to MG ® Jim Poss from Rich Hanson, AMA Government and Regulatory Affairs Representative dated 24 March 2016

2.9. Recommendations for sUAS-Related Severity Definitions (UAH/KU)

Recognizing the importance of considering permanent disability as an undesirable outcome, the following severity definitions for *people on the ground* are recommended. Similarly, recognizing the relative importance of structure penetration and fire hazards, severity definitions for *property on the ground* are recommended.

- Catastrophic
 - Any fatality or permanent total disability to the non-participating public or the UAS flight crew (30% probability of AIS5 or higher)
- Hazardous
 - Severe injury causing incapacitation of the non-participating public or the UAS flight crew (30% probability of AIS4 or higher)
 - Penetration or fire caused to a structure which makes the structure unusable or uninhabitable
- Major
 - Injury requiring hospitalization (30% probability of AIS3 or greater) or causes loss of consciousness
 - Penetration of the structure with limited residual velocity, setting fire to surface of a building
- Minor
 - Injury treatable on an outpatient basis (30% probability of AIS2 or greater)
 - Damage to structure requiring superficial repair
- No Safety Effect
 - Superficial injury (50% probability of AIS1 or greater)

3. Discussion of UAS Design Attributes

3.1. Vehicle Characteristics Contributing to Ground Collision Severity (UAH)

The team developed a taxonomy (Figure 2) for looking at various aspects of UAS ground impact collisions in order to assess the resultant injury severity of the most credible injury sources. This taxonomy will be evaluated throughout the remainder of this report. There are three vehicle characteristics that contribute to fatal UAS ground collisions across all types of platforms and weight classes: kinetic energy (KE), ignition sources based on vehicle power systems, and vehicle rotating components.

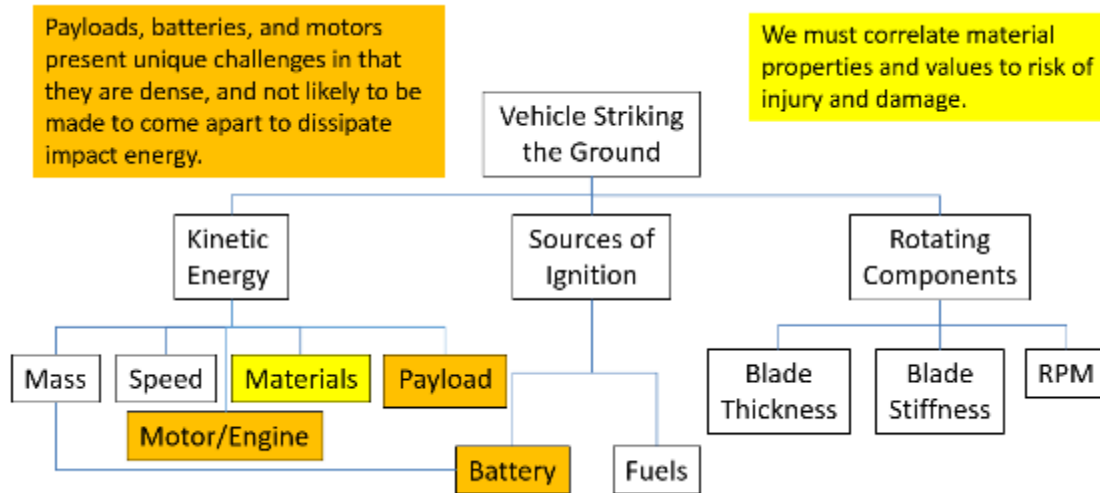


Figure 2 - Ground Collision Severity Taxonomy Defined for the A4 Task

3.1.1. Kinetic Energy (UAH)

It is important to note that for a complete analysis of ground collision severity, KE must be examined both in terms of magnitude and on a per unit area basis. This is necessary because there are several possible human injury mechanisms that come into play during collisions – blunt force trauma, penetrating injuries (soft tissues), and fracturing of bones.⁴⁶ The former mechanism is influenced by the magnitude of impact KE, and the latter two are influenced by impact KE per unit area or energy density. Of the two, only impact KE can be easily and accurately estimated experimentally and measured during testing. Force per unit area is significantly harder to measure experimentally and through testing.

The impact KE of a given vehicle during a collision sequence is a function of vehicle mass and velocity. The following relation is used to calculate impact KE or the KE of a vehicle at given flight condition.

$$KE = \frac{1}{2} mV^2 \quad \text{Equation 3}$$

Vehicle mass (m) plays a key role, but the dominant factor in this relation is velocity (V) because this term is squared in the expression.

Terminal velocity (V_{term}), the maximum free-fall velocity of the aircraft, plays a significant role in assessing the ground collision severity of a platform. V_{term} represents the fastest a vehicle can travel while falling without any additional propulsive force accelerating it toward the Earth other than gravitational force. Accurate estimation or measurement of vehicle terminal velocity is essential for determining impact KE in a credible worst case impact scenario, e.g. complete loss of power and/or control. The expression used in Tier 1 analysis to calculate terminal velocity is

$$V_{term} = \sqrt{\frac{2mg}{\rho AC_d}} \quad \text{Equation 4}$$

⁴⁶ Feinstein, D. L., Heugel, W.F., Kardatzke, M.L. Weinstock, A., "Personnel Casualty Study," IITRI Project No. J6067 Final Report

where g represents gravity, ρ is the ambient air density, A is the representative area swept by flow, and C_d is the drag coefficient or non-dimensionalized drag force. The design factors (things that engineers and developers can control) in this expression are mass, area, and coefficient of drag. It is important to highlight that effective coefficient of drag at any flight condition is highly variable and depends on ambient flow conditions (temperature, velocity, density), vehicle state (orientation with respect to flow), and vehicle configuration (fuselage geometry, payload configuration, and blade design and orientation). Single value estimates of vehicle drag coefficients presented in this paper are taken to be broadly representative of vehicle drag, but readers must understand that this is an estimate and only truly representative of a single flight condition and vehicle. For example, a Phantom 2 falling vertically in a level attitude with a given payload under SSL conditions with the blades oriented perpendicular to the vehicle arms. However, these estimates are shown to be reasonably accurate and sufficient based on the scope of this work and available resources for modeling tasks within the A4 project. The analysis also shows that manufacturers can develop estimates of these parameters from flight test and from computational fluid dynamics simulation using their CAD models to develop reasonable estimates of impact energy and associated mitigations to protect the public.

Most KE values presented in this paper, whether based on terminal velocity, velocity achieved during a fall from a given height (and less than V_{term}), or calculated from a level flight airspeed, are conservative values in that they represent maximum KE available for transfer from an aircraft to an impacted object or person. Although 100% energy transfer is physically unlikely, it is conservative and approximates the worst possible case for a collision scenario. KE transfer is influenced by the energy absorption characteristics of the impacting and impacted object, the alignment of the impacting and impacted objects, and ratio of masses between the impacting and impacted objects. When discussing sUAS characteristics that can be directly controlled by designers, material properties and energy absorption are at the top of the list. Mass is controllable, to an extent, but a designer cannot specify what the sUAS will hit during a collision, nor its orientation. Mass ratios and impacting incidence can only be addressed in general terms of design considerations and engineering “margin” based on best practices and likely scenarios. On the other hand, material selection directly effects what the FAA’s February 2015 Small UAS Notice of Proposed Rulemaking⁴⁷ refers to as *frangibility*. The NPRM states that, “*The FAA is also considering whether to require, as part of the micro UAS approach, that the micro UAS be made out of frangible material, a UAS that is made out of frangible material presents a significantly lower risk to persons on the ground, as that UAS is more likely to shatter if it should impact a person rather than injuring that person.*”

The unmanned aircraft would be made out of frangible materials that break, distort, or yield on impact so as to present a minimal hazard to any person or object that it collides with. Examples of such material are breakable plastic, paper, wood, and foam. A clear example of this concept is a fixed wing UAS with wings mounted such that they can separate from the aircraft during a collision sequence. Wing separation results in lower KE transfer during the collision and represents a viable means of reducing ground collision severity for that platform. Throughout the remainder of the paper, the term energy absorption is taken to be equivalent with the term frangible. Further discussion of energy

⁴⁷ https://www.faa.gov/regulations_policies/rulemaking/recently_published/media/2120-AJ60_NPRM_2-15-2015_joint_signature.pdf, Accessed 12/20/15

absorption and dissipation characteristics of different UAS designs is included in Appendix D: Major Categories of sUAS and Defining Design Attributes.

Energy absorbing materials are ideal choices for the construction of sUAS structural components. However, motors, batteries, and payloads are dense components that do not readily yield, distort, or break on impact. Depending on construction of the aircraft, the payload and batteries can also separate from the aircraft after an impact and become an additional collision hazard. Designs that integrate the payload and batteries into the fuselage are more likely to provide some level of protection to people or property during a collision. At this time, batteries tend to be well integrated into the fuselage of most multi-rotor and fixed wing aircraft; however, there are designs that have less rugged Velcro fasteners that are used to affix the battery to the airframe. A search of UAS websites for imagery documenting externally-mounted batteries yielded examples such as the DJI Flamewheel F550, 3DR IRIS, DJI S800, GPS Ag Scout, Onyx Star Hydra-12, and NEO 800C. Information on the mounting style of the batteries on these aircraft was obtained by searching UAS websites for imagery. Fixed wing payloads tend to be more integrated into their respective aircraft fuselages in order to minimize drag. This has a side benefit of reducing the likelihood of payload separation after a collision. Many fixed wing aircraft also surround their batteries and payloads with energy absorbing material. Most multi-rotor aircraft have their payloads externally mounted to the fuselage on gimbals. This is necessary to produce high-quality imagery. However, this may make the payload more susceptible to separating following a collision or cause it to have limited energy attenuation when the vehicle impacts a person, vehicle or structure. It's important to note that payload separation has not been widely researched and the team's conclusions are mainly based on video evidence from YouTube⁴⁸ posts and conservative assumptions about worst case situations during collisions.

During a collision, there are several energy loss mechanisms that dissipate UAS impact KE. First, the UAS fuselage and payload deform by flexing and, in some cases, breaking. The deformation energy cannot be calculated from experimental impact data from load cells on a crash test dummy or impact pad. Depending on the simulation setup, it can be estimated through finite element analysis modeling. Following the initial contact and deformation, a vehicle will also rebound off the impacted object and have linear and rotational velocities. The post impact KE is influenced by the vehicle material properties, the properties of the impacted object and the angle of incidence between the objects during impact. The post impact KE could be estimated by analyzing photometric data from high speed video or through use of autonomous motion tracking cameras with visual markers placed on the UAS and the impacted object. This method is; however, challenging and costly to execute with good accuracy, requires a number of cameras to capture motion in x, y, and z directions, and is not able to capture and quantify the strain and deformation of the vehicle such that all energy mechanisms can be quantified.

Center-of-mass to center-of-mass impacts are the worst, as the person or object absorbs the maximum amount of energy. Offset impacts and incident angles less than perpendicular lead to rotation of the vehicle after impact and transfer less energy to the person or object. The A4 team assumes that off-center impacts are more probable than center-of-mass to center-of-mass impacts. In many cases, the nose cone width is 20% or less of the total width of the aircraft, which, on an area basis, equates to a 20% chance that in any impact the nose cone will be the impacting component. The impact of the UAS

⁴⁸ Marcel Hirscher Crash Drone Drohne Absturz Ski Alpin 2015, <https://www.youtube.com/watch?v=Jislf5LxPxw> Accessed 03/20/16

on an object results in impulse loading, which can be measured by way of a load cell. The impulse loading can result in deformation as well as a change in the KE of the impacted object. The change in KE of the impacted object, again, can be estimated by way of photometric analysis or motion tracking cameras in a laboratory. This method is, however, challenging to execute with good accuracy, requires a number of cameras to capture motion in x, y, and z directions, and is not able to capture and quantify the strain and deformation of the vehicle. The last way in which the UAS impact energy is dissipated is through direct absorption by the impacted object. The energy that is directly absorbed is the difference between the transferred energy and the change in KE of the impacted object. Absorbed energy is a function of the deformation of the impacted mass and the associated damping caused by the materials from which the impacted object is manufactured. The deformation energy can result in damage if compressive, tensile, or shear limitations of the impacted object are exceeded. In the case of a person being hit by a UAS, deformation and absorbed energy contribute the injuries associated with blunt force trauma.

ERAU and MSU have performed high fidelity modeling of collisions by using complex human body models and finite element analysis software to examine energy transfer, human body response, forces on tissue, and energy absorption by the UAS structure. ERAU's work is also focused on determining whether collision evaluation metrics and methods from the automotive industry are applicable to UAS collisions with the human torso (Section 4.16). MSU modeled human head impacts by a DJI Phantom-type airframe. The focus of MSU's work was evaluation of head accelerations to determine the potential injury severity of impacts. These accelerations are correlated with injury metrics from the automotive industry (Section 4.15). UAH also worked on lower-fidelity parametric-based modeling of collision in order to gain an understanding of the collision dynamics and energy transfer that occurs during UAS collisions with ground objects.

The method used by UAH was to modify a rigid body collision using a coefficient of restitution (CR) that models elasticity and damping based on the two objects in contact. The amount of energy that is retained or transferred by the two objects during a collision depends on CR and is denoted as 'e' in equations.⁴⁹ For a UAS in collision with any object (human, building or vehicle), the UAS transfers some of its energy to the object, retains some of its energy (in the form of translational and rotational energy) and may lose some energy (through deformation). Because CR is a ratio of the relative speed of two objects after collision to the relative speed of the two before collision, a given value of CR correlates to a specific pair of objects.

A perfectly elastic collision has a CR value close to one and bodies involved in the collision collectively have as much of the energy following a collision, meaning that no KE is dissipated by deformation or other losses, and objects rebound quickly with their relative speeds after collision being dependent on their masses. An example is a baseball being hit with a baseball bat. An "*inelastic*" collision has a lower CR value with the colliding bodies deforming during the impact and/or the objects absorb energy. A human torso is assumed to have more inelastic properties (in comparison to say a pool ball), which corresponds to a low CR value, and thus, the torso absorb a large portion of the energy imparted to it by a mass including a UAS.

⁴⁹ <https://www.physicsforums.com/threads/what-is-the-coefficient-of-restitution.763082/>, Accessed 03/20/16

To understand the physics behind this problem, a technical report by E.H. Jakubowski⁵⁰ provides a method for modeling collision dynamics. A collision between two objects (masses m_1 and m_2) can be modelled as a collision between two rigid masses (m_1 and m_2) joined by a spring with stiffness constant, k , and a viscous damper with damping factor, R . The stiffness constant defines the elastic property of a material that enables the object to deform when a stress is applied and to regain its original shape after deformation, thus releasing energy. The damping factor defines the property of the material that controls the rate of deformation, thus absorbing some energy as deformation occurs on the object. A damping factor of zero means that there is no damping, and the object regains its original form after deformation, thus no energy is lost in deformation. A high damping factor ($\approx \infty$) implies that the body undergoes damping and resists deformation from its original form and more energy is dissipated as heat, friction or fracture, etc. Thus, a relation between stiffness constant (k), damping factor (R) and CR (e) can be mathematically established.

Consider a 3 lb mass object colliding with a 6 lb object or a 200 lb object. The initial velocity of the 3 lbs mass is 50 ft/s while the 6 lbs and 200 lbs objects are at rest. The objects are made of steel and are spheres. Another paper by Rod Cross⁵¹ published the CR values and spring constants of a steel ball when impacting a rigid floor. Since, $R = f(m_1, k, e)$, using experimental values from the paper for k (4.14e06 N/m) and e (= 0.844), one can obtain values for R . A MATLAB© code was developed and validated by comparing its results with experimental data in the same paper. The results of the collisions of the 3 lbs object with a 6 lbs object and a 200 lbs object are shown in Table 8.

Table 8. Results of Modelling Collision of a 3 lbs with 6 lbs and 200 lbs Objects

	3 lbs object	6 lbs object	3 lbs object	200 lbs object
Initial Velocity (ft/s)	50	0	50	0
Final Velocity (ft/s)	-11.45	30.73	- 40.83	1.3626
Coefficient of Restitution (e)	0.844		0.844	
Initial Kinetic Energy (ft-lbf)	116.55	0	116.55	0
Final Kinetic Energy (ft-lbf)	6.12	88.04	77.71	5.77
Change in Kinetic Energy (ft-lbf)	-110.43	88.04	- 38.845	5.77
Energy Dissipated (ft-lbf)	-22.39		-33.07	
Change in momentum (lbm-ft/s)	-5.73	5.73	-8.47	8.47
Impulse (lbm-f/s)	-5.73	5.73	-8.466	8.466
Work done (ft-lbf)	-110.37	88.04	-38.76	5.77

As the CR is less than one for these collisions, some energy is dissipated during the collision in form of a permanent strain energy. In the collision between a 3 lbs and 6 lbs object, the 3 lbs object transfers most of its energy to the 6 lbs object. Most of the energy transfer (~80%) results in motion of the 6 lbs object and resulting kinetic energy with only 20% of the energy dissipated in terms of deformation or absorption. This is analogous to a baseball hitting a basketball where most of the energy is transferred to the basketball. For the collision between a 3 lbs object and 200 lbs object, very little energy is transferred to the heavier object in terms of kinetic energy (>5%); however, there is more energy

⁵⁰ Jakubowski, E. H. *Dynamic Formulation of Coefficient of Restitution*. No. RIA-77-U91. SPRINGFIELD ARMORY MA, 1964

⁵¹ Cross, Rod. "The bounce of a ball." *American Journal of Physics* 67.3 (1999): 222-227.

absorbed by the 200 lbs object (~30%). The majority of the energy remains with the 3 lbs object in terms of kinetic energy (~70%). In the limit of an infinite mass, the 3 lbs object would retain even more kinetic energy which is analogous to a tennis ball bouncing off a wall. Because the object 2 is much heavier than object 1, the change in velocity of the larger mass is much less than in the case of the collision between 3 lbs and 6 lbs objects. The modelling results of these two collisions are seen in Figure 3 and Figure 4.

As observed in Figure 3 and Figure 4, the momentum gained by object 2 is same as the momentum lost by object 1. This confirms the conservation of linear momentum. Also, from Newton’s third law, the forces acting on the two bodies are equal and opposite. Looking back at Table 8, the work done on/by an object during the collision is equal to the change in energy of the object due to the collision. The slight error in work done and change in kinetic energy is due to the assumption of same stiffness constant for various masses. The stiffness constant varies with the weight of the objects as well as the material.

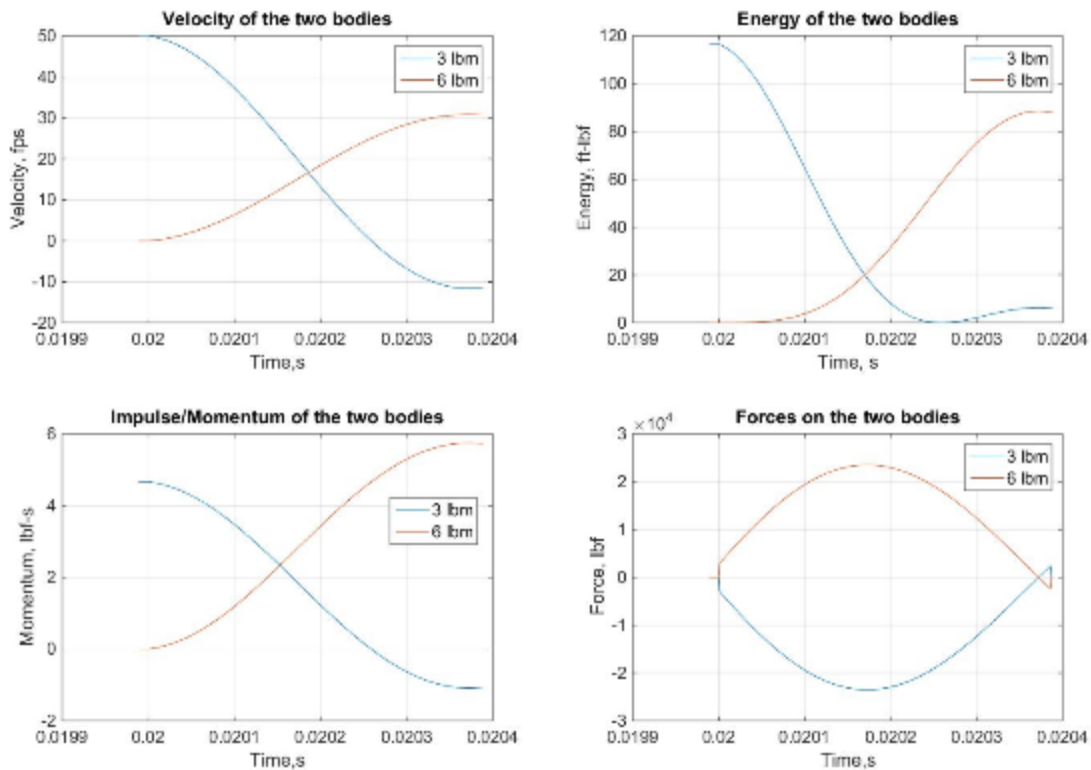


Figure 3 - Model Outputs Detailing the Collision of a 3 lbs Object with a 6 lbs Object

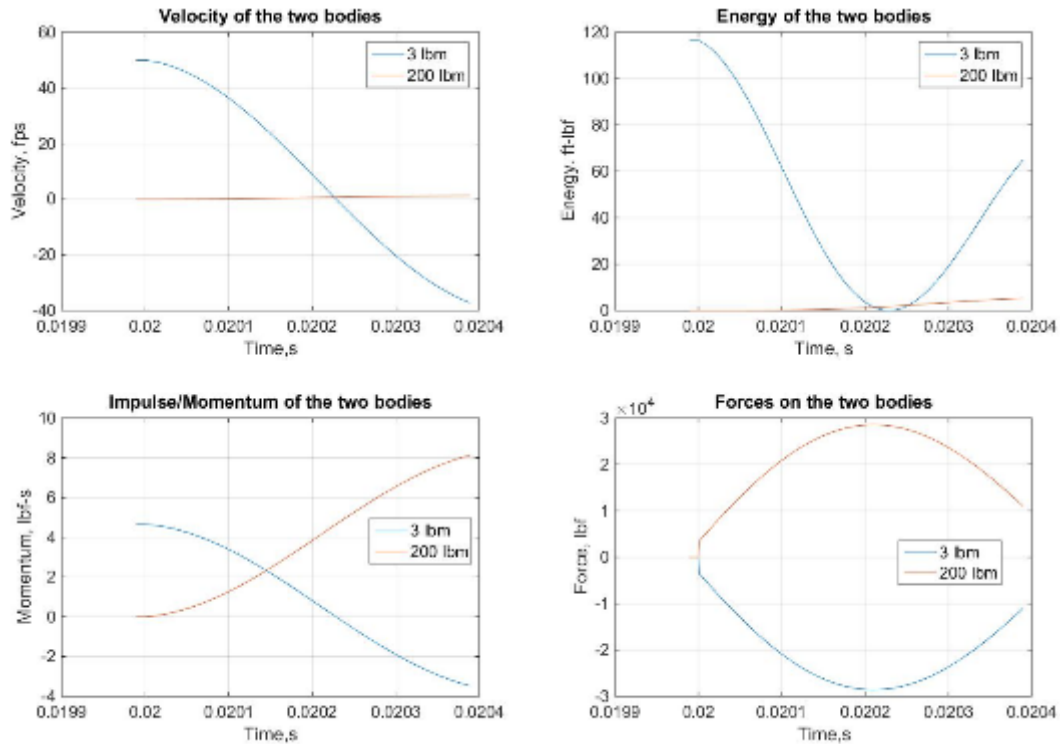


Figure 4 -Model Outputs Detailing a Collision Between a 3 lbs Object and a 200 lbs Object

A similar rationale can be developed from the experimental results of Wichita State University's National Institute of Aviation Research (NIAR) drop tests of DJI Phantom 3 on human dummy models which are presented in greater detail later in this report. Here, the dummy model is comparatively heavier than the UAV. Hence, there will only be a slight energy increase for the dummy but higher loss of energy for the UAV especially for body strikes. The stiffness constant of the UAV is non-linear and upon exceeding high loads, the UAV and payload undergoes fractures. The body is similar and as such will have stiffness and deformation during the collision which makes analysis of the two bodies collisions highly non-linear. Based on analysis of the photometric data from NIAR tests, the coefficient of restitution varies from 0.1 – 0.4. The rebound velocity of the UAV is very low due to permanent strains that are developed in the UAV body and the subsequent motion of the head. Also, much of the energy is dissipated in the UAV in form of cracks, fractures, etc. Additionally, most collisions are not pure center of mass collisions, but rather, oblique (where the initial velocities are not along the line of impact) and eccentric collisions (where the line of impact is not same as the normal to the striking surface between the two bodies). Perfect collisions especially with the unique shapes of UAS platforms makes perfect collisions very difficult to achieve even when these experiments were designed to do so. Offset (oblique or eccentric) collisions convert some of the initial energy to rotational energy. For collisions with increasing amounts of offset, the UAS will experience increasing rotational energy that can be very significant and results in less energy transferred to the body.

Because the dummy head is attached to the rest of the body, a collision with the head will create external forces from the neck and body. The law of conservation of linear momentum cannot be applied here. However, the forces measured at the head causes displacements of the head CG. Thus, work done on the dummy head can be calculated, which is same as the energy absorbed into the head.

Because of the low CR values, the energy absorbed into the dummy head is substantially lower than the initial energy, and the energy dissipated is more than 40% of initial energy.

For initial modeling analysis, a CR value of 0.2 has been assumed for a UAS-human body collision. Low order modeling results of offset collisions are shown in Figure 5. Figure 5 is a presentation of the initial modeling of offset collisions and the relative energy transfer to a body during an offset collision. Figure 5 shows approximately the same average decrease in transferred energy as shown in the more detailed modeling being conducted by ERAU and MSU. More results on offset collision and energy transfer during ground collision are provided in Sections 4.16, and 4.16.1.

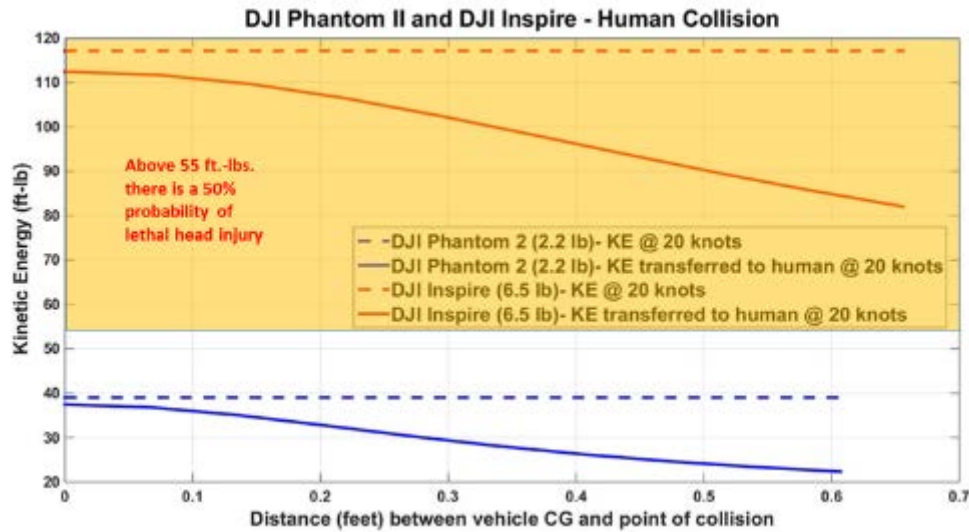


Figure 5 - Low Order Modeling of Impact KE Transfer Based on Vehicle and Body CG Offset

Knowledge Gap: UAH initially assumed CR=0.2 is based on a qualitative assessment of the two colliding bodies, but there was little quantitative rationale. CR values can be calculated experimentally and as such, UAH is developing dynamic modeling for sUAS and human collisions based on the results of the drop testing done at NIAR as part of the Task A11 technical approach. UAH is also beginning finite element analysis modeling, funded internally, to continue examining energy transfer and vehicle deformation during center of mass and offset collision events.

3.1.2. Sources of Ignition (UAH)

Aircraft power sources, either fuel or batteries, can be sources of ignition following ground collision. This report largely focuses on batteries. The AUVSI database and analysis of the FAA’s Section 333 exemption shows that the vast majority of UAS sold in the US and weighing less than 55 lbs use batteries for power. In addition, close to 100% of the exemptions granted for commercial UAS operations are for aircraft that use Lithium Polymer (LiPo) batteries. LiPo batteries can ignite if they are punctured and exposed to air or water, crushed, overcharged, or otherwise poorly maintained.⁵² The literature survey indicates that a LiPo battery fire may be able to exceed temperature limits for some lower quality

⁵² Mikolajczak, Celina, Michael Kahn, Kevin White, and Richard Thomas Long “Lithium-ion batteries hazard and use assessment,” Fire Protection Research Foundation, Springer Science & Business Media, 2012.

roofing standards.⁵³⁵⁴ However, the likelihood of this happening within an operational context is unknown. Additionally, there is poor documentation behind the limited testing that the team has found. LiPo battery fire hazards in a ground collision sequence are poorly documented and require further research with respect to their potential to impact and ignite structures and vehicles.

Table 9 shows the range of battery types that are used in sUAS models. Model names, current and voltage data were collected from manufacturer websites. These batteries range from 3.7 -22.2 volts and 500-22000 milliamp hour (mAh). They have varying degrees of mitigation and fault detections, ranging from battery configurations with no protective measures to battery configurations with hard shell covers and internal monitoring circuitry.

Knowledge Gap: There are large knowledge gaps regarding battery fires. What are the peak fire temperatures and the temperature as a function of time across the range of batteries (Voltage and Ampere ratings) used in sUAS? What is the likelihood of battery separation during impact and the severity of separation, i.e. is it possible to damage a battery during an impact such that it goes into an auto ignition process?

Table 9 - Battery Types and Models from Proposed Battery Failure Research

Battery Design, Current, Type	Battery Name
1S LiPo Batteries	
Soft, Regular, External, Hobby-grade COTS	Eflight 500 mAh 25C
Hard, Smart, proprietary	Parrot Minidrone 550 mAh battery
2S LiPo Batteries	
Soft, Regular, External, Hobby-grade COTS	Gens ace 1550mAh 25C
3S LiPo Batteries	
Soft, Regular, External, Hobby-grade COTS (high Ah)	PULSE LIPO 6000mAh 11.1V 25C
Hard, Smart, proprietary	Phantom 2 5200 mAh Battery
Hard, Smart, proprietary	Blade chroma 6300 Mah
4S LiPo Batteries	
Soft, Regular, External, Hobby-grade COTS (high Ah)	tprc 5400mAh 25c
Hard, Smart, proprietary	Phantom 3 4480 mAh
Hard, Smart, proprietary	3DR Solo 5200 mAh
6S LiPo Batteries	
Soft, Regular, External, Hobby-grade COTS (low Ah)	Tattu 8000mAh 22.2V 25C
Soft, Regular, External, Hobby-grade COTS (high Ah)	PULSE LIPO 22000mAh 22.2V 25C
Hard, Smart, proprietary	Inspire 1 - TB47 4500 mAh

3.1.2.1. Battery Characteristics and Severity Analysis

Lithium Polymer (LiPo) batteries are the leading source of propulsive energy for the sUAS used in the current market. Over 76% (911 of 1186) of UAS below 55 lbs included in the AUVSI UAS database use LiPo batteries for propulsion.¹⁵ In general terms, LiPo batteries are secondary (rechargeable) Lithium Ion batteries that use a polymer-based electrolyte instead of a liquid electrolyte, eliminating the need for a metal casing. This makes the battery light-weight and flexible, hence, the advantage of being manufactured into different shapes. However, due to their flexible foil-based covering, these batteries are less rigid and have less resistance to physical damage compared to the generic hard shell Lithium ion

⁵³ <http://blog.ottawarobotics.org/2011/12/07/who-says-lipo-batteries-are-dangerous/> Accessed on 05/24/2016

⁵⁴ http://c.yimcdn.com/sites/www.polyiso.org/resource/resmgr/technical_bulletins/tb111_jun30.pdf Accessed on 05/24/2016 – UL790 Standard for Standard Test Methods for Fire Tests of Roof Coverings

batteries. Some UAS manufacturers like DJI, 3DR and Draganfly have introduced batteries with the same internal polymer-based electrolyte construction, but with hard-shells and internal monitoring circuits. This section consolidates all available literature on LiPo batteries and provides information on the risks and hazard severities they bring to a UAS, the user and the surroundings. Different safety measures that are currently available for LiPo batteries are also discussed. A complete understanding of Lithium Polymer battery failure modes is necessary because; (1) it provides insight into how batteries can fail in flight (partially or fully), which can result in a crash; or (2) how a crash can potentially trigger battery failures leading to fire hazards.

3.1.2.2. Literature Survey Results on LiPo Batteries

Significant past research has been devoted to identify the risk severity of Lithium Ion batteries.^{55,56} Standards were published to establish performance requirements to enable safe handling and transportation of Lithium Ion batteries in consumer and commercial electronics applications.⁵⁷ These standards lay out testing protocols to assess certain types of electrical, mechanical and environmental abuse.^{58,59,60} Although the test procedures differ slightly for each standard, they all serve the same purpose of certifying that the batteries are sufficiently rugged to avoid failure conditions that lead to fire or explosion during any unintended abuse. Some of the most common standards for Lithium Ion batteries, of which Lithium Polymer batteries are a subset, are listed in Table 10.

Since these standards were defined for all Lithium Ion batteries, they are equally valid for LiPo batteries whether the batteries are made from rigid or non-rigid battery construction. Battery and UAS manufactures were approached during the literature survey to confirm or deny whether they test their battery's adherence to any of the currently published Lithium Ion standards. A few of the batteries that were reviewed from various commonly used sUAS platforms contained markings demonstrating that they meet the requirements of any of these testing standards. Table 11 shows the manufacturers that were approached and their reply to our questions. Data in this table came from manufacturer websites, face-to-face discussions, and email correspondence.

⁵⁵ Mikolajczak, Celina, Michael Kahn, Kevin White, and Richard Thomas Long, "Lithium-ion batteries hazard and use assessment," Springer Science & Business Media, 2012.

⁵⁶ <http://www.rechargebatteries.org/wp-content/uploads/2013/07/Li-ion-safety-July-9-2013-Recharge-.pdf> Accessed on 05/24/2016

⁵⁷ Safety Issues for Li Ion batteries – http://newscience.ul.com/wp-content/uploads/2014/04/Safety_Issues_for_Lithium_Ion_Batteries1.pdf Accessed on 05/24/2016

⁵⁸ UL 1642 Safety Standard for Lithium Batteries http://www.bychoice.com/UL_1642_Ed_5_2012.pdf, Accessed 04/20/16

⁵⁹ IEC 62133:2012 (2nd Edition) Understanding IEC Safety Requirements for Rechargeable Cells & Batteries used in Portable Devices <http://www.accutronics.co.uk/images/uploads/233.pdf>, Accessed 04/20/16

⁶⁰ Lithium Battery Testing Under UN/DOT 38.3 <http://www.tuv-sud-america.com/uploads/images/1397851151678305590956/tuv-sud-lithium-battery-testing-lowres.pdf>, Accessed 04/20/16

Table 10 - Testing Content of Lithium Ion Battery Standards^{58,59,60}

Test Name/ Standard	UL 1642	IEC62133	UN 38.3
External Short Circuit	•	•	•
Overcharge	•	•	•
Forced Discharge	•	•	•
Crush	•	•	•
Impact	•		•
Shock	•	•	•
Vibration	•	•	•
Temperature Cycling	•	•	•
Low Pressure (Altitude)	•	•	•
Projectile/External Fire	•		
Drop		•	•

Table 11 - Battery Standards Adopted by UAS/LiPo Companies

Company/Manufacturer	Yes/No	Lithium Ion Battery Standards	Any logos on casing
DJI	Yes	UL 1642/ IEC 62133	No
3D Robotics	Yes	UL 1642	No
Venom Power	Yes	UN 38.3	No
Hobby King	Yes	UL 1642	No
Hobbico Inc.	Yes	UN 38.3	No

Mechanical tests like crush tests require placing the battery between two parallel plates and applying a compressive force of 13 kN force (UL 1642). It is currently assumed that soft-sided LiPo batteries used in sUAS are flexible and may fail when a high force is applied on them. The short-circuit tests in these standards require that the batteries do not catch fire due to a forced short-circuit. However, LiPo battery fire accidents have happened due to short-circuits despite these protections. Therefore, it is possible that the standards are not being followed or that the current standards are inadequate to ensure safe handling and operation in UAS applications.

Knowledge Gap: There is no research correlating adherence to published standards for safe battery operation in a UAS, especially as it relates to ground collision severity. Therefore, further study and testing is needed to test UAS batteries to these standards and define new standards that are more appropriate for ground collisions severity conditions. This will formally verify that batteries meet their design intent including mitigations associated with fire prevention.

Information on LiPo battery fire characteristics such as maximum and average temperature, burn rate, burn time, etc., is of utmost importance to understand the risk to buildings, vehicles and humans following a LiPo battery fire. An FAA report published in 2010 examines the fire characteristics of large

LiPo batteries that are used onboard aircraft.⁶¹ Five tests were conducted using a single 8000 mAh, 3.7 V LiPo cell, a group of four cells and a group of eight cells. A fire exposure test, pressure pulse test, Halon 1211 Suppression test, external short-circuit test and an auto ignition test were performed. Based on the results, a LiPo battery fire can generate peak temperatures from 750-1065 °F, peak pressure pulses from 2.15-5.30 psi, and burn times from 1.75-2.75 minutes. However, none of the cells caught fire during the short-circuit tests. The cells failed the auto-ignition test and caught fire when the cell surface temperature rose to around 330 °F. Also, the Halon 1211 failed to suppress the LiPo cell fire completely.

Based on these results, the lowest Class C roof (according to standard UL 790) should be able to withstand LiPo battery associated fires without itself catching fire. However, a burn test conducted by a hobbyist using four 4400 mAh, 7S batteries connected in a 7S2P configuration (8800 mAh, 14S) observed an average temperature of 1652 °F for 5-6 minutes.⁶² Such a fire could burn through a class C roof. However, the 7S2P configuration is a very high capacity LiPo battery and would typically only be used by heavy lift UAS.

Knowledge Gap: A greater number of tests with various UAS LiPo batteries must be conducted to provide a statistically and experimentally sound evaluation of whether LiPo battery fires are a threat to Class C roofs.

Another shortcoming of the FAA fire test is that the LiPo batteries tested were representative of LiPo batteries used onboard manned aircraft. Such high capacity batteries are used only in certain sUAS. Current UAS LiPo batteries vary widely in voltage, capacity, number of cells and even chemistry. In the last six years preceding the FAA tests, much innovation in battery chemistry and manufacturing has occurred.

Knowledge Gap: Similar tests as described in the FAA report should be performed with a wide variety of current UAS LiPo batteries of various sizes, manufacturers and chemistries to better assess the risk of LiPo batteries to people and property.

3.1.2.3. LiPo Battery Failure Modes

An explanation of conditions and a typical chain of events leading to a battery failure/fire is provided below for two reasons. First, it is meant to provide insight into how a UAS battery can begin to degrade and then completely fail, which can result in an accident due to partial or full loss of power and a battery fire in flight. Additionally, this section provides more background to discussions about battery dangers and is necessary to transition into a discussion of effective mitigation measures. It is hard to convey information concerning technology to mitigate failures without having explained how and why failures occur in the first place.

Voltage and temperature are the largest contributing factors of Lithium Ion battery failures.⁶³ Like any other battery, a LiPo battery may consist of single or multiple cells and each cell has three major components: the positive cathode, the negative anode and the polymer based electrolyte. For a typical LiPo cell, the cathode is made of Lithium metallic oxide, the anode is made of carbon, and the

⁶¹ Summer, Steven M., "Flammability Assessment of Lithium-Ion and Lithium-Ion Polymer Battery Cells Designed for Aircraft Power Usage," US Department of Transportation, Federal Aviation Administration, 2010.

⁶² <http://blog.ottawarobotics.org/2011/12/07/who-says-lipo-batteries-are-dangerous/> Accessed 04/15/16

⁶³ http://www.mpoweruk.com/lithium_failures.htm, "A Guide to Lithium-Ion Battery Safety, Lithium-Ion Batteries Hazard and Use Assessment, Safety of lithium-ion batteries," Accessed 04/15/16

electrolyte is made of Lithium ions in solid or gelled polymer. Since the LiPo batteries are well sealed and oxygen is required to sustain a fire, all LiPo battery fires ignite at the cathode. However, the first signs of failure may occur at any location inside the battery.

Excessive voltage or temperature can cause failure. As the battery is over-charged, more Lithium ions begin to accumulate near the anode. The chain of events leading to a battery fire starts at the anode, but the eventual fire occurs at the cathode. These ions interact with the excess electrons and get deposited as Lithium metal on the anode (*Lithium Plating*). This reduces the number of available Lithium ions, thus, reducing capacity. The metal formation is dendritic and not homogenous. Excess formation of Lithium dendrites can pierce through the polymer separator and cause an internal short circuit. Additionally, more heat is produced as more voltage is gained by the cell due to increase in internal resistance (I^2R) losses.

When the battery is over-discharged, there are fewer ions surrounding the carbon anode and the anode begins to dissolve in the electrolyte. When the battery is recharged later, carbon deposits are formed throughout the electrolyte which may accumulate and lead to an internal short-circuit in future. Also, excess ions accumulated at the cathode force the metallic oxide to break down and release oxygen. This oxygen can cause venting or react with other volatile gases and catch fire at the cathode. Storage of LiPo batteries over a long time has similar effects as over-discharging.

As battery temperature increases because of overcharging or high ambient temperatures in the surrounding environment, an Arrhenius effect (where the chemical activation rate is exponentially dependent on temperature) begins to take place. Increasing temperature leads to higher reaction rate, and this further causes more I^2R losses. During the first charge of every LiPo battery, the anode reacts violently with the electrolyte to form a Solid Electrolyte Interface (SEI). This layer forms a barricade between the anode and electrolyte and prevents further reactions. As temperatures rises, the SEI layer breaks down, and the electrolyte reacts with the anode and releases more heat. If heating continues, it dissolves the newly formed SEI layer and the process repeats, thereby increasing cell temperature (*thermal runaway*). First, the organic solvents in the electrolyte begin to break down, releasing flammable gases (methane, etc.), but due to lack of oxygen they do not burn. However, the gases try to escape and cause bulging of the battery. If proper venting is not provided, the gases do not escape, increasing internal pressure and temperature. As temperature further rises, the polymer separator that blocks the pathway between the electrodes begins to melt. This leads to an internal short circuit between the electrodes. Eventually the heat forces the cathode to break down and this releases oxygen which reacts with the flammable gases. This starts a fire and the cathode burns violently releasing a sudden burst of heat and pressure.

Though extreme temperature and voltage variations can directly lead to LiPo battery failures, LiPo batteries fail by other means in addition to deliberate or unintended over-charging. LiPo batteries can fail due to over-discharging, over-heating or cooling by the user. The following factors affect the temperature and voltage/capacity of the battery leading to accelerated wear out, and potentially, a hazardous failure (fire or rapid loss of power).

- 1)** Poor LiPo cell mechanical designs, insufficient vents and seals, and poor quality materials, etc. are bound to have a greater number of defects and early failure.

- 2) Manual production, poor material handling procedures, contaminated chemicals, voids in construction, debris inside the casing, poor sealing, poor quality control, and other manufacturing-related factors can lead to capacity losses, over-heating, venting, and early failures.
- 3) All LiPo batteries gradually deteriorate over time in an uncontrolled and irreversible manner. Gradual buildup of the SEI layer on the anode increases its impedance and decreases active chemicals in the electrolyte (this is called *Passivation*). Corrosion, dendritic growth and crystal formation of the electrodes increases cell impedance and reduces capacity, ultimately leading to internal short circuits. Minor defects during battery construction gradually worsen with age and may cause failure.
- 4) Uncontrolled operating conditions like using incorrect battery in a system, high ambient and storage temperatures, lack of cooling, etc. may cause overheating that will ultimately lead to failure.
- 5) Accidental or deliberate mechanical abuse like crushing, dropping, impacts, penetrating, falling in water, etc. can damage the battery leading to onset of failures or a violent explosion.
- 6) External factors like malfunction of the system using the battery or charger failure can also cause the battery to function improperly.

3.1.2.4. Successful Mitigation Measures for Battery Failures

Based on the previous descriptions, LiPo battery failures can be divided into early failures, gradual wear out failures, and random failure. Early failures occur when the battery is first tested at the factory. Significant design or manufacturing defects manifest immediately and cause these failures. Early failures can be identified at factories and appropriate safety measures can be taken to correct the manufacturing processes.

Gradual wear out failures are associated with aging effects and dictated by the manufacturing process and workmanship. Lithium plating on the anode, electrolyte crystal formation and/or breakdown, and electrodes dissolving can occur gradually with age. This reduces the battery capacity and ultimately leads to failure. Onset of these defects does not cause failure immediately, but they gradually wear out the battery until failure occurs. Individual defects can cause battery failure over different time periods, but together they can act synergistically and cause much earlier failure. By adopting better designs and precision manufacturing processes, manufacturers can predict the safe operating time period before a particular defect will lead to failure. However, predicting the safe operating time period for a battery gets very complicated. Because of the possible presence of multiple defects in a single LiPo cell, and many such cells constitute a battery, the safe operating period can be drastically reduced. UAS LiPo battery manufacturers may have to spend research time and money to establish safe operating periods. A common method adopted by manufacturers constitutes accelerated ageing of a sample of batteries and creating probability plots (for example, the Weibull Life Distribution model) for every defect and intersecting all such plots to predict a safe operating timeline for the battery.

Random failures occur when certain defects like electrolyte contamination due to abuse cause sudden LiPo failure rather than a gradual decrease in performance. Such failures occur at a very low rate and

are dependent on user, operating system and environment. However, these failures are catastrophic since these may occur suddenly and cause unwanted damage to the system and its surroundings.

Though the responsibility of effective LiPo battery care falls into the hands of the user, the manufacturer can add safety circuits and different protection methods to either prevent sudden failures or identify undesired battery behavior. Some of the safety measures that manufacturers can implement to prevent failures are as follows:

- 1) Adopting less reactive chemical constituents in the battery can reduce the damage during an explosion. For example, Lithium Cobalt used as the cathode material breaks down chemically at a relatively lower temperature and releases higher energy (heat and pressure) compared to Lithium Iron Phosphate that requires relatively higher temperature and is less exothermic. Since Lithium Cobalt has the higher energy density, it is more widely used to minimize battery weight. However, cobalt use remains an environmental and health concern due to its toxicity.
- 2) Using different material for electrodes that increase cell life. For example, anodes made with graphene, a recent invention, which absorbs more Lithium ions and increases cell capacity, prevents dendritic growth and has low impedance. This increases cell life and safety. Based on graphene's nanostructure, which has greater surface area and lower energy density, the graphene configuration maintains a lower operating temperature.
- 3) Chemical retardants can be added to the battery outer layers in order to neutralize the cell electrolytes if the cells are pierced. This limits the chemical reactions that drive thermal runaway and fires.
- 4) Battery shapes must be designed to dissipate heat generated by internal chemical reactions. Slender, long batteries can cool off faster than short, thick batteries. Hard-sided batteries with cooling fins will maintain lower temperature than those without passive cooling design features.
- 5) Separators used in LiPo batteries are typically made of a plastic material that burns at elevated temperatures. Dendrites or crystals can pierce through the plastic material causing short-circuits. This can be prevented by using a rigid and temperature resistant material for the separator.
- 6) Unintended chemical reactions inside the cell can build up harmful gases that build up internal pressure in the battery. Though it's not desired to release these gases into the environment, cells can have safety vents and circuit interruption devices that release the gases in a controlled manner and break the circuit to prevent further gas generation.
- 7) Proper design and insulation of battery lead terminals can prevent accidental short-circuit.

In addition to these safety measures, manufacturers can add protection systems to the batteries to identify unanticipated charging and temperature related incidents and protect the system and its surroundings. Thermal fuses are added to the battery that break the circuit and stop further charging/discharging by identifying higher and lower limits of temperatures. Electrical fuses are used to identify excess or low current/voltage and break the circuit to prevent further charging or discharging.

Recently, intelligent battery designs have been gaining momentum in the UAS industry. These batteries, unlike regular batteries, have additional circuits to interact with external systems (charger, UAS, ground

control station, and users). Intelligent batteries have circuits to monitor the battery voltage, temperature, etc. and in some batteries, even these parameters for each individual cell. These features add an additional layer of protection to the battery, helping in prolonging battery life and providing optimal functionality to the UAS. Intelligent batteries provide users with visual information of battery charging state and battery health. They can monitor individual cells health and cut-off any defective cells from the battery circuit to prevent further damage, while still powering the system at reduced voltage. Some intelligent batteries can permanently store battery manufacturer's design specifications and log active information like battery temperature and voltage profiles, count of charging/discharging cycles, internal impedance, and any incidents when voltage or temperature limits are reached, etc. This information can be communicated with other devices (chargers or autopilot), thereby monitoring the battery health and alerting users to off-nominal performance.

Knowledge Gap: UAH has submitted a white paper to the FAA entitled *W63 - Lithium Polymer Battery Failure Modes and Effects Analysis*, to evaluate LiPo batteries in accordance with existing Lithium Ion battery standards and perform additional drop and ballistic testing. The goal of this experimentation is to determine if the existing standards are sufficient to ensure safe handling and operation of LiPo batteries that are used in UAS applications, versus the consumer electronics applications (laptops and cell phones) to which current Lithium Ion battery standards apply.

3.1.3. Rotating Components (KU)

The rotating propellers and rotors of fixed wing, multi-rotor, and helicopter-style UAS pose a significant risk of cutting injury to people near the operating UAS. While RPM, blade design, and blade stiffness do play a role in the tendency of a prop to cut, the literature survey indicates that it is safe and not overly conservative to assume that most, if not all, accidental blade contacts will result in some degree of cutting injury.^{64'65'66'67'68} Effective mitigation methods and their pros and cons are discussed in Section 4.10.

3.1.4. Common Hazards Among UAS and Manned Aircraft Characteristics and Certification Standards Associated with the Ground Collision Problem (KU)

Manned aircraft are much larger and have significantly higher characteristic kinetic energies than aircraft in the micro UAS categories. Manned aircraft carry enough KE in their motion and propulsive systems to almost certainly kill a person on contact; however, fatalities due to ground collision of manned aircraft with the non-participating public is not included in hazard severity definitions. This is not the case for micro UAS, where a wide range of injuries from "none" to "fatality" can potentially occur and ground collision severity becomes the focus of the hazard severity discussion. Due to their much smaller size, micro/mini UAS have less chance of causing a lethal impact. There are two documented instances of fatalities as a result of blade lacerations. These were caused by rotorcraft with blade diameters approaching a meter. Figure 6, Figure 7, and Figure 8 illustrate the differences in

⁶⁴ Bloody drone accident Enrique Iglesias slices hand at live concert Mexico
<https://www.youtube.com/watch?v=hOTOymQJMLk>. Accessed 02/15/2016

⁶⁵ DRONE PROPELLERS SLICES MANS HAND OPEN BLOODY YUNEEC Q500 TYPHOON
<https://www.youtube.com/watch?v=0uGLIZShbmQ>.

⁶⁶ Girl Injured by Mini Helicopter (FOX13 News items Tampa Bay) 20-4-2010
<https://www.youtube.com/watch?v=HNZwYHI9xS4>. Accessed ??/??/2016

⁶⁷ Horrible RC Plane Accident <https://www.youtube.com/watch?v=OeGODvfwYXY>.

⁶⁸ Mishap Cutting the arm with an airplane RC propeller <https://www.youtube.com/watch?v=-EfbEvifoZI>.

terminal and cruise velocities and corresponding impact kinetic energy between manned aircraft, UAS and payloads falling from a UAS. Aircraft and payload physical and dynamic characteristics are documented in Appendix C. The aircraft titled “COA UAS” shown in Figure 6, Figure 7, and Figure 8 are UAS owned and operated by KU, and the military UAS portrayed in these plots range from the RQ-11 Raven up to the MQ-1 Predator.

An obvious comparison of UAS and manned aircraft involves comparisons of velocity and kinetic energy. Figure 6 is a plot of terminal velocity for selected UAS and manned aircraft up to 10,000 lbs (with certification basis indicated). The calculations include the estimated effects of drag. For this calculation, the vehicle or payload was considered to simply “fall” without aerodynamic lift. The reference area for drag for fixed wing aircraft was based aircraft wingspan and fuselage length. For rotorcraft, the area was estimated with rotor diameter and a solidity of 0.3. A coefficient of drag (C_d) of 0.96 was estimated for all aircraft based on the computational fluid dynamics (CFD) analysis of the Phantom 3 discussed in Section 4.14.1.

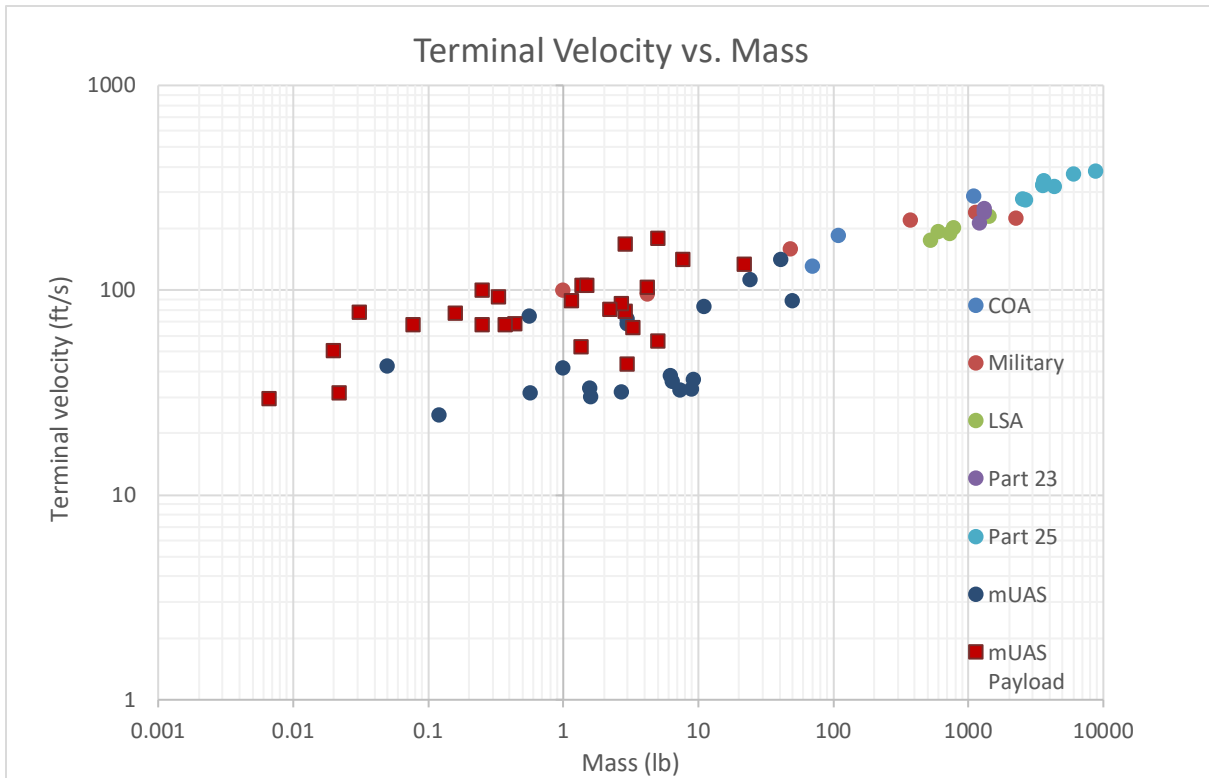


Figure 6 - Comparison of Estimated Terminal Velocity for Several Manned Aircraft and UAS Departing Controlled Flight from 400 ft AGL ⁶⁹/₇₀

⁶⁹ "Compare Drones - Search, Find, and Compare Drone Specs." Accessed April 20, 2016. <http://drones.specout.com/>.

⁷⁰ "Compare Airplanes." Aircraft Comparison. Accessed April 20, 2016. <http://planes.axlegeeks.com/>.

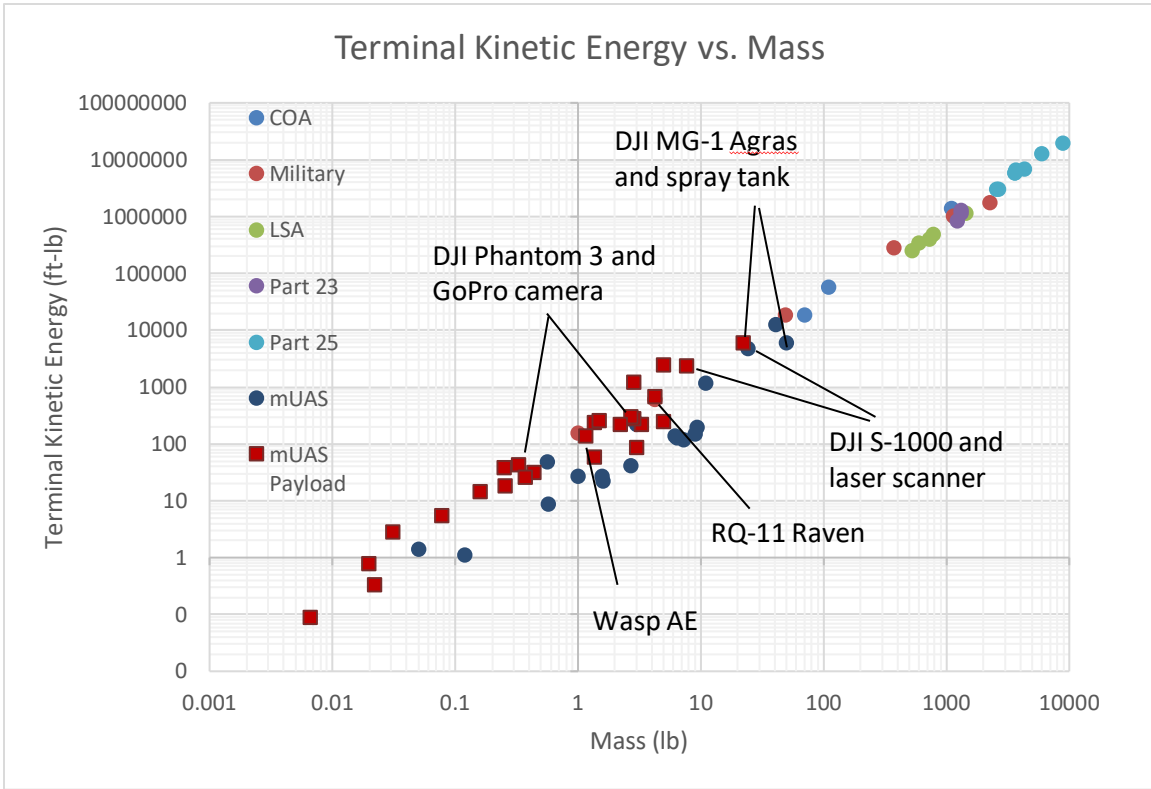


Figure 7 - Comparison of Estimated Kinetic Energy for Several Manned Aircraft, UAS and UAS Payloads Departing Controlled Flight from 400 ft AGL^{69,70}

Figure 7 compares the kinetic energy of a set of small UAS and UAS payloads to several manned aircraft departing controlled flight from 400 ft AGL. The data illustrates an operational difference between manned aircraft and small UAS in terms of kinetic energy.

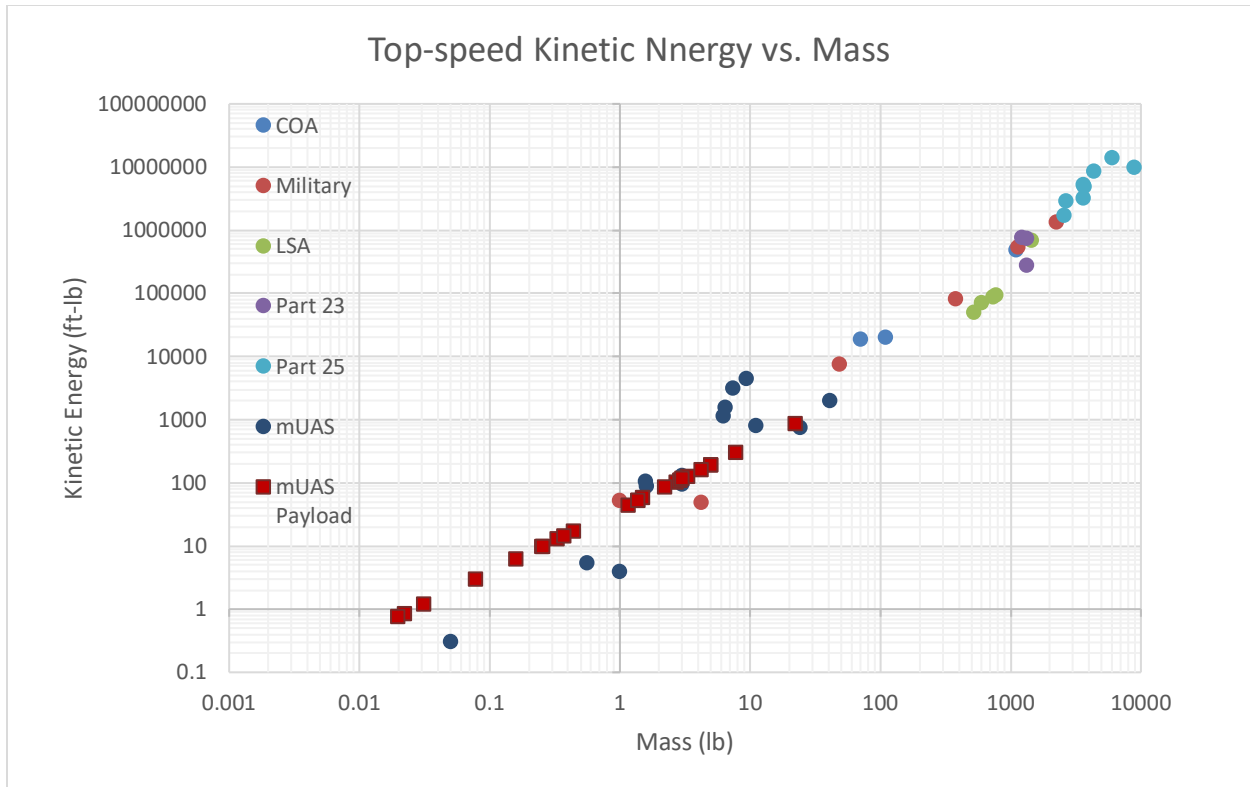


Figure 8 - Estimated Terminal KE for UAS and Manned Aircraft^{69,70}

Figure 8 compares the kinetic energies of the vehicles represented in Figure 6 when flying at top speed. The data follows the same trend seen in the previous plots, that is, that there is a significant difference between the lethality of the UAS/UAS payload and manned aircraft, even the FAR Part 103⁷¹ Ultralight Aircraft and Light Sport Aircraft (LSA).

⁷¹ [http://rgl.faa.gov/Regulatory_and_Guidance_Library/rgAdvisoryCircular.nsf/list/AC%20103-7/\\$FILE/Signature.pdf](http://rgl.faa.gov/Regulatory_and_Guidance_Library/rgAdvisoryCircular.nsf/list/AC%20103-7/$FILE/Signature.pdf), access 05/23/16

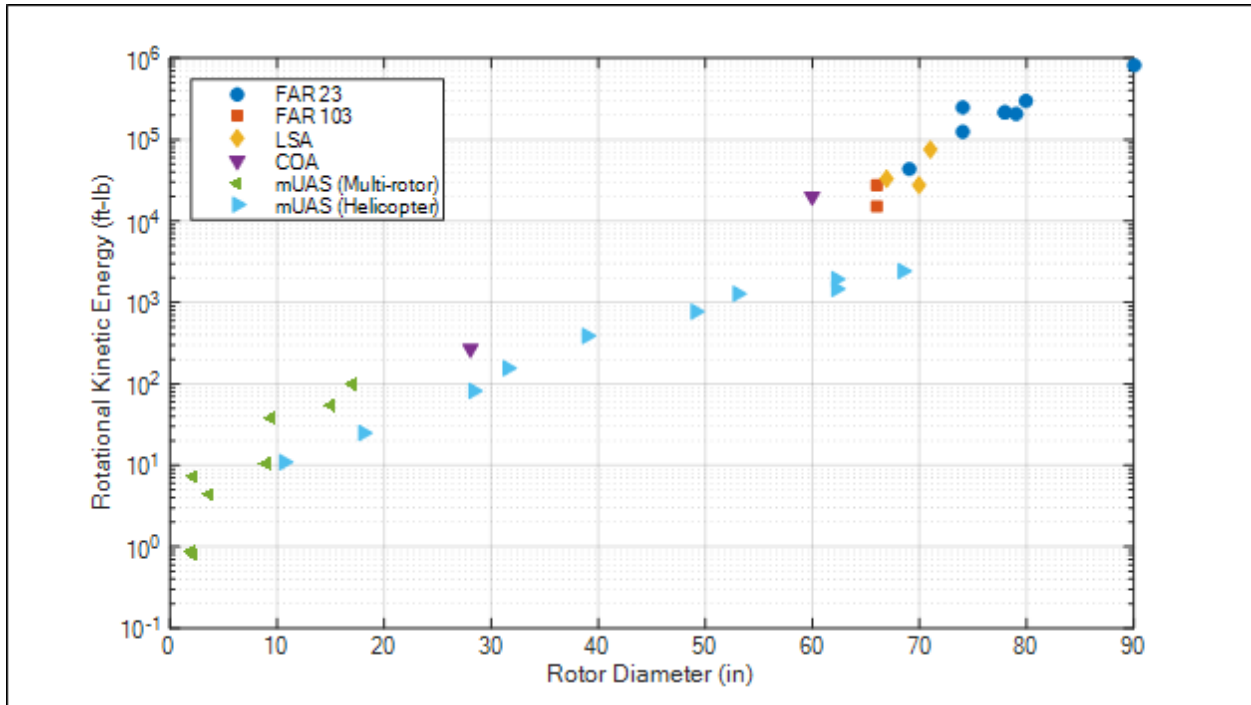


Figure 9 - Comparison Between Rotor Rotational KE for UAS and Manned Aircraft Classes.^{69,70}

Figure 9 shows the estimated rotational kinetic energy of rotors for a range of small UAS and manned aircraft Equation 5 was used to calculate (E_R), based on reported values for rotor mass, diameter, and operating speed.

$$E_R = \frac{1}{2} I \omega^2 \quad \text{Equation 5}$$

Rotor mass moments of inertia were calculated by using the rod approximation in Equation 6.

$$I_{rod} = \frac{1}{12} m D^2 \quad \text{Equation 6}$$

For electric UAS, motor parameters were used to estimate an upper bound for rotor speed. At this point in the analysis, there is a more pronounced crossover between the UAS and manned aircraft because UAS in a helicopter configuration have large rotors that are comparable to manned aircraft props. Prop size; however, is generally not a factor in manned aircraft categorization.

4. Collision Severity Metric Study (UAH)

4.1. Potential Injuries Associated with UAS Ground Collision

There are three main types of injury mechanisms that can result from sUAS collision with a person. The first injury type is blunt force trauma due to high energy impact on the body resulting in acceleration and shearing of organs or the uncontrolled movement of limbs due to impact. The second injury type is penetration injury, which is associated with the application of large forces over small areas, and can be expressed as energy densities – force/unit area. The last type of injury is laceration, which is related to the application of large forces over small areas by propellers and rotors. Lacerations are also impacted by propeller blade leading edge sharpness and blade rigidity.

Sections 4.2 and 4.8 represent two options for the evaluation of vehicle safety. They have developed through the course of this research based on different data inputs and modeling. The initial assessment (Section 4.2) of injury potential due to UAS ground collision is strongly rooted in RCC standards and, ultimately, focuses on the development of scenario-based KE thresholds that are based on estimated exposed areas of people and serve to develop limits for vehicle height and velocities when operating near or over people. However, these RCC thresholds are not directly correlated to injury severity via AIS and they are rooted in the collision dynamics and effects of small, rigid, metallic fragments. The second method (Section 4.8), which was developed as part of the Task A11 – Part 107 Waiver Case Study, used UAS drop testing on an ATD Hybrid III 50th Percentile Male Crash Test Dummy to evaluate injury severity based on Federal Motor Vehicle Safety Standard (FMVSS) 208 and medical literature to develop a means of calculating resultant loading based on impact KE. This resultant loading is then compared with thresholds for head and neck injuries to determine the potential for AIS 3 or greater injury. The latter method has two distinct advantages. First, the collision dynamics examined and used as benchmarks for this analysis are actual UAS impacts to a representative head, versus injuries due to small metallic fragment impacts. Secondly, there is a direct correlation of impact KE to injury severity metrics, by way of FMVSS research and standards, which is completely lacking in a method based purely on RCC thresholds. Regardless of method, impact velocity can be easily estimated experimentally through CFD or measured during testing making impact velocity, and therefore, impact KE, excellent metrics for use by industry when assessing sUAS for injury potential.

4.2. Impact KE Without Injury Correlation (UAH)

The literature survey provided a large range of candidate values for lethal impact KE values. Methods for determining lethal KE values include experimental methods, reference models, and assessment of injury severity. Based on this variability, A4 researchers have spent a considerable amount of time attempting to verify the means by which original researchers obtained the data and understand any statistical methods applied in source material. Figure 10 provides a snapshot of the breadth of different injury and lethality thresholds cited in literature.

On the low end of the spectrum, the RCC document on Inert Debris and AFSCOM⁷² cite 11 ft-lbs as a critical injury threshold. If a falling object remains at or below this impact KE, it would most likely ensure that the object could not produce greater than an AIS level 3 injury in a 1 year old child.⁷³ This is a very conservative number, however, it serves to protect the majority of the population. Moving up the scale, NAVAIR cites 15 ft-lbs as the KE threshold for skull fracture, however, NAVAIR stated, *“For the purposes of this effort, the assumption is made that skull fracture, particularly fractures to the base of the skull, result in a fatal head injury when left untreated for 24 hours.”* NAVAIR further used the blunt trauma criteria to develop a probability of skull fracture based upon cadaver studies on skull fractures.⁷⁴ The 15 ft-lbs KE criteria was derived from a 10% probability of skull fracture and correspondingly a 10% POF if left untreated for 24 hrs. The NAVAIR KE threshold is a low biased value because cadaver study was based on the skulls of elderly people that tend to have more brittle and fracture-prone bones than younger people. Most other KE values found in the literature, regardless of the initial paper reviewed,

⁷² Air Force Space Command Manual 91-710, Volume 1; Safety, 1 July 2004.

⁷³ Range Commander’s Safety Council, Common Risk Criteria for National Test Ranges; Supplement: Standard 321-07, June 2007.

⁷⁴ Raymond, David, et al. “Tolerance of the skull to blunt ballistic temporo-parietal impact,” Detroit, MI: Journal of Biomechanics, Jul 2009, Vol. 42, pp. 2479-2485. Doi: 10.1016.

trace back to one of two studies – either Feinstein or Janser. Both of these studies worked to develop a quantitative assessment of injury hazards (type of injury) and probability for the fatality of injuries based on fragment velocity and mass. These studies also compare the various probabilities of fatality based on the body region (head, thorax, abdomen, or limbs) that is impacted by the debris. Many other KE threshold values cited in RCC documents come from Feinstein’s work.

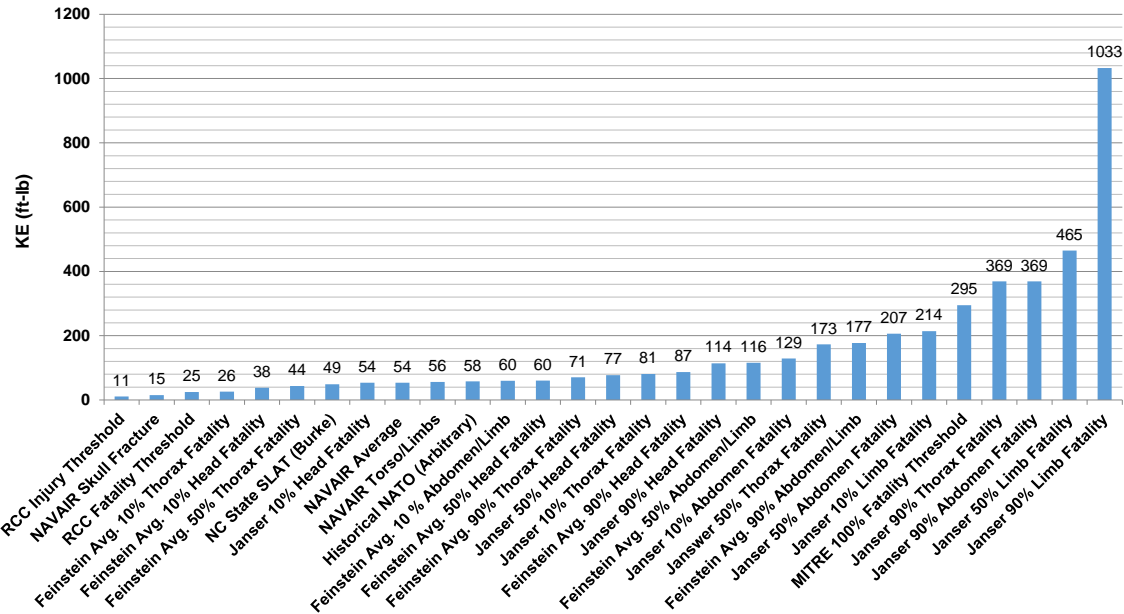
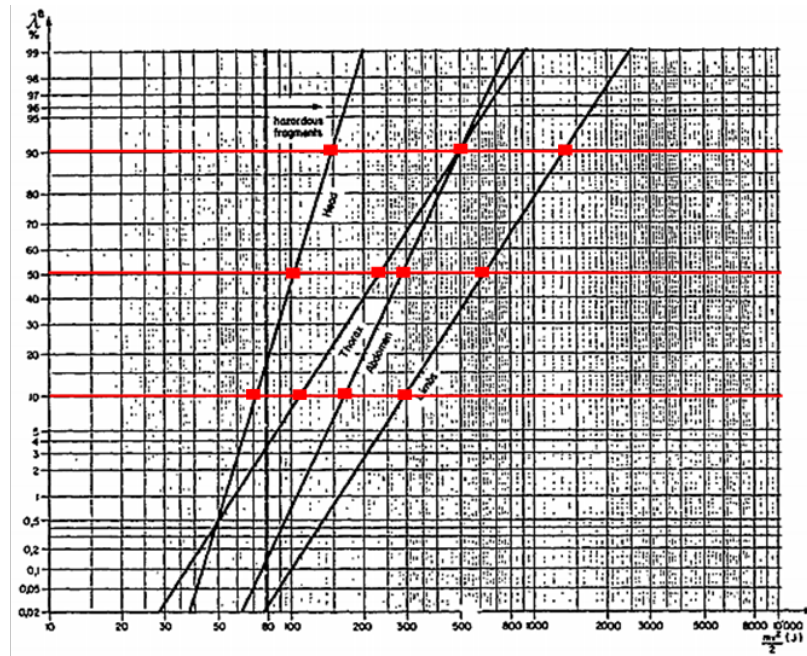


Figure 10 - Injury/Fatality Thresholds from Various Studies

Janser’s plot and data points pulled from the plot are shown in Figure 11. One key difference between Feinstein and Janser is the way in which they both divided up the body regions. Janser developed KE thresholds with associated probabilities of death for the head, thorax, abdomen, and limbs as separate parts, while Feinstein lumped abdomen and limbs into a composite value. This does seem counterintuitive in that abdominal injuries are much more likely to be fatal (blunt trauma to organs) at lower energies than limb injuries – the grouping precludes differentiating the injury thresholds for each body region. Qualitatively, it can also be observed that Janser’s values are significantly higher than those of Feinstein’s, which lends itself to saying that Feinstein’s work represents a more conservative estimate of the impact energies required to injure or kill. While it is not explicitly stated, the more conservative numbers from Feinstein’s were the basis for using this data for the RCC standards. Figure 12 shows an example of Feinstein’s Kill Probability charts and a table of KE values that were derived from Feinstein’s original charts⁴⁶. All table values in Figure 11 and Figure 12 were extracted with a plot digitizer and verified by hand. Of note, the Feinstein values in Figure 12 correlate closely with the 10%, 50%, and 90% POF values in RCC documents. Feinstein’s team developed their data set from testing on live animals and animal carcasses, whereas the source of Janser’s data is not laid out as clearly. It is much harder to qualify Janser’s content because of this fact. This may bolster the rationale for why RCC utilized the Feinstein data to develop the RCC standards. It is important to note that the debris impact

studies are only truly valid for impacting masses up to 2 lbs. Their application to larger masses is a matter of extrapolation, which has been performed in the RCC documents and elsewhere.⁷⁵



	% Prob. Of Death	KE (J)	KE (ft-lb)	AIS
Head	10	73	54	<3
	50	105	77	4,5
	90	155	114	6*
Thorax	10	110	81	<3
	50	235	173	4,5
	90	500	369	6*
Abdomen	10	175	129	<3
	50	280	207	4,5
	90	500	369	6*
Limbs	10	290	214	<3
	50	630	465	4,5
	90	1400	1033	6*

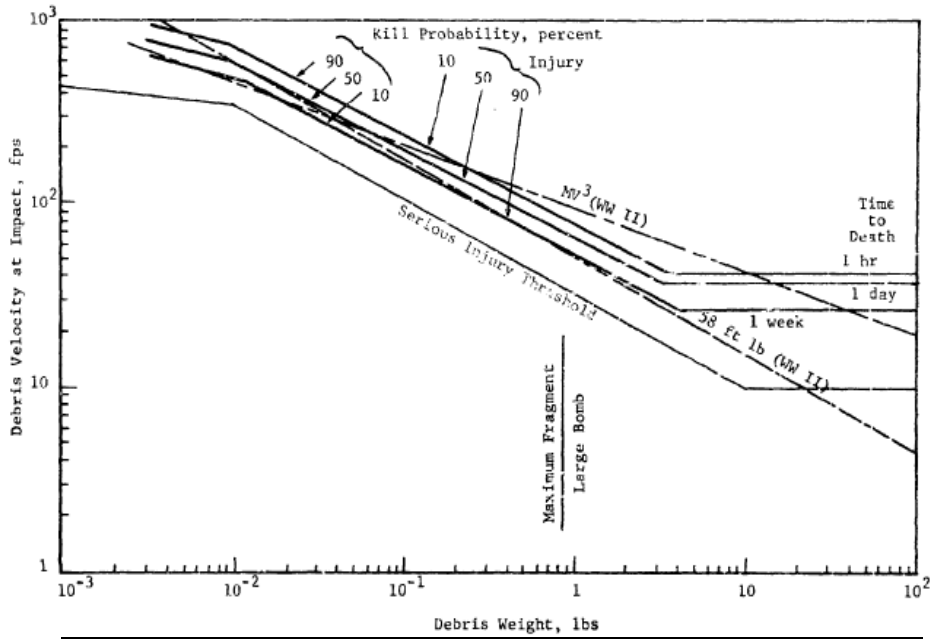
* AIS = 6 is more a function of not having any treatment options more than just an injury being fatal

Figure 11 - Janser KE Thresholds¹⁹

Knowledge Gap: The true injury and lethality potential of larger impacting masses, especially masses with substantially different inherent flexibility than those considered by the RCC, is a significant knowledge gap. The drop testing by NIAR, as part of Task A11, and modeling by MSU and ERAU address some of these questions, but further testing of system impacts by UAS and their impacts on people rather than extrapolation from small, metal debris studies is needed. This can be effectively addressed

⁷⁵ Cole, J.K., L.W. Young, and T. Jordan-Culler. "Hazards of Falling Debris to People, Aircraft, and Watercraft," Sandia National Laboratory. 1997. doi:10.2172/468556.

through more research using validated Finite Element Analysis and dynamic modeling to improve the understanding of energy transfer during UAS impact and how that energy transfer is affected by vehicle orientation during impact, vehicle geometry, and vehicle materials.



	% Prob. Of Death	KE (J)	KE (ft-lb)	AIS
Head	10	51	38	<3
	50	82	60	4,5
	90	118	87	6*
Thorax	10	36	26	<3
	50	59	44	4,5
	90	96	71	6*
Abdomen/Limbs	10	81	60	<3
	50	157	116	4,5
	90	241	177	6*

* AIS = 6 is more a function of not having any treatment options more than just an injury being fatal

Figure 12 - Example Kill Probability Chart and Feinstein Single-Point KE Values⁴⁶

Body Part	Probability of Fatality (Kinetic Energy, (ft-lbf))			Log Normal Parameters	
	10%	50%	90%	α (ft-lbf)	β^*
Head	38	55	79	55	0.2802
Thorax	28	44	72	44	0.3737
Abdomen & Limbs	55	98	157	96	0.4335

* using natural logarithm

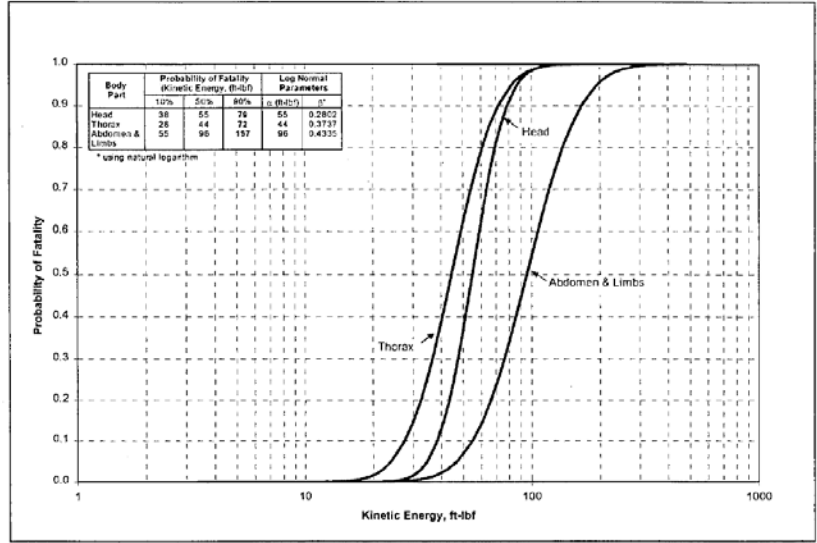


Figure 13 - Probability of Fatality from Debris Impacts for Various Body Parts⁷⁶

RCC 321-00⁷⁶ presents KE thresholds that are correlated with POF. The basic probabilities of fatality, which are mapped to KE based on individual body parts, are shown in Figure 13. These values show that KE values that have a 10% POF for the head, thorax, and abdomen and limbs are 38 ft-lbs, 28 ft-lbs, and 55 ft-lbs, respectively. Figure 14 shows a position-weighted approach to KE threshold development by the RCC. This method averages KE thresholds in terms of the exposed area of each part in either standing, sitting, or prone positions.

⁷⁶ Range Commander's Council, "Common Risk Criteria for National Test Ranges; Inert Debris," Supplement to Standard 321-00, April 2000.

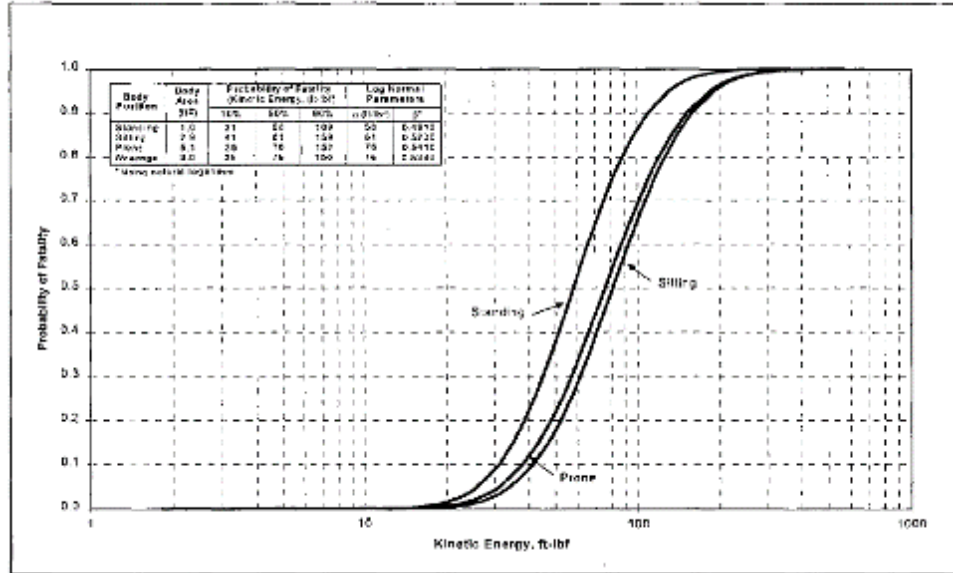


Figure 14 - Probability of Fatality from Debris Impacts for Various Body Positions⁷⁶

These single-point values have one considerable weakness in that they lack an operational context. Many documents, in particular the RCC manuals,^{20,73,76,77} cite assumptions that shape the KE thresholds. For example, one assumption is that debris will be coming down vertically, in which case the head is most vulnerable and thresholds are based on the values for head. Another effect of assuming vertically falling debris is that other possible injuries are to the shoulders and, perhaps, the feet and lower limbs. While a shoulder injury can induce longer-term disability, shoulders can withstand more impact KE than the thorax. An analytical method employed within the RCC documents is to consider the projected area of each region of the body and calculate weighted averages based on the probability of people being in different positions, e.g. standing, sitting, and prone. Figure 15 illustrates correlation of impact KE values with probability of fatality based on an average of the curves developed during position-weighting in Figure 14. The material in the RCC documents represents a military range scenario in which a certain number of personnel are assumed to be in a prone position, which is normal in a tactical environment. It is not representative of a typical civilian population.

⁷⁷ Range Commander's Council, "Common Risk Criteria Standards for National Test Ranges," Supplement: Standard 321-07, June 2007.

Body Position	Body Area (ft ²)	Probability of Fatality (Kinetic Energy, (ft-lb))		
		10%	50%	90%
Standing	1.0	31	58	109
Sitting	2.0	41	81	159
Prone	5.1	38	76	152
Average	3.0	38	76	150

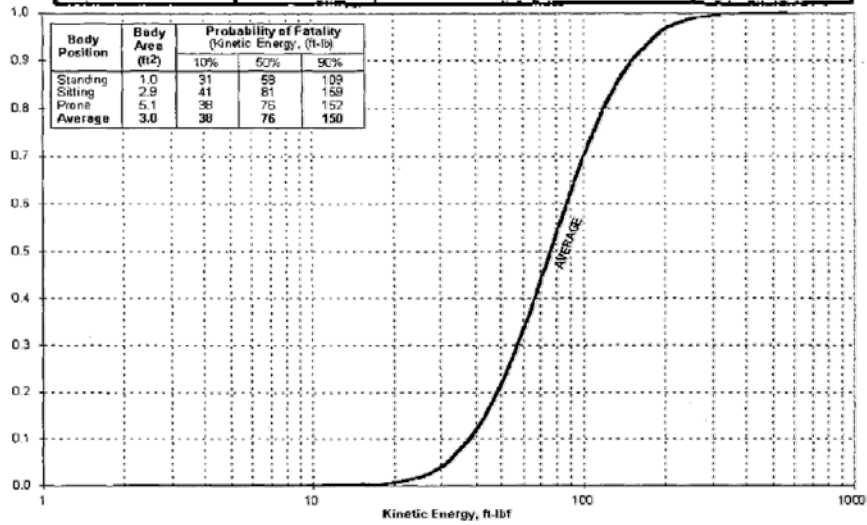


Figure 15 - Average Probability of Fatality from Debris Impacts⁷⁶

4.2.1. Impact Energy using a Modified Body Area Weighted Approach (UAH)

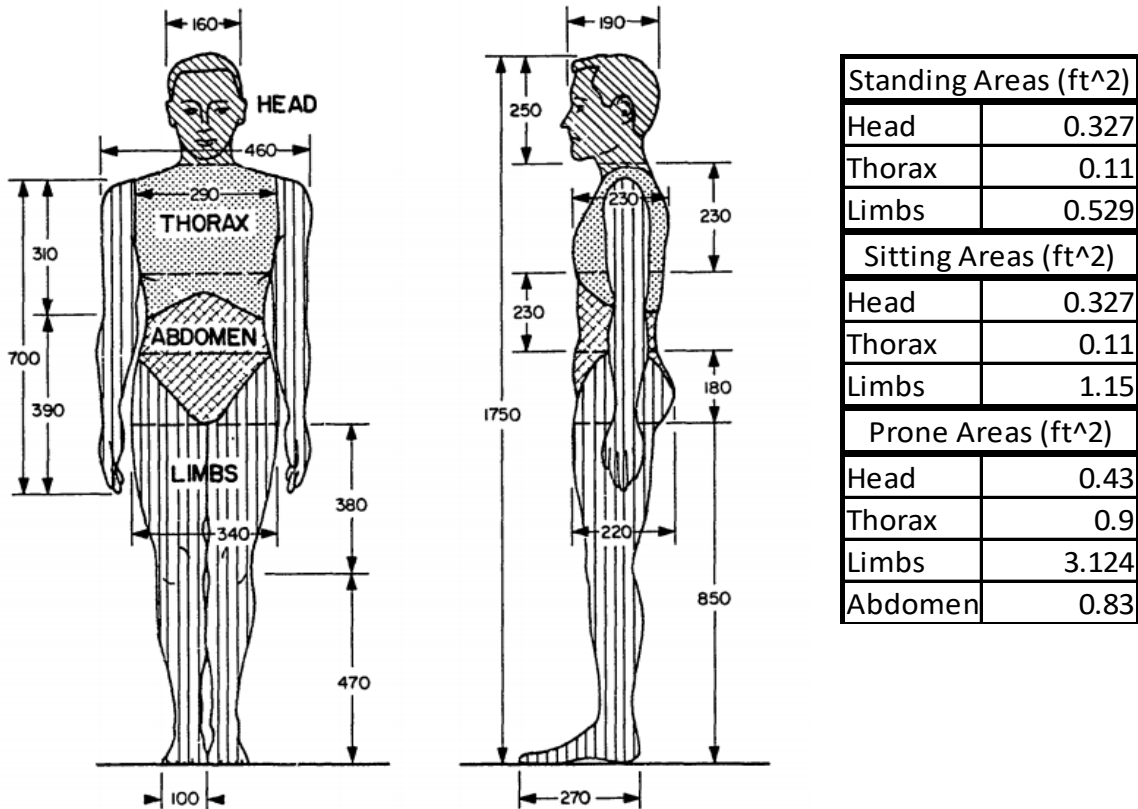


Figure 16 - Janser Standard Man Dimensions and Calculated Projected Areas¹⁹

To address a more realistic scenario for UAS impacts, researchers in the A4 team developed an alternate method based on the RCC position-weighting seen in Figure 15. The modified area weighted method involves taking both the vertical and horizontal projections of the 50th percentile Janser man shown in Figure 16 for the standing and sitting positions. Averaging these two projected areas accounts for a range of UAS impact orientations that can happen anywhere between the horizontal and the vertical. These exposed areas can be recalculated for specific operational conditions to address varying levels of body exposure. A rock concert with nearly everyone standing might only have exposed areas of the upper limbs, thorax and head; whereas a suburban or mid-sized city might have areas where the non-participating public is more widely spaced and all portions of the body are exposed.

Table 12 - Comparison of NASA 50th Percentile Male and Janser Standard Man Anthropometric Model Dimensions

	NASA 50th Percentile	Janser Std. Man	Err	% Err (abs)
Shoulder Height (cm)	147.6	150	-2.4	1.63%
Hip Height (cm)	95.8	94	1.8	1.88%
Shoulder Width (cm)	48.9	46	2.9	5.93%
Chest Width (cm)	33.2	29	4.2	12.65%
Hip Width (cm)	35.8	34	1.8	5.03%
Head Width (cm)	15.7	16	-0.3	1.91%

To calculate the projected areas exposed to a UAS collision, the A4 team used the standard established by the FAA of using the 50th percentile male.⁷⁸ Given that Paul Janser’s “Standard Man” (Figure 16) is close to the NASA 50th Percentile Male, as shown in Table 12, and that Janser’s anthropometric model is cited in RCC,^{20,73,76,77} Sandia Labs,⁷⁵ and NAVAIR⁴³ documentation, these dimensions were used for the calculations. Janser’s anthropometric model was also chosen because it provides greater detail than that of Feinstein. In most dimensions, Janser’s Standard Man and the 50th percentile male are within 10% of one another, with the largest difference being a 12.65% error in chest width based on a difference of 4.2 cm. Based on the Janser body part height and length data, the exposed areas, when viewed from directly above, for three different body positions are shown in Figure 16. These area values were calculated by UAH researchers, and were not published in Janser’s work.

The A4 team first developed area weighted KE thresholds for each POF and body position. These are shown in Table 13 and derived from Figure 13. Equation 8 was used to develop the area-weighted KE thresholds. Equation 7 is unique to Janser’s work because it differentiates between abdomen and limb areas and corresponding KE values. For use with RCC KE values that combine abdomen and limbs, the area terms are combined and used with the abdomen and limbs KE terms. Table 13 shows the KE thresholds taken from the RCC publications based on POF and shows the corresponding AIS definitions with a qualitative alignment to POF. Table 14 shows the projected area calculations for each body position for people in the open. Table 14 also shows the average of the horizontal and vertical projected areas used in the calculations.

$$KE_{avg|lethal} = \frac{(KE_{head}A_{head})+(KE_{Abdo}A_{abdo})+(KE_{thrx}A_{thrx})+(KE_{limb}A_{limb})}{A_{head}+A_{abdo}+A_{thrx}+A_{limb}} \quad \text{Equation 7}$$

The area weighted KE thresholds calculated from RCC KE values and the Janser Standard Man calculated average projected areas are shown in Table 13. The prone position is not being used because this example is meant to portray a typical open area scenario with exposed non-participating public. The prone position is typically needed solely for a military scenario and would only be applicable when considering a beach or pool setting for the general public.

⁷⁸ <https://msis.jsc.nasa.gov/sections/section03.htm>, Accessed 09/22/16

Table 13 – Area Weighted KE Thresholds by Body Position and POF from the RCC
(Derived from Figure 13)

	% Prob. Of Death	KE (J)	KE (ft-lbs)	AIS
Head	1	39	29	<3
	10	52	38	3
	30	65	48	4
	50	75	55	5
	90	107	79	6*
Thorax	1	24	18	<3
	10	38	28	3
	30	49	36	4
	50	60	44	5
	90	98	72	6*
Abdomen/Limbs	1	47	35	<3
	10	75	55	3
	30	104	77	4
	50	130	96	5
	90	226	167	6*

* AIS = 6 is more a function of not having any treatment options more than just an injury being fatal

Table 14 - Area Projections for UAS Analysis of Weighted KE for an Open Area

Exposed Body Area	Vertical Projections from Janser	Vertical Projections for FAA Analysis	Horizontal Projections for FAA Analysis	Average Projections from Horizontal and Vertical
Standing Areas (ft ²)				
Head	0.327	0.327	0.511	0.419
Thorax	0.11	0.11	0.9	0.505
Limbs	0.529	0.529	3.124	1.827
Abdomen		0	0.83	0.83
Sitting Areas (ft ²)				
Head	0.327	0.327	0.511	0.419
Thorax	0.11	0.11	0.9	0.505
Limbs	1.15	1.15	1.012	1.081
Abdomen		0	0	0
Prone Areas (ft ²)				
Head	0.43	Prone position not a common posture except for beaches and swimming pools that have only minor application to this analysis. Vertical projection the same as Janser, but the horizontal projection would be very small.		
Thorax	0.9			
Limbs	3.124			
Abdomen	0.83			

Table 15 shows the area weighted KE threshold values for each POF for standing and sitting in the open area scenario. If the thorax region was used as the sole vulnerable metric, the KE for a 10% POF would be 28 ft-lbs even though the thorax area in the UAS example makes up only 14% of the exposed body area in this collision scenario. By weighting the areas, the KE threshold for a 10% POF increases to 49 ft-lbs standing and 45 ft-lbs sitting. The average of these two positions is 47 ft-lbs. The sitting position is more dangerous since there is less limb and abdomen area exposed to contact than standing, resulting in a more likely contact with the more vulnerable head and thorax areas. For UAS operations in an open area with the non-participating public moving, standing or sitting in close proximity to or below the requested UAS operating area, the FAA regulators would use the KE thresholds in Table 15 and compare them to the vehicle KE characteristics. They could then determine whether additional mitigations in terms of standoff/altitude restrictions or parachutes, for example, were needed to meet the threshold KE requirements associated with the desired level of safety based upon the POF. Using information derived from vehicle KE modeling (Figure 41), Table 16 shows the unmitigated and parachute mitigated weights for each area weighted KE threshold based upon each POF for the open area scenario. Using the 47 ft-lbs area weighted KE threshold for a 10% POF, the average multi-rotor with a weight greater than 0.76 lbs would be restricted from flight over people without any mitigations. However, a multi-rotor with a weight of up to 9.8 lbs and a parachute that descends at a rate of 18 ft/sec would be approved for conducting the flight operation over people with the same level of safety. In lieu of the parachute, the FAA might use a different threshold level because an operational restriction limits the operator to visual line of sight (VLOS) operations with a minimum standoff distance and maximum operating speed to significantly reduce the probability of ground collision. This would increase the unmitigated and mitigated weight for the operation while still allowing the operator to fly in a populated area.

Table 15 - Area Weighted KE Values for UAS in an Open Area

Standing	KE (ft-lbs)
1% POF	32
10% POF	49
30% POF	68
50% POF	84
90% POF	143
Sitting	
1% POF	29
10% POF	45
30% POF	61
50% POF	74
90% POF	125

Table 16 - Weight of Vehicle Derived from Parachute Descent Rates and Area Weighted KE Thresholds for Flight Over People in an Open Air Scenario such as a City Park

	Descent or Horizontal Velocities (fps)	Descent or Horizontal Velocities (kts)	Weight (lbs for 32 ft-lbs KE Threshold for 1% POF)	Weight (lbs for 49 ft-lbs KE Threshold for 10% POF)	Weight (lbs for 68 ft-lbs KE Threshold for 30% POF)	Weight (lbs for 84 ft-lbs KE Threshold for 50% POF)	Weight (lbs for 143 ft-lbs KE Threshold for 90% POF)
	10.0	5.9	20.5	31.7	43.6	54.0	92.2
	12.0	7.1	14.3	22.0	30.3	37.5	64.0
	14.0	8.3	10.5	16.2	22.3	27.5	47.0
	16.0	9.5	8.0	12.4	17.0	21.1	36.0
	18.0	10.7	6.3	9.8	13.5	16.7	28.5
	20.0	11.8	5.1	7.9	10.9	13.5	23.1
	22.0	13.0	4.2	6.5	9.0	11.2	19.1
	24.0	14.2	3.6	5.5	7.6	9.4	16.0
	26.0	15.4	3.0	4.7	6.5	8.0	13.6
	28.0	16.6	2.6	4.0	5.6	6.9	11.8
	30.0	17.8	2.3	3.5	4.8	6.0	10.2
	32.0	19.0	2.0	3.1	4.3	5.3	9.0
	34.0	20.1	1.8	2.7	3.8	4.7	8.0
	36.0	21.3	1.6	2.4	3.4	4.2	7.1
Maximum Vehicle Weights in lbs Unmitigated based upon KE maximums above and slope of KE_{impact}/lbs MGTOW							
Slope of KE_{impact}/lbs MGTOW	64.7	ft-lbs/lbs MTOGW	0.49	0.76	1.05	1.30	2.2

POF – Probability of Fatality

This area weighted KE methodology can be tailored to specific scenarios such as a UAS flying over the crowd at a rock concert where only the upper arms, thorax and head are at risk. The rock concert scenario KE thresholds are derived from the modified exposed body areas in Table 14. Table 18 shows the resulting area weighted KE thresholds for the rock concert scenario. The area weighted KE threshold for 10% POF is reduced to 38 ft-lbs which is consistent with the more vulnerable exposed area being focused on the head and thorax. The thorax is only 40% of the total area. The limbs are now reduced to 25%. The limbs are not given credit for absorbing as much of the KE following collision with the concert goer; therefore, the metric is biased lower. Similar to Table 15, this information is combined vehicle KE modeling to analyze the fatality threat for the rock concert scenario. The unmitigated weight for a UAS is reduced to a 0.59 lbs vehicle for a 10% POF. However, the use of an 18 ft/sec parachute with sufficient deployment altitude would allow approval of a 7.5 lbs vehicle with the same level of safety. Standoff distances as a function of altitude would not be a potential mitigation for this application since the rock concert would not have landing areas or offsets for the UAS. While there may be a wide variety of mitigations that could be employed, the area weighted KE threshold methodology is a more robust way of evaluating KE thresholds related to blunt trauma injuries without arbitrarily focusing on one area of the body.

Table 17 - Projected Area for UAS Analysis of a Rock Concert with Standing Room Only

Exposed Body Area	Vertical Projections from Janser	Vertical Projections for FAA Analysis	Horizontal Projections for FAA Analysis	Average Projections from Horizontal and Vertical
Standing Areas (ft ²)				
Head	0.327	0.327	0.511	0.419
Thorax	0.11	0.11	0.9	0.505
Limbs	0.529	0.400	0.194	0.297

Table 18 - Area Weighted KE Thresholds for UAS Rock Concert Example

Standing	KE (ft-lbs)
1% POF	26
10% POF	38
30% POF	50
50% POF	60
90% POF	98

Table 19 - Weight of Vehicle Derived from Parachute Descent Rates and Area Weighted KE Thresholds for Flight Over People in a Rock Concert

	Descent or Horizontal Velocities (fps)	Descent or Horizontal Velocities (kts)	Weight (lbs for 26 ft-lbs impact KE threshold for 1% POF)	Weight (lbs for 38 ft-lbs impact KE threshold for 10% POF)	Weight (lbs for 50 ft-lbs impact KE threshold for 30% POF)	Weight (lbs for 60 ft-lbs impact KE threshold for 50% POF)	Weight (lbs for 98 ft-lbs impact KE threshold for 90% POF)
	10.0	5.9	16.7	24.5	32.2	38.6	63.1
	12.0	7.1	11.6	17.0	22.3	26.8	43.8
	14.0	8.3	8.5	12.5	16.4	19.7	32.2
	16.0	9.5	6.5	9.6	12.6	15.1	24.6
	18.0	10.7	5.2	7.5	9.9	11.9	19.5
	20.0	11.8	4.2	6.1	8.0	9.7	15.8
	22.0	13.0	3.5	5.1	6.6	8.0	13.0
	24.0	14.2	2.9	4.2	5.6	6.7	10.9
	26.0	15.4	2.5	3.6	4.8	5.7	9.3
	28.0	16.6	2.1	3.1	4.1	4.9	8.0
	30.0	17.8	1.9	2.7	3.6	4.3	7.0
	32.0	19.0	1.6	2.4	3.1	3.8	6.2
	34.0	20.1	1.4	2.1	2.8	3.3	5.5
	36.0	21.3	1.3	1.9	2.5	3.0	4.9
Maximum Vehicle Weights in lbs Unmitigated based upon KE maximums above and slope of KE _{impact} /lbs MGTOW							
Slope of KE _{impact} /lbs MGTOW	64.7	ft-lbs/lbs MGTOW	0.40	0.59	0.77	0.93	1.5

4.3. Evaluation of the Modified Area-Weighted KE Threshold Method (UAH)

The area weighted KE threshold establishes a metric from which the specific vehicle and mitigation measures can be refined for the representative operational situations that is similar to the approach taken by the RCC. This approach provides a risk-based, scenario driven approach to determining KE metrics rather than the use of a single KE value based upon a single body part and POF. An example of this is an agricultural mission where 90% POF is acceptable due to the limited flight over the non-

participating public with exposed people in the standing position only. These metrics specify a desired level of safety that can be directly correlated to vehicle size and operating limits. For an agricultural mission with fewer participants, this method allows for approval of larger vehicle/platform weights with limited certification requirements with risk addressed by operational considerations and not vehicle impact metrics. However, even though impact KE-thresholds can be established based on RCC Mean Curve or Modified Area-Weighted KE Threshold approaches, there is not a quantitative mapping of RCC POF values with injury severity metrics like AIS. The 2008 Update to the AIS standard states probabilities of fatality that correspond to different AIS severity levels, e.g. AIS3 = 8-10% Probability of Fatality. This was done by tracking patient records based on injury type and then calculating a rate of mortality for each injury and developing average mortalities associated with each AIS rating.²⁵ It is tempting to say that 10% POF in AIS is the same as 10% POF from the RCC, but this is a qualitative assumption that is not currently substantiated. AIS ratings are based on a number of factors, e.g. threat to life, mortality: theoretical, expected, actual, amount of energy dissipated/absorbed, tissue damage, hospitalization and the need for intensive care, length of hospital stay, treatment cost, treatment complexity, length of treatment, temporary and permanent disability, permanent impairment, and quality of life. The RCC's data was taken from Feinstein, who conducted analysis of a number of experimental data sets concerning metallic debris impacts on animals and extrapolated to estimated human injury/mortality by way of scaling. The RCC threshold probabilities of fatality are binary in nature, in that they describe whether an impact results in death or not, whereas AIS ratings are meant to describe injury severity along a number of dimensions. Section 4.8 introduces a method that directly correlates impact KE with injury severity assessments and research done on human cadavers.

4.4. KE Sports Ball Analogy (UAH)

Table 20 - RCC KE Thresholds and Comparisons with Sports Balls

Probability of Fatality of Lethal Strike	AFSCOM 1% chance of < AIS 3	1% POF from a head injury while Standing RCC or 10% POF due to a Thorax Injury	10% POF due to a Head Injury RCC	50% POF due to a Head Injury RCC	90% POF due to a Head Injury RCC	90% POF in the Standing Position RCC	100% POF Average RCC
Kinetic Energy (Ft-lbs)	11	28	38	55	79	109	295
Kinetic Energy In Joules	15	38	52	75	107	148	400
Speeds to Achieve Lethal Ranges above (mph)							
Squash Ball (25 g, 0.88 ounces)	77	123	144	173	207	243	400
Tennis Ball (58 g, 2.1 ounces)	50	80	93	112	134	158	260
Baseball (149 g, 5.26 ounces)	32	50	59	71	85	100	164
Hockey Puck (170 g, 6 ounces)	30	47	55	66	79	93	153
Softball (198.4 g, 7.0 ounces)	27	44	51	61	74	86	142
Bowling Ball (16 lbs)	5	7	8	10	12	14	23

	10U	11-12	13-14	High School	College/Pro
Baseball Speed (mph)	45	55	65	80	91
Softball Fast Pitch Speed (mph)	44	52	54	58	69

To assess the value of the various RCC KE injury metrics in relation to the real world and publicly accepted metrics, the RCC KE values for incremental levels of POF were compared with the KE of sports balls based upon their relative mass and their velocities. The analysis determined the required velocities for various sport balls that must be achieved in order to reach the different KE threshold values. This helps to relate the UAS scenario numbers to physical phenomena that might be more relatable to the general public. Table 20 shows a comparison of the various POF thresholds against the KE of sports balls used in publicly accepted venues for families as well as professional athletes. The table shows how fast various balls (squash, tennis, baseball, softball, bowling balls, and a hockey puck) would have to travel in order to achieve the thresholds. Average speeds for baseball and softball pitches are also shown and aligned with their representative age groups, by column. The yellow-highlighted blocks show where the required speeds are close to the fastest recorded speeds for the different balls in the respective professional sports. The table provides a more concrete context for understanding impact energies than the comparison with less well understood UAS platforms. The POF must be combined with probability of actually striking a person to better understand acceptable safety levels.

Knowledge Gap: Development of probability distributions using UAS vehicle aerodynamics and failure modes is vastly different from the ballistic modeling done for space debris and requires additional research to better understand these two characteristics. See Section 4.11 concerning standoff distances and their relationship to severity. This knowledge gap is being addressed in the proposed white papers entitled *W64 - Falling Multi-Rotor Dynamics Study* and *W65 - Probability of UAS Ground Strike to People and Objects*.

4.5. Evolution of RCC Standards and Their Applicability to UAS Ground Collisions. (UAH)

RCC 321-00 published common risk standards for the National Test Ranges and utilized the POF for various impact KEs as shown in Figure 13. As is discussed in Section 4.2, these curves were combined with an area weighting from the Janser Standard Man to develop a S-curve for each body position since

each body part alone does not have an equal probability of being hit by debris based upon a person's position; sitting, standing and prone, as shown in Figure 14. The weighted approach allows for a better assessment of fatalities by accounting for the probability of the debris hitting different body areas as well as accounting for different impact angles that can be assessed through the impact KE values shown in Figure 13. The RCC further modified the curve by averaging the probability for each body position into a composite curve as shown in Figure 15. Figure 15 was specifically developed by the RCC because of the uncertainty associated with which body positions might be encountered in any given impact scenario. Figure 15 represents an equal weighting of the standing, sitting and prone positions based upon Figure 14 and was deemed by Sandia and the RCC to represent conservative values for POF since most situations involving collision in populated areas have a mixed distribution of people in different orientations, and standing and sitting can also represent differences in impact angles. Sandia Labs developed these curves from Feinsein's original work and these curves remain part of the RCC standards today. The limitations of the RCC standards are rooted in the fundamental assumptions made to generate the curves and the basis for POF data.

Sandia Labs was part of the Risk and Lethality Commonality Team (RALCT) that was formed in 1996 to address safety concerns related to the generation of inert debris by flight tests at national ranges. The debris analysis required by the national test ranges "...can vary from hardware shed during normal missile operation to fragments generated by explosion, hypervelocity collision, aerothermal breakup, or a flight termination system." The RCC plots were developed from Feinsein's data and employed weightings for hypervelocity type collisions where the debris contained a larger number of low mass fragments. Figure 13, Figure 14, and Figure 15 represent the weighted KE values for these more numerous, smaller mass fragments. Furthermore, the analysis conducted by the RCC and Sandia Labs shows that the inert debris impacts were largely vertical since it was assumed that the breakup or collisions would occur at very high altitudes. Sandia Labs recommended that the data set and analysis which culminated in Figure 13, Figure 14, and Figure 15 be utilized by range safety personnel until more accurate data and predictive tools for evaluating large mass (> 2lbs) impact on people is developed.⁷⁵ The testing and analysis of the UAS impacts with the ATD dummy against the FMVSS standards forms the initial basis for a better approach to understanding injuries associated with UAS impacts than utilizing fragment analysis from in-flight breakup of hypervelocity missiles.

4.6. Differences Between UAS Collisions and Low Mass, High Volume Debris Following In-flight Breakup (UAH)

Small UAS (sUAS) ground collisions do not occur due to an in-flight breakup at high altitudes with a large quantity of small mass fragments, but rather sUAS platforms tend to have collisions at lower speeds where the whole platform strikes an individual somewhere on the exposed portions of the individual's body. Two fundamental UAS characteristics are addressed to show how the RCC POF metrics may be excessively conservative, as shown by the NIAR results; 1) a sUAS has a larger contact area than that of small debris fragments resulting in less severe injuries for a given impact KE and 2) crash geometries and the elasticity of sUAS cause collisions to be dramatically different than solid, small mass fragments. Crash geometries are defined as the orientation, impact angle and multiple contact areas that define how energy is transferred to the individual during the collision.

4.7. Larger Contact Area of UAS vs. Fragments. (UAH)

The physiological data upon which Feinstein based his analyses was obtained from experiments that had been performed for the Department of Defense on live animals, human cadavers, and skin and gelatin models to determine the injury potential of various blast fragments associated with explosions or blast effects due to an explosion or nuclear blast wave. Tests with animals and human cadavers/skulls were conducted using small ball type projectiles, glass fragments shot from Styrofoam sabots⁷⁹ and dropping subjects/test articles from various heights to create sufficient impact energy necessary for the test. The effect of the larger contact area of the sUAS, when compared to small mass projectiles and glass fragments, is illustrated by way of data published by Fugelso.⁸⁰ The data in Table 21 compares various projectiles falling at terminal velocity or propelled to higher velocities and is based on their ability to penetrate skin and cause blunt trauma resulting in liver fractures. The baseball and golf ball have substantially higher KE when falling at terminal velocity; however, the larger contact area and curved surfaces have extremely low probability of penetrating bare skin and no likelihood of liver fractures when compared with smaller particles such as a penny, nut and bolt that have much lower KE values at terminal velocities, but have a 100% chance of penetrating bare skin and some chance of causing liver fractures. Furthermore, the larger contact areas of small mass fragments versus a full size sUAS prevents the vehicle from striking specific body parts, which is especially true when impact angles are steep. The sUAS physical geometry causes numerous contact points during a collision when descending at impact angles above horizontal making impacts on single body parts, such as the thorax, implausible. For example, the use of blade guards on arms extending away from the main body of the sUAS and landing gear extending down from the sUAS creates barriers to striking small contact areas such as the throat area such that bilateral hemorrhage of carotid arteries is highly unlikely to occur. Bilateral hemorrhage of the thorax was one of the injuries used in the creation of the Feinstein data for the thorax.⁴⁶ Injuries to the thorax become increasingly less plausible when the sUAS is descending at angles greater than 45 degrees. For the waiver submitted for the Phantom 3 Standard and Advanced under Task A11, the descent angles were determined to be greater than 60°, which further reduces the likelihood of any significant impact to the thorax when compared to small fragment projectiles moving horizontally at similar kinetic energies. The use of the thorax impact KE as the sole means of defining regulatory thresholds is excessively conservative in the context of credible impact scenarios and their resulting injury potential for blunt force trauma. The regulatory framework should consider that the potential of laceration injuries to the thorax has a greater likelihood of creating bilateral hemorrhage than blunt force trauma injuries caused by impact KE. The waiver process standards included in this document address appropriate methods for mitigating laceration injuries.

Comparing injury potential of sUAS to data developed from blast fragments with penetration potential and small contact areas does not result in similar contact or collision scenarios that are appropriate for evaluating sUAS. The NIAR tests are actual sUAS collisions that provide actual impact data which is correlated to automotive injury data similar in injury type and forces on the ATD dummy that are more similar to sUAS impacts with a human.

⁷⁹ White, C. S., Bowen, G. I. and Richmond, D. R., Biological Tolerance to Air Blast and Related Biomedical Criteria, Lovelace Foundation, April 1965, U. S. Atomic Energy Commission CEX-65.4.

⁸⁰ Fugelso, L. M., Weiner, L. M., and Schiffman, T. H., *Explosive Effects Computation Aids*, Final Report GARD Project No. 1540, General American Research Division, General American Transportation Corp, Niles, IL.

Table 21 - Injury Characteristics for Some Common Objects⁸⁰

	Object Impacting	Mass (gm)	Velocity (fps)	Area (in ²)	Kinetic Energy (ft-lbf)	Probability of Bare Skin Penetration	Likelihood of Liver Fracture ⁺
Terminal Velocity	Warhead Canister	2600	279	9.0	6936	1.000	Large
	Cable (6ft x 1 in)	1590	77	71.3	323	0.002	Some
	38 Cal. Bullet	16	432	0.11	102	1.000	Large
	30 Cal. Bullet	12	473	0.07	92	1.000	Large
	Warhead Fragment	70	174	0.62	73	0.966	Some
	Baseball	145	109	6.5	59	0.015	No
	Golf Ball	46	106	2.2	18	0.011	No
	22 Cal. Bullet	3	329	0.037	11	1.000	Some
	Penny	3	309	0.42	9.8	1.000	Some
	Nut & Bolt	14	93	0.44	4.1	0.018	No
Propelled	22 Cal. Bullet	3	1476	0.037	224	1.000	Large
	Golf Ball	46	249	2.2	98	0.632	Some
	90 mph Fast Ball	145	132	6.5	87	0.045	Some

⁺ Probability of bare skin penetration and liver fracture based on data of Needles and Rudolph.²⁸

^{*} Assuming a body mass around 68 kg (150 lbs).

4.8. Impact Energy Correlated to Potential Injury Severity (UAH)

This method of evaluating injury potential developed as part of FAA Task A11, is based on well-established research from automotive and medical research. It also incorporates a baseline data set of injury probabilities based on actual UAS impact KE values and collision dynamics. The UAS drop testing and data collection were conducted at NIAR. UAH conducted analysis of the data and a comparison with medical literature. This section begins with a description of the NIAR drop testing, continues with assessment of injury severity from the NIAR testing, and then concludes with development of a method of assessing head and neck injury potential based on impact KE that any manufacturer could conduct. It concludes with an assessment of permissible vehicle weights for flying over people, with parachute mitigations, based on RCC impact KE thresholds and the new Potential Injury Severity assessment.

4.8.1. NIAR Drop Testing

4.8.1.1. Test Setup

NIAR conducted a series of vehicle drop tests on the head of an ATD Hybrid III 50th Percentile Male Crash Test Dummy.⁸¹ The testing consisted of 24 complete tests using a DJI Phantom 3 Standard striking the test dummy to simulate a vehicle collision with a person based on a range of failure flight conditions. NIAR conducted two tests that were considered no tests, for a 30-foot vertical drop and a 62° impact angle drop. These two tests yielded dummy instrument readings, but did not produce any high-speed video or photometric data and as such were deemed as no tests. Table 22 summarizes all of the

⁸¹ Humanetics Innovative Solutions. (08/30/2016) *Hybrid III 50th Male Dummy*. Retrieved from <http://www.humaneticsatd.com/crash-test-dummies/frontal-impact/hybrid-iii-50th>,

completed testing. In addition to the photometric data of the UAS collision sequences and test reports that include dummy head and neck impact loading, force vs. time, and angular rate vs. time data, NIAR provided high speed videos of each collision.

Figure 17 shows a diagram of the drop test equipment setup at NIAR. The sled is a large metal slab that serves as the mounting point for the drop rail uprights, seat and dummy (the dummy is annotated as “ATD” in the diagram). The cameras provided the photometric tracking data to give instantaneous translational and angular velocities of the UAS for a short duration before and after each impact. Figure 18 shows the basic setup from the front right. This figure also shows the impact orientation of the Phantom 3 with respect to the dummy’s head for the vertical, horizontal, and angled impact testing. The UAS impacted directly on top of the head with the payload during all vertical drop testing. The vertical drop testing replicated a UAS failure in hover with the aircraft falling in a level attitude. The angled drop testing replicated a UAS failure in forward flight. For the angle impact tests, the dummy seat was tilted back by either 58° or 62°. The UAS was dropped vertically with an attitude of 58° or 62°. In this way, it replicated an impact with level attitude while descending with the desired impact trajectory angle. This type of impact is characteristic of the Phantom 3, which tends to fall with a level attitude after a complete loss of power (Section 4.14.1). During the horizontal impact tests, the UAS struck the dummy on the forehead with area between the vehicle arms as the point of contact. A pendulum was used to accelerate the UAS to impact speed prior to horizontal impact with the dummy’s head. The UAS was resting on low friction rails so that it would continue moving toward the dummy’s head after the pendulum swing was arrested in the horizontal impact tests.

Table 22 - UAS Drop Testing Summary

Test Details				
NIAR Test Number	Test Number	Orientation	Height	Velocity
UA17A-01	V(90)-20-1	Vertical	20 ft	
UA17A-02	V(90)-20-2	Vertical	20 ft	
UA17A-03	V(90)-20-3	Vertical	20 ft	
UA17A-04	NO TEST	Vertical	30 ft	
UA17A-05	V(90)-30-1	Vertical	30 ft	
UA17A-06	V(90)-30-2	Vertical	30 ft	
UA17A-07	V(90)-30-3	Vertical	30 ft	
UA17A-08	V(90)-40-1	Vertical	40 ft	
UA17A-09	V(90)-40-2	Vertical	40 ft	
UA17A-10	V(90)-40-3	Vertical	40 ft	
UA17A-11	V(90)-50-1	Vertical	50 ft	
UA17A-12	V(90)-50-2	Vertical	50 ft	
UA17A-13	V(90)-50-3	Vertical	50 ft	
UA17A-14	H(0)-4.5-1	Horizontal		17 ft/s
UA17A-15	H(0)-4.5-2	Horizontal		17 ft/s
UA17A-16	H(0)-4.5-3	Horizontal		17 ft/s
UA17A-17	A(65)-36.5-1	62 deg		36.5 ft/s
UA17A-18	A(65)-36.5-2	62 deg		36.5 ft/s
UA17A-19	NO TEST	62 deg		36.5 ft/s
UA17A-20	A(65)-36.5-4	62 deg		36.5 ft/s
UA17A-21	A(58)-46.1-1	58 deg		46.1 ft/s
UA17A-22	A(58)-46.1-2	58 deg		46.1 ft/s
UA17A-23	A(58)-46.1-3	58 deg		46.1 ft/s
UA17A-24	A(58)-51.7-1	58 deg		51.7 ft/s
UA17A-25	A(58)-51.7-2	58 deg		51.7 ft/s
UA17A-26	A(58)-51.7-3	58 deg		51.7 ft/s

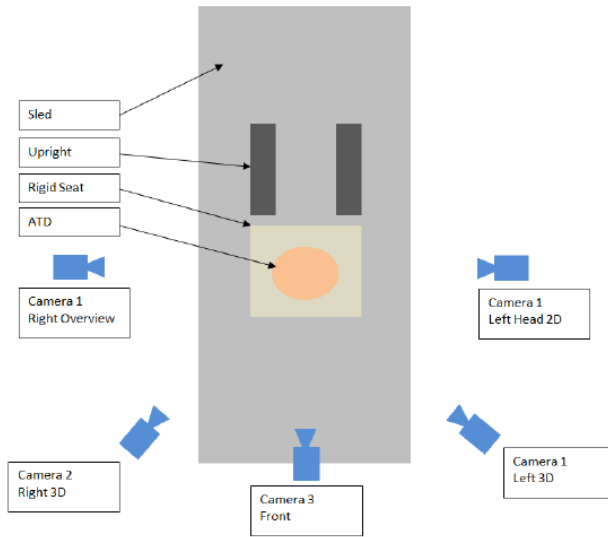


Figure 17 - Top View of Sled Setup for UAS Drop



Figure 18 - Front Left View of Sled Setup (upper left), Vertical Drop Position of Dummy and UAS (upper right), Pendulum Setup for Horizontal Impact Test (lower left), and Dummy and UAS Setup for Angle Impact Test (lower right)

4.8.1.2. NIAR Report Content

NIAR provided comprehensive reports on all 26 tests of which two tests were considered no tests. NIAR summarized all test findings into a 480 page, final report that was submitted to the FAA with the Task A11 Final Report.⁸² Instrumentation and data collected during each test is shown in Table 23 below. Analysis of the data for each test report is provided as a summary table and time histories as shown in Figure 19 and Figure 20, respectively.

Table 23 - NIAR Instrumentation for UAS Drop Tests

Instrumentation		
Type	Location	Direction
Accelerometer	Head	Ax
		Ay
		Az
Angular Rate Sensor	Head	Rx
		Ry
		Rz
Load Cell	Upper Neck	Fx
		Fy
		Fz
		Mx
		My
		Mz
Velocity Gate	UAS	Resultant

Photometric Analysis

Location	Orientation
ATD Head	2D - XZ
UAS	3D

⁸² Arterburn, D., Final Report for the Task A11 – Part 107 Waiver Request Case Study, Doc, 15-C-UAH-UAH-02, 23 September 2016

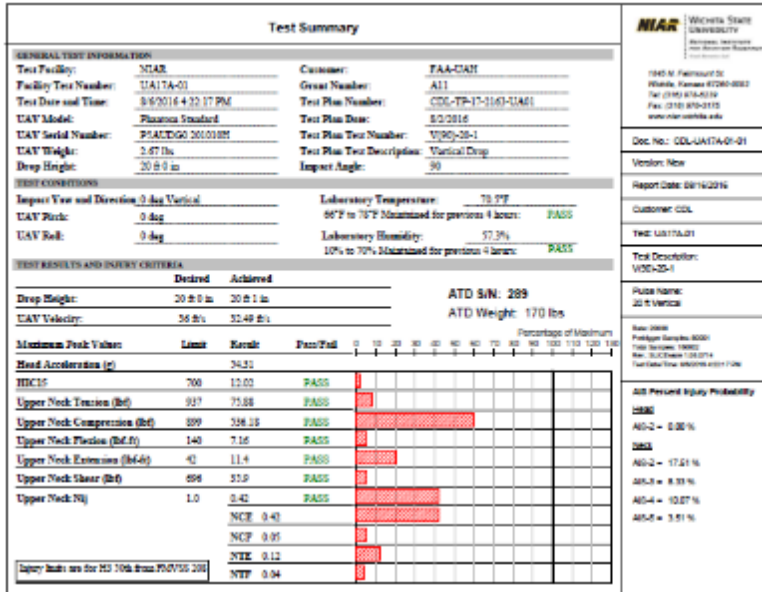


Figure 19 - Example NIAR Test Summary for an Individual Test

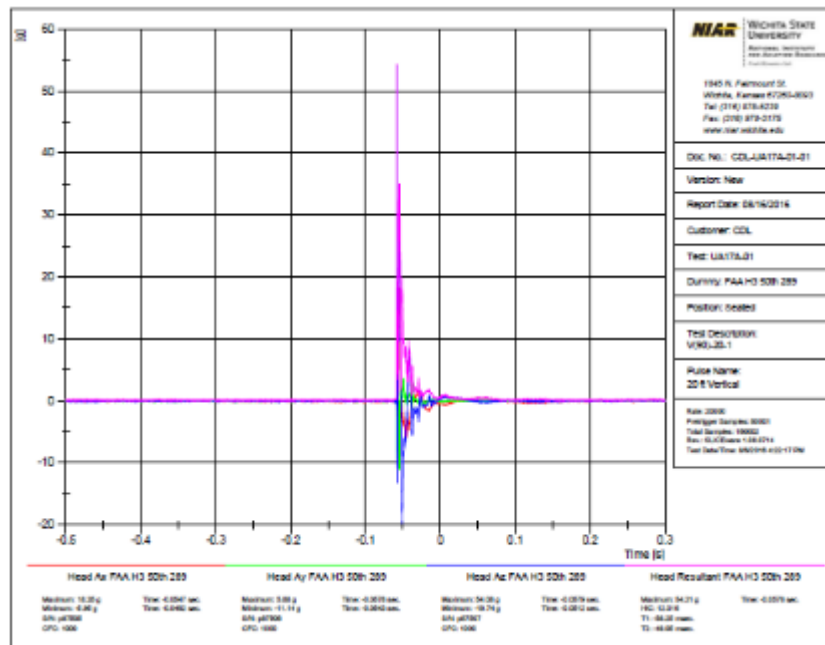


Figure 20 - Example NIAR Time History for an Individual Test

4.8.2. Correlation of Impact Loads and Accelerations with Injury Metrics

The injury potential for specific impact KEs and impact angles was evaluated using injury metrics established by the National Highway Traffic Safety Administration (NHTSA), National Transportation Biomechanics Research Center (NTBRC) in November 1999.⁸³ The NHTSA study was conducted to

⁸³ Eppinger, R., Sun, E., Bandak, F., Haffner, M., Khaewpong, N., Maltese, M., Kuppa, S., Nguyen, T., Takhounts, E., Tannous, R., Zhang, A., Saul, R., Development of Improved Injury Criteria for the Assessment of Advanced Automotive Restraint Systems – II, November 1999.

upgrade the Federal Motor Vehicle Safety Standard (FMVSS) No. 208⁸⁴ frontal crash protection safety standard. “Based on the agency’s analysis of comments received in response to the publication of the NPRM and the accompanying technical reports, the agency has made modifications to the recommended injury criteria and their associated performance limits.... This report, which is a supplement to the previous report, “Development of Improved Injury Criteria for the Assessment of Advanced Automotive Restraint Systems”, (Kleinberger, et. al, NHTSA Docket 98-4405-9) documents these modifications and the rationale.”

The NHTSA report utilizes the Abbreviated Injury Scale (AIS) called out in the Micro-ARC Final Report to establish the injury potential of forces caused by the impact KE of the UAS striking the 50th percentile ATD crash dummy⁸⁵ placed in the seated position. While automotive crashes are systematically different in their causation, the impact forces to the crash dummy have formed the basis for these injury assessments, versus the causation that created the forces. The automotive standards were utilized because of their well-established injury metrics correlated with the AIS since UAS injuries have no substantial database for tracking such injury potential based upon the forces applied to the body. Furthermore, the Micro-ARC Category 3 and Category 4 Performance Standards recommended an injury metric that included no greater than a 30% chance of AIS Level 3 injury or greater following impact with a non-participant. The drop tests and the use of the automotive injury metrics provided the first basis for correlating UAS impact KE with the AIS to address these performance standards.

⁸⁴ <http://www.nhtsa.gov/cars/rules/import/FMVSS/#SN208>

⁸⁵ <http://www.humaneticsatd.com/crash-test-dummies/frontal-impact/hybrid-iii-50th>, accessed 09/29/2016

Table 24 - NIAR Summary Test Results and Injury Metrics

Test Number	UAV Weight (lbs)	Impact Velocity (fps)	Impact KE (ft-lbs)	Impact Angle (deg)	Maximum Resultant Head Acceleration (g)	HIC15 (Max 700)	Probability of Head Injury P(AIS≥2)	Probability of Neck Injury P(AIS≥2)	Probability of Neck Injury P(AIS≥3)	Probability of Neck Injury P(AIS≥4)	Probability of Neck Injury P(AIS≥5)
UA17A-01 V(90)-20-1	2.69	32.49	44.1	90	54.31	12.02	0.00%	17.46%	8.32%	10.05%	3.50%
UA17A-02 V(90)-20-2	2.69	32.31	43.6	90	56.68	14.99	0.00%	18.00%	8.78%	10.38%	3.63%
UA17A-03 V(90)-20-3	2.69	32.5	44.2	90	49.18	15.64	0.00%	18.36%	9.10%	10.60%	3.71%
UA17A-05 V(90)-30-1	2.69	39.75	64.4	90	47.78	19.29	0.00%	18.54%	9.26%	10.72%	3.76%
UA17A-06 V(90)-30-2	2.69	39	63.6	90	48.35	23.45	0.00%	20.02%	10.68%	11.67%	4.12%
UA17A-07 V(90)-30-3	2.69	38.74	62.7	90	66.36	23.02	0.00%	18.18%	8.94%	10.49%	3.67%
UA17A-08 V(90)-40-1	2.69	43.08	77.6	90	78.7	46.62	0.01%	21.40%	12.06%	12.56%	4.46%
UA17A-09 V(90)-40-2	2.69	43.21	78.1	90	54.01	34.13	0.00%	21.80%	12.49%	12.82%	4.56%
UA17A-10 V(90)-40-3	2.69	43.96	80.8	90	78.62	42.79	0.01%	20.22%	10.86%	11.79%	4.16%
UA17A-11 V(90)-50-1	2.69	49.58	102.8	90	82.38	59.54	0.03%	21.80%	12.49%	12.82%	4.56%
UA17A-12 V(90)-50-2	2.69	49.17	101.1	90	71.5	48.04	0.01%	21.20%	11.86%	12.43%	4.41%
UA17A-13 V(90)-50-3	2.69	49.14	100.9	90	119.13	42.24	0.01%	21.40%	12.06%	12.56%	4.46%
UA17A-14 H(0)-4.5-1	2.69	17.25	12.4	0	25.05	7.83	0.00%	12.36%	4.44%	6.93%	2.36%
UA17A-15 H(0)-4.5-2	2.69	17.25	12.4	0	60.65	29.18	0.00%	12.63%	4.61%	7.08%	2.42%
UA17A-16 H(0)-4.5-3	2.69	17.2	12.4	0	43.18	19.94	0.00%	12.49%	4.52%	7.01%	2.39%
UA17A-17 A(65)-36.5-1	2.69	37.03	57.3	65	60.12	39.55	0.01%	19.46%	10.12%	11.30%	3.98%
UA17A-18 A(65)-36.5-2	2.69	36.8	56.6	65	60.88	0.04	0.00%	19.27%	9.96%	11.18%	3.93%
UA17A-20 A(65)-36.5-4	2.69	36.56	55.9	65	55.64	26.25	0.00%	19.08%	9.77%	11.07%	3.89%
UA17A-21 A(58)-46.1-1	2.69	45.95	88.3	58	112.69	107.94	0.35%	19.46%	10.12%	11.30%	3.98%
UA17A-22 A(58)-46.1-2	2.69	46.06	88.7	58	120.49	119.07	0.49%	18.90%	9.60%	10.95%	3.84%
UA17A-23 A(58)-46.1-3	2.69	46.06	88.7	58	130.47	147.82	1.01%	19.27%	9.96%	11.18%	3.93%
UA17A-24 A(58)-51.7-1	2.69	50.37	106.1	58	119.79	137.17	0.79%	18.54%	9.26%	10.72%	3.76%
UA17A-25 A(58)-51.7-1	2.69	50.48	106.5	58	139.15	165.07	1.41%	18.90%	9.60%	10.95%	3.84%
UA17A-26 A(58)-51.7-1	2.69	50.46	106.4	58	126.58	123.64	0.56%	18.90%	9.60%	10.95%	3.84%

Note: Colors in the table represent the magnitude of the individual entry with green being the lowest values and red being the highest values within a column.

A summary of the NIAR test results and injury metrics are shown in Table 24. The observed impact KE values in the NIAR testing correlate to no greater than 12.5% probability of an AIS Level 3 injury or greater based on the NHTSA standards. The probability of skull fracture, based on these impact KE-levels, was substantially lower at a probability less than 1.5%. The injury metrics from the NIAR tests for both skull fracture and neck injuries provide substantial margin to the Micro-ARC injury thresholds established for Category 3 and 4 operations with the most likely injury potential being AIS Level 2 or less injury.

The results of the tests showed significant discrepancy with the levels of safety assessed utilizing the impact KE values extracted from the POF charts in RCC 321-00 shown in Figure 14, the levels of safety derived using the RCC Area Weighted Approach shown in Figure 14 and Figure 15, and those derived using a modified Area Weighted impact KE Approach in Section 4. The discrepancies are shown in Table 25.

Table 25 - Difference in Injury Metrics Between FMVSS 208 and RCC Standards

Test Number	UAV Weight (lbs)	Impact Velocity (fps)	Impact KE (ft-lbs)	FMVSS 208 Standards					RCC Standards for PoF			Area Weighted PoF		
				Probability of Head Injury P(AIS≥2)	Probability of Neck Injury P(AIS≥2)	Probability of Neck Injury P(AIS≥3)	Probability of Neck Injury P(AIS≥4)	Probability of Neck Injury P(AIS≥5)	Head	Thorax	Body and Limbs	Standing	Sitting	Rock Concert
UA17A-01 V(90)-20-1	2.69	32.49	44.1	0.00%	17.48%	8.32%	10.05%	3.50%	21.5%	50.2%	3.6%	6.2%	9.6%	19.5%
UA17A-02 V(90)-20-2	2.69	32.31	43.6	0.00%	18.00%	8.78%	10.38%	3.63%	20.4%	49.0%	3.4%	5.8%	9.1%	18.7%
UA17A-03 V(90)-20-3	2.69	32.5	44.2	0.00%	18.36%	9.10%	10.60%	3.71%	21.8%	50.5%	3.7%	6.2%	9.6%	19.6%
UA17A-05 V(90)-30-1	2.69	39.25	64.4	0.00%	18.54%	9.26%	10.72%	3.76%	71.3%	84.6%	17.9%	26.3%	36.0%	56.9%
UA17A-06 V(90)-30-2	2.69	39	63.6	0.00%	20.02%	10.68%	11.67%	4.12%	69.8%	83.8%	17.1%	25.3%	34.8%	55.5%
UA17A-07 V(90)-30-3	2.69	38.74	62.7	0.00%	18.18%	8.94%	10.49%	3.67%	68.0%	82.8%	16.3%	24.3%	33.6%	54.0%
UA17A-08 V(90)-40-1	2.69	43.08	77.6	0.01%	21.40%	12.06%	12.56%	4.46%	89.0%	93.6%	31.2%	42.6%	54.2%	75.1%
UA17A-09 V(90)-40-2	2.69	43.21	78.1	0.00%	21.80%	12.49%	12.82%	4.56%	89.5%	93.8%	31.7%	43.2%	54.8%	75.6%
UA17A-10 V(90)-40-3	2.69	43.96	80.8	0.01%	20.22%	10.86%	11.79%	4.16%	91.5%	94.8%	34.5%	46.4%	58.2%	78.4%
UA17A-11 V(90)-50-1	2.69	49.58	102.8	0.03%	21.80%	12.49%	12.82%	4.56%	98.7%	98.8%	56.3%	68.6%	78.9%	92.4%
UA17A-12 V(90)-50-2	2.69	49.17	101.1	0.01%	21.20%	11.86%	12.43%	4.41%	98.5%	98.7%	54.8%	67.2%	77.7%	91.7%
UA17A-13 V(90)-50-3	2.69	49.14	100.9	0.01%	21.40%	12.06%	12.56%	4.46%	98.5%	98.7%	54.6%	67.1%	77.7%	91.7%
UA17A-14 H(0)-4.5-1	2.69	17.25	12.4	0.00%	12.36%	4.44%	6.93%	2.36%	0.0%	0.0%	0.0%	<1%	<1%	<1%
UA17A-15 H(0)-4.5-2	2.69	17.25	12.4	0.00%	12.63%	4.61%	7.08%	2.42%	0.0%	0.0%	0.0%	<1%	<1%	<1%
UA17A-16 H(0)-4.5-3	2.69	17.2	12.4	0.00%	12.49%	4.52%	7.01%	2.39%	0.0%	0.0%	0.0%	<1%	<1%	<1%
UA17A-17 A(65)-36.5-1	2.69	37.03	57.3	0.01%	19.46%	10.12%	11.30%	3.98%	55.8%	76.0%	11.7%	18.0%	25.8%	44.3%
UA17A-18 A(65)-36.5-2	2.69	36.8	56.6	0.00%	19.27%	9.95%	11.18%	3.93%	54.1%	75.0%	11.1%	17.2%	24.8%	42.9%
UA17A-20 A(65)-36.5-4	2.69	36.56	55.9	0.00%	19.08%	9.77%	11.07%	3.89%	52.3%	73.9%	0.0%	16.5%	23.8%	41.5%
UA17A-21 A(58)-46.1-1	2.69	45.95	88.3	0.35%	19.46%	10.12%	11.30%	3.98%	95.4%	96.9%	42.4%	54.8%	66.6%	84.7%
UA17A-22 A(58)-46.1-2	2.69	46.06	88.7	0.49%	18.90%	9.60%	10.95%	3.84%	95.6%	97.0%	42.8%	55.3%	67.0%	85.0%
UA17A-23 A(58)-46.1-3	2.69	46.06	88.7	1.01%	19.27%	9.95%	11.18%	3.93%	95.6%	97.0%	42.8%	55.3%	67.0%	85.0%
UA17A-24 A(58)-51.7-1	2.69	50.37	106.1	0.79%	18.54%	9.26%	10.72%	3.76%	99.0%	99.1%	59.1%	71.3%	81.1%	93.5%
UA17A-25 A(58)-51.7-1	2.69	50.48	106.5	1.41%	18.90%	9.60%	10.95%	3.84%	99.1%	99.1%	59.5%	71.6%	81.4%	93.7%
UA17A-26 A(58)-51.7-1	2.69	50.46	106.4	0.56%	18.90%	9.60%	10.95%	3.84%	99.1%	99.1%	59.4%	71.6%	81.4%	93.6%

Notes:

- 1) Color coding of Impact KE is based upon magnitude of KE in comparison to the data listed with the lowest being green and the highest being red.
- 2) Color coding of injury metrics is as follows: Green (0-30%), Yellow (30-50%) and Red (Greater than 50%)

It is important to recognize that the FMVSS 208 standards were developed to analyze impacts to the ATD crash dummies for the range of vehicle crash tests (minor to severe). The ATD data collected during crash testing is correlated with injury data contained in the AIS database as reported by medical professionals who have experience with injury severity and, most importantly, the mortality resulting from such injuries. While automotive crashes are not the same as those of the a UAS ground collision, the impact forces and physics as it relates to the ATD crash dummy are the same and, justifiably, can be analytically evaluated against similar injury metrics associated with automobile accidents until sufficient UAS data becomes available. Consider that the RCC POF metrics established for various impact KE were established from debris analysis with little or no correlation to significant databases associated with injury metrics similar to AIS. To clarify the basis for the establishment of the RCC standards in comparison to the FMVSS 208 standards, it is important to understand how the RCC Standards were developed.

4.8.3. Crash Geometries and the Elasticity of UAS

sUAS platforms are predominantly made of various forms of plastic and foam materials as characterized by the various categories of UAS described in Appendix D. Multi-rotor sUAS are dominated by this type of design and materials resulting in significant flexibility in their structures and frangibility of their payloads during ground collisions. Many fixed wing platforms are made of foam material and break-away wings that further reduce impact forces over those characterized by solid, metal debris fragment masses used to develop the POF metrics in the RCC standards. sUAS fuselages are not fabricated from large amounts of tungsten, aluminum or steel as might be observed from an in-flight breakup of a missile on one of the national test ranges. While the motors of sUAS are made of these types of materials, the motors are rarely the surface or material that is in contact with a human during a ground collision event. Furthermore, the motors are attached to flexible structures especially in monocoque fuselage multi-rotor UAS, like the Phantom 3, resulting in less impact energy if they do contact the human as part of the impact event. A review of the resultant loads from the NIAR tests can also be used to show how these characteristics of a sUAS are substantially different than those of low mass, metallic fragment impact as they relate to skull fracture. Table 23 and Figure 21 show the resultant load factors as calculated for the 10 lbs head of the ATD Hybrid III 50th Percentile test dummy.

Table 26 - Resultant Head Forces from NIAR Tests

Test Number	UAV Weight (lbs)	Impact Velocity (fps)	Impact KE (ft-lbf)	Impact KE (N-m)	Impact Angle (deg)	Test Data Maximum Resultant Head Acceleration (g)	Maximum Resultant Head Force (lbf)	Maximum Resultant Head Force (N)	Sample Mean KE (ft-lbf)	Sample Standard Deviation KE (ft-lbf)	Sample Mean Resultant Load Factor (g)	Sample Standard Deviation of Resultant Load Factor (g)	Max Load Factor from Test Data (g)	McNaughton Calculated Induced Load Factor (g)	3 σ Resultant Load Factor (g)
UA17A-01 V(90)-20-1	2.67	32.49	43.8	59.4	90	54.31	543.1	2415.8	43.6	0.29	53.4	3.8	56.7	49.5	67.4
UA17A-02 V(90)-20-2	2.67	32.31	43.3	58.7	90	56.68	566.8	2521.3							
UA17A-03 V(90)-20-3	2.67	32.5	43.8	59.4	90	49.18	491.8	2187.6							
UA17A-05 V(90)-30-1	2.67	39.25	63.9	86.7	90	47.78	477.8	2125.4	63.1	0.83	54.2	10.6	66.4	71.6	97.4
UA17A-06 V(90)-30-2	2.67	39	63.1	85.6	90	48.35	483.5	2150.7							
UA17A-07 V(90)-30-3	2.67	38.74	62.3	84.4	90	66.36	663.6	2951.8							
UA17A-08 V(90)-40-1	2.67	43.08	77.0	104.4	90	78.7	787	3500.7	78.2	1.72	70.4	14.2	78.7	88.7	120.8
UA17A-09 V(90)-40-2	2.67	43.21	77.5	105.0	90	54.01	540.1	2402.5							
UA17A-10 V(90)-40-3	2.67	43.96	80.2	108.7	90	78.62	786.2	3497.2							
UA17A-11 V(90)-50-1	2.67	49.58	102.0	138.3	90	82.38	823.8	3664.4	100.8	1.01	91.0	25.0	119.1	114.4	155.7
UA17A-12 V(90)-50-2	2.67	49.17	100.3	136.0	90	71.5	715	3180.5							
UA17A-13 V(90)-50-3	2.67	49.14	100.2	135.8	90	119.13	1191.3	5299.2							
UA17A-14 H(0)-4.5-1	2.67	17.25	12.3	16.7	0	25.05	250.5	1114.3	12.3	0.04	43.0	17.8	60.7	14.0	19.0
UA17A-15 H(0)-4.5-2	2.67	17.25	12.3	16.7	0	60.65	606.5	2697.8							
UA17A-16 H(0)-4.5-3	2.67	17.2	12.3	16.6	0	43.18	431.8	1920.7							
UA17A-17 A(65)-36.5-1	2.67	37.03	56.9	77.1	65	60.12	601.2	2674.3	56.2	0.72	58.9	2.8	60.9	63.7	86.8
UA17A-18 A(65)-36.5-2	2.67	36.8	56.2	76.2	65	60.88	608.8	2708.1							
UA17A-20 A(65)-36.5-4	2.67	36.56	55.5	75.2	65	55.64	556.4	2475.0							
UA17A-21 A(58)-46.1-1	2.67	45.95	87.6	118.8	58	112.69	1126.9	5012.7	87.9	0.24	121.2	8.9	130.5	99.7	135.7
UA17A-22 A(58)-46.1-2	2.67	46.06	88.0	119.4	58	120.49	1204.9	5359.7							
UA17A-23 A(58)-46.1-3	2.67	46.06	88.0	119.4	58	130.47	1304.7	5803.6							
UA17A-24 A(58)-51.7-1	2.67	50.37	105.3	142.7	58	119.79	1197.9	5328.5	105.6	0.25	128.5	9.8	139.2	119.7	163.0
UA17A-25 A(58)-51.7-1	2.67	50.48	105.7	143.4	58	139.15	1391.5	6189.7							
UA17A-26 A(58)-51.7-1	2.67	50.46	105.7	143.2	58	126.58	1265.8	5630.6							

Dr. Narayan Yoganandan⁸⁶ studied numerous tests of skull fractures from 1949-2004. The study looked at the peak forces resulting in skull fractures and how testing had led to HIC standards based upon cadaver testing. Table 27 shows the results of the Gurdjian tests that were conducted by dropping cadaver skulls onto steel plates.⁸⁷ The Gurdjian data show that skull fractures at various locations on the skull resulted from impact KE values ranging from 948.3 J±120.1 to 652.6 J±67.6 J (699 ft-lbs±88.6 ft-lbs to 481.3 ft-lbs±49.9 ft-lbs). While the contact areas of the Gurdjian tests were not precisely documented, the contact areas are certainly higher than those of small debris fragments, which leads to dramatically different energy results than those shown in the RCC standards. The sUAS collision tests conducted at NIAR shown in Table 26 resulted in impact KEs substantially lower than those impact KEs required to obtain skull fractures during the Gurdjian tests even at the low end of the standard deviation of the mean. Furthermore, Yoganandan reported that the type and shape of the contactor significantly affected the peak force required to cause a skull fracture.⁸⁶ “For the rectangular impactor, the parietal region was selected as the impact site. The mean fracture force for rectangular plate impacts was 12390 N (±3654). The average fracture force for both impact sites with the circular impactor was 5195 N (±1010). Stiffness was computed as the average slope of the force–displacement curve between 4 and 12 kN for the rectangular plate impactor and 2–6 kN for the circular plate impactor... The contact area of the impactor significantly affected peak forces. Hodgson and Thomas (1971) and Yoganandan et al. (1993, 1991a, 1989, 1991b) advanced similar conclusions on facial bone structures in experimental

⁸⁶ Yoganandan, N, Pintar, F., Biomechanics of temporo-parietal skull fracture, *Clin Biomech (Bristol, Avon)*. 2004 Mar;19(3):225-39.

⁸⁷ Gurdjian, E.S., Webster, J.E., Lissner, H.R., Studies of Skull Fracture with Particular Reference to Engineering Factors, *The American Journal of Surgery*. 1949 Nov, Vol. 78, Issue 5: 736-42

studies in 1970s and 1980s.”⁸⁶ A similar result can be found in a later report by Yoganandan⁸⁸ that used a 48 mm (1.9 in) radius hemispherical anvil impactor to study skull fracture. Yoganandan found dramatically lower energy levels than those reported by Gurdjian as shown in Table 28 using the hydraulic anvil with a small, radial contact area. While the lower energy levels from these tests may initially seem to give more credence to the RCC standards in terms of impact KE, the results are likely due to the stiffness and size of the steel hydraulic ram that imparts contact loads on a small surface area with a very stiff material. The hydraulic anvil’s small contact area has impact dynamics more like a falling metal projectile rather than that of a flexible and frangible sUAS with breakaway camera structures and plastic airframe structures or foam. The mean forces for the static and dynamic tests shown in the Yoganandan paper resulting in skull fracture shown in Table 28 are higher than the largest resultant force recorded during the NIAR drop tests with a flexible Phantom 3. The smallest dynamic force for all regions tested by Yoganandan resulting in a skull fracture was 8,809 N (1,980 lbf). This gives credibility to the assessment that the Phantom 3 impacts would not have resulted in skull fractures and the subsequent low HIC and AIS results shown in the study are valid despite the higher impact KEs of the Phantom 3. The Yoganandan results give credence to the high POF if one solely looks at impact KEs shown in Table 28; however, the resultant forces ultimately lead to a different conclusion due to the difference in character of a steel hydraulic ram contactor when compared to a flexible plastic Phantom 3.

Table 27 –Biomechanical Data for All Skull Fractures from Gurdjian⁸⁷

Biomechanical data from the Gurdjian et al. study for all fractures

Region	Velocity (m/s)	Energy (N m)
Anterior parietal	5.8 ± 0.5	948.3 ± 120.1
Posterior parietal	5.6 ± 0.5	910.9 ± 219.0
All parietal regions	5.8 ± 0.5	943.0 ± 161.3
Mid frontal	4.6 ± 0.3	678.0 ± 156.1
Occipital	4.9 ± 0.4	652.6 ± 67.2
Anterior parietal	5.5 ± 0.8	963.3 ± 180.7
Posterior parietal	5.6 ± 0.2	833.1 ± 68.1
All parietal regions	5.3 ± 0.4	858.4 ± 54.9
Mid frontal	4.8 ± 0.4	773.7 ± 275.7
Occipital	4.8 ± 0.2	700.9 ± 28.8

⁸⁸ Yoganandan, N, Pintar, F., Sances Jr., A., Walsh, P., Ewing, C., Thomas, D., Snyder, R., Biomechanics of Skull Fracture, Journal of Neurotrauma, 1995, Volume 12, Number 4, 659-668.

Table 28 –Biomechanical Data of Skull Fracture Tests Using a 48mm Radius Hydraulic Anvil

ID	Loading rate (m/s)	Force (N)	Deflection (mm)	Stiffness (N/mm)	Energy (J)	Pathology
1	0.002	4464	9.1	790	18.88	Linear fracture—left temporal and parietal bones
2	0.002	5297	8.9	695	18.57	Linear fracture—orbital roof
3	0.002	5915	7.8	1143	14.07	Linear fracture—parietal, temporal, zygomatic bones
4	0.002	6182	15.4	487	44.72	Depressed fracture—inferior parietal, temporal bones
5	0.002	4642	14.1	467	36.28	Multiple depressed fracture—frontal bone
6	0.002	11898	16.6	1290	68.47	Circular fracture—lambda/sutur
7	7.2	14034	5.72	4798	31.46	Linear fracture—vertex to right orbit, frontal bone
8	7.1	13600	4.01	5867	23.51	Multiple fracture—frontal bone, LeFort III
9	7.6	13579	7.40	2540	40.00	Multiple fracture—through vertex, frontal, temporal bones
10	7.3	10009	9.74	2462	43.48	Circular fracture—superior to lambda
11	7.8	8809	3.44	4078	15.59	Multiple fracture—parietal bone, bilateral
12	8.0	11595	4.56	4394	14.06	Circular fracture—vertex region
Mean (1–6)		6399	12.0	812	33.5	
SE		(± 1134)	(± 1.6)	(± 139)	(± 8.5)	
Mean (7–12)		11938	5.8	4023	28.0	
SE		(± 885)	(± 1.0)	(± 54)	(± 5.1)	

As an extension of this analysis, the team looked at simple ways to develop a new impact KE threshold based upon the resultant force methodology introduced in this analysis. If one were to use the lowest resultant force threshold for skull fractures based upon Dr. Yoganandan’s work and the NIAR drop tests data, how could this resultant force be translated into an upper bound for a Phantom 3 in terms of impact KE that is easily testable using flight test or ballistic analysis.

To this end, the team reviewed data for impact KE and the resultant load data from the NIAR tests to look for consistency across the set of data and the variability of the data as shown in Table 25. The table shows that the variability of the resultant load data and the corresponding three σ resultant load data for the NIAR test points conducted with the Phantom 3.

The analysis of resultant load factor versus impact KE is shown in Figure 21. The linear fit of the test data provided an estimate for the impact KE for skull fractures from the Yoganandan work. By extending the linear fit to the intersection of the 198g load factor line from the minimum resultant force for a skull fracture from the Yoganandan tests, the impact KE can be shown to be 181 ft-lbs. To add more conservatism to the analysis, the three σ trend line is used to extrapolate the impact KE for skull fractures rather than the linear fit of the test data. The three σ trend line is shown in equation 9. The intersection of the three σ trend line occurs at an impact KE of 128 ft-lbs. The use of the three σ trend provides a 1.4 safety factor over the linear fit of the NIAR test data.

$$\text{Resultant Load Factor (g)} = 1.5441 * \text{impact KE (ft – lbs)} \quad \text{Equation 8}$$

The 95% confidence intervals for the three σ results for the NIAR test data are shown on Figure 21 and the limits of the confidence interval intersect the 198g line at impact KE of 113 ft-lbs to 148 ft-lbs, respectively. The three σ results provide a 1.2-1.6 safety factor over the linear fit of the test data for the Phantom 3 in terms of determining an impact KE for the Phantom 3 that will not result in a skull fracture. The linear fit approach would allow for simplified testing of

vehicles at various impact geometries and impact KEs using a simplified test that identifies a unique slope from the linear fit (resultant load in g/ft-lb of impact KE) for each platform. The slope of the linear fit of the data accounts for each vehicle's respective flexibility and unique impact characteristics.

As more data is collected for a variety of vehicles, a similar linear fit and associated safety factor approach could be applied to determine the impact KE safety limits for an individual applicant's vehicle based upon the energy absorption characteristics of the specific vehicle's design using simplified drop tests measuring resultant load factor. Similar approaches were conducted for bird strikes in an effort to determine impulse load required to safeguard aircraft against a bird strike where the bird spreads its energy on impact and does not correlate with typical impulse load calculation methods for solid objects.⁸⁹

This approach may provide a means of predicting resultant load factors based upon flight test or ballistic analysis for a range of vehicles. If this method were utilized, a horizontal power flight curve must be segregated from the power off ballistic curves until more horizontal impact data becomes available and a better correlation can be made. It is realistic that flight over people will not involve horizontal powered flight at the same height as non-participants, but rather more vertical impacts whether powered or unpowered.

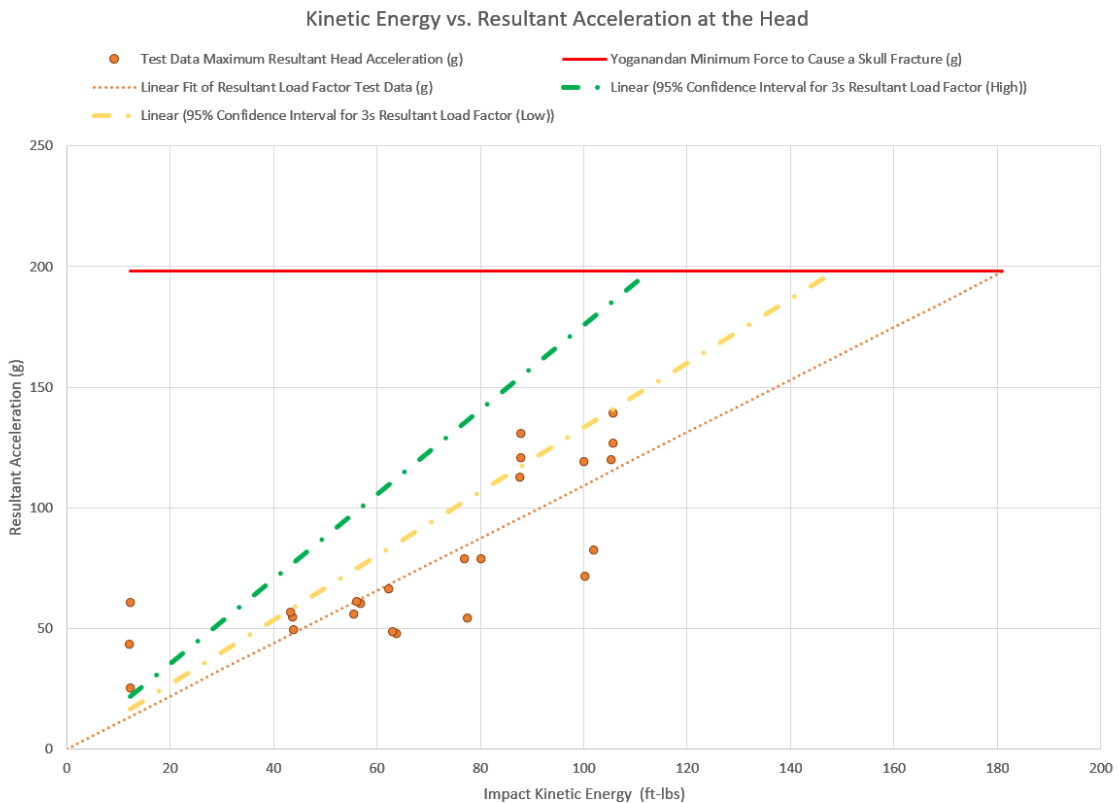


Figure 21 - Analysis of Phantom 3 Resultant Force for Skull Fractures versus Impact KE

⁸⁹ McNaughton, I. I.: The Design of Leading Edge and Intake Wall Structure to Resist Bird Impact. Royal Aircraft Establishment Technical Report 72056, 1972.

To extend this analysis, the skull fracture resultant load must be applied to the metrics for neck injury and AIS3 injuries to verify that this level of resultant load does not cause a neck injury that would exceed the 30% chance of an AIS3 or greater injury. The trends in the data from the NIAR drop tests shown in Table 24 and Figure 22 indicate that the impact KE required to cause head injury may not be the limiting factor in terms of impact KE relative to less than a 30% probability of an AIS3 or greater injury. Neck injury values shown in the limited NIAR tests indicate that neck injuries may be of greater concern than skull fracture. The limits imposed by the slope of the trend line for the three sigma values up to the lower bound of the Yoganandan skull fracture loads of 8,809 N or 1980 lbf resulting from 128 ft-lbs of impact KE will remain below the 30% probability of an AIS3 or greater neck injury based upon the limited data collected during the the Phantom 3 tests as shown in Figure 22.

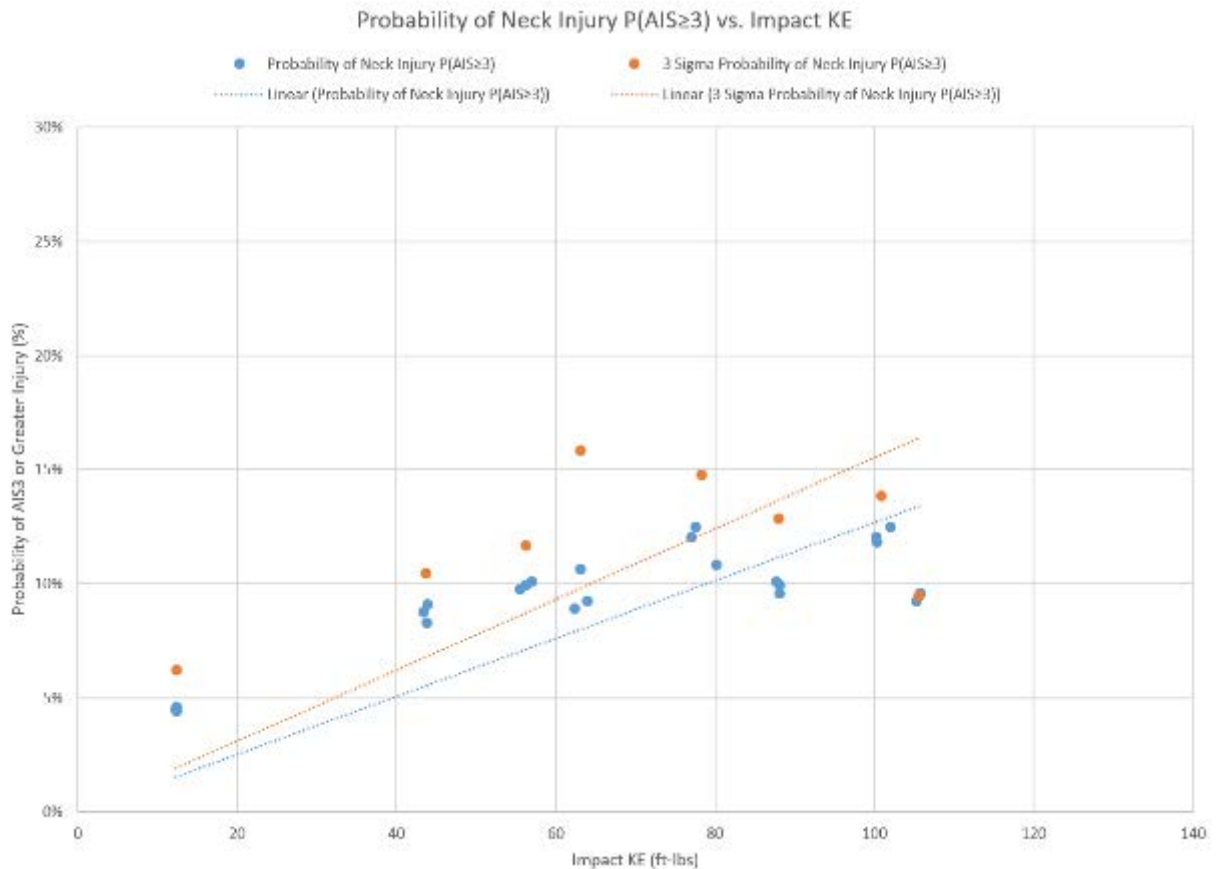


Figure 22 - Probability of Neck Injury Trends from NIAR Test Data

The trend lines shown in Figure 21 and Figure 22 indicate the neck injury data and head injury trends for the flexible Phantom 3 Standard and Advanced aircraft would not result in skull fractures or neck injuries beyond the limits established by the Micro-ARC Final Report⁴¹. Using the RCC standards for impact KEs of 106 ft-lbs for the envelope proposed in the waiver and the 128 ft-lbs maximum impact KE threshold derived from the three sigma resultant load method would have estimated a 98-100% POF value using the RCC standards for head or thorax injury as shown in Figure 13 and 75-80% POF values using the area weighted and average human orientation chart shown in Figure 15 from the RCC standards. This significant gap in perceived level of safety between the RCC standards and the substantially different injury metrics

observed during the NIAR drop tests suggests the RCC data does not represent the collision dynamics and injury mechanics representative of collisions with flexible, plastic sUAS platforms.

As long as the resultant load factor remains below an impact KE that does not exceed 198 g resultant load factor for skull fracture and there is less than 30% probability of having a neck injury exceed AIS3 or greater, then an applicant's vehicle should be considered safe to operate over people. The application of three sigma safety margins can also be applied to these linear fits to increase conservatism to address variation in the test data. The limit of the above analysis is for multi-rotor vehicles made with plastic, flexible structures. The analysis applies to blunt force trauma type injuries only. Laceration and penetration injuries must be addressed separately; however, these injury types have not typically been associated with fatal injuries for sUAS platforms.

The team evaluated the use of the ATD Hybrid III 50th Percentile Crash Test Dummy as an appropriate means of testing sUAS collisions and applying the FMVSS 208 standards for injury potential. The FMVSS 208 metrics have been developed for car collisions at significantly higher levels of energy based upon impact measurements from the ATD Hybrid III 50th Percentile Crash Test Dummy. Could the sUAS collisions with the ATD Hybrid III 50th Percentile Crash Test Dummy be masking potential injury since they were not designed for this lower energy impact collision? In order to evaluate this question, UAH funded additional impact tests at NIAR using a steel plate and wood block of equivalent mass to the Phantom 3. The steel and wood masses were dropped vertically onto the ATD Hybrid III 50th Percentile Crash Test Dummy at similar impact speeds to the Phantom 3 vertical drop tests. The additional impact tests were conducted to compare the impact loads measured by the ATD Hybrid III 50th Percentile Crash Test Dummy using masses of similar material properties to those evaluated during the development of the RCC standards and assess the resultant impact loads against the values observed during the Phantom 3 impact tests. Figure 23 and Table 29 show the results of those tests when compared with the Phantom 3. The ATD Hybrid III 50th Percentile Crash Test Dummy measured substantially higher impact loads for steel and wood masses when compared with the Phantom 3 when dropped at nearly identical impact KEs. Using the resultant load method described above, the steel and wood block would have an impact KE threshold of approximately 23 ft-lbs when compared with the 181 ft-lbs derived from the linear fit of the Phantom 3 data or the 128 ft-lbs three sigma impact KE derived from the resultant load method as shown in Figure 23. Both steel and wood had average probability of AIS2 or greater head injury of 99% when compared with the Phantom 3 average of less than 0.10%. The average probability of an AIS3 or greater neck injury for both steel and wood was 67% and 66%, respectively, for these vertical tests, when compared with the Phantom 3 of less than 12.5%. In all cases, the ATD Hybrid III 50th Percentile Crash Test Dummy was capable of distinguishing the difference in material properties that resulted in uniquely different load measurements and corresponding assessments in injury between the steel, wood and Phantom 3 impacting at nearly identical impact KEs. Furthermore, the injury metrics associated with steel and wood are in concert with the estimates of POF predicted by the RCC standards. This appears logical since the basis for the

RCC standard POF metrics were injuries resulting from inelastic metal fragments.

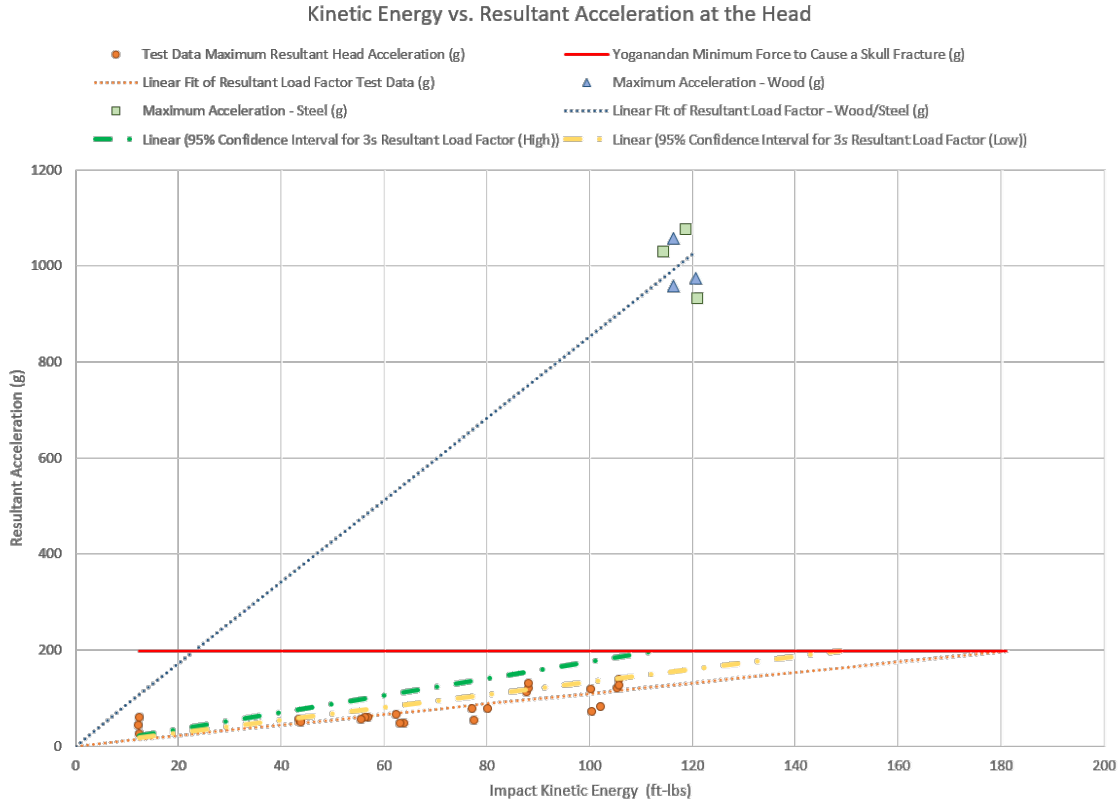


Figure 23 - Resultant Force versus Impact KE for Steel, Wood and Phantom 3

Table 29 – Vertical Drop Test Comparison of Steel and Wood with Phantom 3

Test Number	Test Article	Test Article Weight (lbs)	Impact Velocity (fps)	Impact KE (ft-lbs)	Impact Angle (deg)	FMVSS 208 Standards		RCC Standards for PoF		
						Probability of Head Injury P(AIS≥2)	Probability of Neck Injury P(AIS≥3)	Head	Thorax	Body and Limbs
UA17A-11 V(90)-50-1	UAS	2.69	49.58	102.8	90	0.03%	12.49%	98.7%	98.8%	56.3%
UA17A-12 V(90)-50-2	UAS	2.69	49.17	101.1	90	0.01%	11.86%	98.5%	98.7%	54.8%
UA17A-13 V(90)-50-3	UAS	2.69	49.14	100.9	90	0.01%	12.06%	98.5%	98.7%	54.6%
UA17B-01	Wood	2.69	52.73	116.2	90	99.32%	63.04%	99.6%	99.5%	67.0%
UA17B-02	Wood	2.69	52.72	116.2	90	99.74%	67.06%	99.6%	99.5%	67.0%
UA17B-03	Wood	2.69	53.7	120.5	90	99.68%	68.35%	99.7%	99.6%	70.0%
UA17B-04	Steel	2.7	53.71	121.0	90	99.49%	61.18%	99.8%	99.7%	70.3%
UA17B-05	Steel	2.7	52.2	114.3	90	99.74%	70.44%	99.5%	99.5%	65.6%
UA17B-06	Steel	2.7	53.2	118.8	90	99.70%	71.66%	99.7%	99.6%	68.8%

Notes:

1) Color coding of injury metrics is as follows: Green (0-30%), Yellow (30-50%) and Red (Greater than 50%)

The RCC standards are extremely conservative when applied to sUAS because of the tremendous difference in materials, structures, and corresponding collision dynamics. The NIAR drop tests were worst-case collision scenarios with no blade guards and near center of mass collisions. During a few of the tests, the impacts were slightly offset by no more than an inch, yet the offset collision caused the vehicle to roll away from the ATD dummy quickly, which

resulted in a significant reduction in impact KE over other tests at the same condition. This condition was very evident in the horizontal impact tests. The three horizontal impact tests were all conducted at 12.3 ft/s; however, the resultant load at the head of the ATD dummy for the three tests was 25.05g, 60.65g and 43.18g, respectively. The variation in the first two tests can be seen in the video of the first test that had a slight offset and resulted in the Phantom 3 rotating across the head as one arm struck the head before the other and started the vehicle rotating away from the head. The other two tests had a more center of mass impact between the arms of the vehicle resulting in more energy transfer. The likelihood of less severe offset collisions is increased with the additional of blade guards, landing gear and the breakaway features of the payload for the Phantom 3.

Increasing the threshold of impact KE to 128 lbs for sUAS platforms for flight over people has the additional effect of dramatically increasing the operational envelope for unmanned platforms other than multi-rotors when using parachutes as safety mitigations for flight over people and flight over heavily populated areas. Task A4 looked at the impact of parachutes with various levels of safety defined by RCC standards. The use of parachutes as mitigations for blunt force trauma injuries while flying over people is critical to opening up the envelope for more robust commercial vehicles during flight over populated areas. The parachute standards reviewed in Table 19 are reevaluated in comparison to the 98% confidence level impact KE threshold of 128 ft-lbs based upon the injury metrics in this report for skull fracture and less than a 30% chance of a head or neck injury resulting in an AIS or greater injury. The 28 ft-lbs impact KE value from the RCC standards represents the 1% POF of head injury and 10% probability of a thorax injury as shown in Figure 13. The test results support the new metrics that not only demonstrates the Phantom 3 to be safe during Category 4 Performance Standards as defined by the Micro-ARC Final Report, but many other platforms could meet these standards at substantially higher takeoff weights using parachutes and automatic deployment mechanisms as mitigations for Category 3 and Category 4 Performance Standards. Parachutes used as safety devices in this manner must meet specific standards and provide sufficient altitude to decelerate to the speeds shown in Table 30. It is important to note that 18.0 ft/s is assumed to be the lowest reliable rate of descent that can be achieved with a parachute recovery system. Below this rate of descent, it is questionable whether there is sufficient dynamic pressure to maintain a fully inflated canopy to support deceleration of the vehicle.

Table 30 - Comparison of RCC Standards vs. Modified Impact Energy Thresholds for Various Aircraft Weights when Descending under Parachute.

Descent (fps)	Descent Velocities (kts)	Weight (lbs) Based upon RCC Standards of 28 ft-lbs impact KE (1% PoF due to Head Injury or 10% PoF due to Thorax Injury) while Standing RCC	Weight (lbs) for a 128 ft-lbs impact KE Threshold (based upon sUAS impact test with 98% confidence of no skull fracture and less than 30% chance of an AIS3 or greater injury)
14.0	8.3	9.2	42.0
16.0	9.5	7.0	32.2
18.0	10.7	5.6	25.4
20.0	11.8	4.5	20.6
22.0	13.0	3.7	17.0
24.0	14.2	3.1	14.3
26.0	15.4	2.7	12.2
28.0	16.6	2.3	10.5

4.9. Energy Density and Penetration Injuries (UAH)

One other metric that can be used to evaluate the severity of a UAV collision with a person is energy density - the impact KE divided by the contact area of the collision. This metric most directly relates to penetrating or laceration injuries. Because there are so many potential contact areas on a given platform, this metric is generally very hard to use as a metric for certification. This is demonstrated in Figure 24, where four potential collisions are shown. The degree of variability in collisions and UAV body types makes it challenging to use energy density as a blanket characteristic. Additionally, as a sole characteristic, energy density does not effectively address blunt trauma injuries. Blunt trauma is based on impact energy transfer and transmission through tissue with subsequent damage to tissues. Energy density correlates to injuries where impact energy is focused in a small enough area that the load exceeds local tissue yield strengths. Energy density is quite difficult to measure consistently during experimental testing, but it can be estimated based on likely contact areas and measured or estimated impact velocities.



Figure 24 - Potential Collisions between UAVs and a Human Head

The literature survey identified a range of energy density values that correlate to injuries or casualties; however, none were explicitly linked to fatalities. Table 31 outlines the major energy density threshold values that correlate to skin penetration or laceration from the

literature survey. RCC Supplement 321-07 also cites energy density values ranging from 10 - 109 ft-lbs/in² with the lower values correlating more to penetration of bare skin and the high end being associated with light clothing and skin. Ultimately, the RCC documentation states that the standard value used as a threshold within the RCC is 34 ft-lbs/in. This value is cited as a casualty-producing value, but there are no associated qualifying statements that relate to fatality.

Table 31 - Skin Penetration Threshold Energy Density Values from Literature^{72,73,90,91}

Energy Density (J/cm ²)	Energy Density (ft-lb)/in ²	Metric	Reference	Comment
1.7 J/cm ²	8 ft-lb/in ²	Energy Density Penetration Threshold	AFSCOM Manual Volume 1	Has less than 10% probability of penetration using Lewis S-Curves
7.23 J/cm ²	34 ft-lb/in ²	Energy Density for Chunky Penetration	RCC Supplement 321-07	Conservative threshold that accounts for light clothing and skin in the modeling
10 J/cm ²	47.6 ft-lb/in ²	Skin Penetration Energy Density	Penetration Injury to the Chest by an Attenuated Energy Projectile LA case report and literature review	Case study on ER treatment of a person whom experienced thorax penetration by a non-lethal round. Non-fatal wound with minor hospital stay.
12 J/cm ²	57.1 ft-lb/in ²	Transport Canada's Low Energy RPA Standard	Transport Canada's UAV Systems Program Design Working Group Phase 1 Final Report March 2012	Appears to assume that RCC's definition of "casualty" means fatality

Transport Canada's 12 J/cm² (57.1 ft-lb/in²) threshold⁹⁰ for establishing a category of low energy remotely piloted aircraft is unclear. As a *sole* metric for evaluating collision severity, it does not substantiate the range of potential injury mechanics that can take place during a ground collision event. First, it cites RCC documentation for inert debris as source material and includes a determination of whether a collision is lethal or not. The RCC literature that lays out energy density values does not state that any of them are lethal. Additionally, the study of an emergency room case study on the treatment of a person with a thorax penetration injury states that the chest penetration value is roughly 10J/cm² (47.6 ft-lb/in²).⁹¹ This value is close to the Low Energy RPA standard, but the full case study shows that it proved to be a relatively minor injury that only involved a hospital stay. The Transport Canada documentation does not clearly establish that 12 J/cm² energy density predicts lethality. However, this standard states that the energy densities associated with soccer, tennis, golf, and baseball impacts are not lethal (Table 20). This contradicts research-based threshold values for lethal KE in blunt trauma injuries cited by the RCC. Transport Canada's Low Energy RPA Standard clearly shows the confusion related to the use of energy density as a sole means of determining injury severity. For the sports ball examples in Table 20, baseballs and golf balls are well below the energy

⁹⁰ Transport Canada, UAV Systems Program Design Working Group, "Phase 1 Final Report", March 2012

⁹¹ Rezendo-Neto, J. et. Al, "Penetrating injury to the chest by an attenuated energy projectile: a case report and literature review of thoracic injuries caused by "less-lethal" munitions" World J Emerg Surg. 2009; 4: 26. Published online 2009 Jun 26. doi: 10.1186/17497922426

density threshold and would be deemed to be safe in accordance with the Low Energy RPA Standard. However, the energy of baseballs and golf balls readily exceed the 90% probability of lethal KE value for a head impact (107 J/78.91 ft-lb) as shown in Table 20 which correlates with well-established documentation for baseballs and golf balls causing fatal injuries to

Table 32 - Excerpt from Transport Canada's Low Energy RPA Standard

Item	Typical Maximum Energy (J)	Typical Max. Energy/Unit Area (J/cm ²)	Lethal?
Football	80	-	NO
Soccer ball	270	0.7	NO
Tennis ball	110	3.1	NO
Baseball	140	3.9	NO
Golf Ball	120	8.4	NO – but getting close!
RPA examples			
Maverick	440	440/4 = 110J/cm**2	YES
CyberQuad MAXI	133	133/42 = 3.17J/cm**2	NO
Aeryon Scout	208 (total) 150 after “arms” break off	150/103 = 1.45J/cm**2	NO

The level of energy that can cause harm when imparted on a human is cited in a variety of references, both regarding RPAS and non-lethal weapons. The values in RPAS specific documents range from 33.9J to 53¹J. Equally, the harmful level of energy per unit area is cited anywhere from 6 J/cm², which can cause an eye injury in the most critical geometry collision, to 12.8J/cm².

individuals when struck in the head. As noted in a baseball fatality study, “Dr. Thomas A. Gonzalez from the New York Office of the Chief Medical Examiner reported on a 32 year (1918-1950) longitudinal study of sports fatalities in the New York City area. He was able to confirm 104 deaths with baseball accounting for 43 (41 percent) of them. Of the 43 total baseball fatalities, 25 (58 percent) were due to blows to the head.”⁹²

4.9.1. Impact KE and Energy Density of Actual Vehicles (UAH)

Table 33 shows the terminal velocity/energy characteristics of four multi-rotor platforms - the DJI Phantom 3, DJI Inspire 1 V2, 3DR Solo, and the Blade 350 QX3 - as they relate to energy densities in the four collision types discussed previously. There are several important observations to be made here. The terminal KE values for all vehicles in Table 33 exceed the RCC threshold for 100% POF for an impact to the head in terms of blunt force injury metrics. Because of the different geometries of the vehicles and their possible contact areas, all vehicles have some orientation where the contact area results in a spike in energy density. Energy density even spikes for the 3DR Solo aircraft where the platform collision is on the blunt side of the vehicle. This is because the very flat bottom of the aircraft minimizes contact area and causes a spike in energy density. The Phantom 3 energy density during a collision is highly dependent on vehicle orientation as are all sUAS platforms. In some cases, it exceeds penetration thresholds, but contact at V_{term}, between the arms does not exceed the energy density threshold of 12J/cm² (57.1 ft-lb/in²) as cited in the Transport Canada’s Low Energy RPA

⁹² Gorman, R. and Weeks, D. “Death at the Ballpark”, 2d Edition, McFarland & Company Inc. 2015

Standard. Once again, energy density does definitively address the injury mechanisms that relate these circumstances.

Table 33 - Impact Energy Density for Various Vehicles and Impact Contact Areas

	Payload and head		Fuselage front and head		Fuselage top surface and head		Fuselage bottom surface on head	
	Contact Area (cm ²)	Energy Density (J/cm ²)	Contact Area (cm ²)	Energy Density (J/cm ²)	Contact Area (cm ²)	Energy Density (J/cm ²)	Contact Area (cm ²)	Energy Density (J/cm ²)
DJI Phantom 3	8.90	30.65	31.11	8.77	11.28	24.18	-	-
DJI Inspire 1 V2	5.62	134.91	9.84	77.05	6.50	116.64	1.70	445.99
3DR Solo	8	47.85	3.17	95.71	14.71	26.02	14.71	36.99
Blade 350 QX3	8	22.92	2.89	63.46	4.83	37.97	-	-

Based on analysis of this limited set of cases, and the way it is treated in RCC documentation, energy density is ill-suited to be a stand-alone metric for evaluating the severity of sUAS collisions with people. Recent research conducted by Syracuse University⁹³ on energy density of UAS impacts and penetration injury potential yields results that are in line with the analysis in Table 33. The Syracuse researchers conducted experiments in which they dropped a 3 lbs UAS from 88-96 in above ordnance gel, aluminum sheeting, and pork ribs with a plastic wrapper and without a wrapper. The estimated energy densities, based on image analysis with Syracuse’s Digital Imagery Correlation system were 0.103 J/cm², and 15.6 J/cm² for drops in a level attitude and with the end of a single arm impacting the surface in an edgewise fall, respectively. During the latter impact, the end of the arm penetrated the unwrapped ribs by approximately 20mm. This is to be expected, as the energy density is within the RCC range for penetrating energy density levels and exceeds the 12J/cm² threshold (Table 31). While this penetration of pork ribs was not representative of the human anatomy, the addition of wrapping that was similar to skin did not result in the same penetration for the same energy density.

These results provide an experimental validation of the wide range of impact energy densities that can be achieved with a single vehicle being dropped from the same height, which is also shown, via estimated areas and impact KE values, Table 33. They also highlight a shortcoming in defining how energy densities should be applied toward regulatory decision making. Energy density is a challenging and expensive metric to directly measure as a standard to determine collision severity. As highlighted in the Syracuse testing to evaluate energy density, testing requires high speed cameras and appropriate lighting setups, redundant accelerometers, and proprietary image processing software to analyze the responses of impacting and impacted masses during experimentation.⁹⁴ The need for specialized instrumentation to accurately calculate impact energy density make this metric less desirable to establish as an industry accepted standard.

Energy density provides an appropriate design standard for determining contact areas that may require redesign to reduce collision risk. As was done under the Task A4 by UAH researchers, it is possible to estimate likely contact areas for a vehicle and use derived values of impact KE based on a CONOPS and understanding of failure modes to identify potential areas of the vehicle that may require additional mitigation to reduce the possibility of penetration injuries.

⁹³ Briefing provided by Dr. Mark Glauser and students, Syracuse University, New York State U-SAFE/NUSTAR initiative.

⁹⁴ <http://www.dantecdynamics.com/digital-image-correlation>

Energy density provides a useful metric for identifying potential vehicle configurations or attributes that may create penetration injuries, but these metrics are extremely difficult to test and evaluate during dynamic collisions. Penetration energy will certainly exacerbate blunt force injuries, but there is not a clear understanding of how the energy density metric leads to fatalities or any lethal injury. Therefore, energy density should only be used to complement safety analysis of KE values associated with blunt force trauma to mitigate sharp edges, landing gear configurations and other vehicle attributes that may cause superficial injuries or exacerbate blunt force trauma related injuries.

4.10. Rotating Components and Laceration Injuries (KU)

There is currently no standard relating to sUAS rotating components, lacerations, and design for mitigation. As stated earlier, for an identifiable range of rotorcraft, the danger to persons on the ground from laceration by rotating blades results in more severe consequences than the danger due to blunt trauma. Lacerations represent the most common class of injuries associated with small UAVs. Operators, in particular, are at risk for this kind of injury during takeoff/landing procedures and UAV handling. The severity of laceration-type injuries ranges in severity from minor to fatal, as in the 2013 case of a 19-year-old Brooklyn man killed by his RC helicopter.⁴⁵ The severity of laceration due to spinning blades is based on obvious physical blade characteristics: rotational KE and sharpness.

Perhaps the most practical mitigation of rotating blade injury potential is the use of guards or cages. While there are no standards in place for the mitigation of laceration injury by sUAS, the industrial standards that are most relevant to this topic are standards for mitigation of blade injuries in electrical fans. Propeller and fan injury mitigations must be assessed with regard to performance and durability. Methods for such assessments for electrical equipment fans are well-established in international standards and may form a basis for similar assessments for UAS for which the spinning blade risk exceeds the blunt force trauma risk.

4.10.1. Assessing Blade KE

The rotational KE E_R of an object (such as a rotor) is given by the formula shown in Equation 5 on page 50.

A rotor's mass moment of inertia is a function of its shape and represents the way its mass is distributed within its volume. This shape is specific to each rotor, but for rotors of the same scale, the shape of each blade is similar, varying within a range that can be defined via torsional pendulum testing. Representing each blade as a rod – where the blade's mass is evenly distributed from hub to tip – defines a practical upper bound for a rotor's mass moment of inertia. Since there is typically a greater concentration of mass near the rotor's hub and since most rotors taper toward the edges, the mass moment of inertia of a rotor takes on a value that is smaller than its rod-based equivalent. The mass moment of inertia for a uniform rod of negligible thickness is shown in Equation 6 on page 50

As can be seen from the equation, a rotor blade mass moment of inertia scales in proportion to the square of the rotor's diameter D , assuming a constant mass. In reality, for rotors of a similar shape, rotor mass also scales with the cube of the diameter. This means that a rotor's mass moment of inertia is roughly proportional to its diameter to the fifth power.

$$m_{\text{rotor}} \cong k_1 D^3 \qquad \text{Equation 9}$$

$$I_{\text{rotor}} \cong k_2 D^5$$

Equation 10

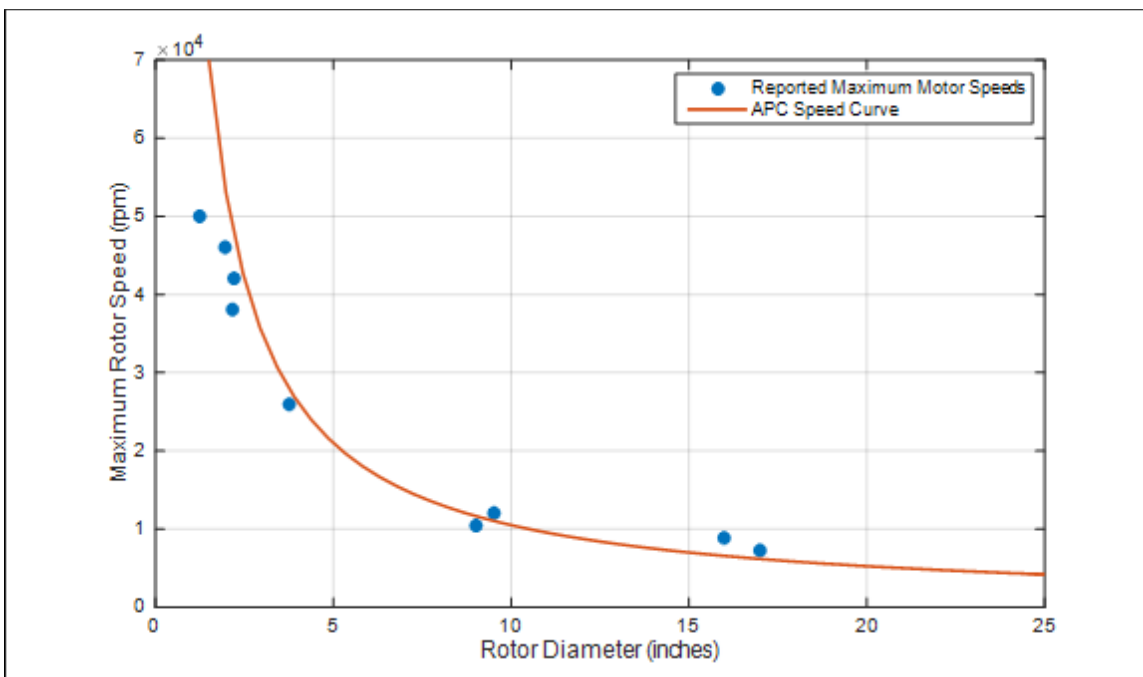


Figure 25 - Rotor Speed vs. Rotor Diameter for Multi-Rotor UAS, Compared with APC RPM Curve

Furthermore, it can be argued that the other major component of rotational KE (rotational speed) is also heavily dependent on rotor diameter. Rotor manufacturer Advanced Precision Composites (APC) provides a set of equations to which their rotors and propellers are designed⁹⁵. These equations take the form of a power function $\omega_{max} = k_3/D$, where k_3 is a constant specific to each rotor type. This reflects the cube-square law relationship between rotor mass and blade cross-sectional strength and governs the maximum speeds at which APC rotors are intended to operate. Figure 25, a plot of the blade diameters versus the reported motor speeds for nine multi-rotor aircraft, shows that full-throttle motor speeds follow the expected trend.

⁹⁵ "APC Propellers." APC Propellers. Accessed April 14, 2016. <https://www.apcprop.com/Articles.asp?ID=255>.

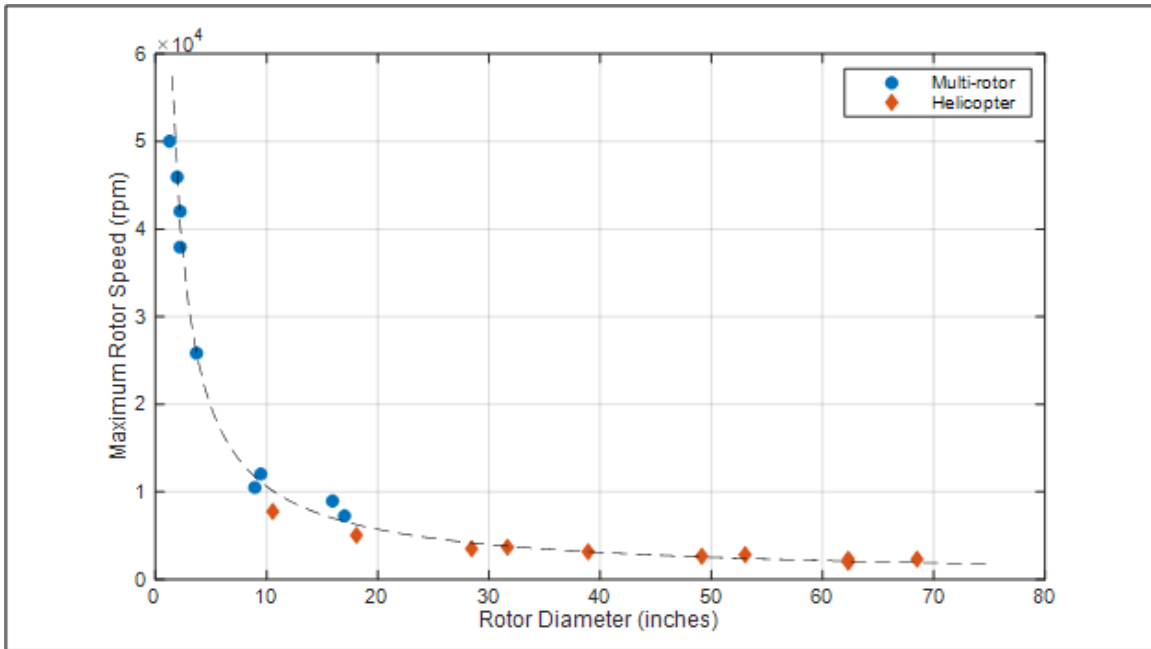


Figure 26 - Rotor Speed vs. Rotor Diameter for Multi-Rotor UAS, Compared with APC RPM Curve.

Figure 26, which includes RC helicopters in the study, in addition to multi-rotor aircraft, reinforces the trend for small UAS.

If an equation of the same k/D form is accepted as an approximation of maximum rotor speed, then an upper bound for rotor rotational energy can be established that is based only on rotor diameter. As a result, rotor diameter is a good candidate for a parameter on which KE and subsequent design/mitigation prescriptions are based. Since the mass of a small UAS rotor is roughly proportional to diameter to the fifth power and its rotational speed is roughly inversely proportional to rotor diameter, a rotor’s rotational KE can be approximated by the following equation.

$$E_R \cong kD^3 \quad \text{Equation 11}$$

The value of k can be determined experimentally, but its value is not critical to the current argument. The point to be taken from the above equation is that *the maximum KE of an installed rotor is heavily correlated to the rotor’s diameter*, a well-known and/or easily obtained measurement. This result indicates that *rotor diameter is a simple metric that can be used to assess the rotational blunt force trauma risk associated with sUAS*. Above some rotor diameter, a rotating rotor will possess enough KE to cause lethal blunt force trauma. For rotors of lower diameter, which correlates with lower mass sUAS, lacerations become the most critical risk.

However, for laceration injuries, the rotational KE is not the only important parameter. The physical characteristics of blades are very important, as described in the next section.

4.10.2. Assessing Blade Cutting Characteristics

Cut formation is a function of input energy and the geometric and mechanical properties of the cutting blade and the object being cut. For soft materials (such as skin and muscle), the material’s fracture toughness is the mechanical property that best predicts the onset of cutting

in a stabbing scenario.⁹⁶ This value varies somewhat in the case of human skin, depending on the bodily location and direction of the cut.⁹⁷ Assuming, however, that skin mechanical properties are reasonably similar throughout the general population (and recognizing their inherent uncontrollability), for a given blade diameter (and the associated kinetic energy), blade properties are the most important parameters for assessing injury potential.

Blade stiffness and blade sharpness are the two most important of these parameters. A sharp blade requires less input energy to initiate a cut than a dull blade, and a stiff blade requires less input energy than a compliant blade – since blade deformation represents the absorption of energy that would otherwise be transferred to the cutting substrate. In turn, blade stiffness and sharpness are governed by the mechanical properties of the blade material and geometric characteristics such as the blade's cross-sectional area moments of area and leading edge radius.

In 2006, McCarthy et al. devised the blade sharpness index (BSI) as an objective measure of the sharpness of a cutting edge and showed how this parameter could be determined both experimentally and analytically. They also demonstrated, in accordance with previous research, that blade edge radius was the geometric feature that most heavily influenced BSI values. Anecdotally, rotors and propellers made from materials such as carbon-fiber-reinforced plastic (CFRP) are more likely to produce laceration-type injuries. This matches the expected trend, since CFRP is stiffer than the plastics that make up other rotors.

Blade sharpness and blade stiffness are parameters that dictate what ratio of energy can be transferred from the blade to an object, and how much energy must be transferred into that object to produce a cut. They do not, however, have much to say about how much energy can be applied to the cutting process.

4.10.3. Laceration Injuries from Quadcopters in the Literature

Available information about recent injuries due to quadcopter and helicopter impacts has been gathered as a function of rotor diameter.^{98'99'100'101'102} Then, using pictures and other descriptions of the injuries, 20 university students rated the severity of the injuries using a severity index based on ratings from 1 to 6, with 1 being the least severe and 6 being fatal. To arrive at this “notional” rating, the students were given a list of words descriptive of injury severity (minor, moderate, serious, severe, critical, and unsurvivable) and were asked to rate

⁹⁶ McCarthy, C.t., M. Hussey, and M.d. Gilchrist. "On the Sharpness of Straight Edge Blades in Cutting Soft Solids: Part I – Indentation Experiments." *Engineering Fracture Mechanics* 74, no. 14 (2007): 2205-224. doi:10.1016/j.engfracmech.2006.10.015.

⁹⁷ Annaidh, A. Ní, M. Ottenio, K. Bruyère, M. Destrade, and M. D. Gilchrist. "Mechanical Properties of Excised Human Skin." *IFMBE Proceedings 6th World Congress of Biomechanics (WCB 2010)*. August 1-6, 2010 Singapore, 2010, 1000-003. doi:10.1007/978-3-642-14515-5_255.

⁹⁸ "Images." RC Groups RSS. Accessed April 15, 2016. <http://www.rcgroups.com/forums/showthread.php?t=1144377>.

⁹⁹ "Images." RC Groups RSS. Accessed April 15, 2016. <http://www.rcgroups.com/forums/showthread.php?t=1382503>.

¹⁰⁰ Alishanmao. "Mini Quadcopter Injury Nasty Deep Propeller Cuts on Finger." YouTube. 2014. Accessed April 15, 2016. <https://www.youtube.com/watch?v=la2JBFIQqvk>.

¹⁰¹ "A Swiss Man Was Killed By His Remote-Controlled Helicopter." Gizmodo. Accessed April 15, 2016. <http://gizmodo.com/a-swiss-man-was-killed-by-his-remote-controlled-helicop-777233761>.

¹⁰² "TOM BASS PARK HOUSTON DEATH - Page 1." TOM BASS PARK HOUSTON DEATH - Page 1. Accessed April 15, 2016. <http://rc.runryder.com/helicopter/t70830p1/?top=1067899114>.

pictures of lacerations available in the literature (Figure 27). They were NOT given the definition of the abbreviated injury score (AIS) that is used for medical triage. Figure 27 plots this crowd-sourced, averaged, notional severity index versus the diameter of the rotor that caused the injury, which resulted in the expected trend: increasing injury severity with increasing rotor diameter. These ratings seem to indicate that laceration injuries due to sUAS encounters are perceived as significant by members of the public.

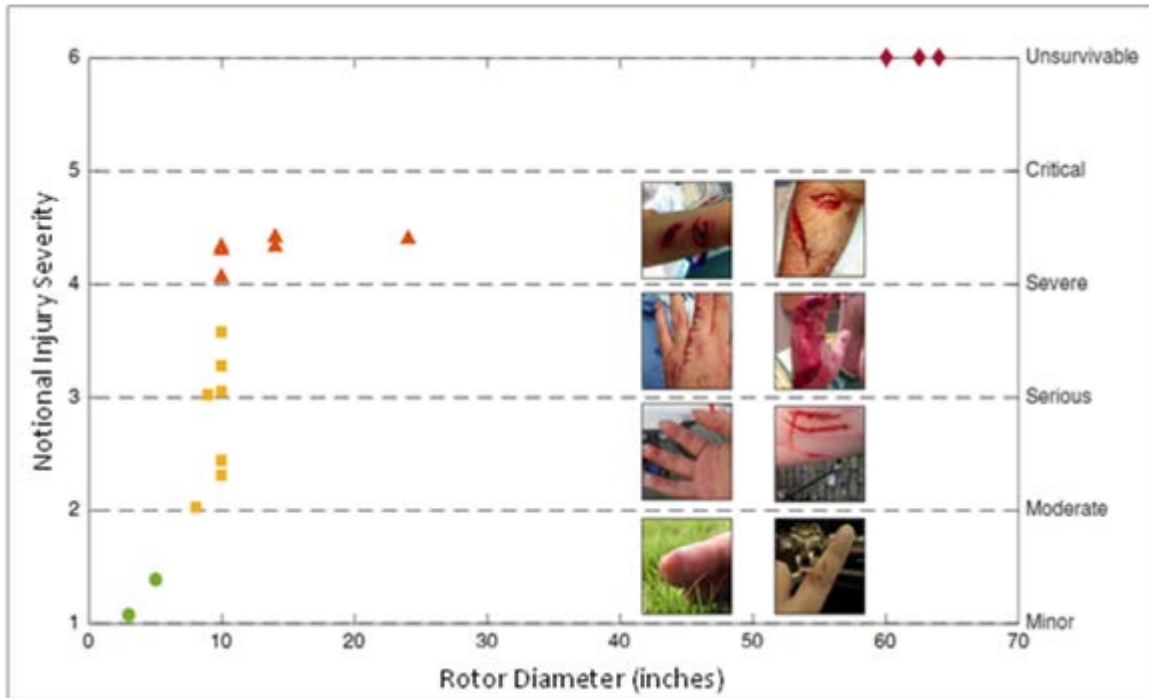


Figure 27 - Notional injury severity index¹⁰³ vs. rotor diameter for reported incidents¹⁰⁴ ¹⁰⁵ ¹⁰⁶ ¹⁰⁷

Unfortunately, injury data is scarce, and the greatest number of injuries is recorded for the most popular rotor size (10”), whereas single data points are plotted for most other rotor diameters. This produces a spread of severity values for the 10” rotor size. This spread is expected since the conditions of each injury (throttle setting, rotor speed, cut angle) are variable. If an acceptable amount of data was available for each rotor size, then a curve could be fit to the data, and uncertainty bounds applied. This data could then be used to make design prescriptions based on rotor diameter.

4.10.4. Proof of Concept Laceration Testing

A proof of concept study has been conducted to: a) develop a protocol for testing for laceration severity; and, b) to develop preliminary evaluations of flesh lacerations by a range of UAS motor

¹⁰³ http://gi.esmplus.com/sharpshop/item/xtrone/img_01_2.jpg

¹⁰⁴ <http://cdn3.volusion.com/fwsku.adwhy/v/vspfiles/photos/RTF001-3.jpg?1418995804>

¹⁰⁵ http://www.personal-drones.net/wp-content/uploads/2013/10/SFC4410_ASSEMBLED.png

¹⁰⁶ http://www.staufenbiel.co.uk/k_staufenb_e/prodpic/UDI-R-C-Discovery-Drone-RTF-with-HD-Camera-044AU818A1_b_0.JPG

¹⁰⁷ <http://g02.a.alicdn.com/kf/HTB1t..VIXXXX9XpXXq6xXFXXE/LISHltoys-L6052-6052W-super-wing-rc-model-airplane-with-6-axis-gyro-control-system-or-with.jpg>

torque/blade combinations. These tests were performed with a prototype of a simulated human arm.

Figure 28 shows the test setup with the simulated arm on a pendulum near the rotor blade.



Figure 28 – Laceration Testing Setup

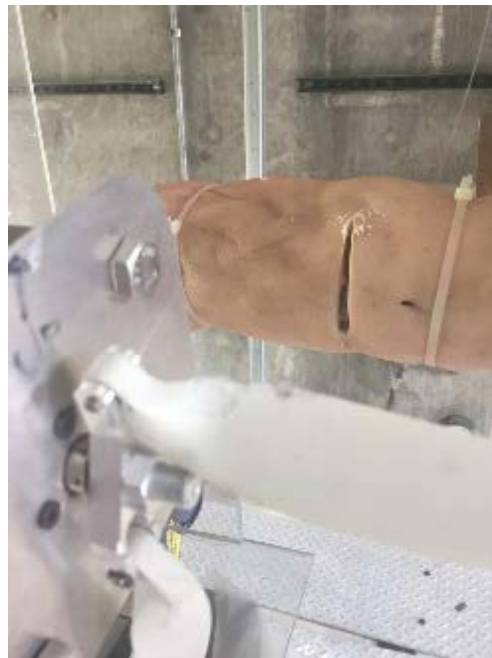


Figure 29 – Example of Deep Laceration from Propeller Strike

Preliminary results show that stiffer, sharper blades do more damage to simulated skin/flesh than less stiff, flat-tipped blades. Figure 30 shows the relationship between notional AIS rating and blade tip velocity for a range of blade types. Note that the most consistent trends (more damage for higher tip velocity) were evidenced for carbon fiber blades. The wide range of

results for molded plastic blades seems to be due to the wide range of blade stiffnesses, which is not captured in the figure.

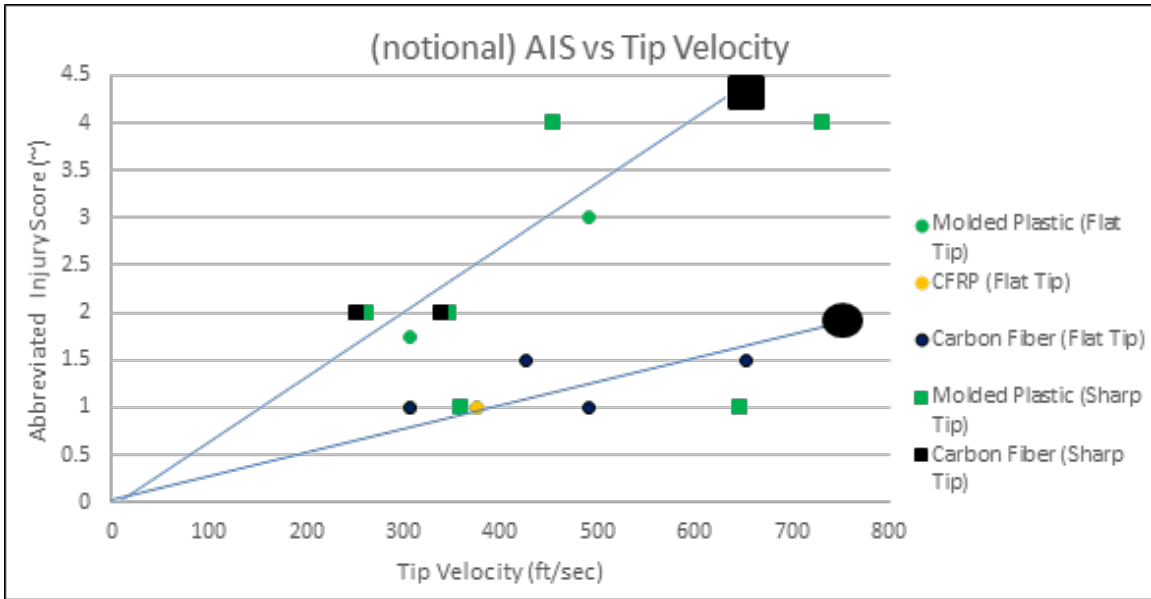


Figure 30 – Injury Severity vs. Tip Velocity

During testing, the motor torque, the current drawn by the motor and the blade RPM were recorded. For deep cutting situations, the current drawn by the motor noticeably “peaked,” which may allow on-board diagnostics to indicate blade impact has occurred. Such a capability may be able to be used as an injury mitigation strategy. Appendix F contains details on the test setup and the motor/blade test matrix.

A suite of laceration tests was performed using the artificial, surgical skin. This skin is meant to simulate areas of the body with moderately tough skin and is rated for a puncture force of 4 N. [Sheets with a range of puncture forces from 2 N to 10 N are available.] The DJI Phantom 3 motor was used with three propeller variants: stock plastic, carbon reinforced plastic, and carbon fiber epoxy. The pendulum was swung with a range of approach velocities, as described below. Since the pendulum with the attached surrogate arm is heavier than a DJI Phantom 3, a velocity conversion was performed based on equivalent kinetic energy.

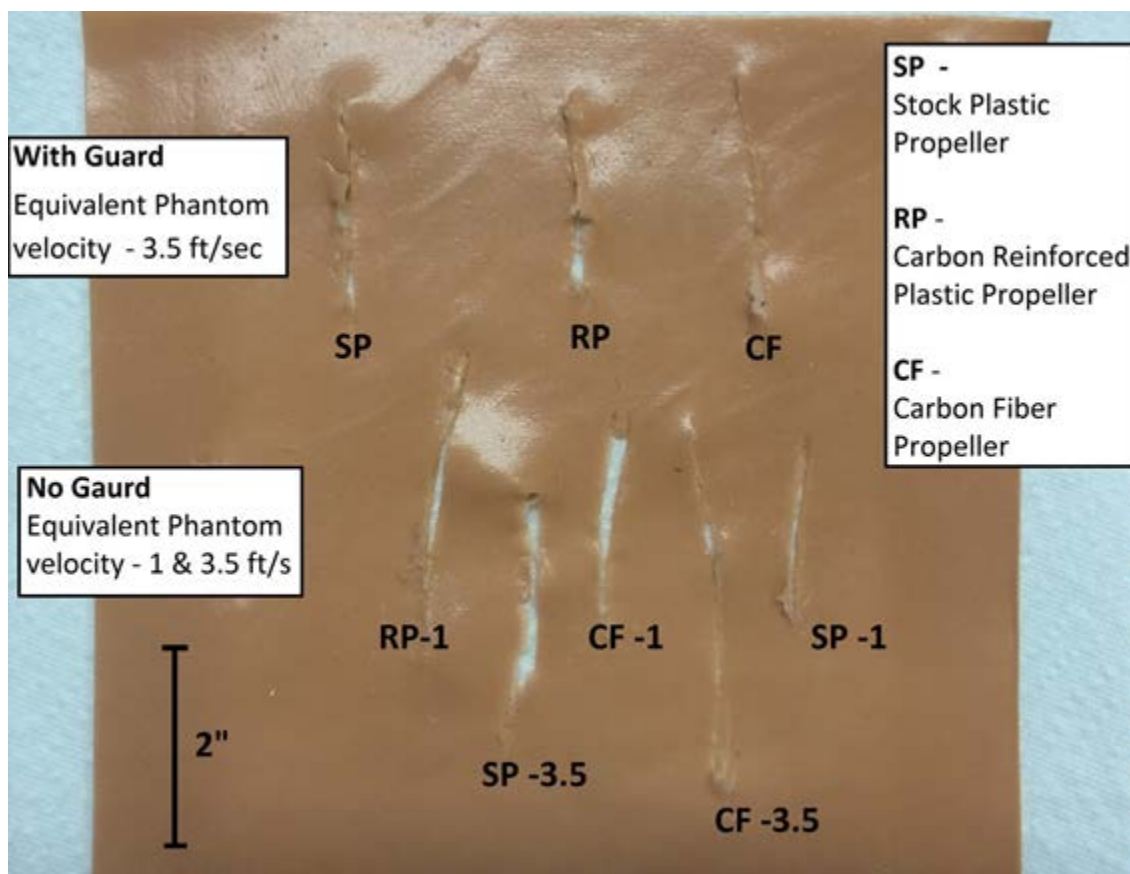


Figure 31 - Lacerations on Syndaver Artificial Skin from Multiple Blade Impacts, Both with and without Blade Guards.

An initial comparison was performed between the three blade types with no guard at an equivalent phantom velocity of 1 ft/s. Figure 31 shows the cuts in the surrogate skin after testing. Cuts were similar across all three propellers; however, the stiffer blades cut slightly deeper causing longer lacerations of the skin.

Tests were also conducted with the stock blade guard, with increasing velocities starting from 1ft/s. No lacerations occurred until 3.5 ft/s when the guard would fail. The primary failure of the guard supports was due to buckling and subsequent fracture. In most guard failure cases the plastic supports were pushed up into the propeller. The stock plastic propellers deflected when this occurred, but still caused laceration similar to the tests without guards. In the case of the reinforced plastic and the carbon fiber propellers, the blades cut through the guards instead of deflecting. On impact the blade tips chipped as well, which could have the potential to introduce carbon fibers into the wound. In size and depth, the lacerations caused upon guard failure were comparable to the no guard case, with the exception of the reinforced plastic which cut considerably less. This was likely due to some type of interference from the guard.

Finally, a set of tests was conducted at the same velocity at which the guard failed, but without a guard, to get a direct comparison of length of laceration with and without a guard. Predictably, this produced deeper and longer lacerations than both the initial tests and the with-guard tests. The carbon fiber blade reached the surrogate bone when struck and the tip of the blade sheared off. This is another test that showed the possibility of carbon fibers entering a

wound. Figure 32 shows the different cut lengths at their respective equivalent Phantom impact velocity.

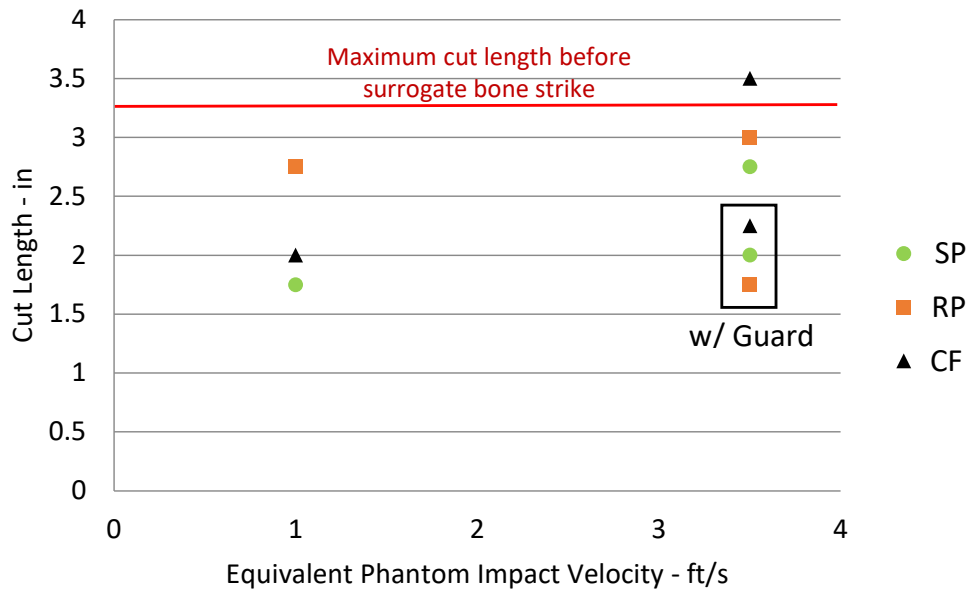


Figure 32 - Laceration length vs impact velocity with and without blade guards

Knowledge Gap: If a good correlation between the laceration testing recently conducted on synthetic skin and laceration injuries in humans is desired, it is recommended that testing be done on cadavers. Such testing would, ideally, more completely capture the effects of blade tip speed (or blade diameter) *as well as* blade stiffness, tip sharpness and leading edge sharpness, which have been shown to significantly affect laceration potential. Knowledge of the effects of blade stiffness and sharpness may provide better guidance on the necessity of blade guards for safe UAS operation.

4.10.5. Blade Injury Mitigation with Guards and Enclosures

Existing design features that can mitigate the risk of laceration injuries include various shrouds and cages, though more often than not, the goal is protection of the rotors, not people. Examples are shown in Figure 33.^{103,104,105,106,107}



F180 Mini



UDI Discovery



LISHToys L6052



Safeflight Copters Quad H



Xtrone

Figure 33 - Rotor Enclosures in Existing Micro UAS^{108,109}

Description and analysis of the sharpness of rotor edges is also a potential mitigating strategy for avoiding cutting injuries due to whirling blades. Guiding documents include EN 71-1 and EC - Type Approval Protocol No 3.^{108, 109} EN 71-1 specifies tests used to evaluate the sharpness of edges and tips on toys. The test for edge sharpness specifies the placement of a piece of self-adhesive tape around the circumference of a mandrel which is then rotated 360° against the edge that is being tested. The edge is considered sharp if greater than 50% of the tape length has been cut during the test. This test is prescribed in EC-Type Approval Protocol No. 3, which deals with the safety of toy rotorcraft. EC-Type Approval Protocol No. 3 also recommends certain steps that should be taken to mitigate injury risk. It recommends brightly marking the tips of rotor blades in order to enhance their visibility. Figure 34 illustrates another method - including an arched structure that prevents the leading edge of the rotor from impacting an object in its path. Toy rotors are intended to abide by these rules, and similar guidelines might be applied to UAVs. In particular, rotor tip marking and manufacturer verification of blade sharpness in accordance with EN 71-1 are relatively simple measures that can be implemented to improve blade safety and classify risks associated with a design.

Knowledge Gap: Blade guard standards exist for consumer grade fans but not for flight worthy stands that must withstand collision while compromising weight. Standards for guards associated with package delivery applications may need additional standards that protect small children’s hands from rotors.

¹⁰⁸ Mechanical and physical properties, BS EN 71-1:2014 (2014).

¹⁰⁹ The Commission and the Expert Group on Toy Safety. Protocol No 3: Rotor blades in helicopter toys (Rev 5) (2015).



Figure 34 - Suggested Safety Feature for Toy Rotors¹⁰⁹

4.10.6. Blade Injury Mitigation Assessment Prototype

IEC/EN 60529 and EN 62262 are European standards that rate the effectiveness of *ingress protection* for electronic equipment such as industrial fans.¹¹⁰¹¹¹ EN 60529 describes the Ingress Protection Code (IP Code) rating system. Figure 35 shows the set of standard probes that are used to rate the physical accessibility of the hazardous parts, such as fan blades.¹¹² The size of probe that can pass through a protective enclosure determines the IP code rating of the enclosure, and probes are sized to represent the back of a hand, a finger, a tool, and a wire. UAV rotors that are deemed laceration risks could be required to be protected by an enclosure that meets a prescribed IP code value, depending on the flight scenario—a higher protection level (IP rating) might be required for flight over crowds or BVLOS. A guard or cage which protects against both sideward and vertical directions might be rated with regard to “ingress” of a head, hand and finger.

¹¹⁰ Degrees of protection provided by enclosures (IP Code), IEC 60529 ED. 2.2 B:2013 (2013).

¹¹¹ Degrees of protection provided by enclosures for electrical equipment against external mechanical impacts (IK code), BS EN 62262:2002 (2002).

¹¹² Danfoss. IP degrees of protection. Electronic Publication EP 101 E. http://www.dmc-global-service.com/main/danweb/vault/commlit/ep101e_ms.pdf.

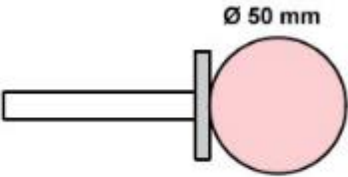
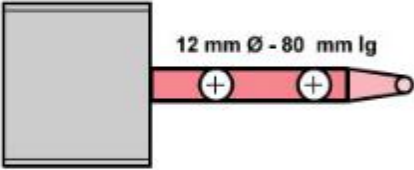
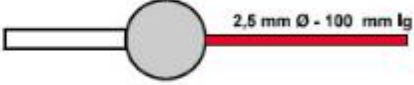
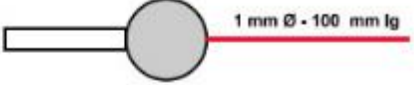
Protection against access with	Access probe	Explanation
Back of the hand		The plate between the sphere and the handle is not a stop but is provided to protect the tester
Finger		The »jointed test finger« has two joints. For the purposes of the IP test it is only to be used up to the first stop face measuring 50 mm x 20 mm, and 80 mm along its length
Tool		The »stop face« takes the form of a 35 mm Ø sphere. It is intended to simulate the knuckle when the tool or wire is held in the hand
Wire		

Figure 35 - Probes for determination of IP Code ratings¹¹⁰

4.10.7. Blade Guard Durability Assessment Prototype

EN 62262 describes the “IK code” system that rates the *durability* or impact resistance of protective enclosures, in terms of kinetic energy of impact with the enclosure. It specifies a series of impact tests that can be used to determine these ratings. IK code prescriptions could be made for enclosures of UAV rotors and propellers which would survive a specified KE of impact with a person for a specified forward or vertical velocity.

4.11. Standoff Distances and Relationship to Severity (UAH)

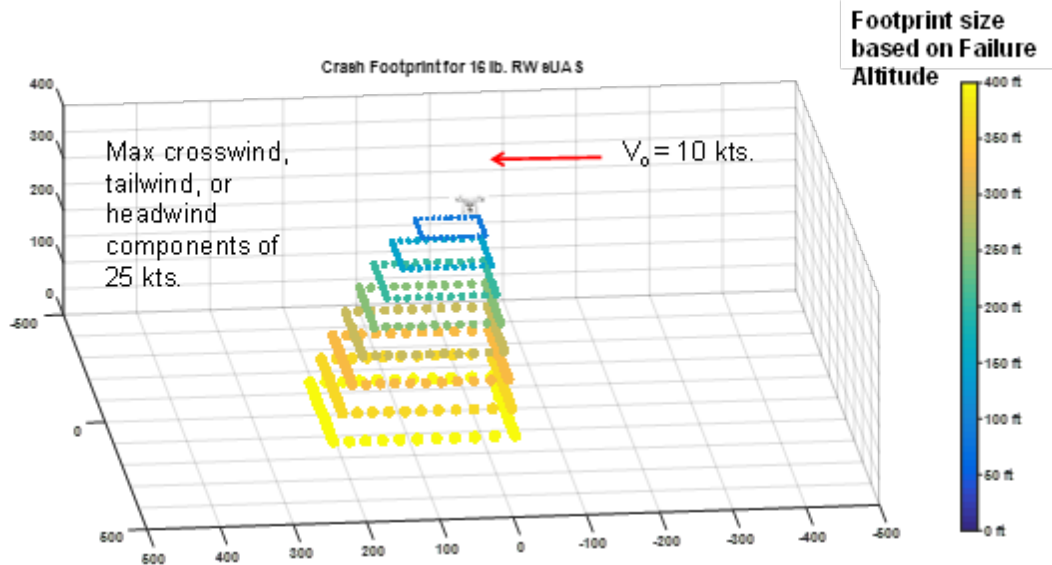


Figure 36 - Example Ballistic Modeling of a Falling Multi-Rotor Aircraft

One of the most effective ways to avoid a collision between a UAS and a vulnerable object on the ground is to use a minimum standoff distance between the aircraft during flight and the object. Recent Section 333 Exemptions specify use standard offset distances of 500 ft in all directions from non-participating people, structures, and vehicles. Modeling work completed by researchers at UAH has determined that this is an overly conservative measure. Figure 36 shows that a 16 lbs multi-rotor UAS that has a failure velocity of 10 kts and faces up to 25 kts crosswind, tailwind, or headwind has less than a 100 ft x 50 ft failure footprint if it fails at 50 ft AGL and a failure footprint of roughly 250 ft x 230 ft for a failure altitude of 400 ft AGL. Even with a 400 ft AGL failure, there is still over a football field size footprint of area ahead of the vehicle and to the sides. In Figure 36, the plot axis limits are set to 500 ft fore/aft, and laterally around the vehicle to show how much additional margin, beyond the failure footprint, is present with 500 ft standoff for non-participants. There is an inherent risk with overly conservative, and one-size-fits-all, procedural control measures, as has been applied to multi-rotor and FW aircraft alike. Operators are likely to violate a restriction that prevents them from performing the commercial service that they provide. Few airborne camera systems used on sUAS combine the requisite zoom and aperture needed to take good pictures from a slant range of 500 ft. While this model highlights the need of adequate analysis in modeling, it also demonstrates that, based purely on physics, required standoff during visual line of site operations is an effective way to prevent UAS collision with vulnerable objects on the ground. However, it does not take into account software failures that could cause a UAS to fly in an uncontrolled manner. Nor does it account for partial power conditions with limited control. The latter case, in which one or more motors may remain functional, represents a knowledge gap that can only be filled by way of a high fidelity study of falling aircraft dynamics.

This analysis of aircraft failure footprints also lends itself to the calculation of the probability that a vehicle will strike a person on the ground. The following shows an example of this analysis based on the ballistic modeling shown above. Figure 37 depicts the failure footprint of a Phantom 3 multi-rotor sUAS in hover over centerfield in a baseball stadium with maximum fore/aft, and crosswind components of 10 knots. In this case, the 100 ft AGL failure footprint is

60 ft x 60 ft and the 25 ft AGL failure footprint is 24 ft x 24 ft. The effective area of the Phantom 3 is 1.72 ft² and the failure footprint or A_{haz} is 2400 ft² when the aircraft is hovering at 100 ft AGL. The simple probability of the aircraft hitting any point in the failure box is calculated by:

$$Pr_{(impact)} = A_{eff}/A_{haz} = 4.7 \times 10^{-4} \quad \text{Equation 12}$$

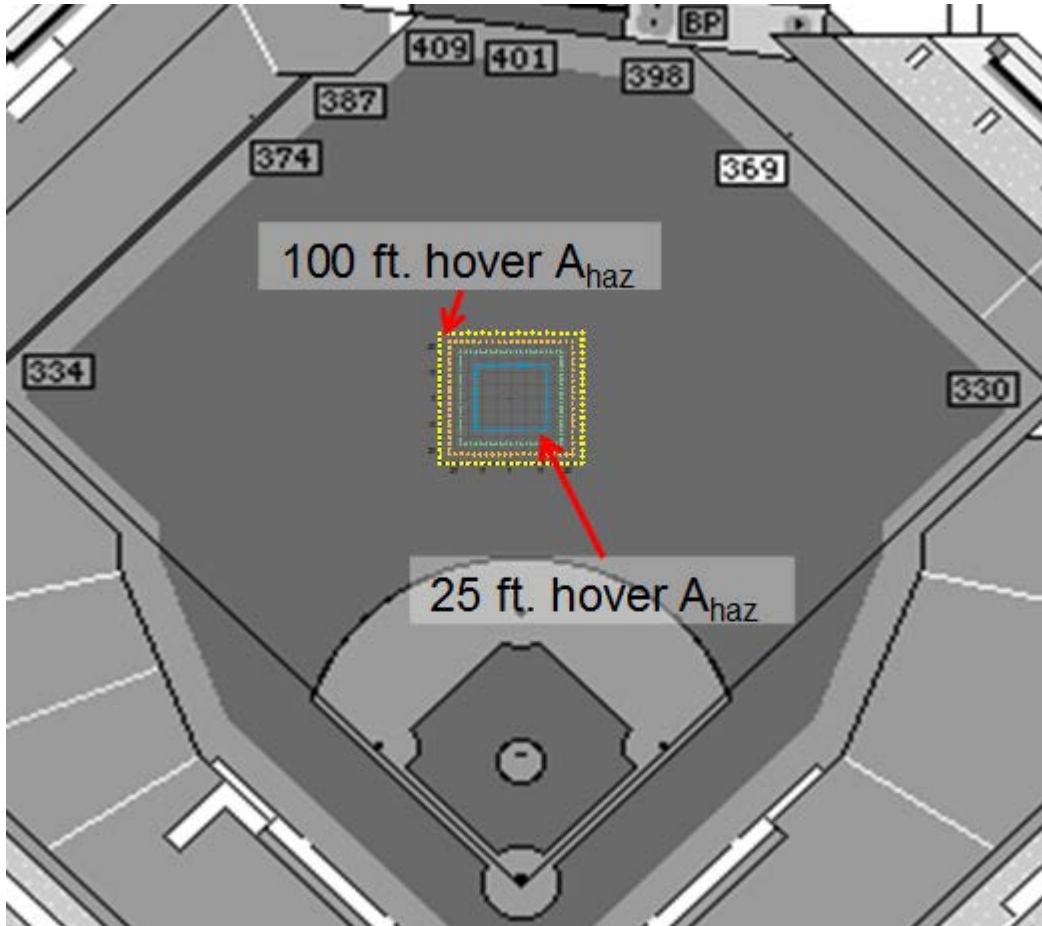


Figure 37 - Diagram of sUAS Operating in Vicinity of People (Baseball Stadium Example)

If a person, represented by 50th percentile male anthropometrics, has an effective area of 1.49 ft² based on the vertical projection of that person's area on to the ground, then the probability that the person is at any location in the hazard area is 4.13×10^{-4} . The joint probability of the aircraft landing at the same location as that person is standing following a failure is 1.95×10^{-7} . This is a very simple representation of the calculation, but it points to the idea that the odds of hitting a person are low. This scenario also shows that the infield and stands, which are near and host higher density local populations, remain completely safe during this flight. The probability of the ground collision is further reduced if the operator remains vigilant and deliberately maintains a standoff distance from those personnel in his visual line of sight.

Knowledge Gap: At this stage, these probability calculations for aircraft failure footprints lack detail in terms of vehicle dynamics to properly define the potential landing area. Current casualty methods address vehicle dynamics solely with ballistic coefficients typically used for

inert debris that has limited aerodynamic properties. UAS platforms may generate significant aerodynamic forces and moments and rarely fail as solely ballistic projectiles. Previous dialogue with the FAA suggested that terminal KE could serve as a potential means of determining target levels of safety for different classes of UAS. Estimation of strike probability provides insight into determining the operational level of safety for sUAS and can be used to establish the minimum requirements of material reliability for these aircraft based on target levels of safety. This knowledge gap is being addressed in the proposed white paper titled *W64 - Falling Multi-Rotor Dynamics Study* and a follow-on effort titled *sUAS Probability of Striking Ground Objects in Operational Areas*.

4.12. Structural Standards for Sheltering (KU)

There are no standards for assessing severity of damage to structures on the ground due to UAS impact. However studies conducted by the Navy are available detailing the KE required for penetration of typical building and vehicle construction.⁴³ Information on damage due to fires from unspent fuel is also available. The fire model is applied almost exclusively to non-electric powered UAVs, where unspent fuel is ignited after a crash. A method to calculate the total thermal energy is presented, which can be applied to a respective crash scenario. Finally, a method to assess casualties within a structure based on the building material type and the ballistic coefficient of the impacting object is examined. The expression used to calculate ballistic coefficient is

$$BC = \frac{M}{C_d A} \quad \text{Equation 13}$$

4.12.1. Impact Damage to Structure Due to KE Effects (KU)

The net KE of a UAS crash into a structure is determined by Equation 14. If the resulting KE_{net} is negative, it is assumed that the impacted structure absorbed the energy through deformation, breaking, and movement, resulting in no structural penetration.

$$KE_{net} = KE_{Aircraft|Blunt} - KE_{absorbed} \quad \text{Equation 14}$$

Equation 15⁴³ is used to calculate the absorbed KE, where ΔKE_n is an absorption parameter related to the structure impacted by the UAS.

$$KE_{Absorbed} = \frac{A_{CrossSection}}{A_{ScalarConstant}} * \Delta KE_n \quad \text{Equation 15}$$

Table 34 and Table 35 give the KE absorption values for two impact scenarios - hitting the roof and hitting the side of the building, respectively. Both tables are populated with common building materials for the respective scenario, and the KE absorption parameter for each material used in Equation 15. These KE parameters were based off of experiments using explosive projectiles (spherical sabot rounds).

Table 34 - Rooftop KE Absorption Values

Roof Type	% Invulnerable Area (nominal), LA _{roof}	KE absorbed by roof (ft-lb) ΔKE _n
4 in. Reinforced Concrete	10	10000
14 in. Reinforced Concrete	15	200000
Plywood/Wood Joist (2x10 at 16 in.)	5	50
Gypsum/Fiberboard/Steel Joist	5	25
Plywood Panelized (2x6 at 24 in.)	5	50
2 in. Lightweight Concrete/Steel Deck and Joists	7.5	2000
Medium Steel Panel (18 gauge)	7.5	1500
Light Steel Panel (22 gauge)	7.5	1000
Steel (automobile)	2.5	200

Note: the units on KE absorbed should be interpreted as ft-lbs for a 0.054 ft² impactor

Table 35 - Side Wall KE Absorption Values

Wall Type	% Invulnerable Area (nominal), LA _{roof}	KE absorbed by wall (ft-lb) ΔKE _n
Steel Siding (22 Gauge)	2	1000
8 in. Unreinforced CMU (Concrete Masonry Unit)	2	500
8 in. Reinforced CMU	2	500
8 in. Reinforced Concrete	2	50000
14 in. Reinforced Concrete	2	200000
6 in. Reinforced Concrete Tilt-Up	2	37500
1/2 in. Plywood Siding	2	100
8 in. Unreinforced Brick	2	10000
Steel (automobile doors)	4	1000

Note: the units on KE absorbed should be interpreted as ft-lbs for a 0.054 ft² impactor

The tests were performed by using spherical sabot rounds to impact the wall and roof materials with calibrated energy levels.¹¹³ The KE parameter is the *average* KE from the testing impacts. As such, this parameter should be interpreted as KE per the area of the impactor. Table 36 summarizes the various impactors used in the tests.

¹¹³ Crull, M., Tatom, J.W., Conway, R.T., "SPIDER 2 Tests-Response of Typical Wall Panels to Debris and Fragment Impact," Minutes of the 34th DDESB Seminar, July 2010

Table 36 - Type and Size of Materials Used for Impact Testing¹¹³

Impactor	Material	Impactor Diameter (in.)	Impactor Weight (lb)	Impactor Diameter (mm)	Impactor Weight (kg)
C1	Concrete	2.25	0.51	57.15	0.23
C2	Concrete	3	1.15	76.2	0.52
C3	Concrete	3.75	2.2	95.25	1
C4	Concrete	5	5.75	127	2.61
C5	Concrete	7.4	17.4	187.96	7.89
S1	Steel	1.125	0.2	28.575	0.09
S2	Steel	1.5	0.5	38.1	0.23
S3	Steel	1.875	1	47.625	0.45
S4	Steel	2.5	2.298	63.5	1.042

At the conclusion of the impact testing, the impact areas from all rounds were averaged to give the average cross sectional area of 0.054 ft². To get the KE for a different cross sectional area, one multiplies the KE Absorption parameter of the respective impacted material from Table 34 or Table 35 by the ratio of the actual area to the baseline 0.054 ft² to determine the KE_{absorbed} value used in Equation 15.

4.12.2. Example Scenario

A DJI-Phantom 3 fails at an altitude of 400 ft and impacts into a structure with a panelized plywood roof with a KE absorption parameter of 50 ft-lbs. This UAS has a KE of 201.21 ft-lbs at terminal velocity [Section 4.8]. The DJI Phantom 3 has a fuselage cross sectional area of 0.2544 ft² obtained from CAD modelling. Using Equation 14 and Equation 15, repeated here, yields the KE_{net} .

$$KE_{Absorbed} = \frac{A_{CrossSection}}{A_{ScalarConstant}} * \Delta KE_n = \frac{.2544ft^2}{0.054ft^2} * 50 \text{ ft-lbs} = 235.56 \text{ ft-lbs}$$

$$KE_{net} = 201.21 \text{ ft-lbs} - 235.56 \text{ ft-lbs} = -34.35 \text{ ft-lbs}$$

The resulting calculated KE is negative, meaning that no structural penetration would be expected.

4.12.3. Real World Case Studies

Table 37 summarizes calculations of impact damage for three small aircraft impacting different types of structures. As observed, the only event that did not have fatalities outside the aircraft occupants had a negative residual KE.

Table 37 - Case Study of 3 Historical Impacts

Aircraft	Robinson R44	Piper PA-28-236	Cirrus Design SR 20
Accident No.	NTSB CHI08FA293	NTSB CEN10FA124	AAB DCA07MA003
GW (lb)	2,500	2,150	3,050
Alternate Weight	1	75	189
Cruise Speed (kt)	110	108	155
Max Speed (kt)	130	123	N/A
Assumed Speed	110	123	140
Kinetic Energy (KE) (ft-lb)	134,000	50,192	163,862
Collision Building	Residential Home 	Office Building 	Brick Skyscraper 
Building Collision Type	Plywood Panelized	8 in. Reinforced Concrete	14 in. Reinforce Concrete
Roof or Wall	Roof	Wall	Wall
KE Absorption	33000	50000	200000
Residual KE	1300000	192	-36138
Lethal Limit (ft-lb)	55		
Fatal/Non-Fatal	Fatal	Fatal	Nonfatal
Actual Events			
Passengers/Crews	2 Fatalities	1 Fatality	2 Fatalities
Third Party Ground	No Injuries	1 Fatality; 1 Serious Injured	Minor Injuries on Ground (Debris)

4.12.4. Damage Due to Secondary Fuel Fire

The secondary fires caused by spilled fuel in buildings can quickly ignite the building itself. To estimate the danger of fire, the thermal flux of the fuel spill can be calculated and applied to common materials found within both office and residential buildings. The first step is calculating the area of the spilled fuel by:

$$D = 10\sqrt{V} \quad \text{Equation 16}$$

where:

D = Diameter of spill

V = Volume of fuel spilled

$$A = \pi \left(\frac{D}{2}\right)^2 \quad \text{Equation 17}$$

The total thermal energy is then calculated by:

$$\dot{Q} = A * \dot{q}_{fuel} \quad \text{Equation 18}$$

where, \dot{Q} = Total Thermal Energy in kW or BTU, and \dot{q} = Thermal Flux. This value is specific for every fuel type. Thermal flux values for common fuel types are shown in Table 38.

If a given building material can survive the total thermal energy for a given volume of a given fuel, the fire is not expected to burn through the structure.

Knowledge Gap: Just as section 3.5 highlights the potential hazards of LiPo batteries and states that experimental data pertaining to burn temperatures and burn duration are needed in order to compare with roofing standards, it is also necessary to examine several case studies of crashed sUAS that leak fuel and experience a secondary ignition of that fuel.

Table 38 - Mass Burning Rate, Heat of Combustion, and Thermal Flux for Select Fuels⁴³

Liquid	Mass Burning Rate, $m_{\dot{}}$ kg/m ² *1/s	Heat of Combustion kJ/kg	Thermal Flux kW/m ²
Acetic Acid	0.033	13,100	400
Acetone	0.041	25,800	1,100
Acrylonitrile	0.052	31,900	1,700
Amyl Acetate	0.102	32,400	3,300
Amyl Alcohol	0.069	34,500	2,400
Benzene	0.048	44,700	2,100
Butyl Acetate	0.1	37,700	3,800
Butyl Alcohol	0.054	35,900	1,900
m-Cresol	0.082	32,600	2,700
Crude Oil	0.045	42,600	1,900
Cumene	0.132	41,200	5,400
Cyclohexane	0.122	43,500	5,300
No. 2 Diesel Fuel	0.035	39,700	1,400
Ethyl Acetate	0.064	23,400	1,500
Ethyl Acrylate	0.089	25,700	2,300
Ethyl Alcohol	0.015	26,800	400
Ethyl Benzene	0.121	40,900	4,900
Ethyl Ether	0.094	33,800	3,200
Gasoline	0.055	43,700	2,400
Hexane	0.074	44,700	3,300
Heptane	0.101	44,600	4,500
Isobutyl Alcohol	0.054	35,900	1,900
Isopropyl Acetate	0.073	27,200	2,000
Isopropyl Alcohol	0.046	30,500	1,400
JP-4	0.051	43,500	2,200
JP-5	0.054	43,000	2,300
Kerosene	0.039	43,200	1,700
Methyl Alcohol	0.017	20,000	340
Methyl Ethyl Ketone	0.072	31,500	2,300
Pentane	0.126	45,000	5,700
Toluene	0.112	40,500	4,500
Vinyl Acetate	0.136	22,700	3,100
Xylene	0.09	40,800	3,700

4.12.5. Casualties within a Structure

The Navy study also considered the effect of the penetration of a structure from falling debris on the area within the building within which a casualty may be expected. The falling debris is first categorized in terms of its ballistic coefficient. Table 39 gives six ballistic coefficient classes for typical debris.

Table 39 - Ballistic Coefficient Classes for Debris Roof Penetration Analysis¹¹⁴

Ballistic Coefficient Class	β range	Representative β Used in the Penetration Analysis	Typical Vehicle Fragments in this Class
1	1.8 to 3 psf	2.3 psf	Skin, doors, interstage structure, skirt, lighter bulkhead parts, straps, fairing sections
2	3 to 10 psf	6.4 psf	Ducts, heavier bulkhead parts, antennas, medium mass interstage parts, some fairing parts, struts, nozzle extension
3	10 to 17.5 psf	13.8 psf	Heavier antennas, interstage structure, telemetry box, small actuators, electronics packages, ACS jets, more massive fairing parts
4	17.5 to 30 psf	21.3 psf	Small engines, batteries, receivers, helium tanks, nitrogen tanks, propellant lines
5	30 to 55 psf	44 psf	Batteries, actuators, large helium tanks
6	55 to 100 psf	69.9 psf	Main engines, heat exchangers, gas generators

The effective casualty area is defined by the FAA as the region associated with an impact location that will result in a casualty if they were to be in the impacted area.

These ballistic coefficient values (Equation 13) are for typical debris that would be found in an aircraft accident, and can also be used to model UAS impacts. The ballistic coefficient class that would be most appropriate to model a small UAV would be Class 1, and would increase as the size of the UAV increases (i.e. Global Hawk with a Class 6 Ballistic Coefficient).

Table 40 presents the different roofing structure types used in the FAA casualty analysis and their associated properties.

¹¹⁴ United States Federal Aviation Administration, Flight Safety Analysis Handbook, Version 1.0, U.S. Dept. of Transportation, Federal Aviation Administration, Washington D.C., 2010

Table 40 - Representative Roof Classes for Debris Penetration Analysis¹¹⁴

Structure Roof Class	Building Description	Typical Roof Construction	Representative Roof for Penetration Analysis
A	Mobile home and trailers Temporary office trailers	22 gage corrugated steel roof, 24 gage corrugated aluminum roof or 1/2 inch plywood roof	24 gage corrugated aluminum
B	Single family dwellings Duplex and fourplex residential dwellings Small condominiums and townhouses Small apartment buildings	Wood roof	5/8 inch plywood
C	Small retail commercial buildings (gas stations, stores, restaurants, strip malls) Small office and medical office buildings	Composite roof (rigid insulation on steel purlins), corrugated steel roof (pre-engineered metal building-type roof, or light weight concrete on corrugated steel decking roof	Composite roof (2 inch rigid gypsum insulation of steel purlines)
D	Manufacturing plants Warehouses Public buildings (large shopping malls, large office buildings, large apartment buildings, hotels, etc.)	Lightweight concrete on corrugated steel decking roof, or reinforced concrete slab roof	3/4 inch lightweight concrete on 22 gage corrugated steel decking

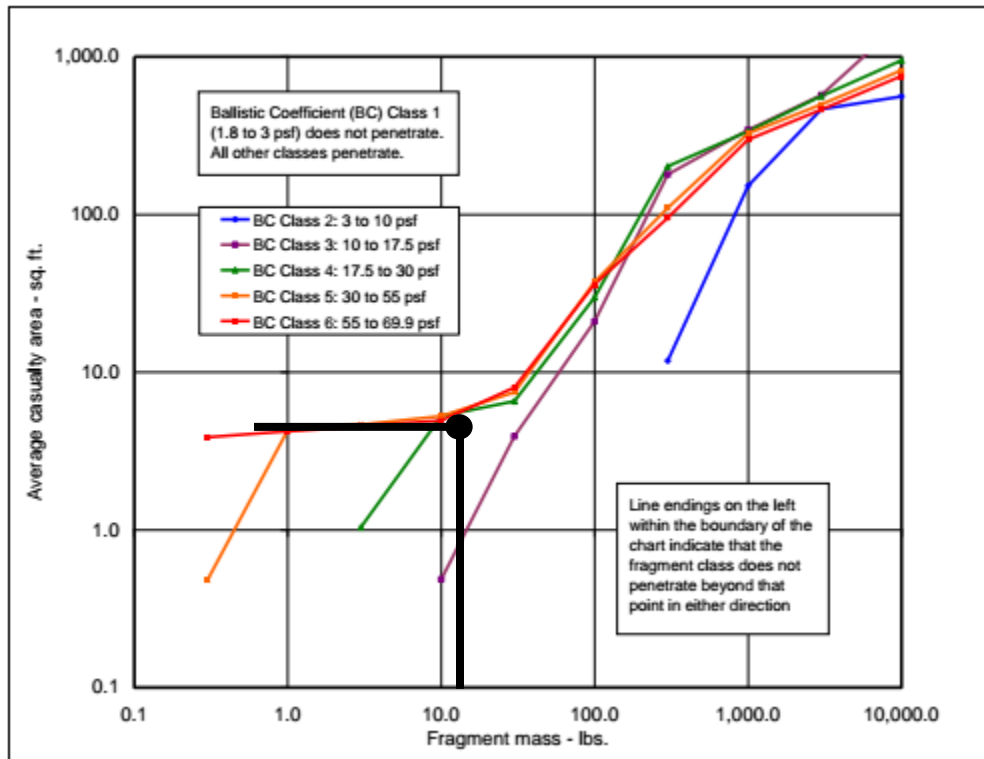


Figure 38 - Penetration Effects on Type A Roof Structure (per Table 40 definition of roofing types)¹¹⁴

Figure 38 assumes that the debris was impacted at terminal velocity with masses ranging from 0.1 lbs to 10,000 lbs. In the scenario of a 2.8 lbs DJI-Phantom 3 drone impact at terminal velocity on a trailer, there would be an average casualty area of approximately 6.25 ft²; indicated by the black dot on Figure 38. The Phantom 3 has an estimated ballistic coefficient of 4.99, which puts it in Ballistic Coefficient Class 2. Based on its mass and average casualty area, it falls to the left of the endpoint of the BC Class 2 penetration line on Figure 38 and will not penetrate a Type A building, which is representative of mobile homes.

4.12.6. Damage to Roofing Materials and Architectural Glazing

Universal Laboratories, UL 2218, FM 4473, and the American Society for Testing and Materials, ASTM D 3746 are three standards that are used to rate the impact resistance of roofing materials, specifically impacts caused by hail.¹¹⁵ Koontz summarizes the testing procedures and rating criteria for each of these. The impact energy associated with the highest impact rating (UL Class 4) is only 23 ft-lbs (31.2 J). This value is much lower than the freefall KE values that are anticipated for micro/mini UAS flying at heights of up to 400 ft, the altitude limit imposed by the FAA.¹¹⁶ Furthermore, these tests consider damage such as denting and cracking, but not roof penetration which is of greater concern when dealing with UAS. As a result, these standards are not relevant to the goals of the current paper.

There are also impact standards for architectural glazing,¹¹⁷ but the examined KE levels are similarly small compared to those relevant to mUAS.

4.13. Vehicle Standards (UAH)

KE required for penetration of a steel automobile roof was included in the NAVAIR study, and is shown in Table 34. The energy is seen to be significantly greater than that for a residential roof or wall system, thus it is unlikely that a sUAS platform would be able to penetrate a car roof. Larger UAS (greater than 55 lbs) are more likely to crumple or crush portions of a vehicle, akin to an auto accident, versus penetrate the vehicle.

Federal motor vehicle safety standard 205 publishes minimum safety guidelines for car windshields and windows. These standards were established by considering the probability of small rocks hitting the windshield or windows at high vehicle speeds (70-100 mph). A half-pound test is performed on tempered glass and laminated glass separately.¹¹⁸ Tempered glass is strong but prone to breaking and is used for windows. Laminated glass is less strong but resistant to penetration and used for windshields. In the half-pound test, a 227 g (0.5 lbs) steel ball is dropped from a height of 2 m (6.6 ft) for tempered glass and 9.14 m (30 ft) for laminated glass, respectively. In the former case, the glass shall not break in 8 of the 10 samples the test is performed on. In the latter case, the ball shall not pass through the glass. For a laminated glass, this translates into 20 Joules (15 ft-lbs) of energy. According to ANSI Z26.1,¹¹⁹ a different standard for laminated and tempered glass, the half-pound test is conducted from a height of 10 m (English), and the contact area between the ball and the windshield must not be more than 6.45 cm² (English). This translates to 3 J/cm² (English) of energy density, beyond which the windshield yields. For a UAV weighing one pound, this energy is reached above 15 ft of altitude. Moreover, during analysis of contact areas of consumer drones like DJI Phantom, DJI Inspire and 3DR Solo with humans, it was observed that the fuselage arm tips can have contact area as low as 1.2 cm² (English). These vehicles have more than 100 J (English) of energy at either maximum

¹¹⁵ Koontz, J. D. "Simulated Hail Damage and Impact Resistance Test Procedures for Roof Coverings and Membranes." RICOWI, 2000.

¹¹⁶ "FAA Doubles "Blanket" Altitude for Many UAS Flights." FAA Doubles "Blanket" Altitude for Many UAS Flights. Accessed April 21, 2016. <https://www.faa.gov/news/updates/?newsId=85264>.

¹¹⁷ "GANA Store — Test Methods/Standards." GANA Store — Test Methods/Standards. Accessed April 21, 2016. <http://store.glasswebsite.com/collections/types?q=Test Methods/Standards>.

¹¹⁸ <https://www.federalregister.gov/articles/2012/06/21/2012-14996/federal-motor-vehicle-safety-standards-glazing-materials>, Accessed 06/02/16

¹¹⁹ http://www.interautoglass.org/content/17473/download/clnt/18339_Draft_ANSI_Z26_11.pdf, Accessed 06/02/16

horizontal velocity or terminal velocity, and with such small contact areas they are likely to break and penetrate car windshields and windows. Even a half-pound UAS flying at 20 kts (33.76 ft/s) can hit a windshield at 22 J (English). If the contact area between this half pound UAS and the vehicle is small, the energy density can even cause the windshield to break. Moreover, the car windows are less resistant to penetration and breaking if more than 5J (English) of energy is transferred. Therefore, car windshields are highly susceptible to damage from UAS.

Knowledge Gap: The effects of sUAS impacts on automobile structures are unknown. Based on KE and energy density analyses, it seems likely that smaller vehicles can penetrate both tempered and glazed glass, but not metal panels. Larger vehicles are highly likely to penetrate glass and may damage exterior panels.

4.14. Modeling, Analysis, and Recommended Severity Criteria

4.14.1. Vehicle KE Modeling, and Analysis (UAH)

One critical task in the A4 project was to conduct limited modeling for benchmarking key severity metrics for sUAS against values found during the literature survey. In order to conduct analysis of vehicle impact KE, impact energy density, and failure footprints, a ballistic model was developed. Baseline KE estimates are also calculated with the closed-form relation shown in Equation 3. The time-stepping ballistic model is used to calculate vehicle speed over time during a fall and also the impact velocity based on falling from any number of heights, whereas Equation 4 only calculates terminal velocity. The physics-based ballistic model was used to determine impact KE based on failure altitude and airspeed. This model uses atmospheric conditions, aircraft failure airspeed and altitude, and the aircraft mass and aerodynamic coefficients as inputs. The model uses a time stepping method to calculate net vehicle acceleration, velocity, and position at any time during a fall. The net acceleration is the difference between gravitational acceleration and deceleration due to drag. The model also uses a lookup function for drag coefficient, which varies based on vehicle velocity. For failure footprint modeling, the ballistic model was altered to account for initial velocity, designated as V_{xo} , horizontal drag coefficients, and winds (cross, head, and tail winds).

Over time, the modeling inputs for both the closed-form V_{term} solution and the time-stepping model were improved. The initial version of the time-stepping model used estimated input values for drag coefficients, generic mass values, and effective areas (both vertical and horizontal planform or projected areas). First, UAH researchers used online sources to obtain images of various vehicles to determine effective areas for mUAS platforms in a level, vertical descent. This effort also included finding and verifying open-source CAD renderings of platforms on the internet.¹²⁰ Researchers also verified dimensions listed in the AUVSI database, based on the airframes in the UAH UAS Fabrication Lab – DJI Phantom 2 and Phantom 3 models, DJI Inspire 1, 3DR Solo, Blade QX350, and the fixed wing SIG Rascal 110. These effective area calculations were used in two ways. First, they became direct inputs to both models. Secondly, it was shown that, on average, a multi-rotor aircraft’s effective area is roughly 30% of the area of a circle with a diameter equal to the diagonal motor-to-motor distance on the vehicle. This second part enables parametrically-based estimation of the effective area of vehicles without image data and analysis of generic vehicles. In order to improve estimated coefficients of drag

¹²⁰ <https://grabcad.com/>, Accessed 02/15/16

for the falling vehicles, CFD simulations of the Phantom 2 and Phantom 3 aircraft were run in STARCCM+. This work was initially out of scope for the A4 project and was completed on internal funding from UAH in order to expedite modeling and analysis progress and more accurately answer questions from the FAA and mUAS panel. The CFD analysis was later resumed during Task A11, which specifically required the ballistic characterization of a Phantom 3 Standard and a Phantom 3 Advanced with blade guards installed.

Table 41 - STARCCM+ Coefficient of Drag Estimates for the Phantom 2 UAS

Velocity (m/sec)	Reynold's Number $\times 10^5$	C_d @90° λ	C_d @90° λ BL	C_d @90° λ TKE
2	0.31587	1.12576	1.11282	1.09164
5	0.78966	1.06275	1.11312	1.07378
10	1.57932	1.04159	1.10048	1.05800
20	3.15865	1.02515	1.12771	1.04260
30	4.73797	1.02766	1.13355	1.03010
40	6.31370	1.00380	1.13689	1.03029
50	7.89662	1.01769	1.14916	1.02952

The CFD analysis of the Phantom 2 in STARCCM+ was comprised of velocity sweeps from 2m/sec - 50m/sec with the aircraft in two orientations – falling vertically through the flow and in an attitude to approximate horizontal flight. The aircraft encountered laminar flow in all simulations. Grid studies were conducted for the laminar flow, laminar flow with specialized boundary layer meshing, and laminar flow with turbulent KE (TKE). In order to ensure adequate meshing, grid density was increased until there was no longer an appreciable impact on drag estimates for the vehicle. Table 41 shows C_d estimates for the Phantom 2 aircraft in a vertical fall with its payload mounted. Modeling inputs for both the closed-form solution and the time stepping model now use a C_d value of 1.0426. The simulation scenario is based on limited flight testing of the Phantom 2, during which it achieved a quasi-steady vertical speed of approximately 19m/sec or 59 ft/sec (Figure 41). The effective C_d value for the Phantom 2, based on the flight test, is 1.07, which puts the CFD estimate within 1% of the observed aerodynamic behavior of the aircraft. Current modeling for all other mUAS (<4.4 lbs) in the study is using a drag coefficient of 0.96, which is the C_d value determined for the Phantom 3 during initial CFD runs. This lower value, compared to the Phantom 2, is due to differences in the payload.



Figure 39 - Images from the Phantom 2 CFD Analysis

Figure 39 depicts gauge surface pressures and the CFD simulated flow field for the Phantom 2 aircraft in a vertical fall. It is important to note that the blades were treated as static during the CFD analysis – there was no wind milling of the blades in the flow. This assumption was borne out during the Phantom 2 flight test in which the blades, during a vertical fall, rapidly came to a stop after the motors were no longer receiving power. Subsequent analysis of the CFD pressure fields showed that the stationary blades, in a position that is perpendicular to the vehicle arms, are responsible for approximately 40% of the total vehicle drag in a vertical fall (Figure 40). This figure shows the total drag coefficient of the vehicle denoted by a blue line that is labeled Phantom 2 90° TFE, and the propeller drag coefficient values, which are in a red oval.

During Task A11, a more refined CFD modeling effort was conducted to evaluate the flat plate draft area of the Phantom 3 sUAS. This modeling and simulation effort showed that the average coefficient of drag values for the Phantom 3 without guards is $C_{d,vert} = 0.9313$ and $C_{d,lat} = 1.077$. The average coefficient of drag values for the Phantom 3 with guards is $C_{d,vert} = 1.124$ and $C_{d,lat} = 1.122$. There is a 42% increase in the vertical flat plate drag area, and a 19.6% increase in the lateral flat plate drag area when the guards were added to the vehicle configuration. Not only do blade guards limit the risk of serious laceration injury, they add flat plate drag area and reduce the aircraft's terminal velocity.

The limited flight test of the Phantom 2 aircraft in falling flight served to validate the accuracy (rather than precision) of the estimated drag coefficient values, and it provided some important insights into other aspects of the falling aircraft. First, the blades stopped turning shortly after the motors stopped receiving power. This is important, as there is an ongoing discussion regarding whether these aircraft can effectively autorotate. It is necessary to lead this discussion off by saying that the correct term is to windmill, as the air will drive the blades in reverse when compared with the direction they spin during thrusting flight. During autorotation for a helicopter, the blades continue to turn in the same direction as they turn in a normal thrusting state. It is highly unlikely that a fixed pitch prop could ever autorotate, since the first step for a helicopter pilot, after losing engine power, is to reduce pitch in order to achieve equilibrium between the driven (net drag producing) section of the rotor and the driving (forward inclined lift generating) section of the rotor. That cannot be done with a fixed pitch prop. The limited flight test indicates that the motor pole resistance to turning prevents the prop from wind milling (reversing direction).

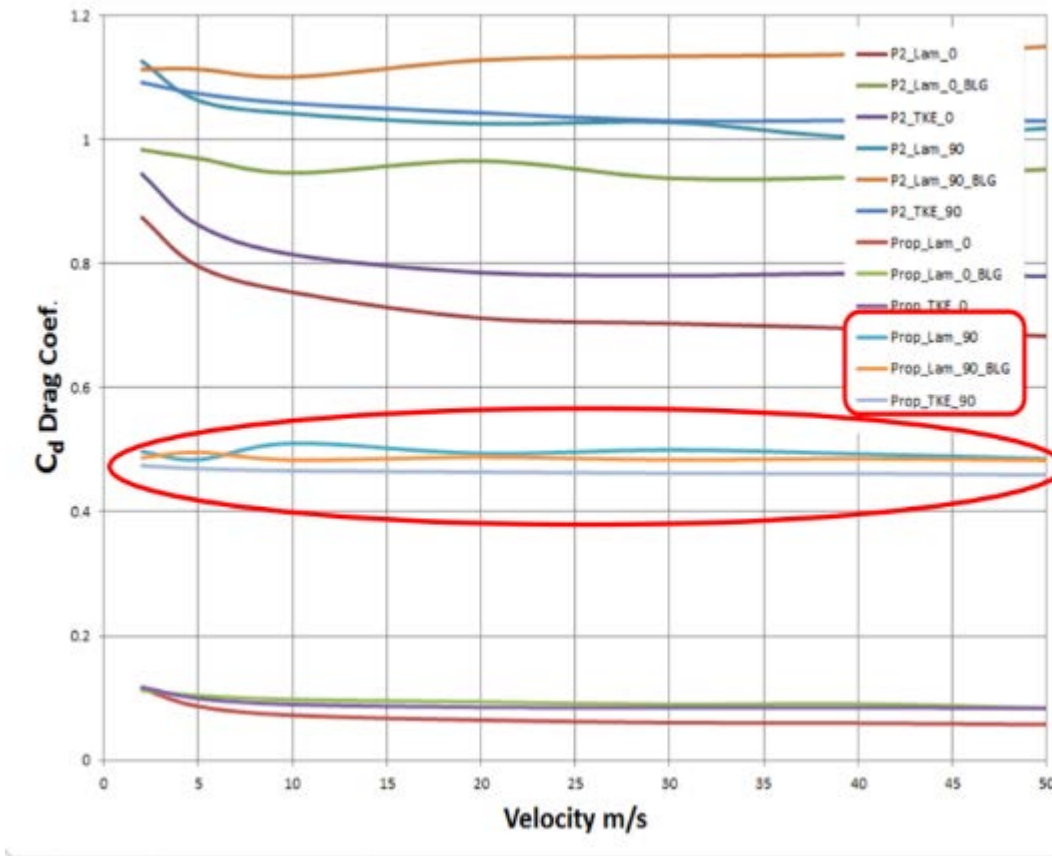


Figure 40 - Plot of Drag Coefficient Versus Airspeed for Phantom 2 CFD Simulations

Based on anecdotes from platform developers, wind milling may only be possible in aircraft that uses gearing between the motor and the prop in order to increase the prop RPM. The gearing, when working in reverse as the prop is driven by air, provides more torque for the prop acting to turn the motor against its poles. Again, that is an assumption based on limited discussions. The next important phenomenon observed during the limited flight test was that the aircraft remained virtually level during its fall. It can be assumed that there may be some amount of tumbling if the aircraft fails during maneuvering flight, but when the Phantom 2 lost power at a hover, it remained level in a steady state fall as shown in Figure 41. This flight test data depicts the results of one out of three power off tests completed. While this helps verify trends and validate modeling inputs, it cannot be considered statistically significant at this point. Additionally, the jagged appearance of the plots in Figure 41 clearly indicates that data logging procedures and equipment need refinement prior to more flights.

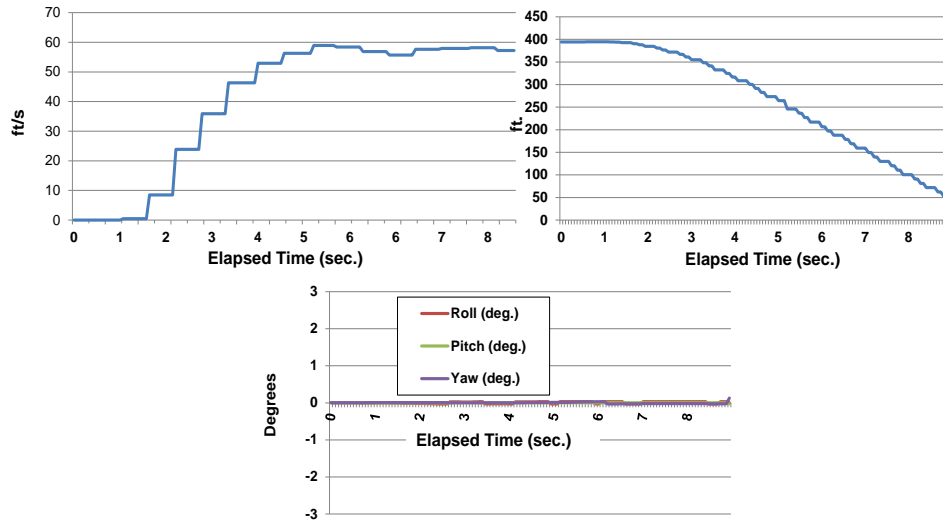


Figure 41 - Phantom 2 Limited Flight Test Telemetry Data; Rate of Descent vs. Time (upper left), Altitude vs. Time (upper right), and Attitude vs. Time (lower)

Based on the improved modeling inputs and verification of the accuracy of the ballistic model, it was possible to use vehicle parameters (A_{eff} , C_d , and MGTOW) to calculate velocities (terminal and otherwise) and impact KE values. The results of this modeling have been extended to a parametric relationship between MGTOW and terminal KE. This relationship has been developed for fixed wing aircraft and multi-rotor aircraft. However, it has not been developed for helicopter style rotary wing UAS. The multi-rotor relationship is considered to be the most accurate because there were more suitable images available for use in calculating effective area. For the other aircraft categories, the effective area was simply calculated by taking the length and width data from the AUVSI database, calculating a “plane” (for fixed wing) or motor-to-motor circular area (for rotary wing), and applying an area ratio (0.3 for multi-rotors, 1.0 for flying wings, and 0.65 for standard fixed wing configurations).

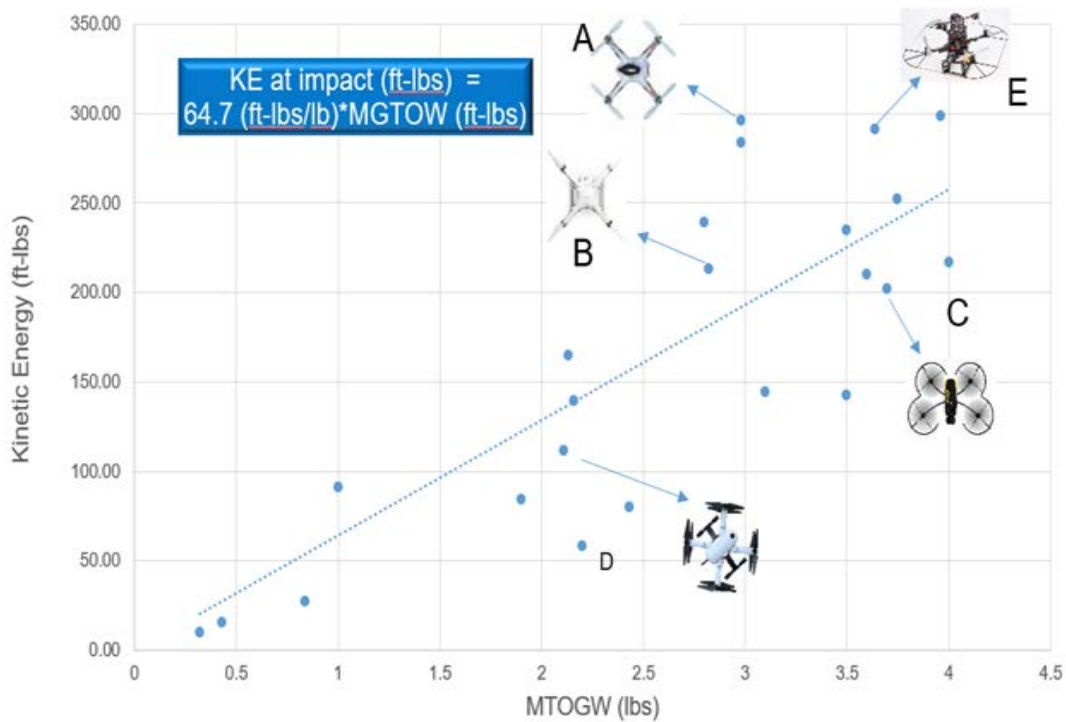


Figure 42 - Relation of MGTOW to KE at Terminal Velocity for Multi-Rotor UAS <4.4 lbs

Based upon this analysis, the A4 team developed slopes of KE versus MTOGGW and compared the values to actual sUAS platforms to determine general characteristics of KE as a function of aircraft weight for both rotary and fixed wing platforms. These plots are shown in Figure 42 and Figure 43. A linear curve fit of the aircraft terminal KE based on MGTOW shows that, on average, multi-rotor aircraft will have 64.7 ft-lbs of terminal KE per pound of weight at terminal velocity. Even a 1 lbs multi-rotor aircraft can exceed the RCC threshold for 50% POF due to head injury if the collision occurs at the center of mass of the vehicle and all the energy is absorbed by the person with a perfect energy transfer. This type of collision is obviously very rare. Figure 43 shows that, on average, a fixed wing sUAS in a dive at terminal velocity, which assumes a flight control malfunction or damaged lifting/control surfaces, has 287 ft-lbs of KE per pound of weight at terminal velocity. This analysis does not pertain to fixed wing aircraft at glide airspeed that remain under control without power.

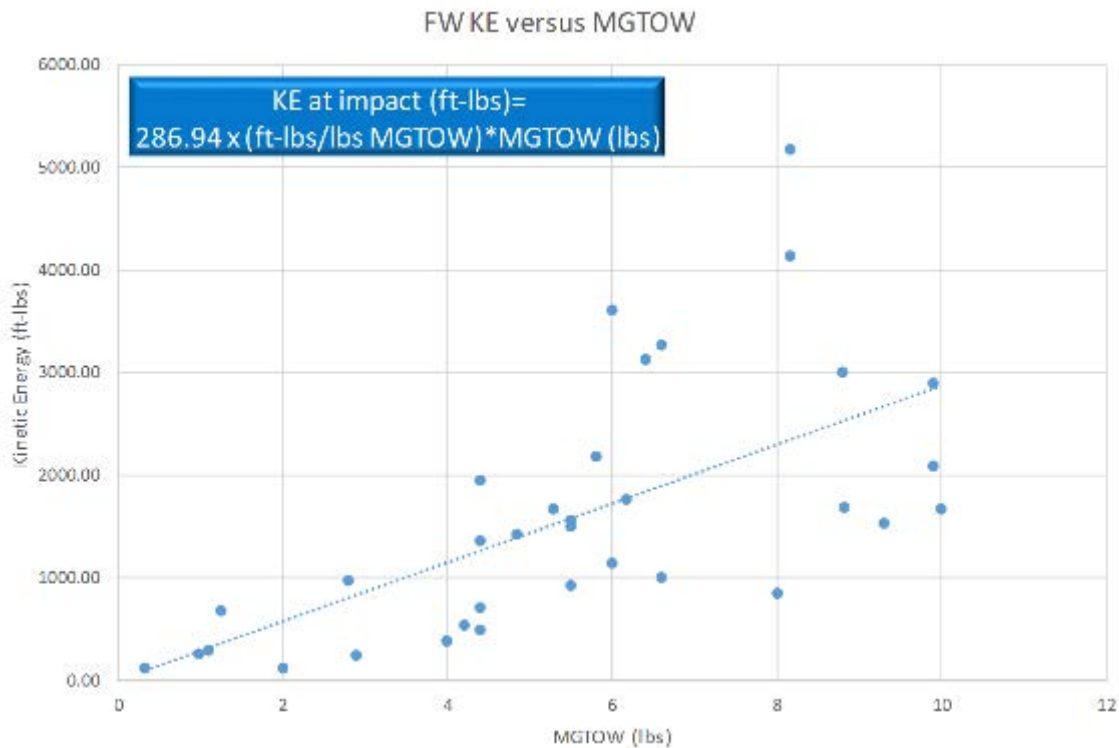


Figure 43 - Relation of MGTOW to KE at Terminal Velocity for Fixed Wing UAS < 10 lbs

Knowledge Gap: The fixed wing sUAS parametric information used to generate the Terminal KE to MGTOW relation is of lower quality than the input data used for the multi-rotor analysis. The quality of this analysis can be improved by obtaining CAD files and/or better imagery (vertical planform and head-on images) for fixed wing aircraft and running CFD analysis on both a standard configuration and a flying wing platform. The A4 team plans to focus on improving fixed wing aircraft modeling during the second half of this project.

4.15. Head Impact Modeling (MSU)

4.15.1. Design of Experiments

To reduce the number of simulations needed for head impact simulations a Design of Experiments (DOE) method was used. Using Taguchi's L16 (Type B) Array, 5 variable will be assessed: Location, velocity, offset mass, and two angles.¹²¹ While there will be slight geometrical dependence in the variables, this initial study provides insight into the sensitivity of the variables. The L16 simulation array is shown in Table 42. The UAS used in this study is the DJI Phantom 3.

¹²¹ Taguchi, Genichi, The System of Experimental Design, Vol 2, Quality Resources, pg 1169, 1987.

Table 42 - L16 Orthogonal Array for DJI Phantom 3

Simulation No.	Location	Velocity (m/sec)	Offset (cm)	Mass (g)	Angle (deg)
1	Front	4	0	1280	-30
2	Front	8	5	1360	0
3	Front	16	10	1440	15
4	Front	24	15	1520	30
5	Back	4	5	1440	30
6	Back	8	0	1520	15
7	Back	16	15	1280	0
8	Back	24	10	1360	-30
9	Top	4	10	1520	0
10	Top	8	15	1440	-30
11	Top	16	0	1360	30
12	Top	24	5	1280	15
13	Side	4	15	1360	15
14	Side	8	10	1280	30
15	Side	16	5	1520	-30
16	Side	24	0	1440	0

4.15.2. Finite Element Analysis – Analysis of DOE

Using the DOE, 16 finite element simulations were completed using the FE solver Abaqus/Explicit. The mesh/geometry (Figure 46) of the human head is comprised of five distinct materials: Skin, cortical bone, cancellous bone, cerebrospinal fluid (CSF), and the brain. The brain constitutive responses in the simulations are determined by a viscoelastic-viscoplastic internal state variable model.^{122,123} The other four materials are models with only elastic properties. These properties are listed in Table 43. The DJI structural material was assumed to be ABS plastic. The elastic properties of ABS are also listed in Table 43.

For the skull, a 3-layered cortical-cancellous-cortical layup was defined. The cortical bone is dense and stiff and the inner cancellous bone is porous, less dense, and less stiff. Because the CSF has such a low shear modulus, all sections (skull, brain, CSF) are assumed to be tied together for the simulation. The brain and Phantom 3 mesh (Figure 46) are comprised of 1,248,377 and 162,522 three-dimensional tetrahedral solid elements, respectively.

To visualize the elastic properties and deflection of the drone, Figure 44 is provided. In Figure 44, the drone at various time steps is superimposed to show the amount of deformation due to an offset frontal impact (Simulation #4 from Table 42). This level of deformation is comparable to the level of deformation observed during the NIAR drop-testing (Figure 45). The drone, along with the head mesh for this same simulation, can be seen in Figure 46. The maximum principle strain in the drone during the impact in Simulation #4 was around 5%, which is about large

¹²² Bouvard, J. L., D. K. Ward, D. Hossain, E. B. Marin, D. J. Bammann, and M. F. Horstemeyer. 2010. "A General Inelastic Internal State Variable Model for Amorphous Glassy Polymers." *Acta Mechanica* 213 (1-2): 71–96. doi:10.1007/s00707-010-0349-y.

¹²³ Prabhu, R., Horstemeyer, M.F., Tucker, M.T., Marin, E.B., Bouvard, J.L., Sherburn, J.A., Liao, Jun, Williams, Lakiesha N., "Coupled experiment/finite element analysis on the mechanical response of porcine brain under high strain rates," *Journal of the Mechanical Behavior of Biomedical Materials*, Vol. 4, 1067–1080, 2011.

enough where it is important to use non-linear material constitutive equations. The FEA model used by MSU was based on vehicle geometry and material properties, but the elastic and plastic deformation response to loading has not been experimentally validated. In order to understand and quantify polymeric deformation properties, physical testing on the material would need to be performed.

Table 43 - Elastic Material Properties for UAS Impact Simulation

Material	Density (kg/m ³)	Elastic Modulus (MPa)	Poisson Ratio
Skin ¹²⁴	1200	16.7	0.42
Cortical Bone ^{125,126,127}	2000	10000	0.22
Cancellous Bone ^{125,126,127}	1000	390	0.19
CSF ^{128,129,130}	1040	0.299	0.496
ABS Plastic	1070	2500	0.35

¹²⁴ Horgan, T J, and M D Gilchrist. 2003. "The Creation of Three-Dimensional Finite Element Models for Simulating Head Impact Biomechanics." *International Journal of Crashworthiness* 8 (4): 353–66. doi:10.1533/ijcr.2003.0243.

¹²⁵ Boruah, S., K. Henderson, D. Subit, R.S. Salzar, B.S. Shender, and G. Paskoff. 2013. "Response of Human Skull Bone to Dynamic Compressive Loading." *Proceedings of the IRCOBI Conference*.

¹²⁶ Bayraktar, Harun H., Elise F. Morgan, Glen L. Niebur, Grayson E. Morris, Eric K. Wong, and Tony M. Keaveny. 2004. "Comparison of the Elastic and Yield Properties of Human Femoral Trabecular and Cortical Bone Tissue." *Journal of Biomechanics* 37 (1): 27–35. doi:10.1016/S0021-9290(03)00257-4.

¹²⁷ McElhaney, James H., John L. Fogle, John W. Melvin, Russell R. Haynes, Verne L. Roberts, and Nabih M. Alem. 1970. "Mechanical Properties of Cranial Bone." *Journal of Biomechanics* 3 (5): 495–511. doi:10.1016/0021-9290(70)90059-X.

¹²⁸ Zhang, L., K. H. Yang, R. Dwarampudi, K. Omori, T. Li, K. Chang, W. N. Hardy, T. B. Khalil, and A. I. King. 2001. "Recent Advances in Brain Injury Research: A New Human Head Model Development and Validation." *Stapp Car Crash Journal* 45 (November): 369–94.

¹²⁹ Mao, Haojie, Liying Zhang, Binhui Jiang, Vinay V. Genthikatti, Xin Jin, Feng Zhu, Rahul Makwana, et al. 2013. "Development of a Finite Element Human Head Model Partially Validated with Thirty Five Experimental Cases." *Journal of Biomechanical Engineering* 135 (11): 111002. doi:10.1115/1.4025101.

¹³⁰ Tse, Kwong Ming, Long Bin Tan, Shu Jin Lee, Siak Piang Lim, and Heow Pueh Lee. 2015. "Investigation of the Relationship between Facial Injuries and Traumatic Brain Injuries Using a Realistic Subject-Specific Finite Element Head Model." *Accident Analysis & Prevention* 79 (June): 13–32. doi:10.1016/j.aap.2015.03.012.

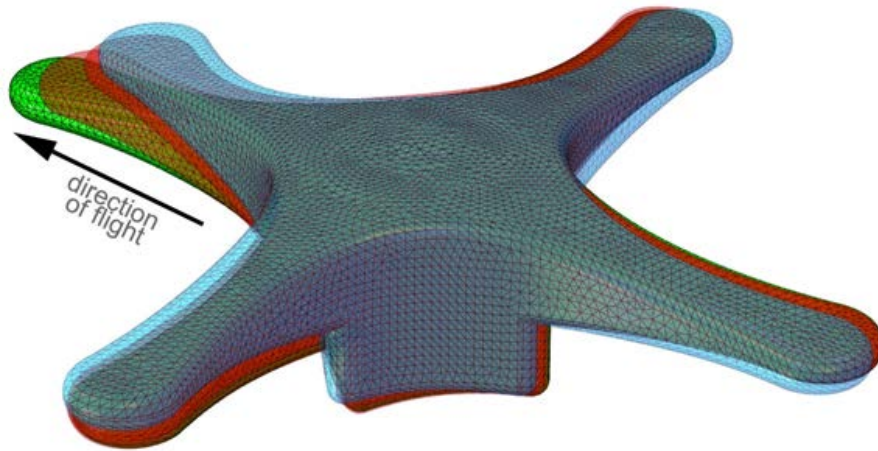


Figure 44 - Deflection of the Drone during Simulation #4. The colors represent the following time steps: Green 0 ms, Orange 0.5 ms, Red 1 ms, Blue 1.5 ms.

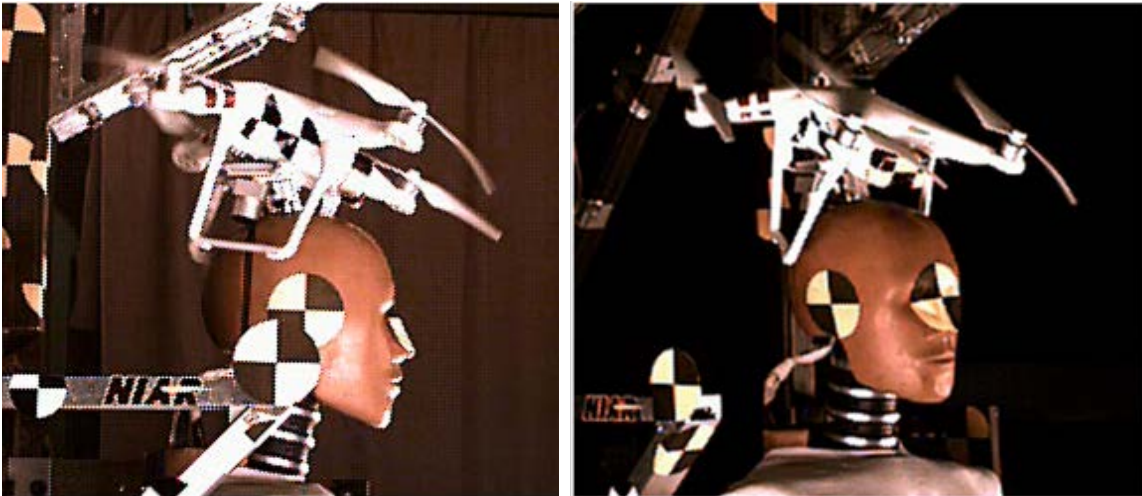


Figure 45 - Phantom 3 Standard Fuselage Deformation During NIAR 50-foot Drop Test Impacts (Test UA17A-13)

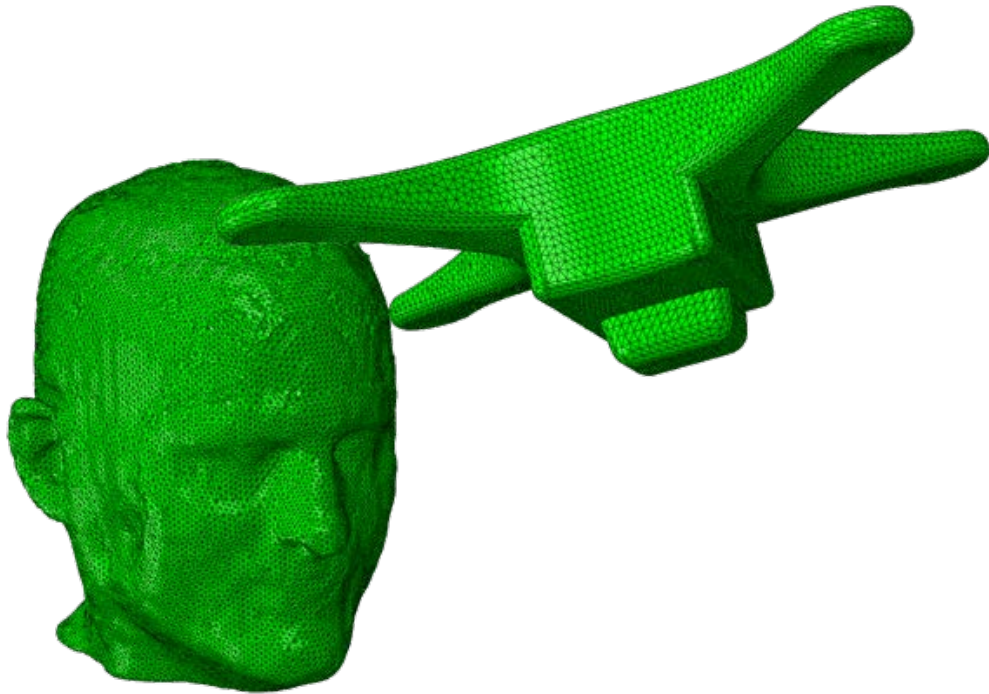


Figure 46 - Mesh of the Human Head and Phantom 3

4.15.3. Head Impact Results and Discussion

For all sixteen simulations in the DOE, the accelerations at the center of gravity were recorded, shown in Figure 48. The raw data (red) was smoothed (blue) using a first order local regression method with a span of 10%. These acceleration–time curves were then inputted into a Radial Basis Function Network (RBFN). As the DOE was created using a non-numeric method (“Front”, “side”, “back”, and “top”), the Location parameter had to be converted to a numeric spherical coordinate system. Using the center of gravity as the origin for the coordinate system, the updated location variables are listed in Table 44. Figure 47 provides a visual representation of the spherical coordinate system. The simulation was conducted with a head model that was constrained at the base of the head, which takes out neck dynamics and energy absorption and may result in high brain CG accelerations that result from modeling assumptions. Additionally, the UAV model does not have blade guards installed or rotors, so it represents a worst possible impact. With blades and blade guards installed, the aircraft will make initial contact with a guard or a blade and induce rotation of the vehicle. Based on the NIAR drop testing results and discussion, (Section 4.8.3) it is known that offset impacts that impart vehicle rotation result in lower impact loading and energy transfer.

Table 44 - Conversion from Named Locations to Spherical Coordinates

Location	Radius (r)	Angle 1 (θ) deg	Angle 2 (φ) deg
Front	1	0	90
Back	1	180	90
Top	1	0	0
Side	1	90	90

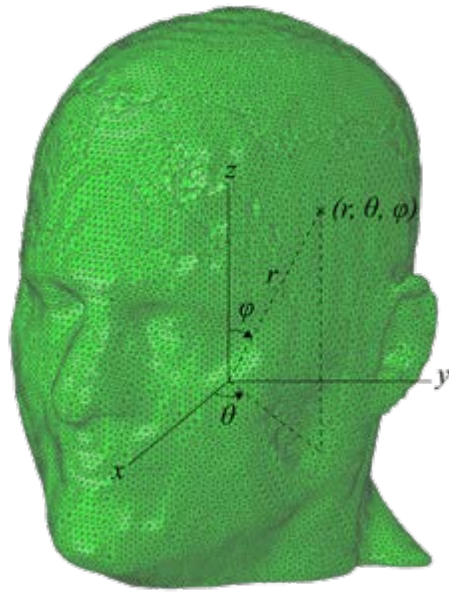


Figure 47 - Spherical Coordinate System for Head Impact Simulations

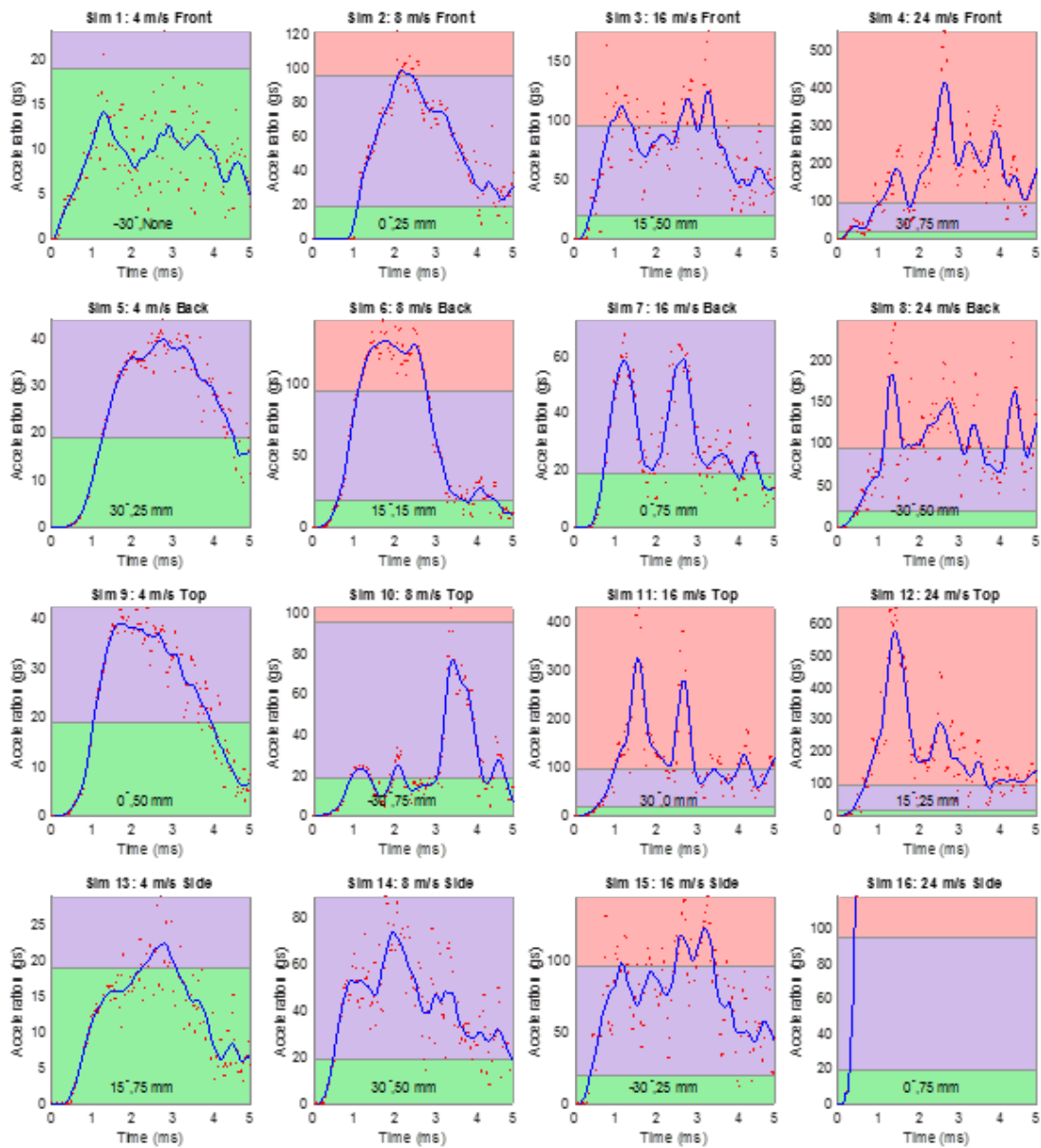


Figure 48 - Acceleration vs Time History for DOE Simulations

From Figure 48, one can observe that for many human head-UAV impact scenarios, the peak acceleration is above 95 Gs (Please see Figure 48: Sims. 2, 3, 4, 6, 8, 10, 11, 12, 15, and 16). In considering the severity of the impact as measured through acceleration in the human brain, during impact, a few of the impact scenarios yielded a peak acceleration that was greater than 150 Gs (Please see Figure 48: Sims. 4, 8, 11, 12 and 16). In correlating the G values in the brain to an injury scale, the Abbreviated Injury Scale (AIS) is an accepted metric for rating injury

severity from impact scenarios. AIS was initially created to ascertain injuries in automobile crashes in the 1970s.^{131'132'133}

Since its conception, AIS has had several revisions, and the current version has been consistently used in trauma centers to assess the injury metric level.¹³⁴ In the latest version of the AIS, a value of 1 indicates minor injury, which normally corresponds to 19 G's as garnered from sports related impact studies and the associated Traumatic Brain Injury (TBI).^{135'136'137} An AIS value of 3 corresponds to serious injury (often resulting in concussion) and 95 Gs. Lastly, AIS values of 5 and 6 indicate critical injuries that are often lethal. So, in Figure 48, impact scenario simulation cases 2, 3, 4, 6, 8, 10, 11, 12, 15, and 16 render to an AIS value of 3 or more. These simulation scenarios indicate that the human subject would have a high probability of concussion from a UAS impact. AIS values of 5 or 6, which are associated with the highest mortality rates, as observed in impact scenario simulations 4, 8, 11, 12 and 16, would impact the human subject's head with deadly force. Essentially, from the simulation results in Figure 48 (Sims. 2, 3, 6, 10 and 15), it can be observed that a UAV (DJI Phantom 3) impact velocity of 8 m/s or more to the head would lead to concussion in the human subject, with AIS values ranging from 3 – 4. Further, the velocities that pertain to UAV, as being the threshold for lethality are 24 m/s or above for impacts occurring on the front, back and side of the human head. However, for the case of top impacts to the human head, the lethal velocity goes down to 16 m/s (Figure 48; Sims. 11 and 12). As such, UAV velocities of around 4 m/s are the only cases (Figure 48; Sims. 1, 5, 9, and 13) where the injury metric does not indicate any concussions.

¹³¹ Committee on Medical Aspects of Automotive Safety, "Rating the severity of tissue damage. I. The abbreviate scale," *JAMA*, Vol 215, 277-280, 1971.

¹³² States, J., Fenner, H., Flamboe, E., Nelson, W. et al., "Field Application and Research Development of the Abbreviated Injury Scale," *SAE Technical Paper 710873*, 1971.

¹³³ Baker, Susan P., O'Neill, Brian, Haddon, William, Jr., Long, William B., "The injury severity score: a method for describing patients with multiple injuries and evaluating emergency care," *Journal of Trauma and Acute Care Surgery*, Vol. 14, 187-196, 1974.

¹³⁴ Senkowski, Christopher K., McKenney, Mark G., "Trauma scoring systems: a review," *Journal of the American College of Surgeons*, Vol. 189, 491-503, 1999.

¹³⁵ Rowson, Steven, Duma, Stefan M., "Development of the STAR Evaluation System for Football Helmets: Integrating Player Head Impact Exposure and Risk of Concussion," *Annals of Biomedical Engineering*, Vol. 39, 2130-2140, 2011.

¹³⁶ Rowson, Steven, Duma, Stefan M., Beckwith, Jonathan G., Chu, Jeffrey J., Greenwald, Richard M., Crisco, Joseph J., Brolinson, P. Gunnar, Duhaime, Ann-Christine, McAllister, Thomas W., Maerlender, Arthur C., "Rotational Head Kinematics in Football Impacts: An Injury Risk Function for Concussion," *Annals of Biomedical Engineering*, Vol. 40, 1-13, 2012.

¹³⁷Vos, P. E., Battistin, L., Birbamer, G., Gerstenbrand, F., Potapov, A., Prevec, T., Stepan, Ch. A., Traubner, P., Twijnstra, A., Vecsei, L., Wild, K. von, "EFNS guideline on mild traumatic brain injury: report of an EFNS task force," *European Journal of Neurology*, Vol. 9, 207-219, 2002.

Due to the need to give two variables to quantify the location, the Taguchi DOE array can provide first order solution. The resolution of the DOE is too low for 6 factors with 4 levels as there is virtually no confounding factors, only main effects. However, the best reproduction that the multi-quadric RBFN could reproduce with minimal error is shown in Figure 49. What this tool enables users to do is to input any loading scenario and get a resultant acceleration–time curve, as shown in Figure 49. The black curve represents the simulation g-force and the red curve is the reproduction of the same test using only the meta-model with the variables corresponding to Simulation 15. For this particular case, the model under-predicts the acceleration.

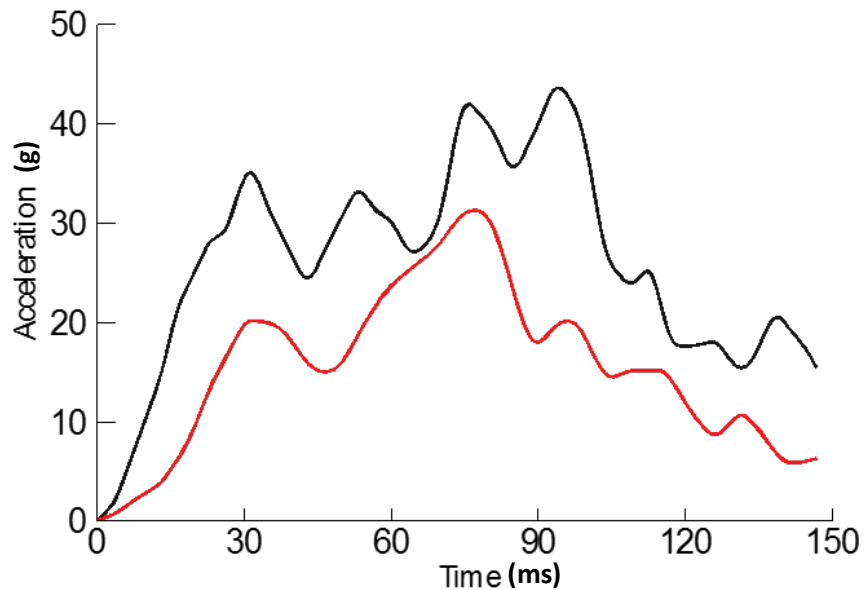


Figure 49 - RBFN Result Using a Multiquaric Minimization Approach

To visualize the stress wave traveling through the head due to the impact, the four images in Figure 50 and Figure 51 are provided. Figure 50 shows the propagation of the von Mises stress through the skull at various time increments. The stress history in the brain (Figure 51) shows an expected wave and distinct coup and countercoup locations.

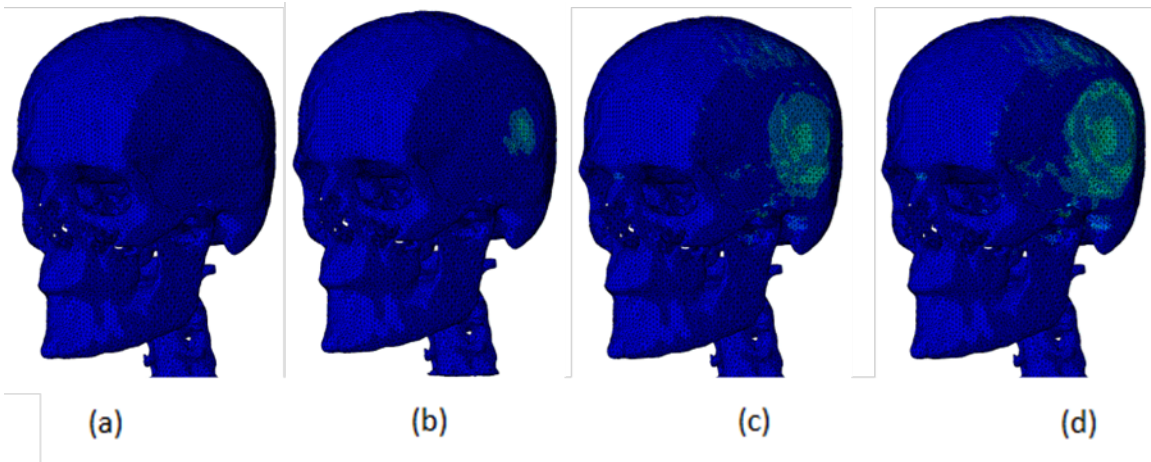


Figure 50 - Stress Wave (von Mises) Propagation through the Skull at Times (a) 0, (b) 0.375, (c) 1, and (d) 1.275 ms

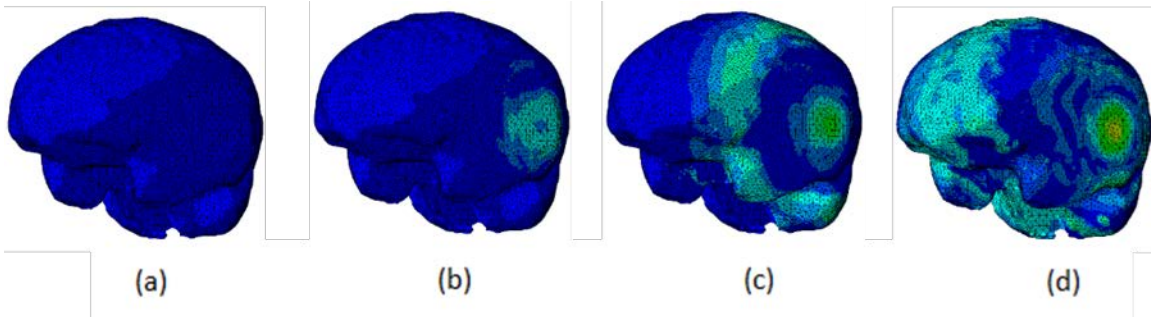


Figure 51 - Stress Wave (von Mises) Propagation through the Brain at Times (a) 0, (b) 0.19, (c) 0.5, and (d) 0.813 ms

4.16. Study of Primary Impact Criteria (ERAU)

To model the ground collision of specific UAS with known masses, two key parameters need to be considered and varied during simulation: (1) impact velocity V and (2) impact angle θ , which is defined as the angle between the head of UAV and vertical direction (z -axis) in a three dimensional coordinate system, as shown in Figure 52.

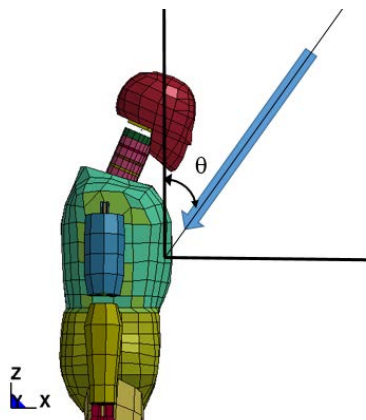


Figure 52 - Coordinate System Definition in the Ground Collision Analysis

Based on the literature review, we can reasonably suggest that θ is in the range of $30^\circ \sim 90^\circ$. The expected impact velocity values are determined by the type and mass of UAS, as well as impact scenarios, i.e. unpremeditated descent scenario (UDS) and loss of control (LCS). In UDS, the expected velocity range is $10 \sim 15$ m/s ($32.8 \sim 49.2$ ft/s), while the velocity in LCS can be up to 30 m/s (98.4 ft/s). In this study, the range of impact velocity is assumed to $5 \sim 30$ m/s ($16.4 \sim 98.4$ ft/s).

Two typical UAS, including one fixed wing (GZ500) and one rotary wing (DJI Phantom 3) vehicle, have been modeled in this study. The finite element modeling started from the CAD models, which describe the profiles of UAS in the IGES format. A meshing tool, HyperMesh¹³⁸ was used to process the CAD models and convert them to finite elements, which are shown in Figure 53 and Figure 54, respectively. The average mesh size is 5 mm. Although the UAS geometry is highly consistent with the physical model, no impact test data are available to validate the model response. A detailed model verification/validation will be performed in the future once the data is available.



Figure 53 - (Left) CAD model and (Right) FE Model for a Fixed Wing UAS GZ500

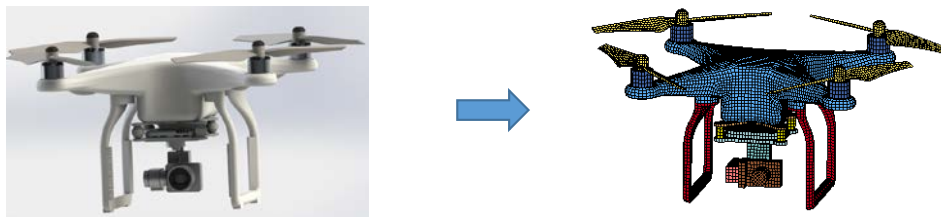


Figure 54 - (Left) CAD model and (Right) FE model with details for a rotary wing UAS Phantom 3

In this study, a numerical Anthropomorphic Test Device (ATD) model was used to study the human body response subjected to the UAS impact. The ATD or Crash Test Dummy is a calibrated test instrument used to measure human injury potential in vehicle crashes. It simulates human response to impacts, accelerations, deflections, forces and moments generated during a crash. A number of ATD FE models have been developed and widely used in the crash safety area. The UAS and ATD models were integrated to simulate their interaction.

All of the simulations were conducted using commercial FEA package LS-DYNA¹³⁹ (Version 971R4), which is widely applied to simulate non-linear, dynamic problems associated with large deformation and impact. In this study, both types of UAS were considered. Each type of UAS were assumed to be made from two different materials, i.e. aluminum alloy and engineering plastic, respectively, to investigate the influence of materials. Therefore, four scenarios were simulated. The configurations of four models are listed in Table 45. In each

¹³⁸ <http://www.altairhyperworks.com/product/HyperMesh>

¹³⁹ <http://www.lstc.com/products/ls-dyna>

scenario, two key parameters- the impact angle θ and velocity V , varied in a certain range. A typical model predicted UAS/ATD interaction event is shown in Figure 55 ($\theta=80^\circ$; $V = 18$ m/s (59.1 ft/s)). The result shows that the impact causes a large indentation on the chest. The torso and UAS are separated after the contact completes and the ATD starts a global motion.

Table 45 - Configurations of the Four FE UAS Models

Model #	1	2	3	4
Material	Aluminum	Engineering plastic	Aluminum	Engineering plastic
Type	Fixed wing	Fixed wing	Rotary wing	Rotary wing
Wall thickness (inch)	0.04	0.04	0.04	0.08
Mass (lb)	5.7	3.1	3.1	3.1

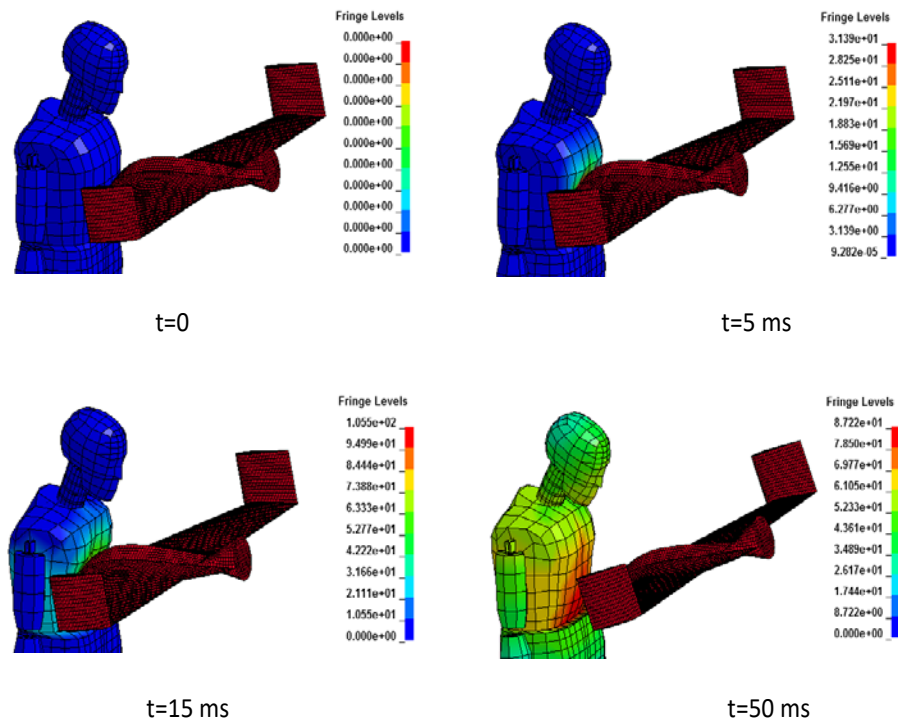


Figure 55 - Typical ATD/UAS Interaction Simulated with the FE Model

NOTES: (UAS type: GZ500; Material: Aluminum alloy; $\theta=80^\circ$ $V=18$ m/s (59.1 ft/s))
Fringe: Displacement in mm

A large number of simulations were carried out with different combinations of UAS type, material, as well as θ and V values. The energy absorption by torso and VC values were calculated and listed in Table G - 1, Table G - 2, Table G - 3 and Table G - 4. The relationship between energy transfer to the torso, VC, and impact parameters are graphically illustrated in

Figure 56. Experimental data¹⁴⁰ show that when $VC=1.3$ m/s, the probability of chest injury of $AIS>4$ is 50%. Therefore, $VC=1.3$ m/s is regarded as the threshold of fatal/non-fatal injuries. In all of the cases, the VC value increases with impact angle θ and impact velocity. For two UAS with the same material (engineering plastic) and same mass (3.1 lb), the rotary wing vehicle causes higher VC due to its thicker wall and lesser degree of deformation. The aluminum fixed wing UAS is riskier than its engineering plastic counterpart with the same wall thickness since it is heavier and stiffer. In the comparison of two rotary wing UAS with the identical mass, the engineering plastic one produces higher VC. This is, again, due to its higher wall thickness. Similar trends can be observed on the energy absorption by the chest. The amount of energy transferred to the torso increases with impact angle and velocity, and the wall thickness has been found to be an important factor. To reduce the injury and energy transfer to the human body by UAS, a lightweight, low stiffness material with smaller wall thickness is desired.

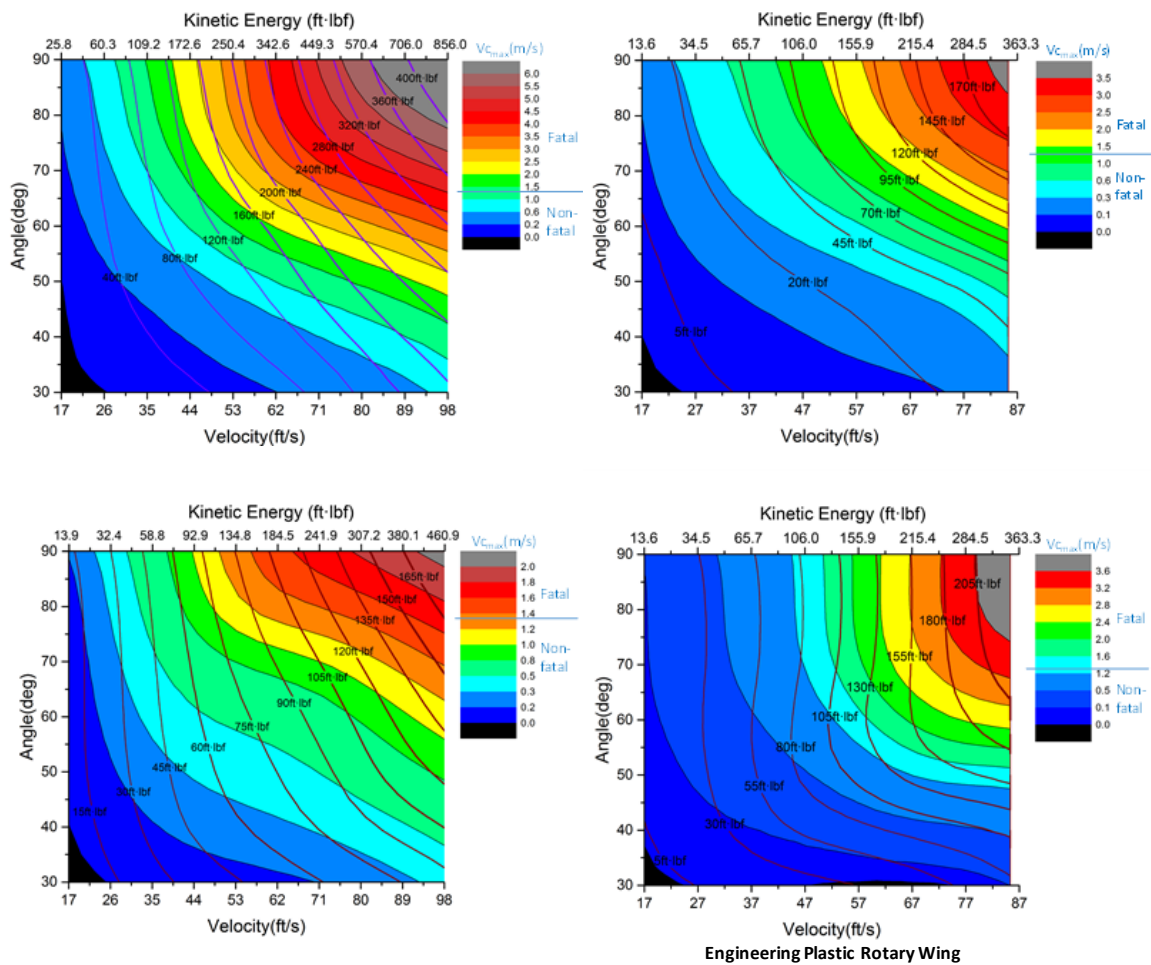


Figure 56. Contour Diagrams Showing the Relationship between Energy Absorption by Torso and VC Values and Impact Parameters (UAS type; material; θ and V)

¹⁴⁰ Viano D, Lau IV (1985), Thoracic impact: a viscous tolerance criterion, Proc. 10th Intern. Techn. Conf. on Experimental Safety Vehicles, pp. 104-114.

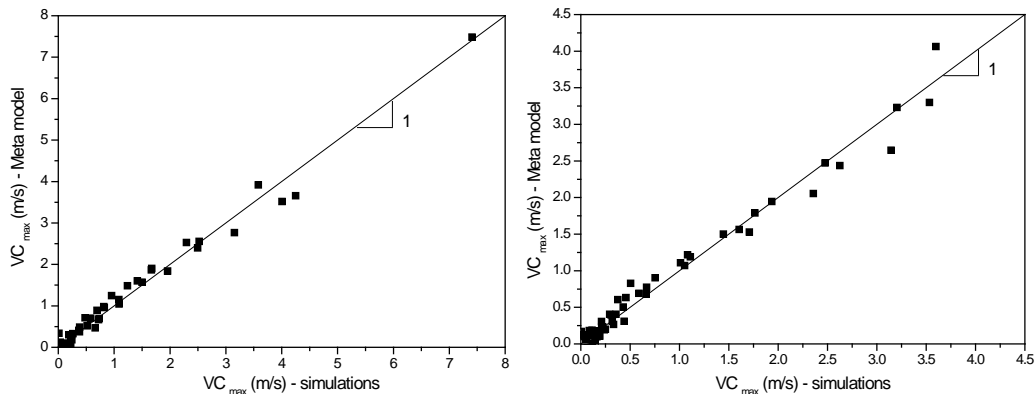
The response of VC to variation of impact parameters can be described with a surrogate or meta model, which is a linear or nonlinear function. Here, a polynomial equation is used, which is written in the following form:

$$VC_{\max} = a + bx_1 + cx_2 + dx_1x_2 + ex_1^2 + fx_2^2 + gx_1^3 + hx_2^3 + ix_1x_2^2 + jx_1^2x_2 \quad \text{Equation 19}$$

where x_1 and x_2 are normalized impact angle ($\theta/180^\circ$) and velocity ($V/50$ m/s ($V/164.0$ ft/s)), respectively. A, b, c, d, e, f, g, h, i, j are constants determined from the curve fitting, and listed in in Appendix H.

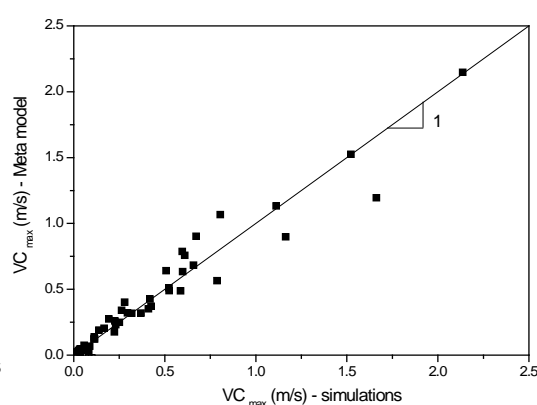
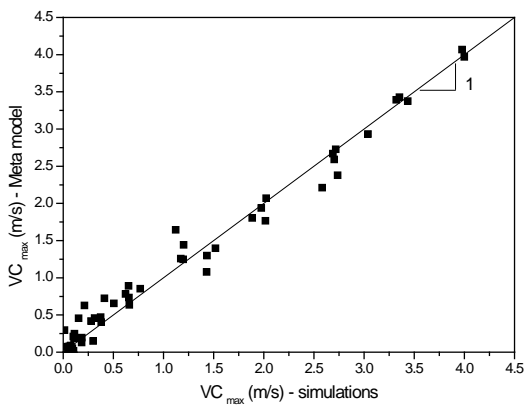
The response predicted using Equation 19

is compared with the data directly obtained from simulations in Figure 57 to validate the meta model. The data points are close to the diagonal line with the slope of 1, which indicates a good agreement.



Aluminum; fixed wing

Engineering plastic; fixed wing



Aluminum; rotary wing

Engineering plastic; rotary wing

Figure 57 - Comparison of the VC results predicted by the meta model and numerical simulations.

4.16.1. Study of Secondary Impact Criteria (ERAU)

After a UAS collides with the ground, it may bounce back at a considerable speed and cause injury or fatality. The impact sequence is described graphically in Figure 58. Analyses combining

numerical simulations and theoretical modeling were conducted to predict the rebound distance R , and then the safe range of personnel on the ground can be estimated.

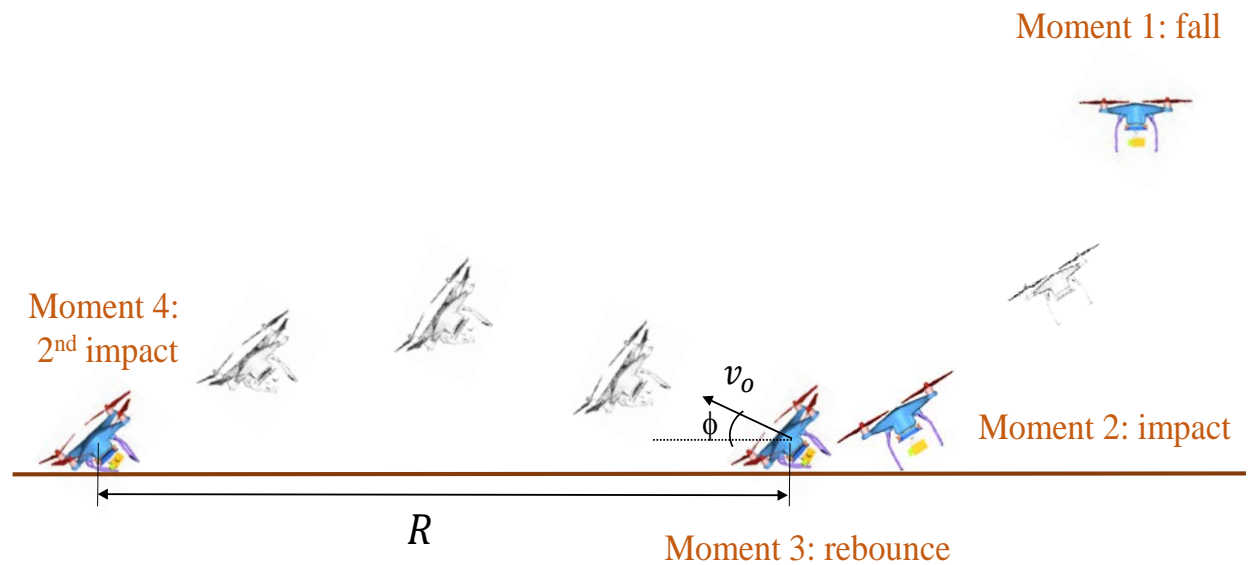


Figure 58 - UAS Collision on the Ground and Rebound

In this procedure, after the first ground collision takes place, the rebound takes a relatively long time, up to several seconds. Simulating such motion of UAS between two impact moments is highly time consuming. If we need to consider a large number of combinations of UAS type, material, mass, impact angle and speed, conducting numerical simulations alone may not be realistic. Instead, a two-step strategy was used. In step one, numerical simulations are performed to model the first impact and predict the rebound angle ϕ and impact velocity v_0 . Based on the information obtained, in step two, an empirical equation is employed to predict rebound distance R without running numerical simulations. Figure 58 shows a simulated typical motion pattern of the rotary UAS after the impact with rigid ground (i.e. step 1). The impact velocity is 10 m/s (32.8 ft/s) and angle is 60° .

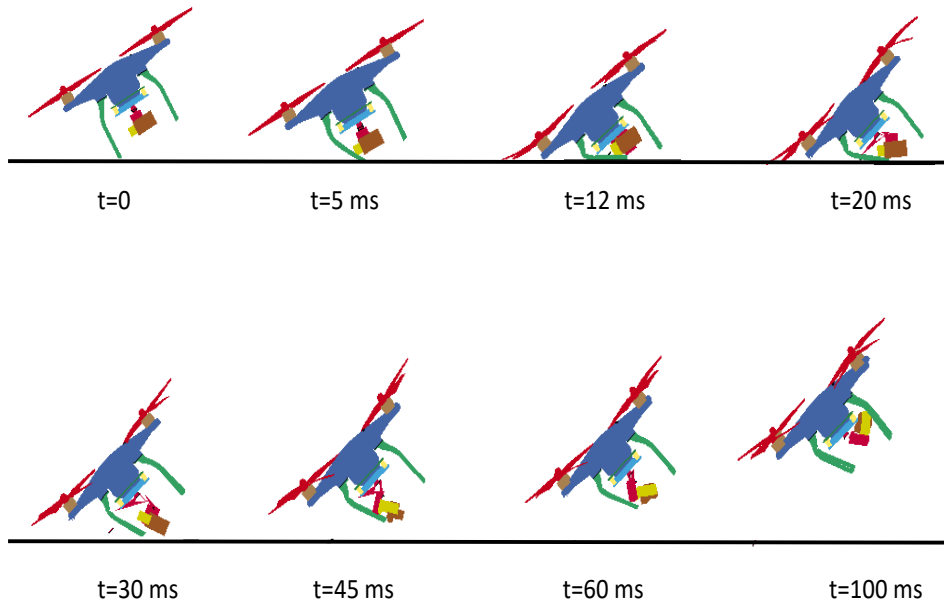


Figure 59 - Model Predicted Rebound Behavior of a Rotary Wing UAS (Phantom 3) Collision on the Ground ($V=32.8$ ft/s; $\theta=60^\circ$)

The empirical equation applied in step 2¹⁴¹ was initially developed to model the ballistic trajectory of a projectile after the propulsive force is terminated and the body is acted upon only by gravity and aerodynamic drag. Here, the equation was applied to predict the bounce behavior of UAS, which has the motion similar to a projectile. The equation reads

$$R = \frac{m}{k} \left(\ln \left(\frac{kTv_0 \cos \phi + m}{m} \right) \right) \quad \text{Equation 20}$$

where m is mass; k is drag coefficient; T is the time of rebound; v_0 and ϕ are rebound velocity and angle, respectively. Parameters k and T can be estimated theoretically⁷, and v_0 and ϕ are calculated using FEA in step 1. With the aforementioned approach, a number of cases were generated using Monte Carlo method and then modeled with the new approach. The results are summarized in Table I - 1, Table I - 2, Table I - 3, and Table I - 4.

Based on the results, meta models were established to describe the relationship between rebound distance and other impact parameters. The meta models were written in the polynomial form as

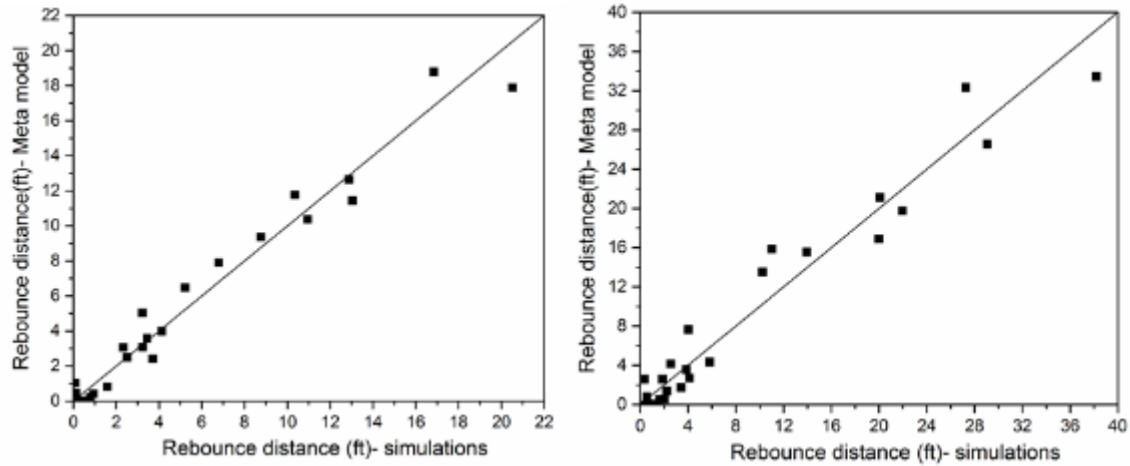
$$Z = a + bx_1 + cx_2 + dx_3 + ex_1^2 + fx_2^2 + gx_3^2 + hx_1x_2 + ix_1x_3 + jx_2x_3 \quad \text{Equation 21}$$

where z is the normalized rebound distance ($R/10$ m (32.8 ft)); x_1 and x_2 are normalized impact angle ($\theta/180^\circ$) and velocity ($V/50$ m (164 ft)) prior to the first impact, respectively; x_3 is the friction coefficient between UAS and ground, which has a significant influence on the results. Constants $a, b, c, d, e, f, g, h, i, j$ were determined by curve fitting their values.

To validate this new approach, several cases were randomly created and simulated without applying the empirical equation. In other words, the whole procedure of these cases was

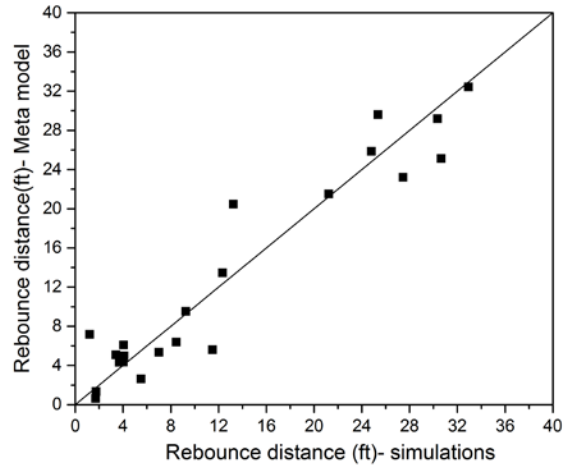
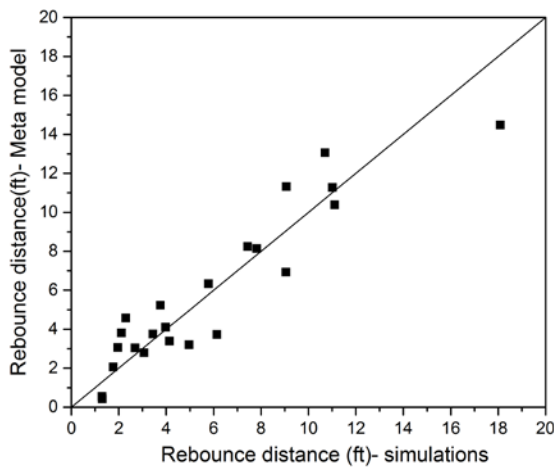
¹⁴¹ Parker GW (1997), Projectile motion with air resistance quadratic in the speed, American Journal of Physics, vol. 45, no. 7, pp. 606–610.

modeled using FEA alone. The simulated rebound distances are compared with the results based on Equation 21 in Figure 60. A reasonable agreement verifies the performance of the new approach.



Aluminum fixed wing

Engineering plastic; fixed wing



Aluminum; rotary wing

Engineering plastic; rotary wing

Figure 60 - Comparison of the Rebound Distance of UAS Predicted by Meta Model and Numerical Simulations

From the results, one can see that material is the most important parameter governing the rebound distance. Two engineering plastic UAS, regardless of the type, have much longer rebound distance than two aluminum UAS. This is due to the higher value of restitution coefficient of plastics. The internal energy generated during the deformation can be converted back to kinetic energy, which causes larger rebound distance. This has been confirmed by the FE model. The results also show that rebound is not sensitive to the type of vehicle, wall thickness or mass. In each type of UAS, a parametric analysis was conducted on all of the three impact parameters, that is rebound angle ϕ , impact velocity v_0 , and coefficient of friction μ . v_0 was found to have the largest correlation to the response, followed by ϕ and μ . Therefore, to reduce the risk of secondary impact, one should select materials with low restitution coefficient for UAS construction.

4.16.2. Study of Penetrating Injury Criteria (ERAU)

The penetrating injury has to be simulated with the human body model rather than ATD model, since the ATD skin is made from synthetic rubber, which is not designed to study the penetration. Besides, the lack of internal organs in the ATD model makes it unsuited for penetrating injury simulations. To resolve this issue, the human torso model with anatomic details was developed. A comparison of ATD torso and human torso model can be seen in Figure 61.

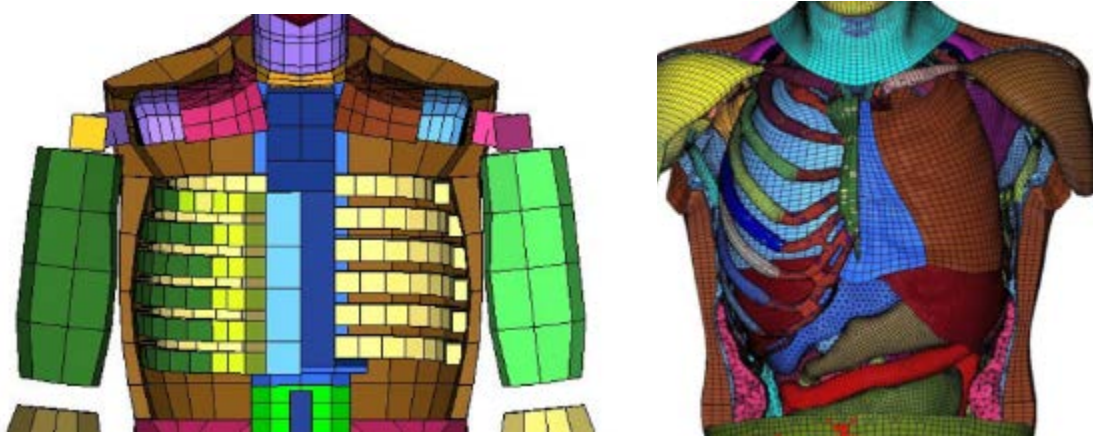


Figure 61 - ATD Torso Model (left) and Human Torso Model (right)

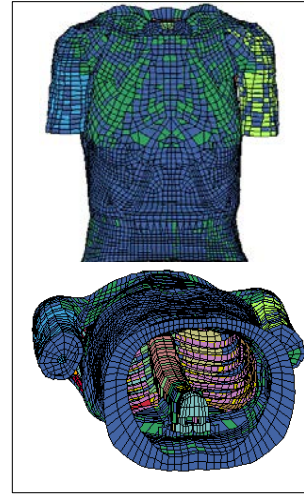
The modeling work started from 2D medical images (CT and MRI), which are available through a visible human project¹⁴². The images incorporate the geometric information of the skeleton of a 50th percentile male adult. An image processing software, Simpleware (Synopsis, Mountain View, CA) was used to segment the images and convert them to a three dimensional geometric model, known as the CAD model. Then a meshing tool, Hypermesh, was used to further convert the CAD model to the finite elements. After that, skin and flesh were added, and then the torso was filled with internal soft tissue. The whole procedure of chest/abdoman modeling is outlined in Figure 62. Mass nodes were attached to the torso model to account for the weight of head, neck and extremities. The material properties of bones and soft tissues are listed in Table 46.

¹⁴² Ackerman MJ (1998). The visible human project. Proceedings of the IEEE, Vol 86, Issue 3, pp. 504-511.

Step 1: Skeleton



Step 2: Skin and flesh



Step 3: Internal soft tissue

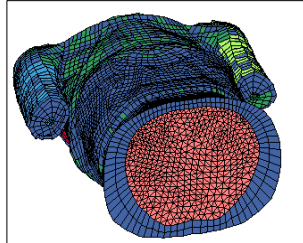


Figure 62. Human Torso Modeling Procedure

Table 46. Material Properties of Bones and Soft Tissues in the Human Torso Model

Material	Structure	Material properties				
Bone	Anatomic components	Density (kg/m³)	Elastic modulus (GPa)	Poisson's ratio	Yield stress (GPa)	Tangent modulus (GPa)
	Rib cortical bone	2000	8	0.3	0.05	--
	Rib spongy bone	1000	0.1	0.3	0.01	--
	Rib cartilage	1000	0.02	0.098	1000	--
	Vertebral disc	1000	0.364	0.3	1000	--
	Vertebral bone	1000	0.364	0.3	1000	--
	Other spongy bones	1099	0.3	0.021	0.055	--
Other cortical bones	2000	11	0.3	0.22	3.66	
Soft tissue	Anatomical components	Density (kg/m³)	Elastic modulus (GPa)	Hysteretic unloading factor	Shape factor for unloading	
	Skin	1100	0.005	0.1	1	
	Anatomical components	Density (kg/m³)	Initial elastic modulus (GPa)	Elastic modulus' exponent	Poisson's ratio	
	Muscle	1000	0.0004	2	0.45	
	Anatomical components	Density (kg/m³)	Elastic modulus (GPa)	Poisson's ratio		
	Internal organs	1000	0.02	0.3		

The aforementioned human torso model was then integrated with the two UAS to simulate the impact response. The loading conditions and impact parameters were consistent with those used in the UAS/ATD collision simulations. Figure 63a and Figure 63b show the simulated deformation response under the impact of a fixed wing and rotary wing UAS, respectively ($\theta=90^\circ$; $V=30$ m/s (98.4 ft/s)). This is an extreme case used to check model robustness and computational stability. The Phantom 3's terminal velocities in the vertical and lateral direction are approximately 60 ft/s falling in a level attitude and 84 ft/s if falling edgewise based on CFD analysis and flight test completed by UAH. The maximum velocity that the Phantom 3 Standard can attain in horizontal flight is 53 ft/s.¹⁴³

¹⁴³ <http://www.dji.com/phantom-3-standard/info#specs>, Accessed 10/6/2016

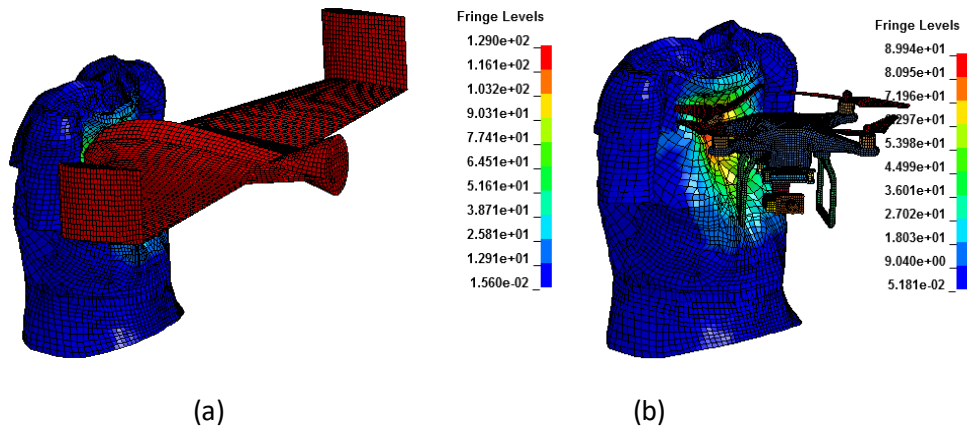
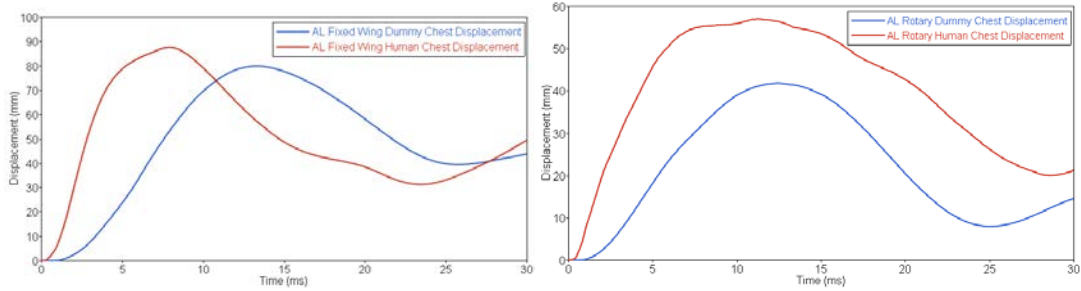


Figure 63 - Model Simulated Typical Deformation Response of Human Torso under the Impact of UAS ($\theta=90^\circ$; $V=30$ m/s (98.4 ft/s)): (a) Aluminum Fixed Wing; (b) Aluminum Rotary Wing

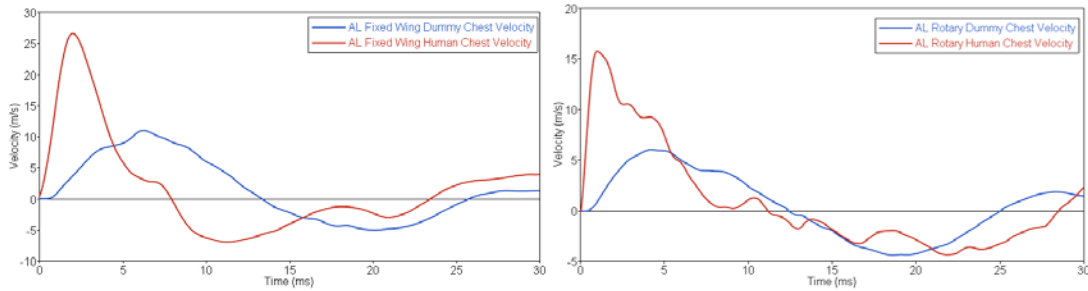
Based on the Task A4 literature survey, no experimental/computational studies on the UAS/chest impact response have been reported in the open publications. In this task, ERAU conducted a comparison of the simulation results based on the ATD and human torso models, respectively. The simulation data under the loading conditions described in Section 8 are plotted in Figure 64 and Figure 65 to compare the chest deflection-time history and velocity-time history, respectively. The results show that the peak deflection and deformation velocity of chest caused by fixed wing UAS are higher than those caused by its rotary wing counterpart. This is probably due to the fact that the particular fixed wing UAS used in this study is heavier and its mass is more focused on its frontal side, which has direct contact with the chest. Therefore, more energy is transmitted into the torso. This can be confirmed in Figure 56. The figures also show the human chest is “softer” than ATD chest. Specifically, maximum deflection and deformation velocity of the human chest is higher than that of the ATD chest under the same loading conditions, regardless the type of UAS. The peak values of both deflection and velocity histories occur earlier in the human chest. The discrepancy between the two model predictions is caused by different materials used in the two models for rib cages. The bony material properties in the human body model are closer to the actual behavior of natural bones, while ATD bones are made from steel, which is much stiffer. Currently, the human torso model is still in its initial version, and internal organs and other anatomic features have not yet been divided in detail. This will be implemented in the further stage, and the biofidelity of the model will be verified.



Aluminum fixed wing

Aluminum rotary wing

Figure 64 - Comparison of Model-Predicted Displacement-Time History of ATD and Human Torso under the Impact of UAS ($\theta=90^\circ$; $V=30$ m/s (98.4 ft/s))



Aluminum fixed wing

Aluminum rotary wing

Figure 65 - Comparison of Model predicted Compression Velocity-Time History of ATD and Human Torso under the Impact of UAS ($\theta=90^\circ$; $V=30$ m/s (98.4 ft/s))

4.17. Frangibility Analysis (KU)

Frangibility is the structural characteristic which allows structure, usually appendages, to break free from whatever it is attached to. Frangibility has been used as a damage mitigation design technique for sign and light poles to protect automobiles from otherwise sustaining substantial damage which may injure or kill occupants. It has also been used to allow landing gear on aircraft to break free from vehicles or low structures on the ground to protect the rest of the aircraft from more substantial damage. It has been suggested that frangibility may offer some advantages to UAS. Indeed, some wings on fixed wing UAS come loose from their insertion slots on fuselages during a crash to prevent them from breaking, which allows easy re-assembly. Also, some quadcopters have had rotor booms break off on impact with the ground, sending the vehicle into a tumble and decreasing the accelerations imposed on payloads, such as cameras.

However, the notion that frangibility significantly reduces the kinetic energy of impact with a person has not been vetted. As a first step toward understanding this notion, the case of a rotor boom designed to break away upon hitting a person has been analyzed.

A frangibility analysis was conducted for the impact of a quadcopter boom, oriented perpendicular to the direction of UAS motion, which becomes separated from the quadcopter and, although some energy is lost in the process, allows the quadcopter to continue on its path, yet put into a spin by the off-center impact shown in Figure 66.

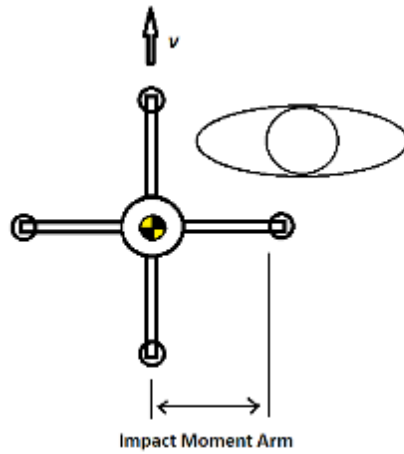


Figure 66 – Model for Analysis of Frangibility Effect on Impact

To accomplish this analysis, CR for the boom impact must be selected. Equation 22 is the general equation for the CR. The initial and final velocities are given by u and v , respectively. Subscript 1 denotes the UAS, and 2 denotes the body being impacted. Using the law of conservation of momentum gives Equation 23. Solving Equation 22 for v_2 and substituting that into Equation 23 and solving for v_1 gives Equation 24. Finally, assuming the initial velocity of the body being impacted is zero, we have Equation 25.

$$e = \frac{v_2 - v_1}{u_1 - u_2} \quad \text{Equation 22}$$

$$m_1 u_1 + m_2 u_2 = m_1 v_1 + m_2 v_2 \quad \text{Equation 23}$$

$$v_1 = \frac{m_1 u_1 + m_2 u_2 + m_2 e (u_2 - u_1)}{m_1 + m_2} \quad \text{Equation 24}$$

$$v_1 = \frac{m_1 u_1 - m_2 e u_1}{m_1 + m_2} \quad \text{Equation 25}$$

The analysis assumes a horizontal motion of the UAS at impact, with no significant change in altitude between immediately before to after. The equations for the resulting quadcopter velocity and angular velocity due to the impulse of impact are given as Equation 26 and Equation 27, where the impulse is represented by j and the perpendicular distance from the CG of the quadcopter to the impact point is r . I is the mass moment of inertia of the quadcopter about the vertical axis.

$$v_1 = u_1 - \frac{j}{m} \quad \text{Equation 26}$$

$$\omega' = \omega + jr/I \quad \text{Equation 27}$$

The analysis for boom failure was conducted in terms of the amount of energy needed to cause boom failure. Such failure will only occur if there is sufficient energy in the impact.

To quantify the kinetic energy transferred by the UAS to the person after collision, the principle of conservation of energy was used. Since the body being impacted is at rest before impact, the total energy in the system immediately before the impact equals the kinetic energy of the UAS

only, but after impact, consists of the final translational and rotation motions as well as the energy lost (work done) due to deformation during the impact, W_{impact} , as shown in Equation 28. After impact the total energy will consist of the final translational and rotation motions as well as the work done during the impact. Replacing the kinetic energy terms with their respective equations yields Equation 29.

$$KE_{total} = KE_{rotational} + KE_{translational} + W_{impact} \quad \text{Equation 28}$$

$$\frac{1}{2} m_1 u_1^2 = \frac{1}{2} I_{zz} \omega'^2 + \frac{1}{2} m_1 v_1^2 + Fd \quad \text{Equation 29}$$

The boom will fail if the energy lost during the impact exceeds the energy needed to fracture or break off. If a boom is designed to fracture before completely breaking, the energy transferred to an impacted person will be less than without any plastic deformation or breaking (assuming there is no other part of the quadcopter impacting the person). To check for the advantage gained by designing for frangibility, it is convenient to define the frangibility factor, f , defined in Equation 30.

$$f = \frac{\sigma_{break\ away}}{\sigma_{fracture}} \quad \text{Equation 30}$$

In this regard, breaking away does not necessarily mean any sort of fracture. Rather, it could be accomplished by a “snap in /snap out” design. Note that a very low frangibility factor may not allow the quadcopter to maneuver or even maintain a hover, since the lifting forces are at the tip of the booms. Analysis shows that, for a given CR (and attendant energy loss in the impact), the boom will fail or break away if the kinetic energy is sufficient *and* if the impact occurs at a distance along the boom which produces enough of a bending moment to cause failure or breaking away.

A study was performed using a hypothetical 6.5 lbs quadcopter consisting of tubular carbon fiber booms similar to many quadcopters in use. Figure 67 shows the kinetic energy required to break a boom as a function of frangibility factor and distance along the boom at which the impact with a person occurs. The kinetic energy required for failure is shown to increase as the impact moment arm decreases until the point that shear stress failure is the governing failure mode (impacts between 3 and approximately 5 inches). [Impacts less than 3 inches from the center of the quadcopter would be on the central body rather than the boom.] Consider first the case in which the UAS is flying at 50 fps, the impact occurs 6 inches from the CG and the CR is assumed to be 0.9. Note that the KE required to break the boom ($f = 1$) is approximately 70 ft-lbs for the impact at 6 inches. At this flight speed, the KE imparted to a person (which declines as a function of impact location) is represented by the dashed line. For this case, the KE of the UAS transferred to the person is approximately 45 ft-lb. Therefore, there is not enough energy available from the collision to cause the boom to break, so person would feel the full 45 ft-lb of impact energy. If, however, the boom can break away with $f = 0.2$, so the person would only feel 14 ft-lb of impact energy before the boom fails, offering substantial relief.

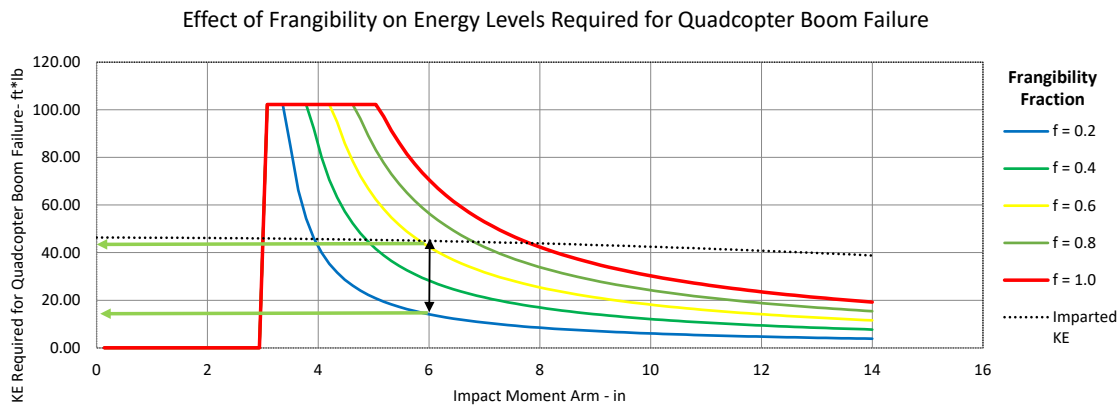


Figure 67 - Kinetic Energy Needed for Failure of Quadcopter Boom Compared with Kinetic Energy Transferred Based on Theoretical Flight Condition $u_1 = 50 \text{ ft/s}$

Now, consider a slower impact, with a flight speed of 20 fps. In Figure 68 the available KE is substantially less, as shown in the dotted line. [The boom failure curves remain the same as in Figure 67 because they are a function of the quadcopter design.] Here, for impacts as far from the CG as 10 inches, no failure would be expected for a frangibility factor more than 0.2. The benefit of frangibility is clearly less for slow impact speeds.

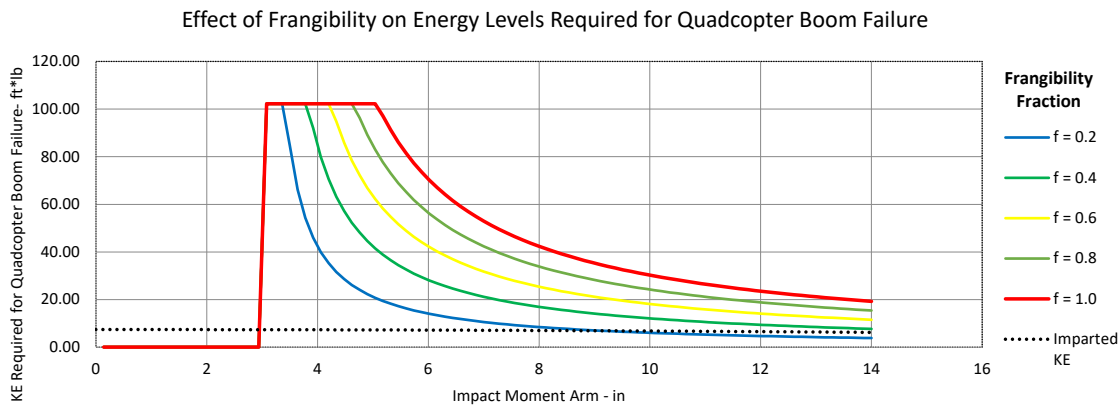


Figure 68 - Kinetic Energy Needed for Failure of Quadcopter Boom Compared with Kinetic Energy Transferred Based on Theoretical Flight Condition $u_1 = 20 \text{ ft/s}$

In summary, frangibility may only be helpful in cases of very high impact speeds, in which case, fracture will be more helpful for impacts relatively far out on the boom. Further, note that for the example given it is assumed that the boom is perpendicular to the flight direction. Most quadcopters fly in the “X” configuration, presenting less of a moment arm and therefore a lower potential for either breakage. Figure 69 illustrates this fact: impacts allowing some KE relief for an impacted person occur relatively far out on the boom (the green cross-hatched area). Impacts with the central body or the root of the booms would not be affected by a frangible design. A boom would not break or break away for impacts too close to the central body, that

is, in cases that the moment arm is so small that there would not be enough of a bending moment. Impacts inboard of the effective frangibility zone would not provide any relief.

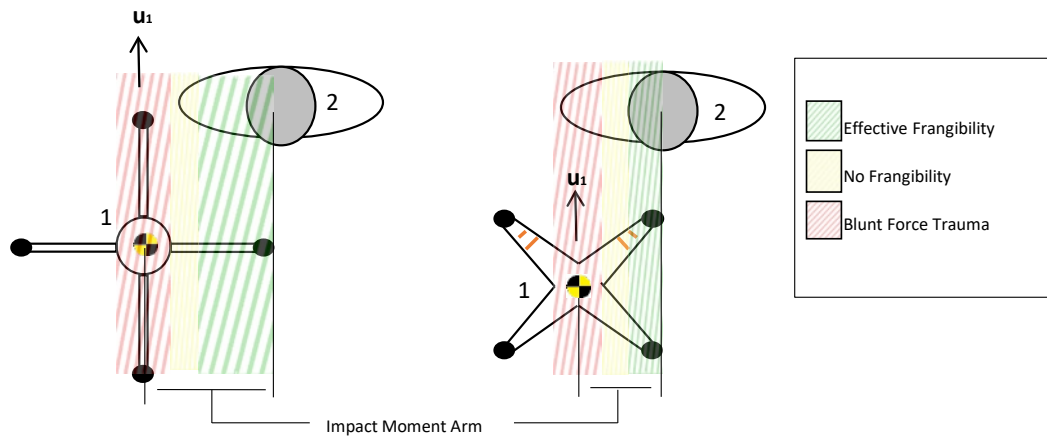


Figure 69 - Frangibility Zones for Impact at Different Attitudes

Knowledge Gap: Frangibility can be helpful to decrease kinetic energy imparted to persons on the ground from impact with a rotor boom or other appendage, depending on UAS speed and boom frangibility factor. A process to assess the degree of relief due to frangibility has been established, but has not been verified through test. If this injury mitigation strategy is to be embraced, verification testing a small number of quadcopters is appropriate.

4.18. Knowledge Gaps Associated with Finite Element Analysis Modeling

Knowledge Gap (MSU): Traumatic injury thresholds for fixed wing sUAS (PrecisionHawk)

Current human head injury analysis has been carried out for a multi-rotor sUAS (the DJI Phantom 3). The resulting FEA results show that certain ranges of impact location and velocity do increase the severity of TBI. However, the same information is not available for fixed wing UAVs, such as the PrecisionHawk. In particular, the interest would be in investigating the worst case scenarios for TBI due to impact with a fixed wing sUAS. This proposed analysis would fill the knowledge gap of injury severity to the human head and associated TBI for a medium size UAV.

Knowledge Gap (MSU): Injury Analysis for Human Neck

As a continuation of the ongoing study for micro and medium size UAV impacts on the human head, a detailed analysis needs to be conducted on the injury metrics for the human neck. Here, an anatomically accurate computational model of the human neck, along with the human head, is essential. Biomechanical analysis of the C1–C7 vertebrae and the brain stem/spinal cord is critical for quantifying injuries to the neck.

Knowledge Gap (MSU): Vibration of the UAV–human head collision

A vibrational analysis of the human head and UAV is critical to understand the magnification of lethality during a UAV–head collision that leads to vibrations within the range of resonant

frequencies of the human head and brain. The hypothesis is that the potential damage to the human brain from vibrations can be more detrimental than the initial impact.¹⁴⁴

Knowledge Gap (MSU): High fidelity, multi-material models for UAS

To improve upon the existing models for micro and medium size UAS, realistic material properties for various systems/components will be included. These simulations will provide more realistic physical behavior of both the UAS and the human.

Knowledge Gap (ERAU): Study of Human Posture and Shielding on UAS Impacts

UAS are often noisy and noticeable to people operating near them. It has been reported that there are substantial numbers of injuries associated with lacerations to hands and arms. Therefore, we plan to study the influence of posture when people are responding to the UAS by reaching out to deflect it or shielding their bodies with their arms and hands (Figure 70). Such injuries are expected to be on the upper extremities. Several typical scenarios will be studied.

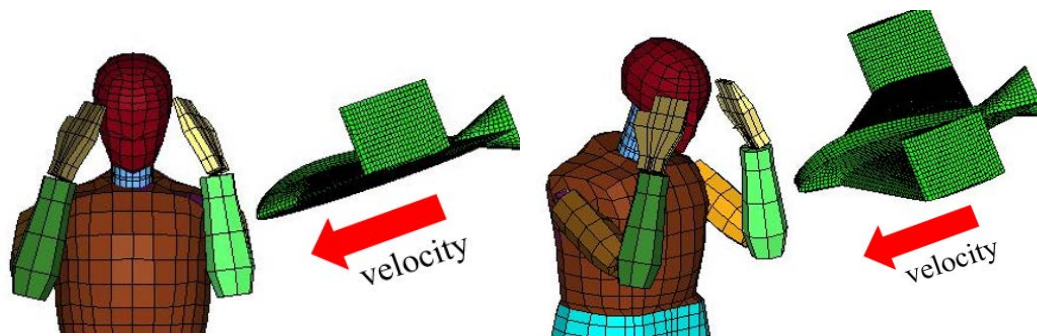


Figure 70 - Impact Modeling with Guarding and Bracing Postures

Knowledge Gap (ERAU): Study of Head and Neck Impacts with Integrated Torso

The approach to study the torso impact response can be extended to the head/neck complex. The head/neck has different injury mechanisms than the torso. Specifically, the head injury, including the skull fracture and brain concussion, is highly related to the translational and rotational accelerations induced by blunt impact. The neck injury is dominated by the combined effect of axial compression and lateral bending. Comprehensive simulations will be conducted to establish the relationship of response and impact parameters (type of UAV, velocity, angle and impact location etc.). Figure 71 shows a typical scenario for the simulation. The model predictions will be compared with the results based on the real head models.

¹⁴⁴ Säljö A., Arrhén F., Bolouri H., Mayorga M., Hamberger A., "Neuropathology and Pressure in the Pig Brain Resulting from Low-Impulse Noise Exposure," *Journal of Neurotrauma*, Vol. 25, 13971397-14061406, 2009.

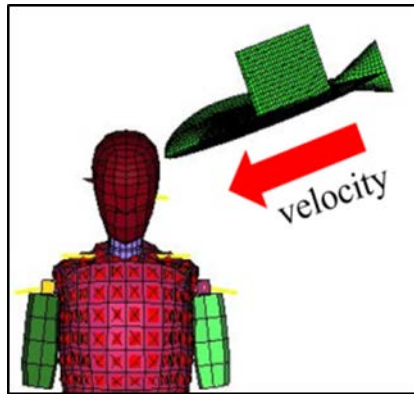


Figure 71 - Head and Neck Impact Modeling

Knowledge Gap (ERAU): Posterior Impacts to the Torso.

The torso impact simulations have only shown the effects of an impact to a person’s front. Given the different anatomy (spine versus ribs of abdomen) and biomechanics (extension versus flexion) after impact, it is likely that trends and assumptions from frontal impact modeling are not representative of posterior impact scenarios. It is critical to evaluate posterior impacts, because anyone hit from behind is much less likely to be bracing for impact or shielding themselves. Figure 72 shows the torso back impact simulations that will be performed using the same approach for frontal impact.

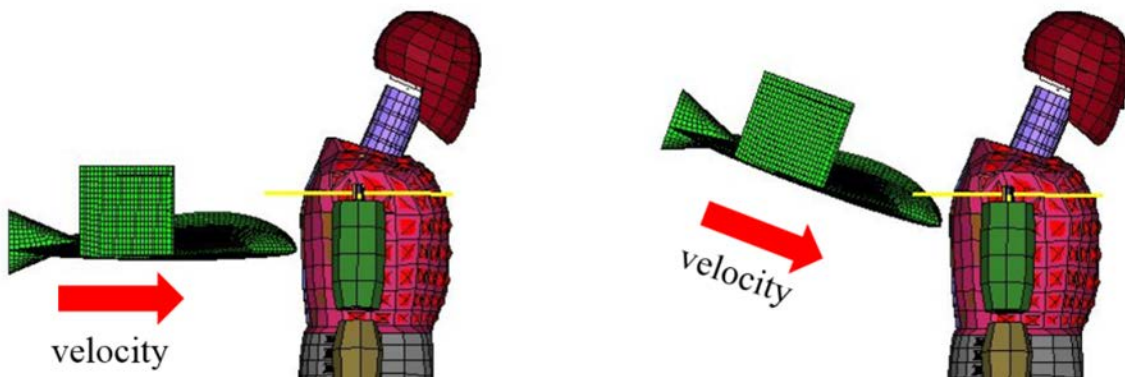


Figure 72 - Posterior UAS Impact Modeling

4.19. Additional Research Proposed to Address Research Gaps

The following topics have been submitted to the FAA for consideration for proposals as a means of addressing knowledge gaps that have been called out in this document. Appendix E provides more details on the knowledge gaps identified during the initial A4 effort and the proposed research that is associated with several of the gaps.

- 1) Parachute mitigation performance (deployment time, deceleration time, final rate of descent): *W69 - Performance Assessment and Standards Development for sUAS Parachute Recovery Systems for use as a Mitigation for Flight Over People*

- 2) Multi-rotor Aircraft Falling Behavior (dynamics based on parametric design, dynamics based on component failures, development of a vehicle falling footprint, impact energy studies): *W64 - Falling Multi-Rotor Dynamics Study*
- 3) Multi-rotor Aircraft Probability of Strike (coupling of vehicle falling footprint estimation with probabilistic analysis of operations in vicinity of people): and *W65 - Probability of UAS Ground Strike to People and Objects*
- 4) Battery Failure Modes and Effects (testing of batteries in accordance with Lithium Ion Battery design standards, and ballistic testing to identify current standards gaps based on the UAS operational environment): *W63 - Lithium Polymer Battery Failure Modes and Effects Analysis*
- 5) Head impacts by fixed wing sUAS: *W71 -- Mid-Sized fixed wing UAS – Human Head Ground Collision Modeling for the Assessment of Skull Fracture*
- 6) Neck injuries due to head impacts by sUAS: *W72 -- Finite Element Modeling Human Neck Injury due to UAS Ground Collisions*

5. Conclusions and Recommendations

5.1. Key mUAS and sUAS Characteristics

The A4 team has reviewed the available research and techniques used to address blunt force trauma, penetration injuries and laceration injuries that present the most significant threats to the non-participating public and crews operating sUAS platforms. The most significant of these characteristics related to ground collision severity are:

- 1) The impact KE and impact orientation based upon a *specific vehicle* is the most significant metric for evaluating blunt force trauma injuries. Blunt force trauma is the most likely cause of fatalities due to UAS collisions for mUAS and sUAS with the exception of single rotor helicopters whose blade mass and blade speed present a lethal impact threat. Impact KE can be easily estimated and measured, based on vehicle velocity, during testing.
- 2) The energy density parameter is the best metric for evaluating the possibility of penetration injuries caused by sharp edges or small impact areas in the vehicle design. This parameter is very challenging to measure during testing.
- 3) Rotor diameter is the metric for severity of injury from rotors and propellers to define when blade guards or other protective measures are required to prevent laceration injuries (which is the most likely type of injury to occur). Single rotor helicopter configurations present a potentially lethal threat to the throat and head area due to the blade mass and speed of larger single rotor helicopters. Rotor diameter is easily measured.

All of the metrics mentioned above are easily estimated during design. Impact energy and rotor characteristics can also be easily tested and validated during development. Energy density is difficult to measure and test since contact areas and measurement techniques are expensive and hard to reproduce. The analysis in this report has shown that basic ballistic modeling can accurately estimate impact KE following power failure when sufficiently detailed CAD modeling for the vehicle fuselage and propulsion system is available. This modeling can be updated as the design is revised. During prototype development and initial flight testing, impact KE evaluations, including the determination of drag, are a straight forward task that is accomplished by verifying power-off terminal velocity for rotary wing aircraft and glide and diving airspeeds for fixed wing

aircraft. Flight test can be used to experimentally validate the worst case impact KE for the most likely failure modes of the vehicle. The same can be done for maximum forward airspeeds. Given sufficiently detailed guidance on appropriate contact areas for evaluation, applicants can assess energy density at critical component contact areas and address appropriate mitigations to reduce the risk of penetration injuries. Lastly, rotor diameter, which closely correlates with laceration injuries, is easily measured by a manufacturer to determine whether blade guards or other mitigations are required. Appendices C and D in the Task A11 Final Report provide recommended testing and analysis standards that operators can use in order to apply for waivers to restrictions on flight over people found in the FAA's Part 107 rules.

5.2. Discussion of AIS, HIC and VC, and Respective Applicability to Ground Collision Severity Evaluation

The AIS, HIC and VC metrics are descriptive of impacts and impact effects. HIC and VC currently require complex finite element modeling and simulation by a vehicle designer during product development. There is limited research in this area, having been mainly conducted by MSU and ERAU, and no recommended standards for the conduct of this modeling and simulation. UAH developed a method correlating impact KE with maximum g-loading thresholds for head and neck injury that is much simpler to use as a standard until more refined methods are created. This method is outlined in Section 4.8 and has its roots in automotive industry crash testing and human head injury impact testing.

5.3. Establishment of mUAS and sUAS Thresholds Other Than RCC

RCC impact KE values relative to their respective POF are excessively conservative when applied to sUAS multi-rotor and FW platforms and the FAA should consider modification of thresholds to better address injury severity associated with flexible, single body UAS rather than high volume, small mass debris as assessed by the RCC. More modeling and correlation with AIS is required to refine the relationship between injury severity and impact KE for a broader number of flexible and frangible UAS for the most common failure modes of the respective vehicles. Based on the recommended method in Section 4.8, manufacturers can provide a 98% confidence assessment of the likelihood of head or neck injury for their respective impact following complete loss of power using flight test validated impact KEs.

During the initial part of Task A4, the team reviewed and evaluated the existing RCC impact KE and energy density thresholds for the categorization of sUAS using the combined effects of KE and weighted distribution of body part areas for the 50th percentile male. This was done to determine KE thresholds that can drive industry consensus standards development in terms of the categorizations defined in the Micro-UAS ARC Report. However, sUAS drop testing (DJI Phantom 3 Standard) on an ATD Hybrid III 50th Percentile Male Crash Test Dummy by NIAR, showed a disconnect between RCC impact KE thresholds and injuries assessed based on load cell measurements and FMVSS 208 from the National Highway Transportation Safety Administration (Section 4.8).

This method of injury correlation with impact KE is, however, quite new and requires more focused research in order to refine and validate it based on understanding sUAS impacts. The A4 team initially assumed a 60% value as the basis for KE transfer until more complete analysis and modeling could be completed by ERAU and MSU. The Task A11 analysis estimated approximately between 44%-67% impact energy transfer to the dummy's head based on pure vertical drops and center of mass impacts. ERAU's work shows there was 50% to 80% energy

transfer for center of mass impacts, with impact velocities of 24 ft/s down to 0.8 ft/s respectively, to the torso when an aluminum fixed wing aircraft was used as the impacting mass. This correlated well with A11 data that showed a lower % of energy transfer as the impact velocity increased. The ERAU modeling of impacts angles of 10° above horizontal followed the direct horizontal impact trends closely. As the impact trajectory became steeper, the percentage of energy transfer dropped off significantly. The trends for a fixed wing sUAS made of plastic and multi-rotor sUAS models made of aluminum and plastic followed these trends closely. These results, which come from low-order modeling at UAH, experimental data from NIAR, and FEA modeling by ERAU highlight a need for focused modeling efforts to understand the impact energy absorption of sUAS, develop energy absorption design parameters, and develop recommended standards for evaluating impact KE absorption. MSU's modeling and simulation work did not include analysis of impact energy transfer; however, the levels of vehicle deformation shown in the MSU simulations are comparable to those witnessed in the NIAR drop testing. This indicates that vehicle elastic and plastic deformation during collisions plays a strong role in energy transfer to the impacted object. MSU's simulation results do show that there is increased risk of injury based on increased impact speed, which is consistent with the other research. It does diverge from the NIAR drop testing, because the MSU simulation results appear to show higher likelihood of AIS-level 3 and higher injuries than what appeared in the NIAR drop testing. It is likely that the lack of neck model and associated degrees of freedom associated with MSU's highly constrained model led to these results. MSU and ERAU have both developed plans to conduct modeling of the entire head and neck complex during impacts. These projects could be complimentary efforts that serve to check and validate one another. The design of experiments in these potential studies could be informed by the way that the NIAR testing was completing under Task A11 in order to continue developing an understanding of the results of those drop tests and remain based in the well-developed injury assessments done within automotive engineering and emergency medicine.

Limitations of the above approach do not address single rotor helicopters as the rotor energy and impacts are substantially different than multi-rotors and FW platforms in the sUAS class. A separate treatment of rotor energy for single rotor helicopters and associated thresholds requires further consideration.

5.4. Parachute Standards for Category 3 and 4 Operations

The use of parachutes to further mitigate injuries can increase the size and weight of vehicles for both Category 3 and 4 performance standards once a performance standard for parachute design and the establishment of operating limits is established to ensure effective parachute use.

5.5. Standoff Metrics and UAS Ground Collision Modeling

Realistic risk models will require substantially better modeling to refine probability analysis and severity of impact for a majority of operations and most common failure modes for UAS platforms having no hardware or software certification requirements.

The A4 team presented a framework for calculating the standoff distances and establishing future probability of occurrence metrics for mUAS and sUAS. Evaluation of metrics based upon ballistic modeling of inert falling masses is useful in the near term; however, UAS platforms do not typically break up into small 2 lbs pieces with purely ballistic trajectories. UAS platforms

typically fail as a complete system that is larger than 2 lbs. They have failure modes and aerodynamics that result in a different probabilistic distribution when a UAS crashes.

5.6. Ground Collision Severity of LiPo Batteries

More extensive research and testing is required to assess the fire potential of batteries used across the spectrum of mUAS and sUAS following ground or air collision.

LiPo batteries lead as the power source for mUAS and sUAS platforms. These batteries are manufactured in a variety of sizes, styles, chemistries and number of cells to meet specific energy requirements. The batteries employ a variety of mitigations to address the potential for fire and explosion when these batteries deteriorate, are punctured during improper handling, or when damaged following a ground or air collision. While manufacturers have anecdotally indicated that they test their batteries to meet current consumer Lithium Ion battery standards, few mUAS or sUAS batteries carry compliance labels from the standards institutions to show clear compliance to the standards. Furthermore, the consumer grade test standards for batteries do not address the energy or force levels representative of a ground collision impact to evaluate fire mitigations and different chemistries and manufacturing methods to properly address the fire hazard to property following collision. LiPo batteries clearly present a wild fire hazard following a ground collision that damages the LiPo batteries when operating in a dry or Red Flag area. Furthermore, contact of damaged batteries with water can create an even more intense fire hazard and potential explosion. The fire hazard to property, such as houses, is not clear relative to current roofing standards. The fire hazard has been assessed in one FAA publication. The LiPo batteries used in the FAA test were representative of LiPo batteries used onboard aircraft. These high capacity batteries are used only on a small number of mUAS.

5.7. Knowledge Gaps

The A4 team recommends the FAA identify funding to address these knowledge gaps in the next year to further refine standards and rulemaking as it relates to ground collision severity. This includes funding the already published research white papers identified in paragraph 4.19. The A4 team identified twenty-three knowledge gaps throughout the literature search and subsequent analysis that are not currently funded under the A4 or A11 task. These knowledge gaps are summarized in Appendix E: Knowledge Gap Roundup, but are addressed in the areas of the paper where they are relevant. These knowledge gaps are aligned with six white papers already submitted to the FAA or that were submitted to the FAA prior to the end of July 2016.

Appendix A: Nomenclature

AFSCOM – Air Force Space Command
AGL – Above Ground Level
AIS – Abbreviated Injury Scale
AMA – Academy of Model Aeronautics
ARC – Advisory Rule Making Committee
ASSURE – Alliance for System Safety of UAS through Research Excellence
AUVSI – Association of Unmanned Vehicle Systems International
BC – Blunt Criterion
 C_d – Coefficient of Drag
CFD – Computational Fluid Dynamics
CFRP – Carbon Fiber Reinforced Plastics
CR – Coefficient of Restitution
CSF – Cerebrospinal Fluid
COA – Certificate of Authorization
DoD – Department of Defense
DOE – Design of Experiments
DSLR – Digital Single-Lens Reflex
 e – Coefficient of Restitution
ERAU – Embry Riddle Aeronautical University
FAA – Federal Aviation Administration
FE – Finite Element
FW – Fixed Wing
GPS – Global Positioning System
GNC – Guidance, Navigation, and Control
HIC – Head Injury Criterion
 I^2R – Internal Resistance Losses
KE – Kinetic Energy
Kts - Knots
KU – The University of Kansas
LiPo – Lithium Polymer Battery
LSA – Light Sport Aircraft
MASPS – Minimum Aviation Performance Standards
mAh – milliamp hour
MSU – Mississippi State University
MGTOW – Maximum Gross Takeoff Weight
mUAS – Micro UAS
NAS – National Airspace System
NAVAIR – U.S. Naval Air Systems Command

NASA – National Aeronautics and Space Administration
NPRM – Notice of Proposed Rulemaking
P – Parallel (example 7S2P battery)
POF – Probability of Fatality
psi – Pounds per square inch
RC – Radio Controlled
RCC – Range Commander’s Council
RPA – Remotely Piloted Aircraft
RPM – Revolutions per Minute
RW – Rotary Wing
S – Serial (example 6S battery)
SARP – Science and Research Panel
SEI – Solid Electronic Interface
SMS – System Management Safety
SSL – Standard Sea Level
sUAS – Small UAS
TBI – Traumatic Brain Injury
TIM – Technical Interchange Meeting
TKE – Turbulent Kinetic Energy
UAH – The University of Alabama in Huntsville
UAS – Unmanned Aerial System(s)
V - Volt
VC – Viscous Criterion
 V_{term} – Terminal Velocity
VLOS – Visual Line of Sight

Appendix B: Aircraft Characterization Tables

The aircraft parametric data used to determine a relationship between MGTOW and terminal KE for multi-rotor mUAS (< 4.4 lbs) is in Table B - 1. All peach-filled cells in the Area Effective column represent actual area ratios instead of applying a factor of 0.3 to the area of the circle with a diameter equal to the vehicle diagonal motor-to-motor distance. The estimated KE and percent error columns are used to calculate the vehicle terminal KE based on the relationship:

$$KE = 64.394 \left(\frac{ft-lbs}{lbs} \right) * MGTOW(lbs) \text{ Equation B - 1}$$

The percentage difference between that quantity and the terminal KE is calculated by Equation 3 and Equation 4. The constant value of 64.394 is the slope of the linear curve fit in Figure 42.

The aircraft parametric data used to determine a relationship between MGTOW and terminal KE for FW UAS (<10 lbs) is in Table B - 2. Standard configuration aircraft were estimated to have an effective area that is 65% of the “box” defined by aircraft length and multiplied by aircraft width. Flying wing aircraft were assumed to have an effective area equal to the length multiplied by the width. Effective area takes into account all surface areas swept by flow. Therefore, it accounts for the upper and lower surfaces of airfoils, all sides of the fuselage, and both sides of vertical surfaces. The estimated KE column and percent error columns are used to calculate the vehicle terminal KE based on the relationship

$$KE = 286.94 \left(\frac{ft-lbs}{lbs} \right) * MGTOW(lbs) \text{ Equation B - 2}$$

The constant value of 286.94 is the slope of the linear curve fit in Figure 43.

Table B - 1 - Multi-Rotor mUAS Parameters

Platform	Manufacturer	Length (ft)	Height (ft)	Width (ft)	Diameter motor-to-motor (ft)	MTOW (lb)	Area Eff (ft^2)	V _{term} (fps)	Vterm (kts)	KE(ft-lbs)	KE (ft-lbs) Estimate	% Err
PD-100 Black Hornet PRS	Proxy Dynamics	0.66	0.16	0.28	0.72	0.03	0.12	15.19	8.99	0.11	1.68	-93.60%
QR Y100	Walkera	0.83	0.3	0.73	0.76	0.32	0.15	45.30	26.82	10.21	17.92	-43.05%
200 QX	Blade	0.47	0.3	0.47	0.78	0.43	0.17	47.95	28.39	15.36	24.08	-36.20%
Bebop drone	Parrot	0.92	0.12	1.05	0.88	0.84	0.37	45.94	27.20	27.55	47.04	-41.43%
The Pocket Drone	AirDroids	0.58	0.25	0.58	0.82	1	0.16	76.64	45.37	91.27	56.00	62.98%
Ghost	Ehang	1.17	0.33	1.17	1.31	1.9	0.62	53.41	31.62	84.24	106.40	-20.82%
BLADE 350 QX3	Blade	1.53	0.62	1.53	1.33	2.11	0.50	62.67	37.11	128.79	118.16	9.00%
AgilCopter	Agile Sensor Technologies	0.92	0.38	0.92	1.30	2.13	0.40	70.51	41.75	164.58	119.28	37.97%
Draganflyer X4	Draganfly Innovations	2.12	0.69	2.12	1.31	2.16	0.49	64.38	38.12	139.12	120.96	15.01%
PlexiDrone	DreamQii Robotics Inc. (Canada)	1.25	0.42	1.25	1.77	2.2	1.20	41.27	24.43	58.23	123.20	-52.74%
Md4-200	Microdrones, GmbH	1.77	0.73	1.77	1.97	2.43	1.07	45.97	27.22	79.79	136.08	-41.36%
ATLAS™ (formerly UFRO)	Unmanned Cowboys, LLC.	1.42	1.42	1.42	1.42	2.8	0.48	74.07	43.86	238.75	156.80	52.27%
Phantom 2	DJI				1.15	2.82	0.54	66.79	39.55	195.51	157.92	23.80%
QR X350 PRO	Walkera	0.95	0.67	0.95	1.28	2.98	0.43	79.95	47.33	295.98	166.88	77.36%
SQ-4 RECON	BCB International, Ltd.	0.98	0.26	0.98	1.39	2.98	0.45	78.30	46.36	283.90	166.88	70.12%
Aries Blackbird X10 (AIR-BBX10)	Adorama Camera, Inc. (United States)	1.48	0.46	1.48	1.94	3.1	0.96	54.73	32.40	144.29	173.60	-16.88%
Solo	3DR		0.83		1.50	3.96	0.76	69.66	41.24	298.59	221.76	34.64%
Firefly	Ascending Technologies, GmbH. (Germany)	1.98	0.54	2.18	1.53	3.5	0.75	65.70	38.90	234.77	196.00	19.78%
beijing creation T21	Beijing Creaton Tech Co., Ltd.	2.3	0.82	2.3	3.25	3.5	1.25	51.13	30.27	142.20	196.00	-27.45%
Draganfly X6	Draganfly Innovations	2.96	0.875	2.75	1.77	3.6	0.89	61.26	36.27	209.93	201.60	4.13%
Asctech Pelican	Ascending Technologies, GmbH. (Germany)	2.14	0.62	2.14	1.38	3.64	0.66	71.76	42.49	291.29	203.84	42.90%
eXom	SenseFly (Switzerland)	1.84	0.56	2.62	1.73	3.7	0.98	59.28	35.10	202.07	207.20	-2.47%
Q500 Typhoon	Yuneec USA	1.38	0.79	1.38	1.85	3.75	0.81	65.80	38.96	252.31	210.00	20.15%
Curiosity	OM UAV Systems (India)	2	0.82	2	2.13	4	1.07	59.02	34.95	216.56	224.00	-3.32%

Table B - 2 - FW mUAS/sUAS Parameters

Platform	Manufacturer	Length (ft)	Height (ft)	Wing Span (ft)	MGTOW (lbs)	Planform Area (ft ²)	V _{term} (ft/s)	V _{term} (kts)	KE (ft-lbs)	Impact Area (ft ²)	KE (ft-lbs) Estimate	% Err
Epsilon 2	Alcore Technologies	0.62	0.16	0.79	0.33	0.32	152.21	90.12	118.81	1.96	89.32	-0.33
Epsilon 1	Alcore Technologies	1.25	0.33	1.57	0.99	1.28	131.71	77.98	266.88	7.74	267.95	0.00
Roll n'Fly	Survey-Copter	1.48	0.92	1.48	1.10	1.42	131.41	77.80	295.20	6.88	297.73	0.01
Locust MAV	Continental Controls and Design	1.48	0.92	1.48	1.10	1.42	131.41	77.80	295.20	6.88	297.73	0.01
Oto-Horus	Oto Melara SPA	0.82	0.10	1.51	1.26	0.80	187.06	110.75	685.18	7.16	341.03	-1.01
X PlusOne	xCraft (United States)	3.22	2.49	5.41	2.00	11.32	62.83	37.20	122.71	91.95	541.32	0.77
Midge	CyberFlight	1.58	1.17	2.71	2.80	2.78	149.96	88.78	978.47	23.07	757.85	-0.29
Eagle Eye	OM UAV Systems (India)	3.12	0.33	5.90	2.90	11.97	73.60	43.58	244.14	109.36	784.91	0.69
Guardian	OM UAV Systems (India)	3.43	0.62	6.56	4.00	14.63	78.19	46.29	380.00	135.19	1082.64	0.65
H3	Siralab Robotics S.r.l. (Italy)	3.43	0.26	6.56	4.00	14.63	78.19	46.29	380.00	135.19	1082.64	0.65
D-3	Fuji Imvac Inc. (Japan)	3.30	0.82	5.25	4.20	11.26	91.30	54.06	544.11	86.59	1136.77	0.52
iSTART	Blue Bear Systems Research, Ltd.	4.01	1.07	5.25	4.40	13.68	84.78	50.19	491.43	86.59	1190.90	0.59
Rover MK-I	Integrated Dynamics	2.16	0.79	2.46	4.40	3.45	168.74	99.91	1947.04	19.01	1190.90	-0.63
T16	Beijing Creaton Tech Co., Ltd.	2.95	0.66	4.92	4.40	9.43	102.10	60.45	712.81	76.05	1190.90	0.40
E-Swift Eye	CyberFlight	2.30	0.43	3.30	4.40	4.93	141.19	83.59	1363.08	34.21	1190.90	-0.14
AV8-R	BrockTek, LLC. (United States)	2.69	0.39	3.30	4.85	5.77	137.07	81.15	1416.04	34.21	1312.70	-0.08
Baaz	OM UAV Systems (India)	2.98	0.74	3.00	5.29	5.81	142.64	84.46	1672.75	28.27	1431.79	-0.17
M-011	Aeroteknikka UAV Oy (Finland)	2.15	0.62	3.12	5.50	6.71	135.37	80.15	1566.40	30.58	1488.63	-0.05
Swallow-P	Carbon-Based Technology, Inc.	4.27	0.98	4.07	5.50	11.30	104.32	61.76	930.17	52.04	1488.63	0.38
PLANC (Photo Link Access Non Combatent)	Theiss Aviation	2.13	0.33	3.28	5.50	6.99	132.65	78.54	1503.98	33.80	1488.63	-0.01
E2 Micro-UAV	Sierra Pacific Innocations (United States)	2.13	0.33	3.28	5.50	6.99	132.65	78.54	1503.98	33.80	1488.63	-0.01
Spectra AP	RPFlightSystems, Inc. (United States)	3.05	0.65	1.75	5.80	5.34	155.85	92.27	2189.22	9.62	1569.83	-0.39
Recce D6	Odin Aero (Norway)	2.79	0.27	6.00	6.00	10.88	111.02	65.73	1149.22	113.10	1623.96	0.29
UX5 HP	Trimble	1.33	0.58	4.00	6.00	3.46	196.93	116.60	3616.17	50.27	1623.96	-1.23
Irkut-2M	Irkut	2.48	0.85	4.66	6.17	7.51	135.49	80.22	1760.31	68.22	1669.97	-0.05
Spy Owl 100	UAS Europe AB	2.13	0.34	3.28	6.40	4.54	177.48	105.08	3133.03	33.80	1732.22	-0.81
Super Ferret	Theiss Aviation	1.48	0.98	4.82	6.60	4.64	178.37	105.60	3263.15	72.99	1786.36	-0.83
SKY-01	China TranComm Technologies Co., Ltd (China)	3.90	1.05	5.90	6.60	14.96	99.31	58.80	1011.65	109.36	1786.36	0.43
SKY-02	China TranComm Technologies Co., Ltd (China)	5.33	1.29	7.52	8.00	26.05	82.85	49.05	853.28	177.66	2165.28	0.61
W200	Embention	2.62	1.48	2.62	8.16	4.46	202.18	119.70	5183.65	21.57	2208.59	-1.35
ALADIN	EMT Ingenieurgesellschaft (Germany)	3.28	1.48	2.62	8.16	5.59	180.70	106.99	4140.59	21.57	2208.59	-0.87
AL-4	Aeroland UAV, Inc. (Taiwan)	2.15	0.66	6.40	8.80	8.94	148.30	87.80	3007.49	128.68	2381.81	-0.26
Avian	Carbon-Based Technology, Inc.	5.15	1.25	4.79	8.82	16.03	110.88	65.65	1685.20	72.08	2387.22	0.29
Pride	Integrated Dynamics	4.59	0.92	6.56	9.30	19.57	103.06	61.02	1534.99	135.19	2517.14	0.39
SKYCAM 1	Integrated Dynamics	3.44	1.64	5.25	9.90	11.74	137.30	81.29	2900.08	86.59	2679.53	-0.08

Appendix C: Aircraft Characteristics and Energy Data

Table C - 1 - Aircraft Characteristics and Energy Data

	Vehicle Mass (lbf)	Cruise Speed (ft/sec)	Maximum Operating Altitude (ft)	Propeller Diameter (in)	Propeller Mass (lbs)	KE (ft-lbs)	Potential Energy (ft-lbs)	Combined Energy (ft-lbs)	Rotational Energy (ft-lbs)
NORMAL FAR 23									
Cessna Skyhawk	2550	209	14000	74	40	1729604.8	35700000	37429604.8	124458.2
Diamond DA40	2645	265	16400	69	21	2884241.1	43378000	46262241.1	43494.4
Cessna Stationair	3600	240	15700	79	57	3219875.8	56520000	59739875.8	202129.2
Cirrus SR-22	3600	309	17500	78	57	5337447.2	63000000	68337447.2	213806.8
Beechcraft Bonanza	3650	297	18500	78	57	4999423.1	67525000	72524423.1	213806.8
Piper Matrix	4340	359	25000	80	75.4	8685458.7	108500000	117185458.7	297514.9
Cessna 340	5990	392	29800	74	72.8	14292660.9	178502000	192794660.9	245783.2
Beechcraft Queen Air	8800	268	26800	90	90	9814459.6	235840000	245654459.6	831309.6
ULTRALIGHT FAR 103									
Quick Silver MX Sprint	524	79	14000	66	10	50780.8	7336000	7386780.8	26856.2
Drifter DR 447	775	88	14000	66		93192.5	10850000	10943192.5	
Loehle Sport Parasol	600	88	14000			72149.1	8400000	8472149.1	
Firestar	725	88	14000	66	8	87180.1	10150000	10237180.1	15159.8
Buckeye Dragonfly	550	38	10500	68		12332.3	5775000	5787332.3	
LSA									
Cessna Skycatcher	1320	191	14625	67	9.3	747747.2	19305000	20052747.2	32286.9
Icon A5	1430	177	10000	71	30	695659.5	14300000	14995659.5	76398.4
Zenith CH 750	1320	117.36	12000	70	10	282311.3	15840000	16122311.3	27517.8
Piper J-3 Cub	1220	202.54	11500	70		777102.7	14030000	14807102.7	
MILITARY									
MQ 1 Predator	2250	198	25000	72		1369705.0	56250000	57619705.0	
Wasp	1	58.68	400			53.5	400	453.5	
GNAT	1140	176.04	25000			548582.2	28500000	29048582.2	
RQ-11 Raven	4.2	27.345	400			48.8	1680	1728.8	
Scan Eagle	48.5	101.27	19500			7723.3	945750	953473.3	
AAI RQ-7 Shadow	375	118.83	15000			82219.7	5625000	5707219.7	
UAS COA									
Meridian	1100	169	400	60	10	487843.2	440000	927843.2	20217.2
G1X-B	70	131	400	28	0.88	18653.3	28000	46653.3	272.2
ELIMCO E500	110	109	400			20293.6	44000	64293.6	
UAS MULTI ROTOR									
Blade Nano	0.05	20	400	1.97	0.0012	0.3	20	20.3	0.9
SkyViper V2900	0.55	25	400			5.3	220	225.3	
UDI 818a	0.56	25	400	3.75	0.0047	5.4	224	229.4	4.4
Hubsan H107c	1	29	400	2.2	0.0007	13.1	400	413.1	0.8
Parrot AR 2.0	1	16	400	9	0.0531	4.0	400	404.0	
Syma X5C	2	47	400			68.6	800	868.6	
DJI Phantom 3	3	53	400	9.5	0.0288	130.9	1200	1330.9	36.9

Table C - 2 Aircraft Characteristics and Energy Data Continued

	Vehicle Mass (lbf)	Cruise Speed (ft/sec)	Maximum Operating Altitude (ft)	Propeller Diameter (in)	Propeller Mass (lbs)	KE (ft-lbs)	Potential Energy (ft-lbs)	Combined Energy (ft-lbs)	Rotational Energy (ft-lbs)
UAS MULTI ROTOR Continued									
Parrot Bebop	3	45	400	9	0.0119	94.3	1200	1294.3	10.5
Blade Chroma	3	59	400			162.2	1200	1362.2	
3D Robotics X8+	7.5	98	400			1118.5	3000	4118.5	
Yuneec Tornado	11	69	400	15	0.05	813.2	4400	5213.2	54.4
DJI S900 Spreading Wings	18	52	400			755.8	7200	7955.8	
KittyHawk	41	56	400	17	0.0656	1996.5	16400	18396.5	97.0
UDI u816		0	400	2.22	0.0084	0.0	0	0.0	7.2
UAS MINI HELICOPTER									
T-Rex 150	0.12	0	400	10.6	0.016	0.0	48	48.0	10.7
T-Rex 250	0.57	0	400	18.1	0.031	0.0	228	228.0	25.0
Blade 450x	1.58	66	400	28.4	0.088	106.9	632	738.9	83.3
T-Rex 450	1.6	60	400	31.6	0.12	89.4	640	729.4	153.2
T-Rex 500	2.7	0	400	38.9	0.26	0.0	1080	1080.0	385.1
T-Rex 550	6.2	110	400	49.1	0.46	1164.9	2480	3644.9	779.9
T-Rex 600E	6.4	125	400	53	0.6	1552.8	2560	4112.8	1266.5
T-Rex 700E	7.3	167	400	62.3	0.95	3161.3	2920	6081.3	1940.9
T-Rex 800E	9	0	400	68.5	0.98	0.0	3600	3600.0	2420.5
T-Rex 700N	9.3	176	400	62.3	0.95	4473.2	3720	8193.2	1454.9

Appendix D: Major Categories of sUAS and Defining Design Attributes

D.1 Analysis of UAS Design Features with Respect to Ground Collision Effects

In the last decade, the majority of UAS users have been military, academia, researchers and hobbyists. These users have put high emphasis on vehicle performance and UAS application development. However, in the last year, the commercial and hobbyist use of UAS has tremendously increased. In the last 2-3 years, the emphasis is on payload capability, endurance, out-of-the-box operability, and resiliency of the vehicle to minor crashes by the operator and, to a lesser extent, safety. As consumer and commercial usage of UAS increases, safety becomes more important because it enables a more flexible and open regulatory framework for commercial use and reduces product liability risks for manufacturers. Furthermore, many potential safety features reduce the risk to the public while also minimizing impacts to expensive payloads and other components of the vehicle important to the consumer.

In today's market, the UAS sold for either commercial or consumer markets have varying numbers of safety features. This is symptomatic of the lack of industry consensus on design standards and indicates a need for performance-based regulatory requirements for vehicle safety. Some manufacturers are actively pursuing safety features such as geofencing and platform stability. This section will analyze the various design, functional and safety features of UAS currently available in the market that contribute towards ground collision severity. In the first sub-section, UAS will be broadly classified based on their contribution towards ground collision severity. Then, the next section will briefly discuss how the different design attributes of fixed wing, multirotor and helicopter UAS play out in terms ground collision severity.

D.1.1 Multi-Rotor with Monocoque Frame

Most of the UAS sold in the hobbyist and lower-end commercial ("prosumer") markets possess a fully monocoque construction with internally-mounted batteries, navigation sensors and circuits. The fuselage surface has smooth contours and few sharp edges. These UAS are mostly of quadcopter configurations with arms that are an integral part of the fuselage. Figure D - 1 depicts several UAS with monocoque construction. In a large number of collision orientations, the UAS surface area in contact with a human is greater than for collapsible and modular designs. The impact loads that are generated during this collision disperse throughout the continuous fuselage frame, deforming and distorting the frame and reducing energy transfer to impacted objects. These aircraft are built for resilience to crashes by consumers. The frames, motors and propellers absorb energy during minor collisions with the ground and are able to be returned to service often without changing any more than the propellers. This results in fewer events where the platforms require expensive maintenance from repair facilities. Most of these UAS dominate the consumer market, weigh up to 4 lbs and carry a camera payload weighing up to 1.5 lbs.¹⁵ The endurance of these UAS vary from 10 - 30 minutes (average 20 minutes) and tend to use proprietary batteries designed by the manufacturers.



Figure D - 1 - Multi-Rotor UAS with Monocoque Body Construction

D.1.2 Multi-Rotor with Collapsible, Modular, or Foldable Construction

In UAS with modular construction, the arms and fuselage (main body) are two completely different parts. The arms are mechanically joined to the main body and, in many cases, can be detached or folded when needed (the DJI Inspire is an exception to this). UAS under this category can be of quadcopter, hexacopter, octocopter or other configurations. Figure D - 2 shows several UAS in this group. In a modular construction, each part of the UAS has its own material characteristic and different mechanical designs. Unlike a continuous body with smooth contours, the fuselage of a modular UAS is more likely to have sharp edges, and an example of this is the upper and lower star plates in the DJI spreading wing series of aircraft (EX: the DJI S1000+ shown in Figure D - 2). For a UAS with many sharp edges, many of the potential contact areas during a collision are smaller, which yields high energy density that can cause penetration or laceration injuries. Moreover, the arms and main body are made of strong materials to lift heavy payloads and resist damage. This improves the structural rigidity but reduces the frangibility (or energy absorption) of the UAS. These UAS are predominantly used by the commercial industry due to their cost, and the construction allows the customers to carry heavy payloads/gimbals, swap different payloads quickly and change defective parts more efficiently. These UAS can weigh between 2-55 lbs and carry payloads that weight 0.5-20 lbs. The endurance of these UAS varies between 10-60 minutes.



Figure D - 2 - Multi-Rotor UAS with Modular Construction

D.1.3 Fixed Wing UAS with Flying Wing Configuration

In UAS with Flying Wing configuration, the wings blend into the fuselage. Figure D - 3 depicts several flying wing UAS. The wing root chord is large and typically spans more than 50% of the fuselage length. These platforms tend to have monocoque or unitary foam bodies. Many of the flying wing aircraft use a pusher prop, which can reduce laceration injuries in head-on impacts with people. In most of these UAS, the forward fuselage is wide and rounded, thus, providing a larger surface area of contact with humans during a ground collision, which tends to reduce injury severity.^{7,145} These UAS are often used by hobbyist and for commercial applications and weigh between 1-7 lbs. One exception to this is the In Situ ScanEagle, which has a max gross takeoff weight of 48.5 lbs.¹⁴⁶ Because of the relatively low MGTOW and construction of most of the flying wing UAS, their impact energy is correspondingly low, thus, causing minimum injuries. The endurance of these UAS varies from 30-60 minutes. Flying wing UAS of higher MGTOW are uncommon because of the larger amount of material that is required in the construction. Moreover, large UAS of standard configuration can achieve similar capabilities by using less material.



Figure D - 3 - Fixed Wing UAS with Flying Wing Configuration

D.1.4 Fixed Wing UAS with Standard Configuration

Fixed wing UAS of standard configuration are commonly used by hobbyists and commercial operators. Figure D - 4 depicts a few FW UAS with standard configurations. In the hobbyist market, the UAS MGTOW ranges from 2-8 lbs and the payload weighs less than 2 lbs. The endurance of these UAS is usually less than an hour. In the commercial market, the MGTOW ranges from 2-55 lbs and they carry payloads weighing up to 20 lbs. The commercial UAS weighing less than 10 lbs have an endurance of 1-2 hours, but UAS with MGTOW greater than

¹⁴⁵ Radi, A. *Human Injury Model for small unmanned aircraft impacts*, Civil Aviation Safety Authority, Monash University, 12/23/2013

¹⁴⁶ ScanEagle Unmanned Aircraft Systems Backgrounder

<http://www.boeing.com/farnborough2014/pdf/BDS/ScanEagle%20Backgrounder%200114.pdf>, Accessed 05/20/2016

10 lbs can fly for 1 - 10 hours. Compared to a flying wing UAS of similar MGTOW, fixed wing UAS with standard configuration can cause more injuries due to their conical shaped nose cones, tractor (front-mounted) props and thin wings. Fixed wing UAS with MGTOW over 15 lbs can pose a significant threat during ground collisions with humans, buildings and vehicles because of their streamlined shape and high mass, which both contribute to high impact KE. However, few UAS in this configuration have breakaway wings to reduce energy transfer during collisions. While the focus of the initial portion of the A4 project has been on mUAS and sUAS, the standard configuration fixed wing UAS can easily be the same size as manned aircraft, whether light sport aircraft (U.S. military Shadow V2 at 467 lbs¹⁴⁷) or passenger aircraft (Global Hawk at 32,250 lbs¹⁴⁸).



Figure D - 4 - Fixed Wing UAS with Standard Configuration

Knowledge Gap: Is there a gross weight threshold above which breakaway wings cannot be used to mitigate ground collision severity?

D.1.5 Helicopter-Style Rotary Wing UAS

Helicopter-Style UAS tend to be restricted to higher-end hobby, commercial and military applications. Their inherent mechanical complexity and dynamic instability, with requirements for more sophisticated control laws, generally place them at a higher average price point than the previously described categories. Additionally, they tend to require greater and more specialized piloting skills than the other types of UAS and are less resilient to minor crashes when operated by the general public. Figure D - 5 shows four examples of Helicopter-Style RW UAS. These aircraft weigh between 5-55 lbs. and have payload capacities between 4 – 15 lbs. Aside from the terminal kinetic energies associated with high maximum gross weights, the most

¹⁴⁷ <http://www.textronsystems.com/what-we-do/unmanned-systems/shadow-family>, Accessed 05/20/2016

¹⁴⁸ <http://www.af.mil/AboutUs/FactSheets/Display/tabid/224/Article/104516/rq-4-global-hawk.aspx>, Accessed 05/20/2016

hazardous design attribute of these aircraft is their large main rotor that has high rotational KE and presents a laceration risk to people regardless of the aircraft size. The vehicle and rotor can pose a lethal blunt trauma risk for all but the smallest of these aircraft.



Figure D - 5 - Helicopter-Style RW UAS

Qualitative Discussion of Multi-Rotor, Fixed Wing, and Helicopter-Style UAS Design Features

D.2 Fuselage Material, Design and Collision Severity

Monocoque Multi-Rotor UAS:

The monocoque fuselage is typically made of plastic material of varying rigidity. Certain UAS in this category (EX: 3DR Solo, on right in Figure D - 6) use materials of slightly higher rigidity to resist damage during collisions. Such UAS will cause more injury than the UAS using materials of lower rigidity (Ex: DJI Phantom 4, on left in Figure D - 6). The fuselage on certain UAS (Ex: DJI Phantom) has less sharp edges, which increases contact surface area during collision and reduces injury risk. UAS with sharp edges (Ex: 3DR Solo) increase risk of laceration injuries. UAS with longer arms or wings are more likely to have an offset collision with objects. This converts most of the impact KE into rotational energy, thus, transferring less energy to the object.



Figure D - 6 - Smooth Contours on Fuselage (DJI Phantom on left); Sharp Edges on Fuselage (3DR Solo on right)

Modular, Collapsible, and Folding Frame Multi-Rotor UAS:

Because the modular construction aircraft tend to use different materials than the monocoque aircraft, these UAS are assumed to have low coefficient of restitution values, and transfer more energy during collisions. The relatively strong and rigid arms on most of these UAS are made of carbon fiber rods or hardened plastic. UAS that use hardened PCB boards as the main body (left in Figure D - 7) can cause laceration injuries. Other UAS that use a plastic or carbon fiber case around the PCB board are small and rigid (right in Figure D - 7). Following a collision, there is little distortion of the modular UAS fuselage, thus, there is maximum energy transfer to the object. Also, owing to their larger size, offset collisions are more common with these UAS. Much of the UAS translational energy is converted into rotational energy in an off-set collision and less is transferred to the impacted object. However, as shown in Figure D - 8, off-set collisions from UAS with gross weight greater than 5 lbs will still transfer significant amounts of energy. It is important to note that the offset impact modeling in Figure D - 8 portrays a UAS in horizontal flight impacting a static object and that the UAS in this model only has 2 degrees of freedom – horizontal translation and rotation in the horizontal plane. This lower fidelity modeling was completed as a means of gaining initial insight into collisions during the first half of the A4 project while ERAU was developing and calibrating much higher fidelity simulations.



Figure D - 7 - Sharp edges on Fuselage main body (left); Plastic casing on the main body (right)

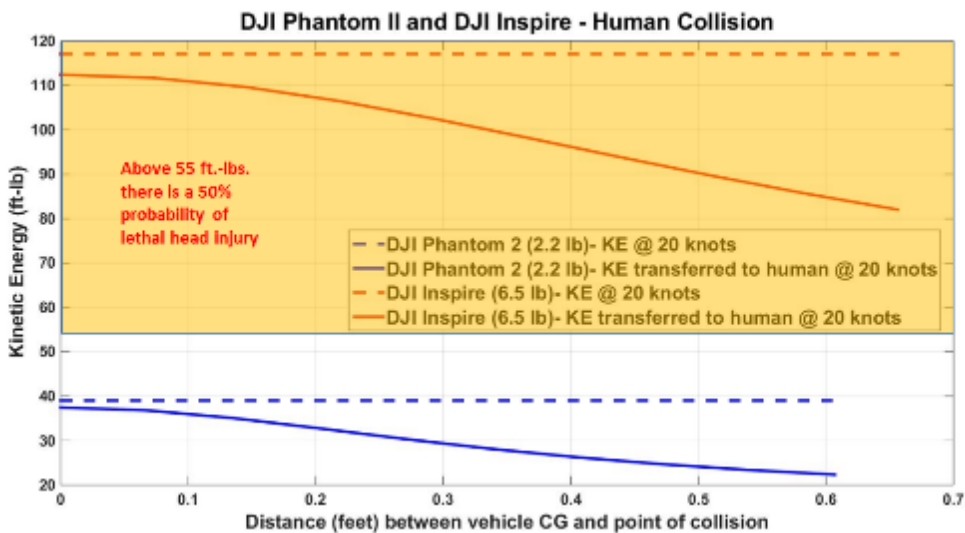


Figure D - 8 - Low Order Off-set Collision Modeling of Multi-Rotor UAS Offset Impact

Flying Wing FW UAS:

Within the models found during the literature survey, all of the flying wing UAS used by hobbyists are purely made of foam-based material, while the flying wing UAS used in the commercial market tend to be made of foam material with carbon composites or hardened plastic on the leading edges. The fuselage and wing leading surfaces are rounded and provide maximum area of contact with a human during a collision (Figure D - 9). Collisions with these UAS transfer comparatively less energy to humans and are more likely to cause only minor injuries. The propellers on most flying wing UAS are rear-mounted. Thus, direct collision with the fuselage centerline is not as severe as with a tractor propeller. Off-set collisions are probable, simply based on the ratio of center area to total frontal area. In some UAS, the wings may break off on impact and this reduces overall energy transferred to humans.



Figure D - 9 - Fixed wing UAS with conical-shaped fuselage and fore-mounted engine/propellers (Upper Red/White aircraft); Rounded Leading Edge and Nose Cone (Lower Black and Yellow aircraft)

Standard Configuration Fixed Wing UAS:

Based on the literature survey, many fixed wing UAS used for hobbyist applications are made completely of foam material or foam-covered plastic and weigh less than 10 lbs. Fixed wing UAS used in commercial applications and weighing less than 10 lbs are made of an internal foam structure covered with plastic or composites for improved durability. Fixed wing UAS used in commercial and military applications and weighing greater than 10 lbs are constructed using a variety of materials including composites and aluminum. The propellers are either rear-mounted or fore-mounted. However, head-on collision with a conically-shaped fuselage and a tractor propeller (EX: red aircraft in Figure D - 9) seems likely to cause significant injury. These UAS behave similarly to the flying wing UAS during an off-set collision. However, these UAS cause more injuries because their wing leading edge is less rounded than those on flying wings. For large, heavier UAS with composite and/or metal construction, the energy absorption characteristics of the airframe will tend to be low, thus it is expected that there will be higher energy transfer and greater risk of injury. Based on the current level of information in the

literature survey and limited modeling, it is assumed that larger fixed wing UAS (above 55 lbs and approaching the weights of light sport aircraft) will readily exceed impact energy lethal thresholds and will require commensurate levels of operational restriction or certification.

Helicopter-Style RW UAS:

All helicopter-style UAS use plastics, carbon composites and aluminum for construction of the body, main rotor, tail rotor and landing gear. A thin plastic cowling is commonly used as an outer cover for the fuselage. Based on the material and design requirements for structural stiffness, helicopters are assumed to have very limited energy absorption or frangibility during a collision. A collision with a helicopter-style UAS in most orientations will always involve collision with the rotor. Main rotor strikes are likely to produce significant lacerations. Larger models like the Schiebel Camcopter (Figure D - 21) may be an exception to this generalization because the fuselage size is comparatively large with respect to the rotor, and the probability of being hit by the fuselage is greater. The great mass (440 lbs MGTOW¹⁴⁹) of that vehicle creates a serious risk to any person or structure that it collides with because it is almost as large as a kit airplane.

D.3 Propeller Materials, Design and Collision Severity

All Multi-Rotor UAS:

UAS Manufacturers use materials like carbon-fiber-reinforced polymer (CFRP), fiber glass reinforced nylon, etc. to make propellers. UAS below 5 lbs typically use flexible propellers of 9 inches in diameter. UAS weighing more than 5 lbs typically use 10-inch diameter propellers that are rigid to prevent fluttering. Flexible propellers can bend and break during collision, thus, reducing energy transfer to humans and satisfying requirements for frangibility. However, flexible propellers are typically thin and have sharp leading edges that can easily cause laceration injuries. A few exceptions have leading edge corners that are rounded and thick, which could reduce laceration risk (Figure D - 10). However, this is an assumption based on current knowledge and requires further testing to validate. Rigid propellers, like carbon fiber propellers, are less likely to break following an impact and pose a higher laceration risk because of their resilience. These blades are more likely to remain intact after one or more impacts, so they remain a cutting risk until the propellers stop. Several UAS have shrouded or guarded propellers that prevent laceration injuries during a collision (Figure D - 11). However, if a human hand gets accidentally stuck between the guards and propellers, the laceration injury is severe due to the difficulty in quickly extracting the hand.¹⁵⁰

¹⁴⁹ <https://schiebel.net/products/camcopter-s-100-system-2/>, Accessed 05/20/2016

¹⁵⁰ https://www.youtube.com/watch?v=ji3Hii_LZOc&oref=https%3A%2F%2F, Accessed 05/10/2016



Figure D - 10 - Propeller with Sharp LE (left); Propeller with Sharp LE and Rounded Corners (right)



Figure D - 11 - Propeller Guards (left); Shrouded Propellers (right)

All Fixed Wing UAS:

Propellers used in fixed wing UAS use similar materials as multirotor UAS. The propeller diameter on fixed wing UAS increases as the weight of the UAS increases, because there are upper limits on blade loading that cannot be exceeded if the aircraft is to be able to fly. Higher diameter propellers (above 12 inches) are more rigid than smaller diameter propellers and cause severe blunt and/or penetration injuries on impact with humans.¹⁵¹¹⁵² As a warning, the link in footnote 152 is exceptionally graphic. The propellers on most flying wing UAS are rear-mounted. The propellers on fixed wing UAS of standard configuration are either fore-mounted or rear-mounted. UAS with rear-mounted propellers are comparatively safer than fore-mounted propellers during head-on collisions. The propellers on few UAS fold back when motors are turned off (Figure D - 12).

¹⁵¹ RC Plane Accident, <https://www.youtube.com/watch?v=XZf0k1kWEr4>, Accessed on 05/24/16

¹⁵² RC Plane Accident – Why you shouldn't stay near the propeller!, <https://www.youtube.com/watch?v=tzXyYX7hZvw>, Accessed on 05/24/16

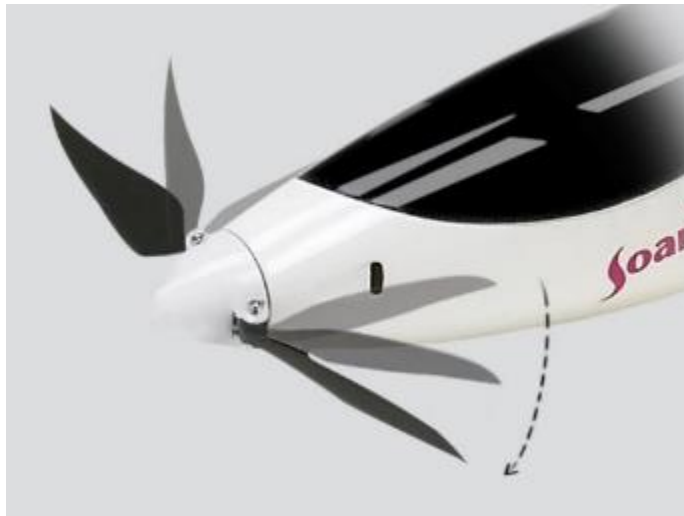


Figure D - 12 - Folding Propellers

Helicopter-Style RW UAS:

The propellers on helicopter UAS have a high density internal foam structure and an external composite or plastic covering. Unlike multi-rotor or fixed wing propellers, these propellers are all rigid. These propellers typically have high tip speeds. An analysis of a Rotomotion SR20¹⁵³ indicated tip speeds of 260-435 ft/sec. This combination of rigid design, high density materials and high tip speed produces high rotational energies and can cause significant lacerations and even lethal injury due to blunt trauma.

D.4 Battery location and Collision Severity

Monocoque Multi-Rotor UAS:

All UAS with a monocoque construction use Lithium Polymer batteries. Most of these batteries are mounted inside the fuselage (Figure D - 13). LiPo batteries are inherently hazardous but are provided with protection methods that identify and/or prevent certain battery failures. Most consumer UAS use smart batteries with hard-plastic cases that provide battery status to user, increase battery safety and offer resistance to minor physical abuse.¹⁵⁴ During a ground collision, internal batteries may experience minor impact loads and be safe for continued operation. Internal batteries that experience strong impact loads during ground collision may begin to develop defects or get crushed. Sufficient data is unavailable to address this issue. However, internally-mounted smart LiPo batteries with hard-plastic casing are assumed to be safer than other types of LiPo batteries.

¹⁵³ http://www.tetracam.com/PDFs/SR20_uav_sheet.pdf Accessed on 05/24/2016

¹⁵⁴ <http://store.dji.com/product/phantom-3-intelligent-flight-battery>, etc., Accessed on 05/24/2016



Figure D - 13 - Smart Battery and Internal Compartment (left) Battery Held Firmly inside Fuselage (right)

Modular, Collapsible, and Folding Frame Multi-Rotor UAS:

Some folding-frame multi-rotor UAS, like the DJI Inspire, have the batteries mounted inside the fuselage in the same manner as monocoque UAS. For all other types of UAS, the batteries are mounted either above or below the fuselage with Velcro, zip ties, etc. (Figure D - 14). During ground collisions, the external batteries strapped using Velcro or zip ties can separate from the main body and strike surrounding objects. If the impact force generated is very high, the batteries can burst and catch fire.

UAS weighing more than 10 lbs use high voltage, high capacity batteries that have a soft plastic covering (EX: the blue material in the left image of Figure D - 15). Previous studies show that batteries of higher voltage and capacity burn for a longer time at elevated temperatures.¹⁵⁵ Such batteries can pose a fire risk to buildings and vehicles depending on where they fall, e.g. a wooden structure or a forested area during a dry season.



Figure D - 14 - Battery Mounted above Main Body with Velcro (left); Battery Mounted Below Main Body (right)

¹⁵⁵ Summer, Steven M. "Flammability Assessment of Lithium-Ion and Lithium-Ion Polymer Battery Cells Designed for Aircraft Power Usage," US Department of Transportation, Federal Aviation Administration, MONTH? 2010.

Flying Wing FW UAS:

Flying wing UAS use internally mounted LiPo batteries of moderate capacity. These batteries are protected from impact loads by the surrounding foam material, decreasing the risk from battery failure due to impact in this category of UAS. The batteries must be firmly held inside the fuselage to prevent any displacement within the fuselage during ground collision. Otherwise, the shifting batteries may impact onto other sensors and/or force out the casing on the UAS (Figure D - 15).



Figure D - 15 - LiPo battery Held Firmly inside FW UAS (left), LiPo Battery Mounted Loosely inside FW UAS (right)

Standard Configuration Fixed Wing UAS:

Most of the UAS in this category use LiPo batteries, but a few UAS with MGTOW above 40 lbs use internal combustion engines (Figure D - 16). The Boeing Insitu Scan Eagle uses heavy fuel, i.e. kerosene-based fuels like JP8 and the Shadow uses 100L aviation fuel.^{146,147} Both of these fuels pose two problems during a ground collision. First, they are toxic and can lead to contamination of the ground if spilled during a collision. Fortunately, the fuel capacity is lower than a manned aircraft. Additionally, they are both ignition sources and could, under the right conditions, lead to secondary fires following a ground impact. The batteries are internally-mounted, similar to the flying wings. The commercial fixed wing UAS use strong composites material that holds the fuselage together and protects batteries and engines during collision. However, large impact forces generated during severe collisions can cause batteries to fail or break fuel tanks. This may subsequently lead to fire.



Figure D - 16 - Rear-Mounted Engine on a 50 lbs UAS (left); LiPo Batteries inside the Fuselage of a 33 lbs UAS (right)

Helicopter-Style RW UAS:

Helicopter UAS use either LiPo batteries or internal combustion engines for propulsion. For example, the Schiebel Camcopter S-100 (Figure D - 21) is powered by a 55hp Wankel engine and has a 15.8 gallon fuel tank for 100LL aviation fuel.¹⁴⁹ The quantity of fuel carried by these vehicles is on the order of a subcompact car. Leaked fuel can either cause a fire if there is an ignition source or requires hazmat cleanup of the fuel spill. In Helicopter UAS, the batteries are mounted either on the sides of the fuselage or in the belly of the fuselage (Figure D - 17). During a ground collision, side mounting batteries pose more risk of failure than internal mounting.



Figure D - 17 - Batteries on Side of Fuselage (left); Batteries inside the Fuselage Belly (right)

D.5 Landing Gear Materials, Construction, and Collision Severity

Monocoque Multi-Rotor UAS:

Landing gear on UAS with monocoque construction are made of the same material as the fuselage. The different designs of landing gear are comprised of skid landing gear with pointed ends, pointed cantilever landing gear, continuous landing gear, etc. (Figure D - 18). During a collision, the pointed and skid landing gear can cause more injury than continuous landing gear due to the high energy density associated with smaller contact area. Direct collision with landing gear causes the UAS to spin away or into the person, thus, either preventing or increasing injury probability. Due to the small size of UAS, it is almost certain that collision with landing gear will also involve collision with the payload.



Figure D - 18 - Skid Landing Gear (left); Pointed Cantilever Landing Gear (center); Continuous Landing Gear (right)

Modular, Collapsible, and Folding Frame Multi-Rotor UAS:

As UAS MGTOW increases, landing gear material rigidity increases to support the UAS weight. Carbon composites are typically used for the landing gear. Most of these UAS use pointed landing gear to eliminate the additional material and weight of a continuous landing gear. Due to the higher MGTOW and associated impact loads, collision with pointed gear can cause penetrating injuries to humans. Additionally, the UAS may spin into the person, causing more injuries during a secondary collision. Because the landing gear are spread wide apart, collision with landing gear may not always include collision with the payload. In some UAS, the landing gear can be retracted (Figure D - 19). Such a feature provides a clear field of view for the

payload during operation, but following a failure, the payload or the arms will be the first components to strike an object.



Figure D - 19 - Retracted Landing Gear

Flying Wing Fixed Wing UAS:

To date, the flying wing fixed wing UAS found in the literature survey do not use any landing gear. They are recovered by either skid-landing or deep stall landing.

Standard Configuration Fixed Wing UAS:

UAS with MGTOW less than 10 lbs are mostly hand-launched and recovered by skid-landing or deep stall landing. They do not use any landing gear. UAS with MGTOW greater than 10 lbs are launched using a catapult, rail or runway and recovered by skid-landing or runway-landing (Figure D - 20). All these UAS have a landing gear that protrudes out of the fuselage. These are made from strong composite material and can transfer high energy during collision. Moreover, all UAS with externally mounted payloads have large landing gear to protect the payload.



Figure D - 20 - Fixed Wing UAS with Skid Landing Gear (left); Standard Landing Gear (right)



Figure D - 21 - Camcopter S-100 Landing Gear

Helicopter-Style RW UAS:

All Helicopter UAS have a skid type landing gear to support the weight of the vehicle. Figure D - 21 shows that these skids are rigid and likely to have small contact areas on bottom or at the ends.

D.6 Payload Location, materials and Collision Severity

All Multi-Rotor UAS:

Multicopter UAS generally have payloads attached beneath the fuselage main body, between the legs of the landing gear. These payloads range from small cameras to DSLR cameras or custom payloads that weigh as much as 20 lbs. The camera payloads are typically a metal structure



Figure D - 22 - Small Gimbals and Camera (left); Large Gimbals and Cameras (right)

enclosed inside a plastic casing. Although small in size, these camera payloads are dense and rigid. Direct collision with these payloads will increase the severity of injuries when compared to other portions of the aircraft when colliding with a person at the same speed. Moreover, the payload structure is a sphere or cuboid supported by a gimbal with many edges. The energy density of a payload impact is very high because of the small contact areas (Figure D - 22). Also, strong composite material is used for camera gimbals and mounts that integrate various sensors. As payloads become heavier, their structure has many flat and curved edges. Human collisions with heavy payloads can lead to severe injuries that can be lethal, especially in

platforms with retractable landing gear that do not mitigate energy absorption upon collision with people or property. Some new UAS with camera payloads and landing gear inside the fuselage reduce the risk of injury (Figure D - 23). However, these type of vehicles are typically not found on multi-rotor platforms. Larger gimbals holding large cameras can have sharp edges that can increase the severity of injury due to a collision.



Figure D - 23 - UAS with Internal Payloads or Landing Gear

All Fixed Wing UAS:

Fixed Wing UAS weighing less than 10 lbs typically use camera payloads that are located inside the fuselage with the lenses protruding out through a hole in the fuselage (Figure D - 24). During any collision, the payload is secure inside the fuselage and has no direct contact with any object. In some UAS, a part of the imaging payload extends out of the fuselage to provide a larger field of view. The payloads are typically of low weight and do not add to the collision severity of the UAS. For larger UAS, correspondingly larger payloads are mounted either partially or completely outside the fuselage. Some payload mounts are of high strength designed to protect expensive sensors. However, these can incite severe injury to humans. If the payloads are designed to break off from the UAS during collisions, the impact energy transferred to humans can be reduced.

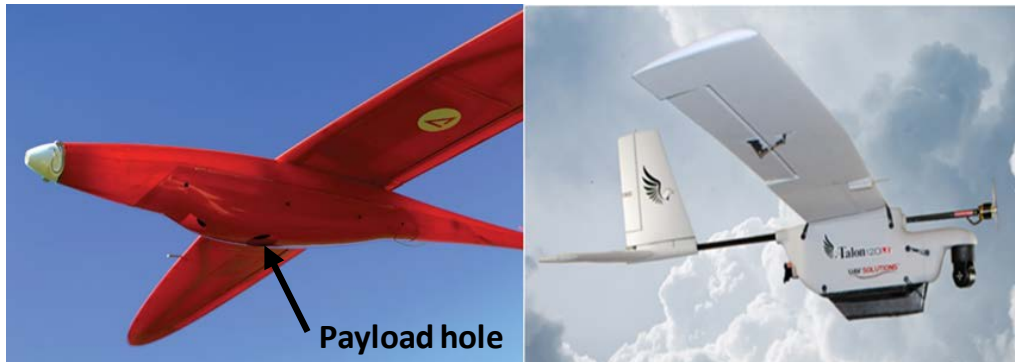


Figure D - 24 - Payload inside the Fuselage (left); Payload Protruding Outside the Fuselage (right)

Helicopter-Style RW UAS:

Most helicopter-style UAS carry the same payloads as fixed wing UAS of similar MGTOW. The payloads on a helicopter are externally mounted, either under the fuselage nose or between the landing gear, and can cause injury during collision. Hobbyist helicopter-style UAS typically do not carry any payloads.

D.7 Guidance, Navigation and Control (GNC) Systems

All UAS use GNC systems for operators to control their flight. When a UAS fails mid-flight due to loss of power or a loss of control, having multiple redundancies of control is beneficial. The redundant GNC system may not always recover the aircraft to a level flight condition, but may prevent it from an uncontrolled descent. Consumer and commercial UAS provide the users/operators multiple redundant control systems like RC receivers, iPad, iPhone, PC, GPS-based navigation or vision-based autonomous navigation. With these types of hardware configurations, these aircraft can be operated in a full GPS-guided and stabilized configuration from a ground control station using way point navigation. Many such systems are being delivered with a variety of autonomous flying modes even though current regulations require the vehicle to be in visual line of sight of the operator. Consumer grade and commercial grade systems can be flown in a combination of stabilized control modes with the pilot flying the platform using visual line of sight to avoid obstacles with a few recent systems including obstacle avoidance systems integrated with GNC. The systems typically have a means of degrading to a lower level of stability when manually selected by the pilot or when system failures occur, but not all systems degrade gracefully. Hacking of these systems and electrical interference can cause failure modes that have led to erratic behavior and collision with people or property on the ground. Current GNC systems typically do not include obstacle detection for avoiding ground and mid-air collisions. In GPS-denied areas, unless the pilot is adept at manual flight control, current GNC systems do not help prevent collisions. Few GNC systems used in multirotor UAS, excluding quadcopters, can sustain flight or a controlled descent and land the aircraft immediately when a motor or propeller fails. In fixed wing UAS, following a loss of propeller, etc. the GNC system can put the aircraft into a glide profile. Because glide airspeed is well below that of a dive at terminal airspeed or even typical cruise speeds, there is lower impact KE and thus reduced collision severity. However, if the GNC system fails following a loss of power, the multirotor and helicopter UAS tend fall as an inert mass with aerodynamic drag only to slow their descent.

D.8 Existing Mitigations

In addition to the design and functional features described in the previous sub-sections, manufacturers employ some additional systems to warn users of a possible collision or reduce the severity of collisions. One common mitigation among all categories is the throttle hold switch that enables power-on operations and system checks without arming the ESCs. This prevents random motor starts and allows users to work on the aircraft and then move away prior to starting the motors.

Multirotor UAS:

Most consumer UAS add an on-board visual and/or audible warning system that helps the user to identify battery power levels, flight status, etc. Additionally, these warning systems also alert the user and nearby people of a UAS in an uncontrolled descent, thus, providing some time to take evasive actions and avoid collision. Parachutes (Figure D - 25) can be used on multirotor UAS to reduce the total KE in an uncontrolled descent and minimize the severity of impact. Vehicles such as the Altus X-8 - by CNN under the FAA's Pathfinder Program - have integrated parachute systems to mitigate descent rates for flight over people. Anecdotally, 18 ft/sec is the lower limit rate of descent for parachutes. Below this rate of descent, the upward airflow into the canopy does not have enough dynamic pressure to maintain a fully inflated canopy. Typically, manufacturers specify that their parachutes are sized for 18-24 ft/sec rate of descent. New parachute systems are being developed to decrease deployment and deceleration time to reduce injury to people on the ground and damage to the vehicle and payload. Parazero demonstrated such a capability at the 2016 AUVSI symposium with a patent pending design for near-zero deployment time using a novel configuration.¹⁵⁶ Another possible mitigation strategy is electronic. For example, the Yuneec Typhoon H has a built-in collision avoidance feature that is meant to protect the aircraft, people, and property.¹⁵⁷



Figure D - 25 - Visual Warning Systems on Multirotor UAS (left); Parachutes on Multirotor UAS (right)

¹⁵⁶ <http://dronelife.com/2016/03/14/parazero-safeair-parachute-drone/>. Accessed 05/25/2016

¹⁵⁷ "Typhoon H." Yuneec. 2016. <http://www.yuneec.com/Typhoon-H..> Accessed April 15, 2016.

Knowledge Gap: Additional testing is required to validate parachute systems for small multi-rotors and develop operational standards for these systems for flight over people. UAH is planning to submit a white paper in June 2016 that proposes to create a survey of UAS parachute designs and conduct instrumented flight testing of the parachute performance to develop a statistically significant database of parachute deployment times (command to inflation time), deceleration times (deployment to steady state drop velocity time), rates of descent, and distances that vehicles fall during deployment. It is expected that the flight testing will enable researchers to provide comments regarding the reliability of different designs and considerations for successful use of the parachutes to lower impact velocity/energy.

Some multi-rotor platforms are beginning to stop their rotors upon deployment of the parachute under various aircraft conditions that result from failures of one or more rotors, violent shaking of the vehicle, or when the aircraft achieves attitudes beyond certain parameters as shown in the Altus Delta LRX Specification.¹⁵⁸

¹⁵⁸ http://media.wix.com/ugd/c4706c_3216ab35cfd340ce8c0b09fa6c1c49f3.pdf, Accessed 05/29/2016

FW UAS:

Fixed wing UAS often do not adopt any warning systems used in consumer multicopter UAS. However, some UAS may have anti-collision lights on the wing for the pilots and other airspace users to identify aircraft orientation (Figure D - 26). Large fixed wing UAS use parachutes as a safety mechanism for uncontrolled descent. These parachutes reduce the descent speed of the UAS and minimize the ground collision energy of the aircraft (Figure D - 26). Many of these vehicle types use mitigations such as breakaway wings, foam wings and fuselage, foldable propellers upon engine failure, and glide profiles to reduce impact energies and energy transfer to people and property on the ground. Glide profiles following loss of data link or engine loss can allow these vehicles to glide away from groups of people and property into designated safe zones when operated at sufficient altitudes.



D-Figure D - 26 - Fixed Wing UAS with Landing and Position Lights (left) and Parachutes (right)

Helicopter-Style UAS:

Many of these UAS have activated anti-collision lights and warning noises to reduce ground collision severity when the flight management unit is armed along with throttle hold functions. However, there are fewer mitigation measures implemented on these vehicles than many of the other categories.

Appendix E: Knowledge Gap Roundup

Knowledge Gap: FAA Registry data includes vehicle types for commercial operators. Both the aircraft registry and the UAS on-line registry need to be continuously harvested to maintain a clear understanding of actual vehicles that are being used across the National Airspace System (NAS) to refine research focus of the A4 and other tasks.

Knowledge Gap: UAH initially assumed $CR=0.2$ is based on a qualitative assessment of the two colliding bodies, but there was little quantitative rationale. CR values can be calculated experimentally and as such, UAH is developing dynamic modeling for sUAS and human collisions based on the results of the drop testing done at NIAR as part of the Task A11 technical approach. UAH is also beginning finite element analysis modeling, funded internally, to continue examining energy transfer and vehicle deformation during center of mass and offset collision events.

Knowledge Gap: There are large knowledge gaps regarding battery fires. What are the peak fire temperatures and the temperature as a function of time across the range of batteries (Voltage and Ampere ratings) used in sUAS? What is the likelihood of battery separation during impact and the severity of separation, i.e. is it possible to damage a battery during an impact such that it goes into an auto ignition process?

Knowledge Gap: There is no research that correlates adherence to published standards to safe battery operation in a UAS, especially as it relates to ground collision severity. Therefore, further study and testing is needed to test UAS batteries to these standards and define new standards that are more appropriate for ground collisions severity conditions. This will formally verify that batteries meet their design intent including mitigations associated with fire prevention.

Knowledge Gap: A greater number of tests with various UAS LiPo batteries must be conducted to provide a statistically and experimentally sound evaluation of whether LiPo battery fires are a threat to Class C roofs.

Another shortcoming of the FAA fire test is that the LiPo batteries tested were representative of LiPo batteries used onboard manned aircraft. Such high capacity batteries are used only in certain sUAS. Current UAS LiPo batteries vary widely in voltage, capacity, number of cells and even chemistry. In the last six years preceding the FAA tests, much innovation in battery chemistry and manufacturing has occurred.

Knowledge Gap: Similar tests as described in the FAA report should be performed with a wide variety of current UAS LiPo batteries of various sizes, manufacturers and chemistries to better assess the risk of LiPo batteries to people and property.

Knowledge Gap: UAH has submitted a white paper to the FAA entitled *W63 - Lithium Polymer Battery Failure Modes and Effects Analysis* to evaluate LiPo batteries in accordance with existing Lithium Ion battery standards and perform additional drop and ballistic testing. The goal of this experimentation is to determine if the existing standards are sufficient to ensure safe handling and operation of LiPo batteries that are used in UAS applications, versus the consumer electronics applications (laptops and cell phones) to which current Lithium Ion battery standards apply.

Knowledge Gap: The true injury and lethality potential of larger impacting masses, especially masses with substantially different inherent flexibility than those considered by the RCC, is a significant knowledge gap. The drop testing by NIAR, as part of Task A11, and modeling by MSU and ERAU address some of these questions, but further testing of system impacts by UAS and their impacts on people rather than extrapolation from small, metal debris studies is needed. This can be effectively addressed through more research using validated Finite Element Analysis and dynamic modeling to improve the understanding of energy transfer during UAS impact and how that energy transfer is affected by vehicle orientation during impact, vehicle geometry, and vehicle materials.

Knowledge Gap: Development of probability distributions using UAS vehicle aerodynamics and failure modes is vastly different than the ballistic modeling done for space debris and requires additional research to better understand these two characteristics. See Section 4.11 concerning standoff distances and their relationship to severity. This knowledge gap is being addressed in the proposed white papers entitled *W64 - Falling Multi-Rotor Dynamics Study* and *W65 - Probability of UAS Ground Strike to People and Objects*.

Knowledge Gap: With the current lack of data, it is recommended that testing be done on cadavers, pigskin and/or synthetic surrogate tissue to more completely capture the effects of blade diameter on laceration injury risk. Furthermore, while diameter is likely the simplest and most influential factor on cutting risk, blade material and sharpness are still factors, but their effects are more complicated to quantify. It is suggested that follow-on testing be done to quantify the effects of blade material and blade sharpness on the risk for laceration, as there are certain design prescriptions that could result from such testing, for instance, minimum tip/edge radius requirements or upper limits on the stiffness of a blade. KU is planning on the submission of a white paper in July 2016 to investigate probability and severity of laceration due to blade strike to further investigate the role of rotor diameter in laceration hazards.

Knowledge Gap: Blade guard standards exist for consumer grade fans but not for flight worthy stands that must withstand collision while compromising weight. Standards for guards associated with package delivery applications may need additional standards that protect small children's hands from rotors.

Knowledge Gap: At this stage, these probability calculations for aircraft failure footprints lack detail in terms of vehicle dynamics to properly define the potential landing area. Current casualty methods address vehicle dynamics solely with ballistic coefficients typically used for inert debris that has limited aerodynamic properties. UAS platforms may generate significant aerodynamic forces and moments and rarely fail as solely ballistic projectiles. Previous dialogue with the FAA suggested that terminal KE could serve as a potential means of determining target levels of safety for different classes of UAS. Estimation of strike probability provides insight into determining the operational level of safety for sUAS and can be used to establish the minimum requirements of material reliability for these aircraft based on target levels of safety. This knowledge gap is being addressed in the proposed white paper titled *W64 - Falling Multi-Rotor Dynamics Study* and a follow-on effort titled *sUAS Probability of Striking Ground Objects in Operational Areas*.

Knowledge Gap: Just as section 3.5 highlights the potential hazards of LiPo batteries and states that experimental data pertaining to burn temperatures and burn duration is needed in order to

compare with roofing standards, it is also necessary to examine several case studies of crashed sUAS that leak fuel and experience a secondary ignition of that fuel.

Knowledge Gap: The effects of sUAS impacts on automobile structures are unknown. Based on KE and energy density analyses, it seems likely that smaller vehicles can penetrate both tempered and glazed glass, but not metal panels. Larger vehicles are highly likely to penetrate glass and may damage exterior panels.

Knowledge Gap: The fixed wing sUAS parametric information used to generate the Terminal KE to MGTOW relation is of lower quality than the input data used for the multi-rotor analysis. The quality of this analysis can be improved by obtaining CAD files and/or better imagery (vertical planform and head-on images) for fixed wing aircraft and running CFD analysis on both a standard configuration and a flying wing platform. The A4 team plans to focus on improving fixed wing aircraft modeling during the second half of this project.

Knowledge Gap: Current human head injury analysis has been carried out for a multi-rotor sUAS (the DJI Phantom 3). The resulting FEA results show that certain ranges of impact location and velocity do increase the severity of TBI. However, the same information is not available for fixed wing UAVs, such as the PrecisionHawk. In particular, the interest would be in investigating the worst case scenarios for TBI due to impact with a fixed wing sUAS. This proposed analysis would fill the knowledge gap of injury severity to the human head and associated TBI for a medium size UAV.

Knowledge Gap: As a continuation of the ongoing study for micro and medium size UAV impacts on the human head, a detailed analysis needs to be conducted on the injury metrics for the human neck. Here, an anatomically accurate computational model of the human neck, along with the human head, is essential. Biomechanical analysis of the C1–C7 vertebrae and the brain stem/spinal cord is critical for quantifying injuries to the neck.

Knowledge Gap: A vibrational analysis of the human head and UAV is critical to understand the magnification of lethality during a UAV–head collision that leads to vibrations within the range of resonant frequencies of the human head and brain. The hypothesis is that the potential damage to the human brain from vibrations can be more detrimental than the initial impact.¹⁵⁹

Knowledge Gap: To improve upon the existing models for micro and medium size UAS, realistic material properties for various systems/components will be included. These simulations will provide more realistic physical behavior of both the UAS and the human.

Knowledge Gap: UAS are often noisy and noticeable to people operating near them. It has been reported that there are substantial numbers of injuries associated with lacerations to hands and arms. Therefore, we plan to study the influence of posture when people are responding to the UAS by reaching out to deflect it or shielding their bodies with their arms and hands (Figure 66). Such injuries are expected to be on the upper extremities. Several typical scenarios will be studied.

¹⁵⁹ Säljö A., Arrhén F., Bolouri H., Mayorga M., Hamberger A., “Neuropathology and Pressure in the Pig Brain Resulting from Low-Impulse Noise Exposure,” *Journal of Neurotrauma*, Vol. 25, 13971397-14061406, 2009.

Knowledge Gap: The approach to study the torso impact response can be extended to the head/neck complex. The head/neck has different injury mechanisms than the torso. Specifically, the head injury, including the skull fracture and brain concussion, is highly related to the translational and rotational accelerations induced by blunt impact. The neck injury is dominated by the combined effect of axial compression and lateral bending. Comprehensive simulations will be conducted to establish the relationship of response and impact parameters (type of UAV, velocity, angle and impact location etc.). Figure 67 shows a typical scenario for the simulation. The model predictions will be compared with the results based on the real head models.

Knowledge Gap (MSU): The torso impact simulations have only shown the effects of an impact to a person's front. Given the different anatomy (spine versus ribs of abdomen) and biomechanics (extension versus flexion) after impact, it is likely that trends and assumptions from frontal impact modeling are not representative of posterior impact scenarios. It is critical to evaluate posterior impacts, because anyone hit from behind is much less likely to be bracing for impact or shielding themselves. Figure 68 shows the torso back impact simulations that will be performed using the same approach for frontal impact.

Knowledge Gap: Frangibility can be helpful to decrease kinetic energy imparted to persons on the ground from impact with a rotor boom or other appendage, depending on UAS speed and boom frangibility factor. A process to assess the degree of relief due to frangibility has been established, but has not been verified through test. If this injury mitigation strategy is to be embraced, verification testing a small number of quadcopters is appropriate.

Appendix F: Laceration Testing Materials

Table F - 1 - Blades and Motors Used In Testing

Blades

Molded Plastic	DJI Phantom 3 9450 APC 1147 14" Glider Folding Blades
Carbon Fiber Reinforced	DJI Phantom 3 9450
Carbon Fiber Epoxy	DJI Phantom Tri Blade 9450 12" Folding Blades 13" Blades

Motors

Brushless	DJI 2312a Ati 2628/10 HiMax HC4220-770
-----------	--

Appendix G. Results of UAS/ATD impact simulations

Table G - 1 - Aluminum Fixed Wing UAS

Impact angle (°)	Impact velocity (ft/s)	Kinetic energy (ft·lbf)	Internal energy dissipated by ATD chest (ft·lbf)	Energy absorbing ratio	VC _{Max}	
					ft/s	m/s
90	16.4	23.9	19.4	0.81	0.8	0.2
90	26.2	61.1	50.4	0.82	2.4	0.7
90	36.1	115.5	98.0	0.85	4.9	1.5
90	45.9	187.1	163.8	0.88	8.3	2.5
90	59.0	309.5	232.7	0.75	11.7	3.6
90	98.4	859.2	447.0	0.52	24.3	7.4
80	16.4	23.9	19.4	0.81	0.8	0.2
80	26.2	61.1	49.2	0.81	2.3	0.7
80	36.1	115.5	89.4	0.77	4.7	1.4
80	45.9	187.1	152.1	0.81	8.2	2.5
80	59.0	309.5	225.9	0.73	13.2	4.0
70	16.4	23.9	16.8	0.70	0.6	0.2
70	26.2	61.1	42.8	0.70	1.6	0.5
70	36.1	115.5	77.7	0.67	3.1	1.0
70	45.9	187.1	137.2	0.73	5.5	1.7
70	59.0	309.5	203.4	0.66	10.4	3.2
70	72.2	462.0	263.1	0.57	13.9	4.3
60	16.4	23.9	13.7	0.57	0.3	0.1
60	26.2	61.1	32.8	0.54	0.9	0.3
60	36.1	115.5	73.6	0.64	2.4	0.7
60	45.9	187.1	114.5	0.61	3.6	1.1
60	59.0	309.5	143.9	0.46	6.4	2.0
60	72.2	462.0	209.2	0.45	7.5	2.3
50	16.4	23.9	11.4	0.48	0.2	0.1
50	26.2	61.1	31.8	0.52	0.5	0.1
50	36.1	115.5	55.0	0.48	0.8	0.2
50	45.9	187.1	88.7	0.47	1.2	0.4
50	59.0	309.5	116.8	0.38	2.7	0.8
50	72.2	462.0	190.3	0.41	4.1	1.2
50	85.3	645.5	226.1	0.35	5.5	1.7

40	16.4	23.9	8.4	0.35	0.1	0.0
40	26.2	61.1	21.0	0.34	0.2	0.1
40	36.1	115.5	36.2	0.31	0.5	0.1
40	45.9	187.1	59.7	0.32	0.8	0.2
40	59.0	309.5	90.8	0.29	1.2	0.4
40	72.2	462.0	148.6	0.32	1.9	0.6
40	85.3	645.5	202.6	0.31	2.7	0.8
40	98.4	859.2	214.8	0.25	3.6	1.1
30	16.4	23.9	6.7	0.28	0.0	0.0
30	26.2	61.1	17.2	0.28	0.1	0.0
30	36.1	115.5	27.4	0.24	0.3	0.1
30	45.9	187.1	38.3	0.20	0.4	0.1
30	59.0	309.5	52.3	0.17	0.8	0.2
30	72.2	462.0	61.6	0.13	1.2	0.4
30	85.3	645.5	172.2	0.27	1.7	0.5
30	98.4	859.2	191.5	0.22	2.2	0.7

Table G - 2 - Engineering Plastic Fixed Wing UAS

Impact angle (°)	Impact velocity (ft/s)	Kinetic energy (ft·lbf)	Internal energy dissipated by ATD chest (ft·lbf)	Energy absorbing ratio	VC _{Max}	
					ft/s	m/s
90	16.4	12.6	9.3	0.74	0.4	0.1
90	26.2	32.3	24.0	0.74	1.1	0.3
90	36.1	61.1	43.7	0.72	2.2	0.7
90	45.9	99.0	70.6	0.71	3.6	1.1
90	55.8	145.9	102.6	0.70	5.8	1.8
90	65.6	202.0	137.2	0.68	8.1	2.5
90	75.4	267.1	163.3	0.61	10.5	3.2
90	85.3	341.4	185.9	0.54	11.8	3.6
80	16.4	12.6	9.2	0.73	0.4	0.1
80	26.2	32.3	22.8	0.71	1.0	0.3
80	36.1	61.1	40.6	0.66	1.9	0.6
80	45.9	99.0	67.5	0.68	3.4	1.1
80	55.8	145.9	101.7	0.70	5.6	1.7
80	65.6	202.0	131.0	0.65	7.7	2.4
80	75.4	267.1	162.2	0.61	10.3	3.1
80	85.3	341.4	187.9	0.55	11.6	3.5
70	16.4	12.6	7.5	0.60	0.3	0.1
70	26.2	32.3	17.1	0.53	0.7	0.2
70	36.1	61.1	33.7	0.55	1.4	0.4
70	45.9	99.0	50.1	0.51	2.2	0.7
70	55.8	145.9	76.7	0.53	3.3	1.0
70	65.6	202.0	107.9	0.53	4.8	1.4
70	75.4	267.1	127.8	0.48	6.4	1.9
70	85.3	341.4	153.7	0.45	8.6	2.6
60	16.4	12.6	5.0	0.40	0.2	0.1
60	26.2	32.3	10.6	0.33	0.4	0.1
60	36.1	61.1	19.3	0.32	0.7	0.2
60	45.9	99.0	37.8	0.38	1.2	0.4
60	55.8	145.9	46.0	0.32	1.5	0.5
60	65.6	202.0	71.1	0.35	2.5	0.8

60	75.4	267.1	92.2	0.35	3.5	1.1
60	85.3	341.4	120.7	0.35	5.3	1.6
50	16.4	12.6	3.1	0.25	0.1	0.0
50	26.2	32.3	6.7	0.21	0.2	0.1
50	36.1	61.1	11.8	0.19	0.4	0.1
50	45.9	99.0	16.9	0.17	0.5	0.2
50	55.8	145.9	22.9	0.16	0.7	0.2
50	65.6	202.0	30.1	0.15	1.0	0.3
50	75.4	267.1	35.0	0.13	1.2	0.4
50	85.3	341.4	47.6	0.14	1.7	0.5
40	16.4	12.6	1.9	0.15	0.0	0.0
40	26.2	32.3	4.7	0.15	0.1	0.0
40	36.1	61.1	7.6	0.12	0.2	0.1
40	45.9	99.0	13.0	0.13	0.3	0.1
40	55.8	145.9	17.7	0.12	0.5	0.1
40	65.6	202.0	25.8	0.13	0.6	0.2
40	75.4	267.1	34.0	0.13	0.8	0.3
40	85.3	341.4	43.4	0.13	1.0	0.3
40	85.3	454.4	45.3	0.10	1.4	0.4
30	16.4	12.6	1.4	0.11	0.0	0.0
30	26.2	32.3	3.4	0.11	0.1	0.0
30	36.1	61.1	6.0	0.10	0.1	0.0
30	45.9	99.0	9.0	0.09	0.2	0.1
30	55.8	145.9	13.7	0.09	0.3	0.1
30	65.6	202.0	19.2	0.10	0.4	0.1
30	75.4	267.1	22.7	0.08	0.5	0.1
30	85.3	341.4	28.0	0.08	0.6	0.2
30	98.4	454.4	33.2	0.07	0.8	0.2

Table G - 3 - Aluminum Rotary Wing UAS

Impact angle (°)	Impact velocity (ft/s)	Kinetic energy (ft·lbf)	Internal energy dissipated by ATD chest (ft·lbf)	Energy absorbing ratio	VC _{Max}	
					ft/s	m/s
90	16.4	12.8	9.9	0.77	0.3	0.1
90	26.2	33.0	25.2	0.76	0.9	0.3
90	36.1	62.5	47.8	0.76	2.0	0.6
90	45.9	101.2	81.5	0.81	3.6	1.1
90	59.0	167.5	99.8	0.60	5.0	1.5
90	98.4	465.0	189.2	0.41	7.0	2.1
80	16.4	12.8	9.9	0.77	0.3	0.1
80	26.2	33.0	24.1	0.73	0.9	0.3
80	36.1	62.5	45.5	0.73	2.0	0.6
80	45.9	101.2	79.9	0.79	3.8	1.2
80	59.0	167.5	92.4	0.55	5.4	1.7
70	16.4	12.8	9.0	0.70	0.2	0.1
70	26.2	33.0	22.0	0.67	0.6	0.2
70	36.1	62.5	43.9	0.70	1.7	0.5
70	45.9	101.2	70.8	0.70	2.2	0.7
70	59.0	167.5	87.7	0.52	2.2	0.7
70	72.2	250.9	101.7	0.41	2.7	0.8
60	16.4	12.8	9.7	0.76	0.1	0.0
60	26.2	33.0	22.3	0.68	0.6	0.2
60	36.1	62.5	43.3	0.69	1.3	0.4
60	45.9	101.2	67.5	0.67	1.9	0.6
60	59.0	167.5	76.3	0.46	1.7	0.5
60	72.2	250.9	90.2	0.36	2.0	0.6
50	16.4	12.8	9.5	0.74	0.1	0.0
50	26.2	33.0	20.5	0.62	0.4	0.1
50	36.1	62.5	36.9	0.59	0.8	0.2
50	45.9	101.2	62.4	0.62	1.2	0.4
50	59.0	167.5	67.8	0.40	1.4	0.4
50	72.2	250.9	78.3	0.31	1.7	0.5
50	85.3	348.7	116.5	0.33	2.6	0.8

40	16.4	12.8	7.5	0.59	0.1	0.0
40	26.2	33.0	16.7	0.51	0.2	0.1
40	36.1	62.5	34.2	0.55	0.4	0.1
40	45.9	101.2	60.4	0.60	0.7	0.2
40	59.0	167.5	67.9	0.41	0.8	0.3
40	72.2	250.9	81.0	0.32	1.0	0.3
40	85.3	348.7	101.1	0.29	1.4	0.4
30	16.4	12.8	5.5	0.43	0.1	0.0
30	26.2	33.0	8.4	0.25	0.1	0.0
30	36.1	62.5	30.3	0.48	0.2	0.1
30	45.9	101.2	33.5	0.33	0.3	0.1
30	59.0	167.5	45.5	0.27	0.4	0.1
30	72.2	250.9	57.5	0.23	0.5	0.1
30	85.3	348.7	67.0	0.19	0.8	0.2
30	98.4	465.0	76.3	0.16	1.0	0.3

Table G - 4 - Engineering Plastic Rotary UAS

Impact angle (°)	Impact velocity (ft/s)	Kinetic energy (ft·lbf)	Internal energy dissipated by ATD chest (ft·lbf)	Energy absorbing ratio	VC _{Max}	
					ft/s	m/s
90	16.4	13.3	10.7	0.80	0.3	0.1
90	26.2	34.0	26.2	0.77	1.0	0.3
90	36.1	64.2	47.6	0.74	2.2	0.7
90	45.9	104.1	79.7	0.77	3.9	1.2
90	55.8	153.5	112.3	0.73	6.5	2.0
90	65.6	212.5	147.3	0.69	8.8	2.7
90	75.4	281.0	187.9	0.67	10.9	3.3
90	85.3	359.1	233.4	0.65	13.1	4.0
80	16.4	13.3	10.0	0.75	0.4	0.1
80	26.2	34.0	25.8	0.76	1.0	0.3
80	36.1	64.2	47.6	0.74	2.1	0.7
80	45.9	104.1	79.3	0.76	3.9	1.2
80	55.8	153.5	113.7	0.74	6.7	2.0
80	65.6	212.5	147.9	0.70	8.9	2.7
80	75.4	281.0	188.4	0.67	11.3	3.4
80	85.3	359.1	231.8	0.65	13.1	4.0
70	16.4	13.3	9.2	0.69	0.3	0.1
70	26.2	34.0	23.4	0.69	0.9	0.3
70	36.1	64.2	45.4	0.71	2.0	0.6
70	45.9	104.1	74.1	0.71	3.8	1.2
70	55.8	153.5	110.6	0.72	6.2	1.9
70	65.6	212.5	147.8	0.70	9.0	2.7
70	75.4	281.0	183.0	0.65	10.0	3.0
70	85.3	359.1	227.9	0.63	11.0	3.4
60	16.4	13.3	9.0	0.68	0.2	0.1
60	26.2	34.0	24.8	0.73	0.6	0.2
60	36.1	64.2	53.6	0.83	1.2	0.4
60	45.9	104.1	78.1	0.75	2.5	0.8
60	55.8	153.5	134.8	0.88	4.7	1.4
60	65.6	212.5	152.4	0.72	6.6	2.0
60	75.4	281.0	166.0	0.59	8.5	2.6
60	85.3	359.1	190.8	0.53	8.9	2.7

50	16.4	13.3	7.0	0.53	0.2	0.0
50	26.2	34.0	20.8	0.61	0.4	0.1
50	36.1	64.2	38.3	0.60	0.6	0.2
50	45.9	104.1	100.0	0.96	1.2	0.4
50	55.8	153.5	98.7	0.64	2.2	0.7
50	65.6	212.5	156.2	0.74	4.7	1.4
50	75.4	281.0	169.1	0.60	5.0	1.5
50	85.3	359.1	173.7	0.48	3.7	1.1
40	16.4	13.3	5.2	0.39	0.1	0.0
40	26.2	34.0	12.4	0.36	0.2	0.1
40	36.1	64.2	41.5	0.65	0.2	0.1
40	45.9	104.1	66.7	0.64	0.3	0.1
40	55.8	153.5	69.1	0.45	0.4	0.1
40	65.6	212.5	78.9	0.37	0.5	0.2
40	75.4	281.0	85.2	0.30	0.7	0.2
40	85.3	359.1	87.0	0.24	1.3	0.4
40	98.4	476.9	84.4	0.18	1.7	0.5
30	16.4	13.3	2.1	0.16	0.0	0.0
30	26.2	34.0	7.2	0.21	0.1	0.0
30	36.1	64.2	11.6	0.18	0.2	0.0
30	45.9	104.1	15.5	0.15	0.3	0.1
30	55.8	153.5	23.5	0.15	0.2	0.1
30	65.6	212.5	33.3	0.16	0.2	0.1
30	75.4	281.0	60.9	0.22	0.3	0.1
30	85.3	359.1	79.1	0.22	0.3	0.1
30	98.4	476.9	81.0	0.17	0.5	0.1

Appendix H. Parametric Values of the Meta Model to Describe the VC Response of ATD Chest Due to UAS Impact

Table H - 1 - Parametric Values in Equation 19

UAS	a	b	c	d	e	f	g	h	i	j
Aluminum fixed wing	7.68	-67.08	-17.55	33.21	200.92	37.06	-203.43	-30.50	-12.03	30.12
Plastic fixed wing	3.46	-33.92	0.19	-21.44	110.06	0.56	-114.70	-4.45	31.20	47.12
Aluminum rotary wing	6.53	-55.44	-18.88	54.93	163.36	32.23	-158.90	-33.34	14.01	-46.98
Plastic rotary wing	0.22	-0.55	-2.84	6.37	-1.20	7.66	-3.54	-2.79	-22.77	31.21

Appendix I. Results of UAS/Ground Impact Simulations

Table I - 1 - Aluminum Fixed Wing UAS

Impact angle (°)	Impact velocity (ft/s)	Friction coefficient	Rebounce angle (°)	Rebounce velocity (ft/s)	Rebounce distance (ft)
30	65.6	0.3	7.69	45.9	16.9
30	65.6	0.6	7.61	35.9	10.4
30	65.6	0.8	8.16	28.1	6.8
30	82.0	0.5	8.44	48.5	20.5
45	16.4	0.2	6.46	11.6	1.0
45	32.8	0.4	8.50	19.5	3.4
45	32.8	0.5	7.62	17.6	2.5
45	32.8	0.7	8.35	13.3	1.6
45	32.8	0.8	8.07	9.6	0.8
45	32.8	0.9	10.90	6.2	0.5
45	49.2	0.8	11.18	16.6	3.2
45	65.6	0.5	16.59	22.9	8.8
45	65.6	0.8	31.14	10.9	3.2
45	82.0	0.5	13.65	30.6	13.0
45	98.4	0.5	9.15	36.7	12.9
60	32.8	0.3	11.66	13.8	2.3
60	65.6	0.6	13.25	17.3	4.1
60	82.0	0.2	12.47	29.2	11.0
60	98.4	0.4	10.88	21.4	5.2
75	16.4	0.6	60.64	1.8	0.1
75	49.2	0.3	33.74	11.4	3.7
75	65.6	0.6	84.62	4.6	0.1
75	65.6	0.8	-74.70	4.0	0.3
75	65.6	0.9	-67.41	4.4	0.4

Table I - 2 - Engineering Plastic Fixed Wing UAS

Impact angle (°)	Impact velocity (ft/s)	Friction coefficient	Rebounce angle (°)	Rebounce velocity (ft/s)	Rebounce distance (ft)
30	65.6	0.3	13.04	14.23	8.31
30	65.6	0.6	16.59	10.82	6.12
30	65.6	0.8	20.92	8.09	4.25
30	82.0	0.5	17.35	15.09	11.65
45	16.4	0.2	21.47	2.87	0.57
45	32.8	0.4	29.67	4.55	1.78
45	32.8	0.5	28.90	3.85	1.26
45	32.8	0.7	16.44	3.36	0.62
45	32.8	0.8	12.92	2.24	0.22
45	32.8	0.9	34.70	0.95	0.09
45	49.2	0.8	20.01	4.27	1.18
45	65.6	0.5	21.52	6.82	3.12
45	65.6	0.8	36.81	3.57	1.23
45	82.0	0.5	24.89	9.62	6.69
45	98.4	0.5	19.96	12.21	8.86
60	32.8	0.3	29.44	3.48	1.04
60	65.6	0.6	36.83	2.84	0.78
60	82.0	0.2	27.14	8.88	6.09
60	98.4	0.4	29.95	6.29	3.36
75	16.4	0.6	84.11	2.24	0.10
75	49.2	0.3	65.52	1.47	0.17
75	65.6	0.6	-61.21	2.08	0.37
75	65.6	0.8	-45.91	2.23	0.50
75	65.6	0.9	-40.48	2.60	0.68

Table I - 3 - Aluminum Rotary Wing UAS

Impact angle (°)	Impact velocity (ft/s)	Friction coefficient	Rebounce angle (°)	Rebounce velocity (ft/s)	Rebounce distance (ft)
30	65.6	0.3	4.53	46.9	10.7
30	65.6	0.6	4.96	38.3	7.8
30	65.6	0.8	7.97	32.7	9.1
30	82.0	0.5	3.95	50.9	11.0
40	16.4	0.2	16.45	10.8	2.0
40	32.8	0.4	18.18	18.3	6.1
40	32.8	0.5	19.40	16.0	5.0
40	32.8	0.7	22.18	13.8	4.1
40	32.8	0.8	23.76	13.2	4.0
40	32.8	0.9	24.70	12.6	3.8
40	49.2	0.8	9.40	18.5	2.1
40	65.6	0.5	7.65	30.5	5.8
40	65.6	0.8	7.89	22.4	3.4
40	82.0	0.5	6.26	37.6	7.4
40	98.4	0.5	5.28	43.5	11.1
50	32.8	0.3	12.29	15.4	3.1
50	65.6	0.6	8.81	16.9	2.7
50	82.0	0.2	11.89	38.2	18.1
50	98.4	0.4	7.61	33.4	9.1
60	16.4	0.6	63.02	2.0	0.1
60	49.2	0.3	11.34	13.8	2.3
60	65.6	0.6	23.06	8.9	1.8
60	65.6	0.8	30.96	6.9	1.3
60	65.6	0.9	26.22	7.3	1.3

Table I - 4 - Engineering Plastic Rotary Wing UAS

Impact angle (°)	Impact velocity (ft/s)	Friction coefficient	Rebounce angle (°)	Rebounce velocity (ft/s)	Rebounce distance (ft)
30	65.6	0.3	11.43	46.2	25.4
30	65.6	0.6	19.91	37.5	27.5
30	65.6	0.8	21.71	31.8	21.2
30	82.0	0.5	12.59	50.4	32.9
40	16.4	0.2	15.28	14.7	3.4
40	32.8	0.4	33.12	20.2	11.5
40	32.8	0.5	22.01	13.1	3.7
40	32.8	0.7	27.36	12.6	4.0
40	32.8	0.8	28.65	12.5	4.1
40	32.8	0.9	28.04	12.6	4.1
40	49.2	0.8	36.40	16.9	8.4
40	65.6	0.5	11.92	31.5	12.3
40	65.6	0.8	20.64	21.3	9.2
40	82.0	0.5	8.05	39.4	13.3
40	98.4	0.5	12.57	48.4	30.3
50	32.8	0.3	31.69	14.1	5.5
50	65.6	0.6	16.93	20.2	7.0
50	82.0	0.2	17.86	41.5	30.6
50	98.4	0.4	18.60	36.6	24.8
60	16.4	0.6	-11.20	6.8	0.5
60	49.2	0.3	-31.55	6.6	1.2
60	65.6	0.6	45.73	10.9	3.7
60	65.6	0.8	57.57	7.9	1.7
60	65.6	0.9	55.97	7.7	1.7

Appendix J. Parametric Values of the Meta Model to Describe the Rebound Distance of UAS After Collision on the Ground

Table J - 1 - Parametric Values in Equation 21

UAS	a	b	c	d	e	f	g	h	i	j
Aluminum fixed wing	-0.113	-0.213	4.094	-0.863	0.533	-1.364	0.248	-6.815	2.083	-1.052
Plastic fixed wing	0.761	-4.556	4.449	-1.621	6.412	0.848	0.581	-9.949	3.705	-1.645
Aluminum rotary wing	0.594	-3.561	1.148	-0.314	5.202	0.349	0.631	0.027	-0.272	-1.772
Plastic rotary wing	2.089	-14.432	1.584	-0.298	26.052	2.641	0.785	-3.364	-1.174	-2.159